



Universidade do Porto
FEUP Faculdade de
Engenharia

Development of an ultrasonic frequency equipment for fatigue testing

Ricardo Vieira Lobo

Dissertation submitted to:
Faculty of Engineering of the University of Porto

For the degree of:
Masters in Mechanical Engineering

Advisor:
Professor Abílio de Jesus (University of Porto)

Co-Advisors:
MSc. Felipe Klein Fiorentin (INEGI)
Professor Hélder Puga (University of Minho)
Dr. Filipe Silva (INEGI)

Department of Mechanical Engineering
Faculty of Engineering of the University of Porto

Porto, 2022

The work presented in this dissertation was performed at the INEGI laboratory of Mechanical Testing.

Ricardo Vieira Lobo
E-mail: up201706652@fe.up.pt

Faculdade de Engenharia da Universidade do Porto
Departamento de Engenharia Mecânica
Rua Dr. Roberto Frias s/n,
4200-465 Porto
Portugal

Abstract

Nowadays, it is increasingly common to design mechanical components taking into account their longevity. In the aeronautical, railway and automotive industries, the number of mechanical components subjected to a number of load cycles between 10^7 and 10^{10} cycles has been increasing. In many materials recurrently used in the engineering world, fatigue failures have been verified after 10^7 load cycles, that is, in the Very High Cycle Fatigue (VHCF) regime. Obtaining information about the behavior of different materials in the VHCF regime is becoming more crucial, and with the development of ultrasonic testing equipment it is possible to experimentally define the behavior of different materials in this regime.

The main objective of this dissertation is the development of an ultrasonic fatigue testing equipment which operates at a frequency of 20 kHz. Thereby, the designed components that integrate the dynamic system of this fatigue equipment need to have their first longitudinal natural frequency similar to the excitation frequency of the utilized piezoelectric transducer, 20 kHz. This equipment needs to be able to apply a maximum static load of 10 kN to the specimen, in order to carry out tests with different stress ratios, R . Thereby, in a first phase, it was carried out a literature review on the history and evolution of the VHCF regime, principles of fracture mechanics, ultrasonic machines and the expected behavior of materials in the VHCF regime. The literature review was followed by a conceptual design phase, in which the final layout of the ultrasonic fatigue testing equipment was defined in SOLIDWORKS.

After the final layout was established, a functional validation of each of the components and the selection of the various mechanical components were conducted. For this purpose, analytical calculations and different finite element analyses on Abaqus were carried out, static analysis for certain components and modal analysis in applicable cases. Afterwards, the manufacturing materials of the various components were established and presented. Subsequently, the final stiffness of the equipment was determined. Then, technical drawings of the various ultrasonic fatigue equipment components were produced and the manufacturing process of different components of the fatigue equipment began.

The main goal of this dissertation has been accomplished. The project of a ultrasonic fatigue testing equipment that operates at a frequency of 20 kHz and is capable of applying a static load of 10 kN to the specimen has been concluded.

Keywords: Fatigue, Very High Cycle Fatigue, Ultrasonic, Stress Ratio, Finite Element Method, Fatigue Testing.

Resumo

Actualmente, é cada vez mais comum projetar componentes mecânicos tendo em conta a sua longevidade. Nas indústrias aeronáutica, ferroviária e automóvel tem vindo a aumentar o número de componentes mecânicos sujeitos a ciclos de carga entre os 10^7 e 10^{10} ciclos. Em muitos materiais utilizados recorrentemente no mundo da engenharia, as falhas de fadiga têm sido verificadas após os 10^7 ciclos de carga, ou seja, no regime Very High Cycle Fatigue, VHCF. A obtenção de informação acerca do comportamento de diversos materiais no regime VHCF é cada vez mais crucial, sendo que, com o desenvolvimento de equipamentos de teste ultra-sónicos é possível definir experimentalmente o comportamento de diversos materiais neste regime.

O objetivo principal desta dissertação é o desenvolvimento de um equipamento de testes de fadiga ultra-sónico que opere a uma frequência de 20 kHz. Deste modo, os componentes projetados para integrar o sistema dinâmico deste equipamento de fadiga, necessitam de ter a sua primeira frequência natural longitudinal semelhante à frequência de excitação do transdutor piezoelétrico utilizado, 20 kHz. Este equipamento necessita de ser capaz de aplicar uma carga estática máxima de 10 kN ao provete a ser testado, de modo a realizar testes com diferentes razões de tensão, R . Sendo assim, numa primeira fase foi feita uma revisão literária sobre a história e a evolução do regime VHCF, princípios da mecânica da fractura, máquinas ultra-sónicas e o comportamento esperado dos materiais no regime VHCF. A isto, seguiu-se uma fase de *design* conceptual, na qual o *layout* final do equipamento de testes de fadiga ultra-sónico ficou definido no SOLIDWORKS.

Após o *layout* final ser definido, procedeu-se à validação funcional de cada um dos componentes e à escolha dos diversos componentes mecânicos. Isto foi feito com recurso a cálculos analíticos e diversas análises de elementos finitos no Abaqus, foram realizadas análises estáticas a diversos componentes e análises modais aos casos aplicáveis. De seguida, procedeu-se à determinação dos materiais de fabrico dos diversos componentes. Posteriormente, realizou-se a determinação da rigidez final do equipamento. Por fim, foram realizados os desenhos técnicos dos diversos componentes do equipamento ultra-sónico e iniciou-se a produção dos mesmos.

O principal objetivo da dissertação foi atingido, sendo que o projeto do equipamento de testes de fadiga ultra-sónico que opera a uma frequência de 20 kHz e que é capaz de aplicar uma carga estática de 10 kN ao provete a ser testado foi concluído.

Palavras-chave: Fadiga, Very High Cycle Fatigue, Ultra-Sónico, Razão de Tensão, Método dos Elementos Finitos, Testes de Fadiga.

“Esforço,
Dedicação,
Devoção,
E Glória.”

Dedicado aos meus avós

Agradecimentos

Em primeiro lugar, gostaria de agradecer aos meus pais por garantirem que nunca me faltasse nada e por toda a força e apoio que me deram ao longo do meu percurso académico.

Gostaria também de agradecer à minha irmã, Raquel, por estar sempre presente para mim.

Aos meus eternos avós por me apoiarem sempre e por nunca me deixarem desistir.

À minha namorada, Carlota, por me motivar diariamente e por me meter sempre a rir quando eu mais preciso.

A todos os meus amigos que me acompanharam durante esta jornada da minha vida e com quem eu criei imensas memórias.

Ao Professor Abílio de Jesus pelos seus conhecimentos, por me escolher para a elaboração do presente trabalho e por sempre me guiar para o caminho correto ao longo da realização deste projeto.

Ao Eng. Felipe Fiorentin por toda a sua ajuda e disponibilidade. Os seus conhecimentos, experiência e paciência foram essenciais para que o projeto fosse concluído.

À Eng. Rita Dantas pela sua contínua vontade de ajudar e disponibilidade.

Ao Professor Hélder Puga pela partilha de conhecimentos.

Ao Eng. Filipe Silva pela sua orientação e ajuda.

Muito Obrigado

Ricardo Lobo

Institutional Acknowledgements

Firstly, I would like to express my deepest appreciation to FCT - Foundation for Science and Technology for supporting the work developed in the present document through the project Giga-Cycle Fatigue Behaviour of Engineering Metallic Alloys (GCYCLEFAT), with the reference PTDC/EME-EME/7678/2020.

Additionally, I would like to express my gratitude to INEGI – Institute of Science and Innovation in Mechanical and Industrial Engineering for providing me an excellent working environment at the laboratory of mechanical testing.

Lastly, I would be remiss in not mentioning all INEGI collaborators who welcomed me and made me feel included.

Contents

1	Introduction	1
1.1	Framework and motivation	1
1.2	Project objectives	2
1.3	Outline	3
1.4	Tools	3
2	Background Theory	5
2.1	History and evolution of the VHCF	5
2.2	Ultrasonic machines	8
2.2.1	Typical ultrasonic testing machine	8
2.2.2	Elastic waves, analytical stresses and displacements	11
2.2.2.1	Constant transversal section specimen	13
2.2.2.2	Variable transversal section specimen	16
2.2.3	Different types of ultrasonic machines	20
2.2.3.1	Ultrasonic testing at unconventional conditions	20
2.2.3.2	Ultrasonic torsion test equipment	22
2.2.3.3	Tension/Torsion ultrasonic fatigue testing equipment	24
2.2.3.4	Three-point bending fatigue testing machine	25
2.2.3.5	Ultrasonic fretting fatigue testing	26
2.2.4	Ultrasonic machines and parts available in the market	28
2.3	Behavior of the materials under the VHCF regime	31
2.4	Fundamentals of fracture mechanics	36
3	Structural Development of an Ultrasonic Fatigue Testing Equipment	41
3.1	Ultrasonic testing equipment requirements	41
3.2	Pre-existing structure	42
3.3	Layout of the ultrasonic machine	44
3.3.1	First iteration	44
3.3.2	Final design of the ultrasonic fatigue testing equipment	47
3.3.2.1	Section A	49

3.3.2.2	Section B	52
3.3.2.3	Section C	55
3.3.2.4	Section D	59
3.4	Analytical and numerical analysis of the designed ultrasonic fatigue equipment	61
3.4.1	Analysis of the original pre-structure	61
3.4.2	Analysis of the new designed components and subassemblies	71
3.4.2.1	Analysis and validation of Section A subassembly	72
3.4.2.2	Analysis and validation of Section B subassembly	77
3.4.2.3	Analysis and validation of Section C subassembly	90
3.4.3	Thread stresses	108
3.4.4	Ultrasonic booster and horn	111
3.5	Stiffness evaluation of the fatigue equipment	125
3.6	Assembly procedure to execute a VHCF test in the developed equipment	132
3.6.1	Testing specimens at a $R=-1$ constant stress ratio	132
3.6.2	Testing specimens at a $R>-1$ stress ratio	133
3.7	Bill of Materials	136
3.8	Estimated cost of the ultrasonic fatigue equipment	138
4	Conclusions and Future Work	139
4.1	Conclusions	139
4.2	Future work	140
A	Derivation of Equations Presented in Chapter 2	147
A.1	Dynamic Equilibrium Equation	147
A.2	Resonance Length and Amplitude of Vibration	149
B	Titanium Ti-6Al-4V Properties	153
C	Definition Drawings of Components	157
D	Bolts Tightening Torque	173

Abbreviations

FCT	Foundation for Science and Technology
FEA	Finite Element Analysis
HCF	High Cycle Fatigue
INEGI	Institute of Science and Innovation in Mechanical and Industrial Engineering
LCF	Low Cycle Fatigue
<i>S-N</i> Curve	Stress amplitude - Number of loading cycles Curve
VHCF	Very-High Cycle Fatigue

Symbols

a	Length of the crack
a_c	Crack length at instability
a_f	Final crack length
a_i	Initial crack length
A_0	Vibration amplitude
c	Velocity of wave propagation
C	Bearing basic dynamic load rating
C_0	Bearing basic static load rating
d_a	Abutment diameter shaft
d_b	Nominal diameter of thread
d_p	Pitch diameter of thread
d_r	Root diameter of thread
D_a	Abutment diameter housing
e	Volume dilatation
E	Young's modulus
E_d	Dynamic elastic modulus
f	Excitation frequency
i	Radius of gyration
k	Stiffness
K_f	Practical stress concentration factor
K_t	Stress concentration factor
K_I	Stress intensity factor for the first mode
K_T	Torque coefficient
K_{IC}	Fracture toughness of the material
n_e	Effective number of threads
N_f	Number of cycles a component can withstand before failure
p	Pitch
P_{cr}	Critical load
q	Notch sensitivity factor
\dot{q}	Average power density dissipated
Q	First moment of area
r_a	Fillet radius housing
r_b	Fillet radius shaft
R	Stress ratio
SF	Safety factor
$S(x)$	Cross sectional area
t	Time

T_t	Preload tightening torque
T_{nf}	Friction torque
u, v and w	Displacements over the Cartesian coordinates
x, y and z	Cartesian coordinates
Y	Stress intensity magnification factor
$\frac{\Delta a}{\Delta N}$	Crack growth rate
ΔK	Stress intensity range
ΔK_I	Stress intensity range for the first mode
ΔK_{th}	Fatigue crack propagation threshold
∇^2	Laplace operator
ε	Strain
η	Loss coefficient
λ	Slenderness ratio
ν	Poisson's ratio
ρ	Density
σ	Stress
σ_a	Stress amplitude
σ_b	Thread bending stress
σ_{BD}	Bending stress
σ_{f0}	Endurance limit
σ_{f0}^c	Practical endurance limit
σ_m	Mean stress
σ_t	Direct tensile stress
τ_{tr-max}	Transverse shearing stress
τ_s	Torsional shear
ω_n	Natural frequency

List of Figures

Figure 2.1	Average number of loading cycles of some components	5
Figure 2.2	Layout of basic ultrasonic testing machine and its stress and displacement fields	8
Figure 2.3	Layout of basic Ultrasonic testing machine	9
Figure 2.4	Layout of Ultrasonic testing machine for testing materials at different values of R	11
Figure 2.5	Propagation of Longitudinal Waves	12
Figure 2.6	Displacement and strain variation along an elastic bar	13
Figure 2.7	Ultrasonic variable cross section specimen	16
Figure 2.8	Ultrasonic fatigue testing at high temperatures	21
Figure 2.9	Ultrasonic fatigue testing at low temperatures	21
Figure 2.10	Bathias's High pressure piezoelectric fatigue machine	22
Figure 2.11	Ultrasonic torsion test equipment in Bathias's laboratory	23
Figure 2.12	Torsional ultrasonic fatigue test system schematic figure	23
Figure 2.13	Torsional piezoelectric transducer, ultrasonic horn and specimen	24
Figure 2.14	3D model of the multiaxial fatigue testing device	24
Figure 2.15	Horn and specimen for tension/torsion biaxial testing	25
Figure 2.16	Bathias's three-point bending fatigue machine	26
Figure 2.17	Ultrasonic fretting fatigue test system developed in Bathias's laboratory	27
Figure 2.18	MEG 20 - Fully reversed fatigue machine - 3R	28
Figure 2.19	Ultrasonic fatigue testing system USF-2000A - Shimadzu	29
Figure 2.20	Ultrasonic transducer 3300W – 20kHz - Sonic Power	29
Figure 2.21	20 kHz Catenoidal Tapped Horn made of Titanium - Sonitek	30
Figure 2.22	Boosters with different amplifications (ratio between the displacement of the top and displacement of the bottom) - BRANSON	30
Figure 2.23	Mechanisms of fatigue initiation	31
Figure 2.24	"Fish-eye" with focus on the internal inclusion	32

Figure 2.25	Illustration of a fracture surface showing different stages of VHCF crack development	33
Figure 2.26	Traditional concept of $S-N$ curve	33
Figure 2.27	Stepwise $S-N$ curve for a carburized steel	34
Figure 2.28	General stepwise $S-N$ curve for a high strength steel	35
Figure 2.29	Loading modes of crack propagation	36
Figure 2.30	Crack length over number of cycles for different stress ranges .	37
Figure 2.31	Crack growth per cycle as a function of the stress intensity range	38
Figure 3.1	Pre-existing structure	42
Figure 3.2	Power Screw and Linear Ball Bearing existing in the original structure	43
Figure 3.3	First design of the ultrasonic fatigue testing equipment	44
Figure 3.4	Schematic figure of an universal traction machine	46
Figure 3.5	Section view of the final design of the ultrasonic machine with the identification of the corresponding sections	48
Figure 3.6	Section A shown in more detail	49
Figure 3.7	Section view of Section A with respective component identification	50
Figure 3.8	20 kHz Piezoelectric Transducer MPInterconsulting - 3KW . . .	50
Figure 3.9	Top view of the Vibration Absorbing Flange	51
Figure 3.10	Section view of the Vibration Absorbing Flange	51
Figure 3.11	Section B shown in more detail	52
Figure 3.12	Section view of the Section B	53
Figure 3.13	Original Linear Ball Bearing fixing hardware	54
Figure 3.14	1-RSCC3/500KG-1 Load Cell from HBM	55
Figure 3.15	Zoomed view of section C	55
Figure 3.16	Section view of the Section C	56
Figure 3.17	52210 - SKF - Double direction thrust ball bearing	57
Figure 3.18	Nomenclature and identification of the different abutment dimensions of the double direction thrust ball bearing	57
Figure 3.19	View of the connection between Section B and Section C	58
Figure 3.20	Section view of the connection between Section B and Section C	59
Figure 3.21	Close-up view of Section D with increased transparency in the lower cast iron block	59
Figure 3.22	Section view of the Section D	60
Figure 3.23	Chrome Steel Guide Shaft From The Original Structure	61

Figure 3.24	Buckling end conditions	62
Figure 3.25	Identification of the original upper cast iron block	64
Figure 3.26	Free body diagram of the upper cast iron block	65
Figure 3.27	Shear force distribution of the upper cast iron block	65
Figure 3.28	Bending moment distribution of the upper cast iron block	66
Figure 3.29	Second Moment of area of section of rectangular beam	67
Figure 3.30	Bending stress distribution along the cross sectional area at $x = \frac{L}{2}$	68
Figure 3.31	Shear stress distribution along the cross sectional area at $x = \frac{L}{2}$	69
Figure 3.32	Von Mises equivalent stress distribution along the cross sectional area at $x = \frac{L}{2}$	69
Figure 3.33	Deflection of the upper cast iron block	71
Figure 3.34	Symmetry view of the subassembly of upper cast iron block and vibration absorbing flange on Abaqus	72
Figure 3.35	Demonstration of the application of symmetry conditions on the Section A subassembly	73
Figure 3.36	Mesh density of the Section A subassembly	73
Figure 3.37	Boundary condition and loads on the Section A subassembly without the symmetry conditions	74
Figure 3.38	Von Mises stress on the full Section A subassembly (MPa)	75
Figure 3.39	Von Mises stress on the upper cast iron block (MPa)	75
Figure 3.40	Vertical displacement on the upper cast iron block (mm)	75
Figure 3.41	Von Mises stress on the vibration absorbing flange (MPa)	76
Figure 3.42	Vertical displacement on the vibration absorbing flange (mm)	76
Figure 3.43	Final design of the S690 steel support plate	78
Figure 3.44	Free body diagram of the support plate	79
Figure 3.45	Shear force distribution of the support plate	79
Figure 3.46	Bending moment distribution of the support plate	80
Figure 3.47	Bending stress distribution along the cross sectional area of the support plate at $x = \frac{L}{2}$	81
Figure 3.48	Shear stress distribution along the cross sectional area of the support plate at $x = \frac{L}{2}$	81
Figure 3.49	Von Mises equivalent stress distribution along the cross sectional area of the support plate at $x = \frac{L}{2}$	82
Figure 3.50	Deflection of the support plate	83
Figure 3.51	Symmetry view of the Section B subassembly presented in the Figures 3.11 and 3.12 on Abaqus	84
Figure 3.52	Mesh density of the Section B subassembly	84

Figure 3.53	Demonstration of the application of symmetry conditions on the Section B subassembly	85
Figure 3.54	Boundary condition and loads on the Section B subassembly without the symmetry conditions	86
Figure 3.55	Von Mises stress on the full Section B subassembly (MPa) . . .	86
Figure 3.56	Von Mises stress on the support plate (MPa)	87
Figure 3.57	Vertical displacement on the support plate (mm)	87
Figure 3.58	Von Mises stress on the locking support (MPa)	87
Figure 3.59	Vertical displacement on the locking support (mm)	88
Figure 3.60	Von Mises stress on the booster support (MPa) - Front	88
Figure 3.61	Von Mises stress on the booster support (MPa) - Back	88
Figure 3.62	Vertical displacement on the booster support (mm) - Front . . .	89
Figure 3.63	Vertical displacement on the booster support (mm) - Back . . .	89
Figure 3.64	Final design of the S690 steel traction plate	91
Figure 3.65	Free body diagram of the S690 steel traction plate	91
Figure 3.66	Shear force distribution of the traction plate	92
Figure 3.67	Bending moment distribution of the traction plate	92
Figure 3.68	Bending stress distribution along the cross sectional area of the traction plate at $x = \frac{L}{2}$	93
Figure 3.69	Shear stress distribution along the cross sectional area of the traction plate at $x = \frac{L}{2}$	94
Figure 3.70	Von Mises equivalent stress distribution along the cross sectional area of the traction plate at $x = \frac{L}{2}$	94
Figure 3.71	Deflection of the traction plate	96
Figure 3.72	Bolt tightening torque influence analysis assembly on Abaqus .	97
Figure 3.73	Mesh density of the bolt tightening torque influence analysis .	97
Figure 3.74	Von Mises stress on the section view of the assembly of the bolt tightening torque influence analysis (MPa)	98
Figure 3.75	Von Mises stress on the section view of the bearing holder (MPa)	99
Figure 3.76	Vertical displacement on the section view of the bearing holder (mm)	99
Figure 3.77	Von Mises stress on the section view of the bearing solid ring (MPa)	100
Figure 3.78	Symmetry view of the Section C subassembly presented in the Figures 3.15 and 3.16 on Abaqus	101
Figure 3.79	Mesh density of the Section C subassembly on Abaqus	101

Figure 3.80	Demonstration of the application of symmetry conditions on the Section C subassembly	102
Figure 3.81	Boundary condition and loads on the Section C subassembly without the symmetry conditions	103
Figure 3.82	Von Mises stress on the full Section C subassembly (MPa)	104
Figure 3.83	Von Mises stress on the traction plate (MPa)	104
Figure 3.84	Vertical displacement on the traction plate (mm)	104
Figure 3.85	Von Mises stress on the simplified solid bearing (MPa)	105
Figure 3.86	Vertical displacement on the simplified solid bearing (mm)	105
Figure 3.87	Von Mises stress on the upper bearing case (MPa)	105
Figure 3.88	Vertical displacement on the upper bearing case (mm)	106
Figure 3.89	Von Mises stress on the lower bearing case (MPa)	106
Figure 3.90	Vertical displacement on the lower bearing case (mm)	106
Figure 3.91	Critical points and stress components	108
Figure 3.92	Loss coefficient, η , against Young's Modulus, E , chart	111
Figure 3.93	3D Booster design and Abaqus Modal Analysis assembly	113
Figure 3.94	Abaqus Modal Analysis on the chosen Booster (m)	114
Figure 3.95	Abaqus Modal Analysis on the chosen Booster - Vibration Node (m)	114
Figure 3.96	Horn measurements and modal analysis	115
Figure 3.97	Results of the different Abaqus modal simulations regarding the Horn	116
Figure 3.98	Results of the final Abaqus modal simulation regarding the Horn	117
Figure 3.99	Load and boundary condition of the static Abaqus simulation regarding the Horn	118
Figure 3.100	Results of the static Abaqus simulation regarding the Horn (Pa)	118
Figure 3.101	Results of the dynamic Abaqus simulation regarding the Horn (Pa)	119
Figure 3.102	Results of the dynamic Abaqus simulation regarding the Horn (m)	120
Figure 3.103	Identification of the dimensions for the K_t calculation	123
Figure 3.104	Equivalent spring system of the ultrasonic fatigue equipment	126
Figure 3.105	Finite element analysis on the Squared Section Bar	128
Figure 3.106	Specimen drawing	128
Figure 3.107	Finite element analysis on the Resonant System	129
Figure 3.108	Assembly to realize fully reversed ultrasonic fatigue tests	132
Figure 3.109	First part of the assembly procedure to conduct ultrasonic fatigue tests at a stress ratio $R > -1$	133

Figure 3.110 Second part of the assembly procedure to conduct ultrasonic fatigue tests at a stress ratio $R > -1$ 134

Figure 3.111 Last part of the assembly procedure to conduct ultrasonic fatigue tests at a stress ratio $R > -1$ 135

Figure A.1 Balance of forces on an element of length dx 147

List of Tables

Table 2.1	Time consumed on ultrasonic and conventional machines	6
Table 3.1	Component identification of Figure 3.3	45
Table 3.2	Component identification of Figure 3.7	50
Table 3.3	Component identification of Figure 3.12	53
Table 3.4	Component identification of Figure 3.16	56
Table 3.5	Performance parameters of the 52210 - SKF - Double direction thrust ball bearing	57
Table 3.6	Abutment dimensions	57
Table 3.7	Component identification of Figure 3.22	60
Table 3.8	Number of elements of each component of the subassembly presented in the Figure 3.36	74
Table 3.9	Mechanical Properties of the AISI P20 steel at 20°C	77
Table 3.10	Mechanical Properties of the S690 Structural Steel	78
Table 3.11	Number of elements of each component of the subassembly presented in the Figure 3.52	85
Table 3.12	Number of elements of each component of the subassembly presented in the Figure 3.73	98
Table 3.13	Number of elements of each component of the subassembly presented in the Figure 3.79	102
Table 3.14	Minimum Values of the Mechanical Properties of the Ti-6Al- 4V at room temperature	112
Table 3.15	Number of elements of each component of the Booster Modal Analysis	113
Table 3.16	Number of elements of each component of the Horn Modal Analysis	116
Table 3.17	Surface Condition Modification Factor	122
Table 3.18	Ultrasonic Horn Dimensions	123
Table 3.19	Number of elements of each component of the Resonant Static Analysis	129

Table 3.20 Vertical displacement of the different parts of the fatigue equipment 130

Table 3.21 Utilized Components from the Original Structure 136

Table 3.22 Designed and Chosen Components 136

Table 3.23 Fixing Hardware 137

Table 3.24 Estimated Price for Manufacturing the Designed Components . 138

Table 3.25 Price of the Chosen Components 138

Chapter 1

Introduction

In Section 1.1, the framework and motivations of the present dissertation are presented. The project objectives are discussed in Section 1.2, and the outline of this dissertation is presented in Section 1.3. Finally, a description of the tools used to develop the present project is presented in Section 1.4.

1.1 Framework and motivation

Understanding the fatigue behavior of materials is essential in the current engineering world. The ability to accurately predict the longevity of materials permits the creation of more reliable and, of course, safer components. Nowadays, fatigue life is one of the most important design criteria of an engineering component and is measured by the number of load cycles it can withstand before fatigue failure takes place [1]. Based on the fatigue life concept, it is possible to divide the fatigue in three regimes according to the number of load cycles to failure. When the failure occurs between 10^4 and 10^5 loading cycles the regime is called Low Cycle Fatigue, LCF. When the failure occurs between 10^5 and 10^7 loading cycles the regime is called High Cycle Fatigue, HCF. For failures above 10^7 loading cycles the regime is called Very High Cycle Fatigue, VHCF [2].

In the modern world, the number of mechanical components designed to withstand a number of loading cycles superior to 10^7 has been increasing in the aerospace, automotive, military and transportation industries, raising the interest in the fatigue behaviour of different materials in the VHCF regime. However, the fatigue studies carried out within the last century have been mainly focused on the LCF and HCF regimes, due to the costs and time constraints that would result from testing materials in the VHCF regime in conventional fatigue machines. Therefore, the development of high power piezoceramic actuators allowed the development of ultrasonic fatigue testing machines that are capable of experimentally defining the behaviour of materials in the VHCF regime in significantly less time when compared with the conventional hydraulic fatigue machines [3].

This dissertation integrates the Giga-Cycle Fatigue Behaviour of Engineering Metallic Alloys research project by carrying out the structural development of an ultrasonic fatigue testing equipment. The developed work was performed at Institute of Science and Innovation in Mechanical and Industrial Engineering (INEGI).

1.2 Project objectives

This dissertation's primary objective is to develop an ultrasonic fatigue testing equipment under the following constraints:

- A dynamic system that has a resonance frequency near the excitation frequency of the piezoelectric transducer, 20 kHz;
- Reuse as many components as possible from a pre-existing structure;
- The dynamic components must be designed in order to be able to considerably amplify the external displacement imposed by the piezoelectric transducer;
- The developed equipment must be capable of performing fully reversed longitudinal ultrasonic fatigue tests, $R = -1$, and non fully reversed ultrasonic fatigue tests, $R > -1$;
- The developed equipment must be able to apply a maximum 10 kN static load to the specimen;
- The ultrasonic fatigue equipment must be able to measure the static load applied to the specimen.

To ensure that the main goal is achieved, multiple intermediate objectives were established:

- Literature review on the history and evolution of the VHCF;
- Literature review on the principles of fracture mechanics;
- Literature review on the ultrasonic machines, namely concerning the longitudinal ultrasonic testing machines;
- Literature review on the expected behavior of materials under the VHCF regime;
- Study and establishment of the final layout of the ultrasonic fatigue testing equipment, complying with the parameters set for the present project;
- Static analytical analysis and Finite Element analysis on the different designed components, for purposes of validation;
- Mechanical components selection and definition of the manufacturing material of the different designed components;

- Analytical determination of the final stiffness of the equipment and the load/rotation ratio of the utilized power screw;
- Production of the technical drawings of the various ultrasonic equipment components.

1.3 Outline

The dissertation is divided into four different chapters:

- **Introduction:** The framework and motivation of the thesis are presented. Additionally, the main goals and steps to achieve them are described;
- **Background Theory:** This chapter presents a literature review on the main topics that concern this dissertation: History and evolution of the VHCF regime, principles of fracture mechanics, ultrasonic machines and the expected behaviour of materials under the VHCF regime;
- **Structural Development of an Ultrasonic Fatigue Testing Equipment:** In this chapter, the pre-existing structure is presented and analyzed. Additionally, the final layout of the equipment is established and all the designed and chosen components are validated. Furthermore, the stiffness of the equipment and the load/rotation ratio of the utilized power screw are analytically calculated;
- **Conclusions and Future Work:** The final chapter of the dissertation includes the final remarks of the developed work and a discussion about future works.

1.4 Tools

The following softwares were utilized for the development of this dissertation:

- **SOLIDWORKS** - development of the CAD model of the final layout of the ultrasonic fatigue testing equipment;
- **Abaqus** - Finite Element analysis.

Chapter 2

Background Theory

This chapter's goal is to introduce readers to the foundations of VHCF, Very High Cycle Fatigue, regime testing equipments. The fundamentals of fracture mechanics will be discussed, additionally an approach to the ultrasonic fatigue testing equipments, their key characteristics, and current solutions available in the industry will be presented, as well as a review of the behavior of materials under the VHCF regime.

2.1 History and evolution of the VHCF

In the field of mechanical engineering, many components are subjected to cyclic loading, motor parts, vehicle parts, railway wheels, rails, bridges, medical equipment, and extremely pressured power plant components including engines and rotors must withstand more than 10^7 cycles of loading. These high numbers of cycles can be a result from high frequency or a long product life. In the Figure 2.1 it is shown the average number of cycles that various components go through over their lifetime [4].

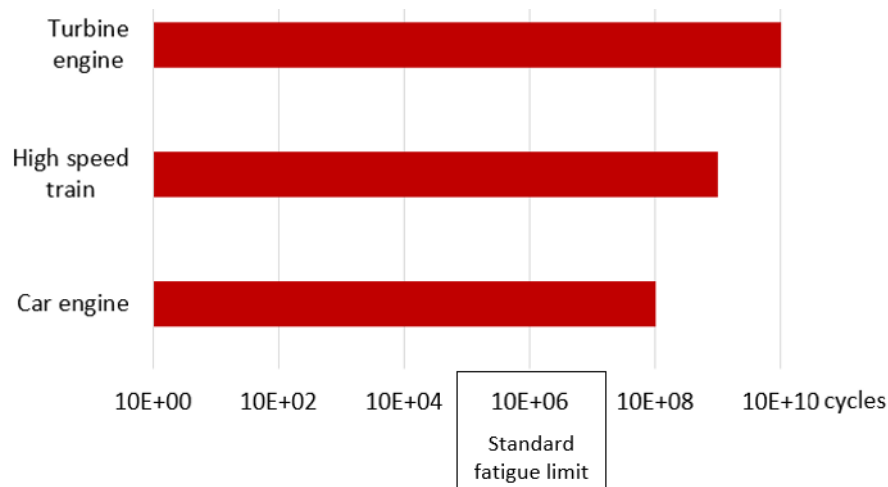


Figure 2.1: Average number of loading cycles of some components

It is possible to divide the fatigue in three regimes according to the number of cycles to failure. When the failure occurs between 10^4 and 10^5 loading cycles the regime is called Low Cycle Fatigue, LCF. When the failure occurs between 10^5 and 10^7 loading cycles the regime is called High Cycle Fatigue, HCF. For failures above 10^7 loading cycles the regime is called Very High Cycle Fatigue, VHCF [2].

At the close of 20th century, the concept of materials failing after a large number of cycles became stronger in the academy, particularly in Japan. Afterwards in 1999, Bathias stated that there is no infinite fatigue life in metallic materials. Assuming that the fatigue life of engineering components and structures can range above 10^7 cycles, it is very important to determine a safe fatigue strength up to 10^{10} cycles, this is in the VHCF's regime [4, 5, 6].

Generally, the shape of the *S-N* curve, Stress amplitude - Number of loading cycles Curve, beyond 10^7 cycles is unknown except in some statistical approaches, however this is not a very rigorous method [6]. Testing samples up to 10^{10} cycles in a conventional fatigue machine creates a problem. It would be very expensive and time consuming. Just to exemplify, testing one sample up to 10^9 cycles on a conventional servo-hydraulic machine operating at 100 Hz would take more than three years for a single specimen [4]. As a result, it's no surprise that achieving results under the VHCF regime necessitated the use of a different testing procedure.

The ultrasonic fatigue testing methods were developed to give a reliable method of testing specimens up to fatigue failure in a much faster and less expensive manner than the conventional testing methods. The frequency of ultrasonic fatigue testing ranges from 15 kHz to 30 kHz, with a typical frequency being 20 kHz [4]. In Table 2.1, the differences in time used by conventional and ultrasonic machines for various numbers of cycles in the VHCF regime are compared [7].

Table 2.1: Time consumed on ultrasonic and conventional machines.

Number of Cycles	Conventional(100 Hz)	Ultrasonic(20 kHz)
10^7	1 day	9 minutes
10^9	4 months	14 hours
10^{10}	3 years	6 days

Near the beginning of the 20th century, Hopkinson developed the first 116 Hz electromagnetic resonance device, which cleared the way for ultrasonic fatigue testing. The maximum frequency of fatigue testing with a mechanically system had never exceeded 33 Hz before that.

In 1925, Jenkin used similar techniques to test copper, iron, and steel wires at the frequency of 2.5 kHz and in 1929, Jenkin collaborated with Lehmann to develop a pulsating air resonance system that were capable of achieving a frequency of 10 kHz [4].

The year 1950 is remembered as a major milestone in the evolution of ultrasonic fatigue testing techniques. Mason introduced piezoelectric transducers that were capable of translating 20 kHz electrical voltage signals into controlled mechanical displacements, and used high power 20 kHz ultrasonic waves to induce fracture of materials in fatigue. This design of Mason's 20 kHz machine

has been used as the basis for most modern ultrasonic fatigue testing machines. After that, even higher frequencies of fatigue testing were achieved, such as 92 kHz by Girard in 1959, and 199 kHz by Kikukawa in 1965 [4].

As stated before, nowadays the most used frequency is still the 20kHz, because using much higher frequencies will lead to high strain rates, causing the samples to overheat, leading to undesirable temperatures and changing the results [4, 5].

In the year of 1959, Neppiras proposed to apply the ultrasonic fatigue testing techniques to the determination of the $S-N$ curves. This proposal originated a series of research work within the scope of measuring fatigue life and fatigue limits under constant amplitude loading conditions, $R=-1$. Where R is the stress ratio, that is usually defined as the minimum stress value divided by the maximum stress value [8].

In 1973, Mitsche presented the first ultrasonic data on the $\frac{\Delta a}{\Delta N}$ versus ΔK curves, using ultrasonic fatigue technologies, being $\frac{\Delta a}{\Delta N}$ the crack growth rate and ΔK the stress intensity range. Mitsche was one of the first to apply ultrasonic technology to fatigue fracture propagation testing [4, 9]. In the Section 2.4, an approach on the principles of fracture mechanics will be presented.

In 1994, Bathias in collaboration with Wu and Ni, developed the first computer control system for ultrasonic fatigue testing which allowed them to control a piezoelectric fatigue machine. It was a significant step forward in the development of ultrasonic fatigue technologies since it enabled them to conduct tests that followed certain load sequences, and so characterize the fatigue properties of materials under variable amplitude loadings.

The ultrasonic fatigue technologies, which generates very-high cycle fatigue data in a short amount of time, that can be directly used on a wide range of fields, such as aviation, automobiles, railways, offshore, and other constructions are gaining popularity and significance. It is one feasible method for getting very high cycle fatigue data [4, 9].

2.2 Ultrasonic machines

2.2.1 Typical ultrasonic testing machine

As previously stated, most modern ultrasonic fatigue testing machines are based on Mason's 20 kHz machine, and nowadays, the primary experimental methodologies and data linked to VHCF have been established and gathered on the basis of Bathias investigations and published scientific publications [7].

An ultrasonic fatigue test machine usually works at an excitation frequency that corresponds to one of the natural frequencies of the specimen. On a conventional fatigue test machine, the external load system is different from the natural frequencies of the specimen. In other words, the specimen is in forced vibration [4].

The most common and basic ultrasonic testing machine is the longitudinal testing machine, which configuration is shown in Figure 2.2. This type of ultrasonic testing machine only allows to produce fully reversed fatigue tests, $R = -1$, being R the stress ratio which is given by the ratio between the minimum stress and maximum stress. It can be seen that the points A, B, C and the top of the piezoelectric transducer are stress nodes. The specimen centre is a displacement node, null displacement, and the stress amplitude is maximum there. This type of ultrasonic machine is called a longitudinal ultrasonic testing machine [4].

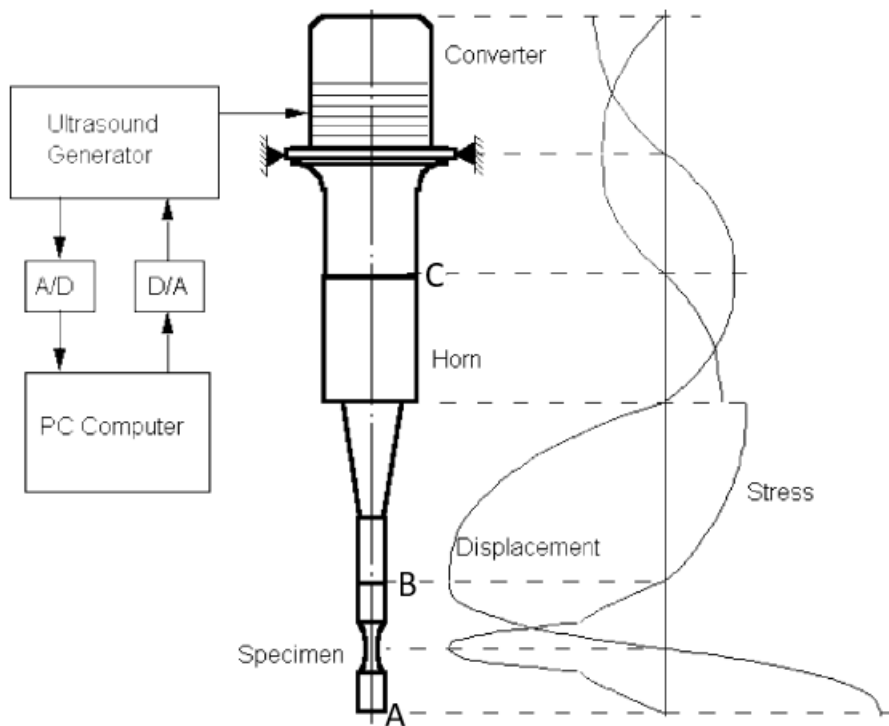


Figure 2.2: Layout of basic ultrasonic testing machine and its stress and displacement fields (Adapted from [4])

The basic longitudinal ultrasonic machine is made up of the following components:

1. A **Power Generator** capable of transforming a 50 or 60 Hz voltage signal into ultrasonic 20 kHz electrical sinusoidal signal and it must control the amplitude of the transducer in order to ensure that the system's resonance regime is maintained [4, 7].
2. A **Piezoelectric Transducer** fed by the power generator, which transforms the electrical signal into longitudinal ultrasonic waves and mechanical vibration of the same frequency. The Piezoelectric transducer must function within a narrow frequency band in order to tolerate minor inaccuracies on the specimens resonance, or variations in this resonance owing to crack propagation [4, 5].
3. An **Ultrasonic Horn** that amplifies vibrations from the transducer to achieve the desired stress amplitude in the specimen's center section.
4. The **Test Specimen** that must be developed such that it can resonate at the desired excitation frequency [5].

On certain longitudinal ultrasonic machines, between the Piezoelectric transducer and the Ultrasonic Horn, there is a **Booster**. It can be seen in Figure 2.3 a basic structure layout of a longitudinal Ultrasonic Machine that has a Booster included. The function of the Booster is to amplify or minimize the amplitude of the vibrations from the transducer and it serves as a link between the Piezoelectric transducer and the Ultrasonic Horn, allowing the support of the entire resonance system. The Booster presents a crucial role in the ultrasonic fatigue machines capable of subjecting the specimen to a static preload, R different from -1, due to its fixation. However, the Booster is not a mandatory component for the ultrasonic machines [7].

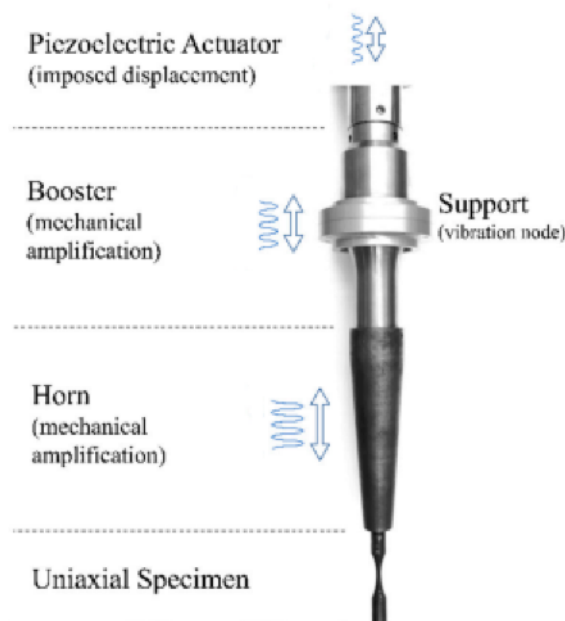


Figure 2.3: Layout of basic Ultrasonic testing machine (Adapted from [10])

The resonant system is composed by the piezoelectric transducer, the booster, the ultrasonic horn and the specimen, sequentially assembled together in series by screw connections (usually studs are used to ensure the correct connection between the different components). The booster, the ultrasonic horn and the specimen need to be designed so that their first natural longitudinal frequency coincides with the excitation frequency of the piezoelectric transducer. As it can be seen in the layouts presented in the Figures 2.2 and 2.3, the specimen has one free end. And so, the loading applied to the specimen is a consequence of its own inertia. The higher the inertia of the specimen, mass or displacements, the greater the stresses. The resonant system is linear, in other words: there is a constant relation between the displacement amplitudes and stress amplitudes. It is necessary only to measure the amplitude of one of them [4, 10].

The mechanical vibrations are transmitted from the piezoelectric transducer, element to element, down to the bottom of the specimen with the displacement and stress field schematically shown in Figure 2.2. The specimens usually have a dumbbell, Gaussian or hourglass shape where the thinner middle part acts as a stress concentrator. The system needs to be designed in order to have stress-free zones at the interfaces between the components.

The piezoelectric transducer is the "heart" of the machine and the most important mechanical component of all the assembly. It is constituted by ceramic plates that expand or contract when an electrically induced tension is applied. The tension is proportional to the expansion or the contraction; that is, the tension is proportional to the displacement in the mechanical system [4].

Besides the Resonant System and the Power Generator, the Ultrasonic Testing Machines also include a cooling system. Due to the effect of the internal friction the temperature increases significantly on the specimen, influencing its behaviour. Therefore, the specimen must be cooled. The most common is to use clean, dry compressed air to cool the specimen [7].

Additionally, it is common for the Ultrasonic Testing Machines to have a measurement or data acquisition system which can be made of various instrumentation devices like strain gauges, sensors to measure displacement (or velocities) during the tests, pyrometers and other data-gathering transducers [5, 10].

As it was stated before, the longitudinal testing machines layout demonstrated in the Figures 2.2 and 2.3 only allow to test different materials at a stress ratio, R , equal to -1. However, it is possible to realize tests at different values of stress ratio by adding a second horn to the layout. In the Figure 2.4 it is schematically demonstrated the application of the second horn. It can be seen that the new horn is connected at the free end of the specimen and it is fixed to the base, allowing the application of a static compression or tension force. Therefore, the various values of R will be determined by the application of the static force. The new horn also needs to have a longitudinal resonance frequency that is equal to the excitation frequency of the transducer. If the resonance system also includes a booster, the layout must have two horns and two boosters in order to realize tests at different values of R [10].

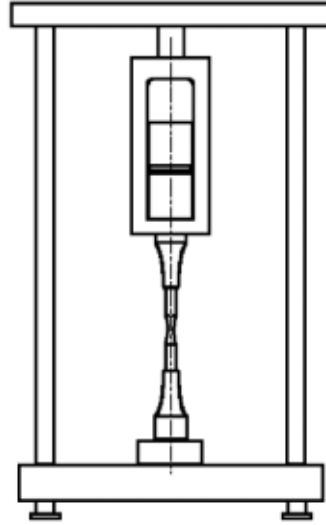


Figure 2.4: Layout of Ultrasonic testing machine for testing materials at different values of R (Adapted from [4])

2.2.2 Elastic waves, analytical stresses and displacements

The ultrasonic fatigue test machines, as was previously mentioned in the preceding subsection, have an excitation frequency that is exactly one of the natural frequencies of the specimen (usually 20-30 kHz). This is contrary to the conventional fatigue machines, where the specimen is excited by an external load at a frequency that differs from its natural frequencies [4, 5].

Piezoelectric transducers with frequencies between 20 and 30 kHz are preferred over those with higher frequencies mostly due to the specimen's resonance length, which is inversely proportional to frequency. In order to properly understand this statement it is essential to carefully review the elastic wave theory [7].

For an isotropic three dimensional elastic case, the three governing general differential equations are [4]:

$$\rho \frac{\partial^2 u}{\partial t^2} = \frac{E}{(1+\nu)} \left(\frac{1}{1-2\nu} \frac{\partial e}{\partial x} + \nabla^2 u \right) \quad (2.1)$$

$$\rho \frac{\partial^2 v}{\partial t^2} = \frac{E}{(1+\nu)} \left(\frac{1}{1-2\nu} \frac{\partial e}{\partial y} + \nabla^2 v \right) \quad (2.2)$$

$$\rho \frac{\partial^2 w}{\partial t^2} = \frac{E}{(1+\nu)} \left(\frac{1}{1-2\nu} \frac{\partial e}{\partial z} + \nabla^2 w \right) \quad (2.3)$$

Where t is the time, x , y and z are the Cartesian coordinates and u , v and w the correspondent displacements over these directions, respectively. In addition, E is the Young's modulus, ν is the Poisson's ratio, ρ is the density, ∇^2 is the Laplace operator and e is the volume dilatation, which is written as :

$$e = \frac{\partial u}{\partial x} + \frac{\partial v}{\partial y} + \frac{\partial w}{\partial z} \quad (2.4)$$

According to the Elastic Wave Theory, there are two possible types of waves that can exist in an infinite and isotropic elastic body. These waves are the longitudinal wave and the transverse wave [4].

The longitudinal wave is characterized by a displacement of particles that is parallel to the wave travelling direction. In the Figure 2.5 it is illustrated the propagation of longitudinal waves. After an initial stimulation applied to the material, the particles will move from their equilibrium position to another position. The interaction between the moving particles will cause the different transverse to propagation sections of the material to compress and to expand until the particles reach the initial equilibrium position [7].

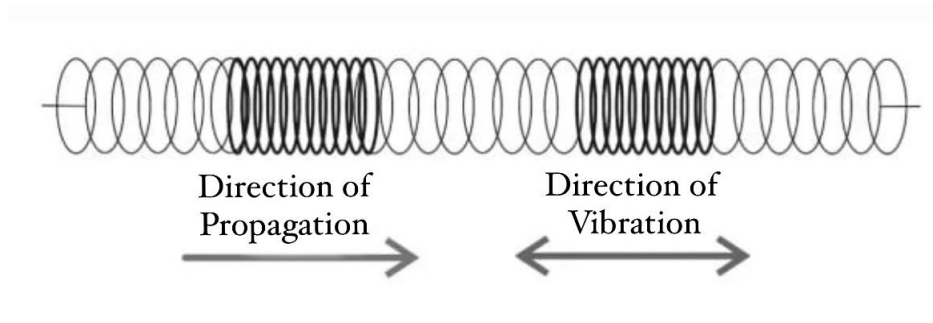


Figure 2.5: Propagation of Longitudinal Waves (Adapted from [7])

The velocity of longitudinal wave propagation is given by the following equation:

$$c = \sqrt{\frac{E(1-\nu)}{(1+\nu)(1-2\nu)\rho}} \quad (2.5)$$

It is possible to write the velocity of wave propagation in the following way for the transverse wave, which occurs when the wave traveling direction and particle displacement are perpendicular to one another.

$$c = \sqrt{\frac{E}{2(1+\nu)\rho}} \quad (2.6)$$

2.2.2.1 Constant transversal section specimen

Considering a one-dimensional specimen with a straight cylinder body (constant transverse section), such as the elastic bar depicted in Figure 2.6, it is easier to perceive that a longitudinal wave starting at one end of the elastic bar will travel through the bar and then be reflected at the other end, returning to its initial point of entry [4, 5].

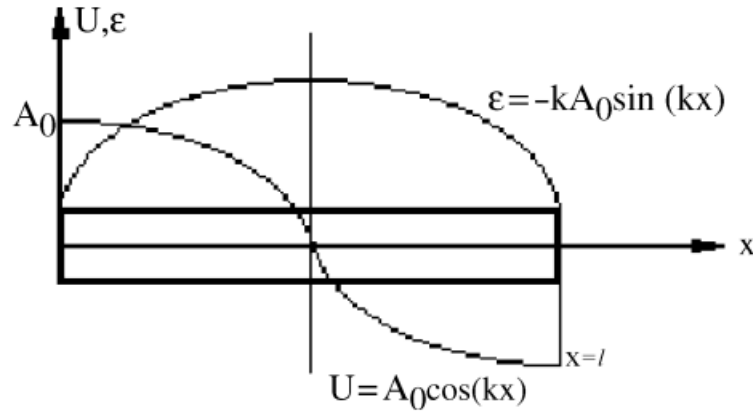


Figure 2.6: Displacement and strain variation along an elastic bar [4]

Since it is being considered a one-dimensional specimen, certain simplifications can be made. For one-dimensional bodies $\nu = 0$, so the longitudinal wave velocity, c , can be determined by using the equation 2.5 :

$$c = \sqrt{\frac{E}{\rho}} \quad (2.7)$$

And the three general differential equations, 2.1, 2.2 and 2.3, can be now reduced to a single equation:

$$\frac{\partial^2 u}{\partial t^2} = \frac{E}{\rho} \frac{\partial^2 u}{\partial x^2} \quad (2.8)$$

Whose solution is given by:

$$u = \sum_{n=1}^{\infty} u_n(x, t) \quad (2.9)$$

Where:

$$u_n(x,t) = \left(A_{n-1} \cos \frac{n\pi ct}{l} + B_{n-1} \sin \frac{n\pi ct}{l} \right) \cos \frac{n\pi x}{l} \quad (2.10)$$

With A_{n-1} and B_{n-1} being constants.

In the Figure 2.6 it can be understood that during a longitudinal ultrasonic fatigue test, the displacement is set to be maximum at both ends of the specimen whereas the strain vanishes at the same places. What was stated previously can be displayed as:

$$\left(\frac{\partial u}{\partial x} \right)_{x=0,l} = 0 \quad (2.11)$$

Therefore, for the first mode of vibration, the equation 2.10 can be reduced to:

$$u(x,t) = A_0 \cos(k_1 x) \sin(\omega t) \quad (2.12)$$

Where A_0 is the amplitude of displacement and:

$$k_1 = \frac{\pi}{l} \quad (2.13)$$

And, additionally:

$$\omega = \frac{\pi c}{l} \quad (2.14)$$

The vibration amplitude at each point along the bar, shown in the Figure 2.6, is given by

$$U(x) = A_0 \cos(k_1 x) \quad (2.15)$$

Where A_0 is the displacement amplitude at both ends of the bar. The strain, ε , can be obtained by taking the derivative over x of the equation 2.15:

$$\varepsilon(x,t) = -k_1 A_0 \sin(k_1 x) \sin(\omega t) \quad (2.16)$$

With its amplitude being given by :

$$\varepsilon(x) = -k_l A_0 \sin(k_l x) \quad (2.17)$$

As stated in the preceding section, the excitation frequency of an ultrasonic fatigue testing equipment coincides to one of the specimen's natural frequencies, so the correct length of the specimen, resonance length, must be calculated in order to obtain the correct natural frequency [4].

For the present specimen one-dimensional case and for the first mode of vibration, where f is known and it is the excitation frequency that corresponds to the first natural frequency of the specimen, the correct length of resonance can be obtained through the equations 2.7, 2.13 and 2.14, originating:

$$l = \frac{1}{2f} \sqrt{\frac{E_d}{\rho}} \quad (2.18)$$

Where E_d is the dynamic elastic modulus and:

$$f = \frac{\omega}{2\pi} \quad (2.19)$$

The equation 2.18 shows that the resonance length is inversely proportional to the excitation frequency, as stated in the beginning of the present subsection (2.2.2). This explains why extremely high frequencies cannot be utilized, as they contribute to challenges in machining, displacement or strain measurements, and energy dissipation, leading to the increase of the temperature of the specimen and uncertain results [4].

Now, it is possible to go back to Figure 2.6 and make some observations taking into account the preceding equations. At the center of the specimen, $x = \frac{l}{2}$, we have a displacement node, which is where the maximum stress and strain occurs.

For $x = \frac{l}{2}$:

$$u = 0, \quad \varepsilon(\text{Amplitude}) = -kA_0, \quad \sigma(\text{Amplitude}) = -E_d k A_0 \quad (2.20)$$

And at both ends of the specimen, we have the nodes of stress and strain, which is where the maximum displacement occurs.

For $x = 0, l$:

$$U(\text{Amplitude}) = A_0, \quad \varepsilon = 0, \quad \sigma = 0 \quad (2.21)$$

2.2.2.2 Variable transversal section specimen

In the most cases, the specimen utilized in the ultrasonic fatigue testing machines have a reduced section in the middle of its length in order to obtain a stress concentration, an example of a variable transversal section specimen is shown in Figure 2.7.

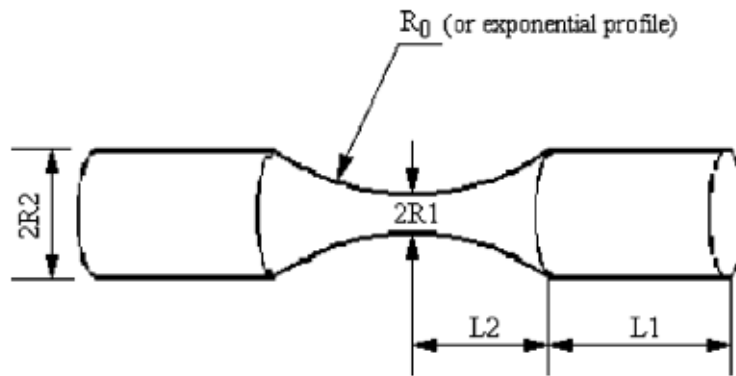


Figure 2.7: Ultrasonic variable cross section specimen [4]

Typically, a numerical methodology, such as the Finite Element method, is required for the accurate estimation of the dimensions of a specimen with a variable cross section. However, if the center part is in an exponential profile, as shown in Figure 2.7, an analytical solution for the resonance length, stress and strain fields was developed by Kong [4, 11].

For a specimen with a variable cross section, the longitudinal wave equation may be expressed as:

$$\rho S(x) \frac{\partial^2 u}{\partial t^2} = \frac{\partial f}{\partial x} \quad (2.22)$$

Where $S(x)$ is the cross sectional area and f is the force acting on the cross sectional area at the same x coordinate. The force, f , can be expressed as:

$$f = E_d S(x) \frac{\partial u}{\partial x} \quad (2.23)$$

Therefore, combining the equations 2.22 and 2.23 and additionally considering that $c = \sqrt{\frac{E_d}{\rho}}$ the following equation can be obtained:

$$\frac{\partial^2 u(x,t)}{\partial t^2} = c^2 \left\{ p(x) \frac{\partial u(x,t)}{\partial x} + \frac{\partial^2 u(x,t)}{\partial x^2} \right\} = 0 \quad (2.24)$$

Where

$$p(x) = \frac{S'(x)}{S(x)} \quad (2.25)$$

The solution of the equation 2.24 is:

$$u(x,t) = U(x) \sin(\omega t) \quad (2.26)$$

The amplitude of vibration, $U(x)$, at each x coordinate along the specimen, can be obtained through the following equation:

$$U''(x) + p(x)U'(x) + k^2 U(x) = 0 \quad (2.27)$$

Where:

$$k = \frac{\omega}{c} \quad (2.28)$$

The formulation of the aforementioned equation, 2.27, will be provided in Appendix A. Considering that the curve on the central part of the specimen shown in Figure 2.7 is a profile of hyperbolic cosine, it is possible to define the curve in the subsequent manner:

$$y(x) = R_2, \quad L_2 < |x| \leq L \quad (2.29)$$

$$y(x) = R_1 \cosh(\alpha x), |x| \leq L_2 \quad (2.30)$$

Where:

$$L = L_1 + L_2 \quad (2.31)$$

And:

$$\alpha = \frac{I}{L_2} \cosh^{-1}\left(\frac{R_2}{R_1}\right) \quad (2.32)$$

Through the equations presented above, the Figure 2.7 specimen's resonance length, L_1 in the present case, can be defined as:

$$L_1 = \frac{1}{k} \arctan \left\{ \frac{1}{k} [\beta \coth(\beta L_2) - \alpha \tanh(\alpha L_2)] \right\} \quad (2.33)$$

Where:

$$\beta = \sqrt{\alpha^2 - k^2} \quad (2.34)$$

As it can be seen in the equation 2.33, the resonance length is dependable of L_2 so if the value of L_2 is unknown, the resonance length can only be determined through an iterative process.

The solution of the equation 2.27 is going to be presented next.

For $|x| \leq L_2$ (variable cross section) :

$$U(x) = A_0 \varphi(L_1, L_2) \frac{\sinh(\beta x)}{\cosh(\alpha x)} \quad (2.35)$$

And for $L_2 < |x| \leq L$ (constant cross section):

$$U(x) = A_0 \cos(k(L - x)) \quad (2.36)$$

Where φ takes the following value:

$$\varphi(L_1, L_2) = \frac{\cos(kL_1) \cosh(\alpha L_2)}{\sinh(\beta L_2)} \quad (2.37)$$

The specimen's resonance length final equation, 2.33 and the different final equations that provide the amplitude of vibration, $U(x)$, 2.35 and 2.36, will be formulated in Appendix A.

Finally, we can obtain the strain field and consequently, through the Hooke's law, the stress field for both of the parts of the specimen shown in Figure 2.7.

For the reduced section part $|x| \leq L_2$:

$$\varepsilon(x) = A_0 \varphi(L_1, L_2) \frac{[\beta \cosh(\beta x) \cosh(\alpha x) - \alpha \sinh(\beta x) \sinh(\alpha x)]}{\cosh^2(\alpha x)} \quad (2.38)$$

$$\sigma(x) = E_d A_0 \varphi(L_1, L_2) \frac{[\beta \cosh(\beta x) \cosh(\alpha x) - \alpha \sinh(\beta x) \sinh(\alpha x)]}{\cosh^2(\alpha x)} \quad (2.39)$$

For the cylindrical part $L_2 < |x| \leq L$:

$$\varepsilon(x) = k A_0 \sin(k(L-x)) \quad (2.40)$$

$$\varepsilon(x) = E_d k A_0 \sin(k(L-x)) \quad (2.41)$$

2.2.3 Different types of ultrasonic machines

2.2.3.1 Ultrasonic testing at unconventional conditions

Due to the wide variety of applications and environments that a given material can be submitted, it is of interest to study its different behaviors when submitted to non conventional situations. Many of the environments and applications to which they are subjected can greatly influence their fatigue resistance.

As a consequence of the changes in the behavior of materials at different temperatures, tests where the specimen is subjected to very high or very low temperatures are required. This type of tests aims to understand how the VHCF could be affected by different extreme temperatures. The test temperatures vary with the material to be tested as each material has different characteristics, behaviours and brittle to ductile transition temperatures [12].

These tests are also of high importance to the ultrasonic testing realized at room temperature. As said before in the previous subsection, the temperature on the specimen tends to increase due to the internal friction and without a cooling system it would affect the results. Knowing the permissible temperature range that provides the best results, the test can be paused to allow the specimen to cool down. In other words, the machine operates for some fractions of a second. Throughout this period, the specimen will heat up. The machine then pauses for a period of time (fractions of a second) to allow the specimen to cool, and this process is repeated throughout the tests to maintain a temperature that is reasonably low and constant. For high temperatures tests it is used a high-frequency inductor and the test temperature can reach up to 1000 °C [13].

In Figure 2.8 it is shown a high temperature ultrasonic fatigue test. Throughout the test, the temperature of the specimen is continually checked to guarantee a constant temperature. Due to the Young's modulus and density decrease at high temperatures, the length of the ultrasonic fatigue specimen will be shorter than that the specimens used for ambient temperature testing. For temperature sensitive materials, this change in the Young's modulus must be taken into account [13, 14].

For Ultrasonic testing at low temperatures, liquid nitrogen, liquid hydrogen or liquid helium are used to create a cryogenic temperature atmosphere. In Figure 2.9 it is shown the machine built in Bathias laboratory for low temperature ultrasonic testing. The machine consists of three parts: a cryostat, a mechanical vibrator and a controlled power generator. The cryostat contains liquefied gases to keep the testing temperature constant. For a load ratio $R > -1$ ultrasonic fatigue tests at cryogenic temperatures are also possible by adding a second horn to the other end of the specimen [13].

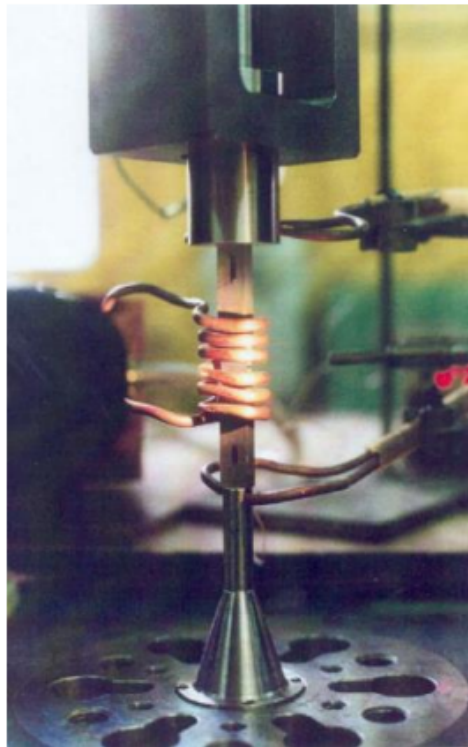


Figure 2.8: Ultrasonic fatigue testing at high temperatures [13]

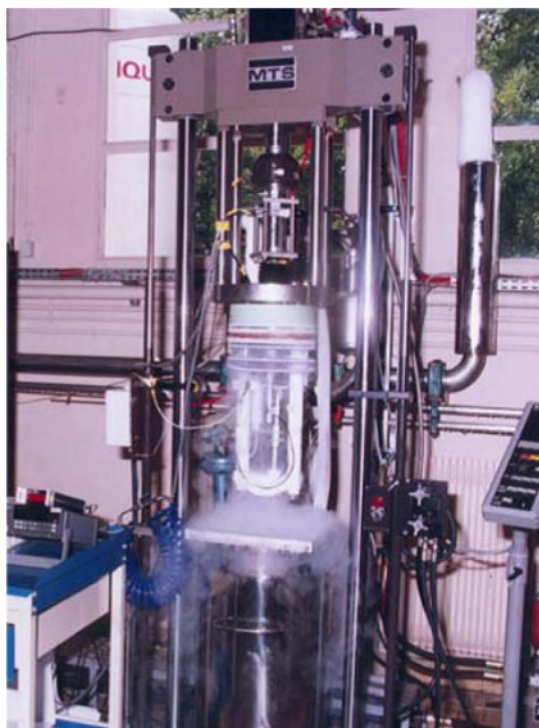


Figure 2.9: Ultrasonic fatigue testing at low temperatures [13]

In addition to the ultrasonic tests realized at extreme temperatures it is also important to investigate the behaviour of the materials under High Pressures. A high pressure piezoelectric fatigue machine has been built in Bathias's laboratory. It is schematically represented in Figure 2.10. This piezoelectric fatigue machine can function under a pressure up to 300 bar. With the use of this ultrasonic system, it is feasible to comprehend and advance research on how high pressures might change a material's behavior in the VHCF regime and, in turn, how high pressures can affect its $S-N$ curve [13].

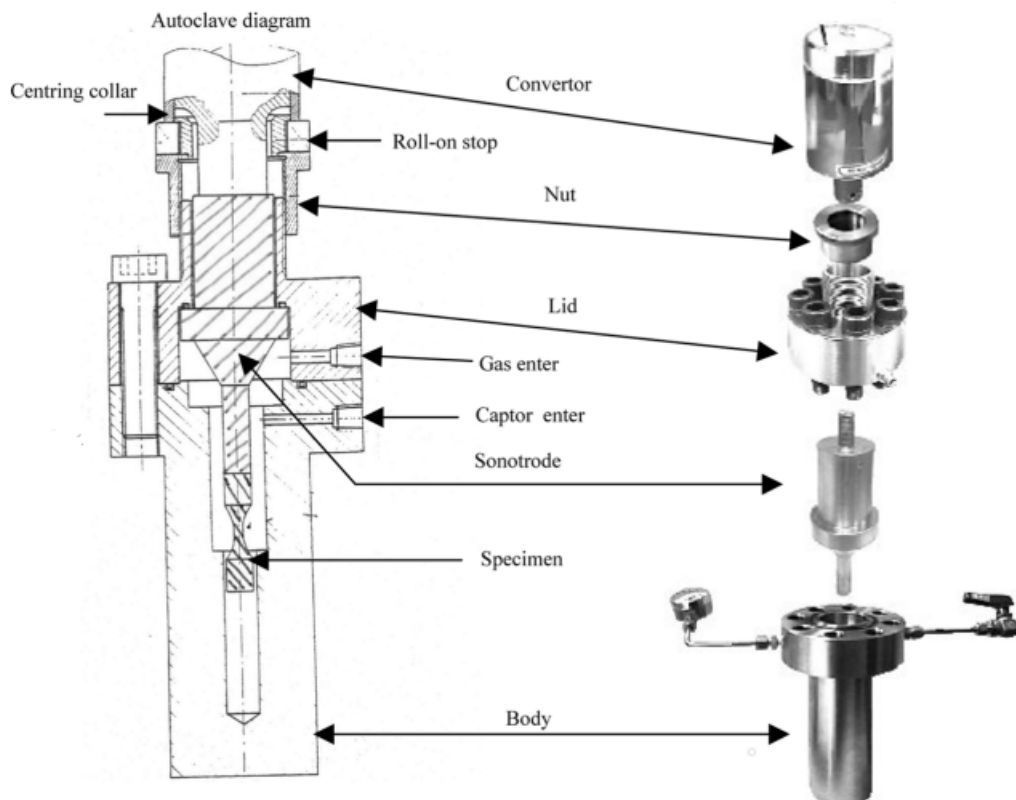


Figure 2.10: Bathias's High pressure piezoelectric fatigue machine (Adapted from [4])

2.2.3.2 Ultrasonic torsion test equipment

There are two types of ultrasonic torsion fatigue testing machines: (i) direct and (ii) indirect. The first one is based on a torsional piezoelectric converter. The second one (i.e. indirect machine) is based on an longitudinal piezoelectric converter.

Bathias and co-workers developed a torsion piezoelectric system that works in the continuous regime. This testing system is an 'indirect' machine based on a longitudinal piezoelectric transducer. The developed system consists of two perpendicular ultrasonic horns and transforms longitudinal vibration into angular vibration. This ultrasonic torsion machine is controlled by a high performance computer and includes an air-cooling system that allows continuous constant

amplitude torsion tests to be carried out. In Figure 2.11 it is shown this torsion piezoelectric system [15].

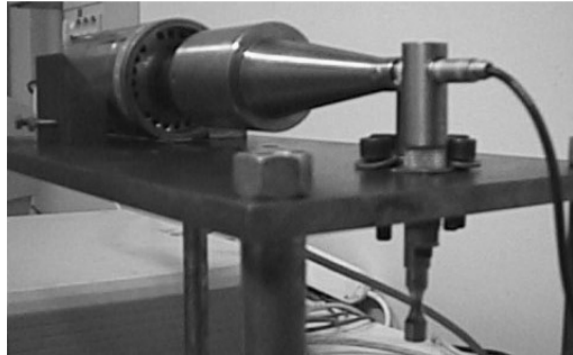


Figure 2.11: Ultrasonic torsion test equipment in Bathias's laboratory [4]

The test device designed by Bathias and co-workers is illustrated in Figure 2.12 and it is comprised of two sections referred as sections A and B. Section A is composed of a piezoelectric transducer and an ultrasonic horn (with longitudinal resonance), this section is only capable of inducing longitudinal vibration. To transform the longitudinal displacements provided by section A into a torsional vibratory motion, section B was coupled to section A by mean of a pin. Section B is composed of another ultrasonic horn and the specimen. The second horn has a torsional resonance that is equal to the longitudinal resonance of the first one [16].

The system described above presents a limitation. The connecting component (i.e. the pin) is subject to ultrasonic bending, resulting in a limited in-service lifetime. This implies that the pin needs to be changed after approximately 10^{10} cycles [15].

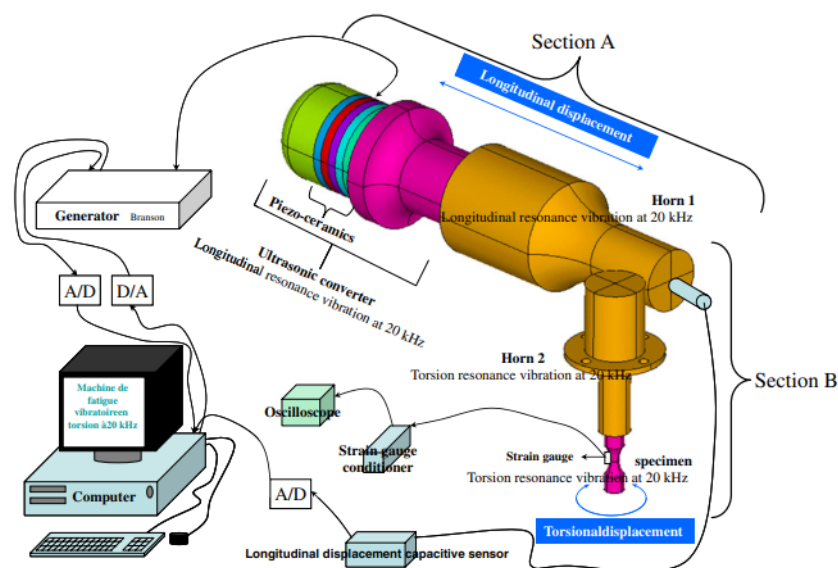


Figure 2.12: Torsional ultrasonic fatigue test system schematic figure (Adapted from [16])

A piezoelectric torsional transducer, such as the one seen in Figure 2.13, can be used to build a direct and simpler ultrasonic torsional machine. The disadvantage of employing two perpendicular horns and the failure of their connecting pin can be overcome by using a direct piezoelectric torsional transducer [15].

It is possible to acquire a stress ratio, R , in these experiments that is different from $R=-1$. Another horn has to be inserted into the specimen's free end in order to do that. This horn needs to be fixed and can apply a static torsion to the specimen [12].



Figure 2.13: Torsional piezoelectric transducer, ultrasonic horn and specimen (Adapted from [12])

2.2.3.3 Tension/Torsion ultrasonic fatigue testing equipment

A multiaxial ultrasonic fatigue testing device, which allows for a combined tension/torsion loading, was recently developed and presented in [17]. This equipment uses a piezoelectric longitudinal transducer, an ultrasonic booster, a custom horn and specimen, which are presented in the Figure 2.14. This horn was developed to convert the actuator's longitudinal displacement into both axial and rotational motion, subjecting the specimen to a combined stretch/compression and rotational motion [10].

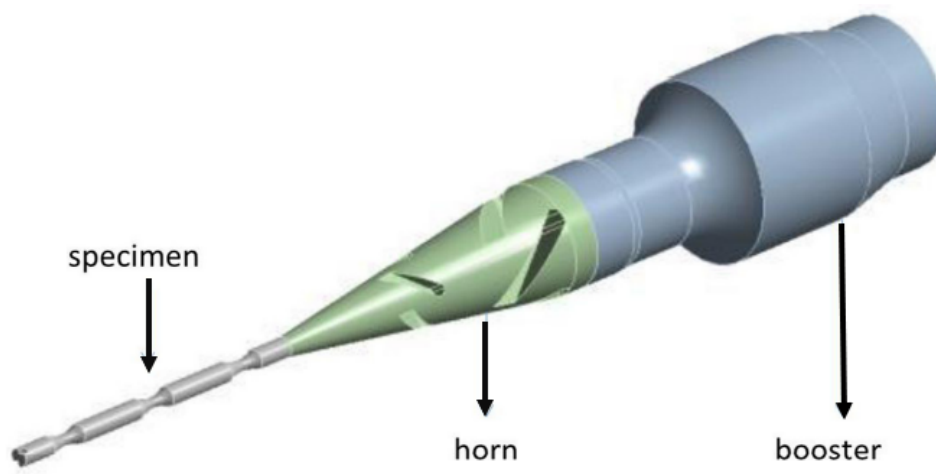


Figure 2.14: 3D model of the multiaxial fatigue testing device (Adapted from [18])

The utilized specimen in this fatigue equipment presents three "throats", as it can be seen in the Figure 2.15. A cylindrical specimen with three "throats" design was considered since it presents its first axial mode and its third torsional mode at a similar inherent natural frequency [19]. The fatigue failure is expected to occur in the central "throat", which is where the maximum tension/-torsion combined motion is achieved, leading to maximum stresses and higher temperatures. After further analysis, it was experimentally confirmed that the combination of stresses is the highest on the middle "throat", suffering with the highest combination of axial and shear stresses [17].

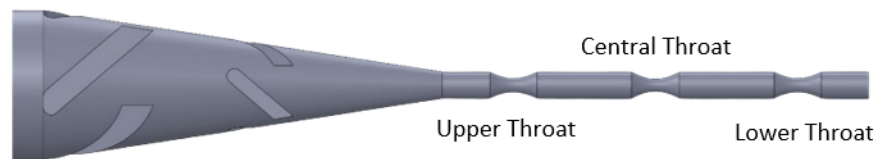


Figure 2.15: Horn and specimen for tension/torsion biaxial testing (Adapted from [19])

2.2.3.4 Three-point bending fatigue testing machine

The three-point bending ultrasonic fatigue testing system developed in Bathias's laboratory is illustrated in Figure 2.16. It consists of a generator, a piezoelectric transducer, a booster, a horn, the specimen and the control system. The difference between the three-point bending ultrasonic fatigue system and the longitudinal ultrasonic fatigue machine is that the three-point bending ultrasonic fatigue test provides transverse vibratory loading to the fatigue specimen [20].

The specimen will suffer transverse displacements through the axial displacements of the horn and will be in three-point bending, with its central section being under bending and shearing forces. An initial displacement of the specimen originated by the vertical displacement of the movable plate of the INSTRON, will cause the specimen to be statically loaded and under an average stress. The booster seen in the Figure 2.16 needs to be secured in a vibration node such that it contributes as little as possible to the system's vibration.

Dynamic loading was provided by the ultrasonic transducer, which is controlled by a computer control system. This Three-point bending ultrasonic fatigue machine has a 20 kHz resonance frequency; so, the booster, horn and specimen in the bending fatigue system must have a 20 kHz resonance frequency [20].

The three-point bending fatigue testing machine described above and shown in Figure 2.16 is capable of working from $R = 0.1$ to $R = 0.5$ and beyond, at 20 kHz. The establishment of different R values can be obtained through the movement of the movable plate of the INSTRON. The maximum displacement amplitude in the middle of the three-point bending specimen is of the order of $30 \mu\text{m}$ [13].

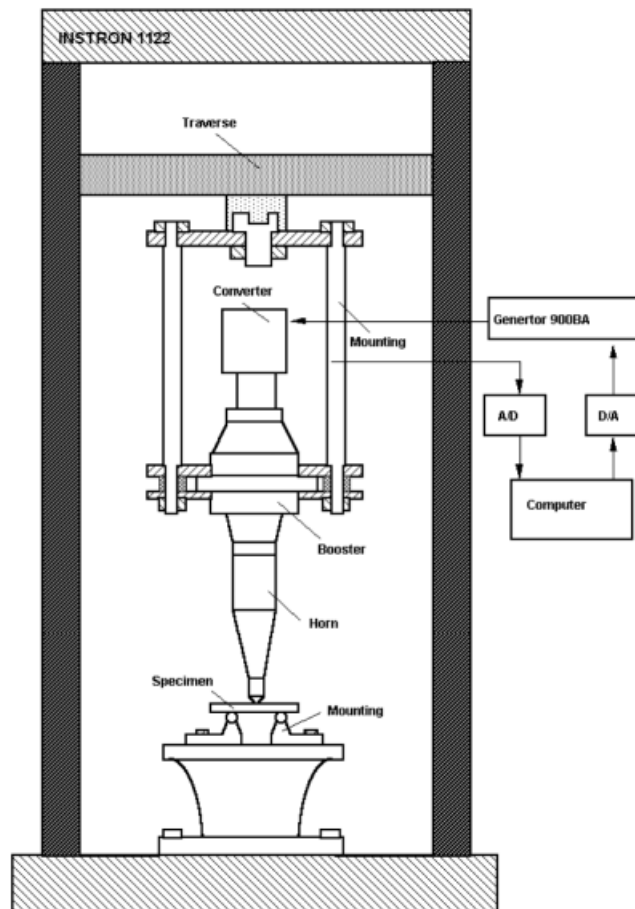


Figure 2.16: Bathias's three-point bending fatigue machine [4]

2.2.3.5 Ultrasonic fretting fatigue testing

Fretting can result in fretting wear or fretting fatigue, both of which can significantly worsen the material's fatigue characteristics. It is originated by an oscillatory sliding motion of small slip amplitude between two surfaces in contact. It frequently happens in clamped joints and is typically induced by high frequency, low amplitude vibratory movements [21].

Fretting fatigue is a combination of fretting friction and the fatigue process, it is conditioned by the magnitude and distribution of contact pressure, the amplitude of relative slip, friction forces, surface conditions, materials of the contact surfaces, cyclic frequency and the environment. Wheel shafts, steam and gas turbines, bolted plates, wire ropes, and springs are a few common real-world examples where fretting fatigue failures can be observed [4].

In order to study the characteristics and the influence of fretting fatigue, it was developed in Bathias's laboratory an Ultrasonic fretting fatigue testing system that is able to provide data for the purpose of determining the $S-N$ curves of a given material with fretting.

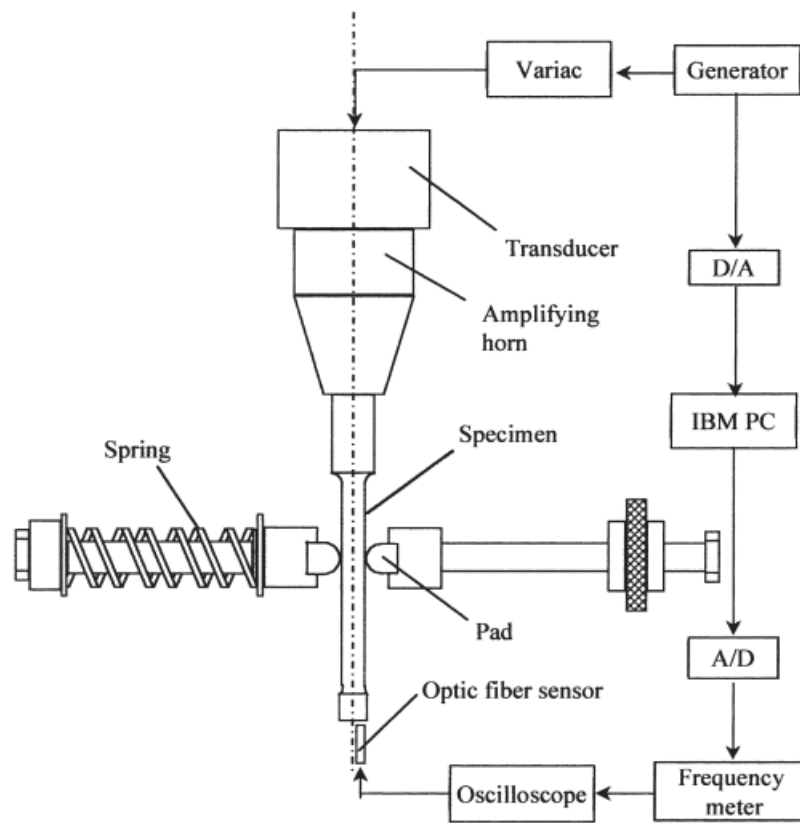


Figure 2.17: Ultrasonic fretting fatigue test system developed in Bathias's laboratory (Adapted from [21])

The Ultrasonic fretting fatigue testing system that was developed in Bathias's laboratory can be seen in Figure 2.17. It is based on a longitudinal ultrasonic fatigue test machine and has a resonant frequency of 20 kHz. The specimen used in this machine has an elongated uniform throat in order to accommodate the application of the fretting pads. The system has a fixture to hold the two cylinder pads pressed against the specimen by two springs, whose displacement controls the normal contact force applied to the specimen. Different values of relative slip amplitude can be obtained by changing the position of the pads along the specimen axis. This whole system is controlled by a computer. The specimen fracture will occur where the fretting pads are acting [22].

2.2.4 Ultrasonic machines and parts available in the market

The importance of ultrasonic testing, as well as the demand for it, has steadily increased over the years. The significance of knowing how various materials react after 10^7 cycles is growing, and the use of ultrasonic technology to build testing systems is becoming increasingly unavoidable. This is due to the speed with which reliable data can be obtained using ultrasonic technology, as well as the low cost of the tests when compared to the expense of using conventional machines.

In order that, nowadays there are already a variety of ultrasonic fatigue testing machines available in the market. In the Figure 2.18 is presented a fully reversed fatigue machine built and sold by a company named 3R, based in France.



Figure 2.18: MEG 20 - Fully reversed fatigue machine - 3R [23]

The MEG 20 is a completely reversed fatigue testing machine ($R=-1$) operating at 20 kHz. It is compact, allowing it to be put on the work table. It is set to terminate automatically when the specimen breaks. This fatigue testing system consists of two components: a testing frame in which the transducer permits the testing specimen to be subjected to a fatigue stress at 20 kHz, and a separate control cabinet responsible for the system's control and data acquisition [23].

Another example of the ultrasonic testing machines available on the market is the Shimadzu USF-2000A, which can be seen in the Figure 2.19. The Shimadzu USF-2000A ultrasonic fatigue testing system operates at a frequency of $20 \text{ kHz} \pm 500 \text{ Hz}$ and can be configured to produce fully reversed fatigue tests, standard configuration, or tests with an average tensile stress loaded, mean stress configuration. This fatigue testing system allows to load the specimen with a maximum average tensile stress load of 1.5 kN. By applying a tensile stress to the specimen, different values

of R can be obtained, enabling the investigation of the fatigue behavior of different materials under different tensile loads.



Figure 2.19: Ultrasonic fatigue testing system USF-2000A - Shimadzu [24]

The full Shimadzu USF-2000A system is composed by an ultrasonic resonance system, a computer responsible for the interface board and test control, a cooling system and an average stress loading mechanism [24]. However, due to the high price of the ultrasonic testing machines available on the market, many researchers end up developing their own systems because the system's fundamental working concept is not overly complex and it is not difficult to design or construct. There are a large number of different solutions for transducers available in the industry. In the Figure 2.13 it is presented a torsion transducer sold by BRANSON. In the figure bellow it is possible to see another solution available, it is a 20 kHz transducer sold by Sonic Power, which is a company based in Germany.



Figure 2.20: Ultrasonic transducer 3300W – 20kHz - Sonic Power [25]

A huge number of ultrasonic material retailers provide a vast selection of 20 kHz tuned horns and boosters for purchase. There are also several options available for different tuning frequencies. In the Figures 2.21 and 2.22, it is presented a titanium horn sold by Sonitek and different boosters with various amplifications sold by BRANSON, respectively. BRANSON also presents a vast number of horn models with different tuning frequencies in their catalog [26].



Figure 2.21: 20kHz Catenoidal Tapped Horn made of Titanium - Sonitek (Adapted from [27])

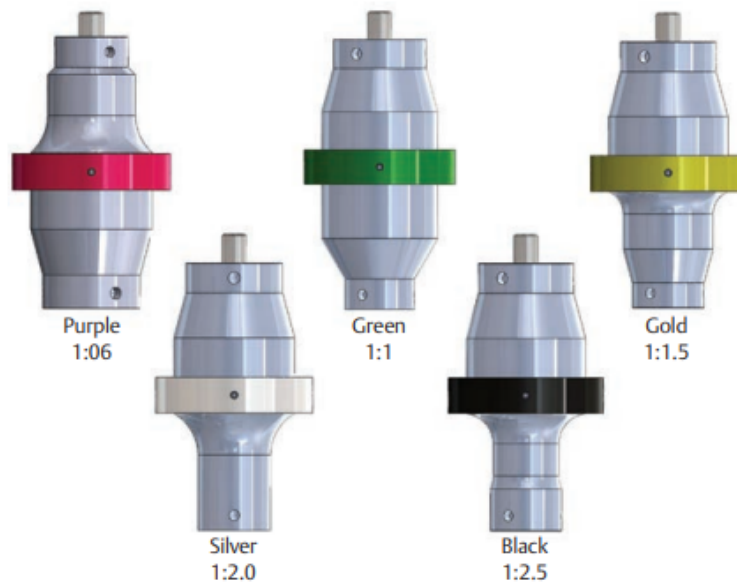


Figure 2.22: Boosters with different amplifications (ratio between the displacement of the top and displacement of the bottom) - BRANSON (Adapted from [26])

2.3 Behavior of the materials under the VHCF regime

As stated before, the VHCF regime is established to a number of loading cycles superior to 10^7 [22]. There are numerous reasons why structural components may fail under repeated loading cycles, including geometrical and manufacturing imperfections or notches, insufficient or inadequate maintenance, overloads in operational conditions or secondary efforts not considered in normal service conditions, and environmental factors such as extreme temperatures or corrosion [28].

Defects like inclusions or porosities, common sites for fatigue crack nucleation, are present in most materials as a result of deoxidization additions, impurities or entrained exogenous material [29]. In the gigacycle fatigue regime, VHCF, for brittle and well-polished materials the crack initiation usually occurs inside the specimen and not at the surface like on the other fatigue regimes, low cycle fatigue (less than 10^5 cycles) and in the conventional megacycle range (10^6 to 10^7 cycles).

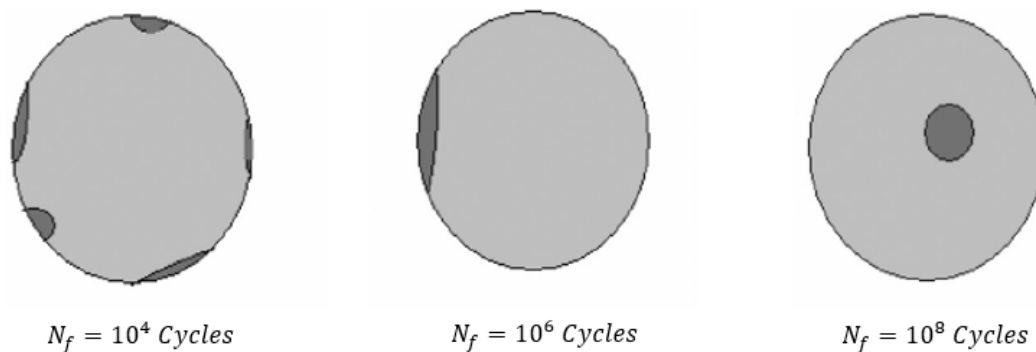


Figure 2.23: Mechanisms of fatigue initiation (Adapted from [4])

According to Bathias and Paris, there are three forms of fracture initiation in a cylindrical specimen with a polished surface, depending on whether the specimen is at a low cycle, high cycle, or very high cycle regime. Through the Figure 2.23 it is possible to verify that for the smallest number of cycles to rupture, the initiation sites are multiple and on the surface. For the specimen at the high cycle regime, usually there is only one crack initiation site which is also on the surface. For a much higher number of cycles to rupture, VHCF, the initiation site is located in an internal zone as stated before.

For specimens of nickel, titanium alloys and high strength steels in the VHCF regime, the initiation sites are usually located in an internal zone. For ductile materials, the crack initiation appears at the surface of the specimens in the VHCF regime, especially in castings where voids at the surface are the main locations for crack formation. [4].

At the VHCF regime there are three main factors that influence the crack initiation mechanisms [4][28] :

1. Anisotropy of metals: Plasticity emerges only if the grain orientation and grain size are in agreement with dislocations sliding at the surface or in the volume of the metals at the gigacycle regime, where the plastic strain is very modest.
2. Stress Concentration: When the applied load is low, it is thought that stress concentration owing to metallurgical micro structural misfit becomes a significant factor. Effective concentrators include defects and grain size.
3. Statistical Conditions: The likelihood of finding a significant stress concentration in the bulk of the metals is higher than on the surface.

The characteristic feature of VHCF fracture surface is the formation of the “fish-eye” when a nucleation at an internal zone occurs. It could be defined as the circular area that surrounds fatigue initiating site and was formed as a result of internal circular crack propagation. The initiation sites are usually found at inclusions located in the interior of the specimens [1]. In the Figure 2.24 it is possible to visualize the "fish-eye" and the internal inclusion that originated the fatigue crack.

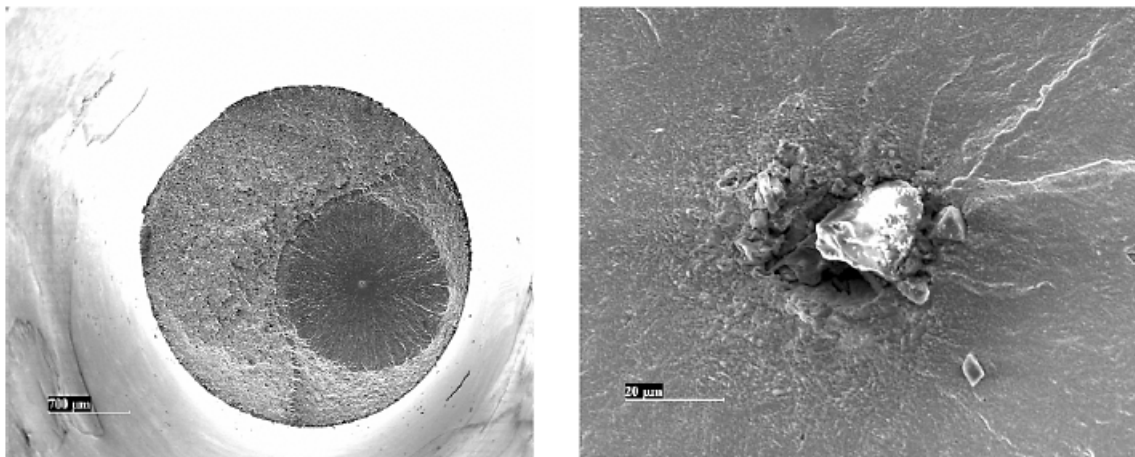


Figure 2.24: "Fish-eye" with focus on the internal inclusion [4]

As shown in Figure 2.25, the fatigue failure in the VHCF regime is divided into multiple stages. The first stage is the Crack Formation from a microstructural defect. The fatigue crack might be created by either cracking or de-cohesion of the defect from the matrix, followed by early crack formation from the defect cavity, depending on the kind of microstructural defect. The duration of this stage is expected to be short due to the high notch severity of the defect cavity. The next phase is the Initial Crack Growth. This phase covers the initial crack propagation from the microstructural defect which is governed by an extremely slow mechanism of crack growth and results in the formation of a rough area on the fracture surface adjacent to the fatigue initiating defect. It has been observed by many researchers that 90 to 99% of the total VHCF life is consumed in this phase [1, 9].

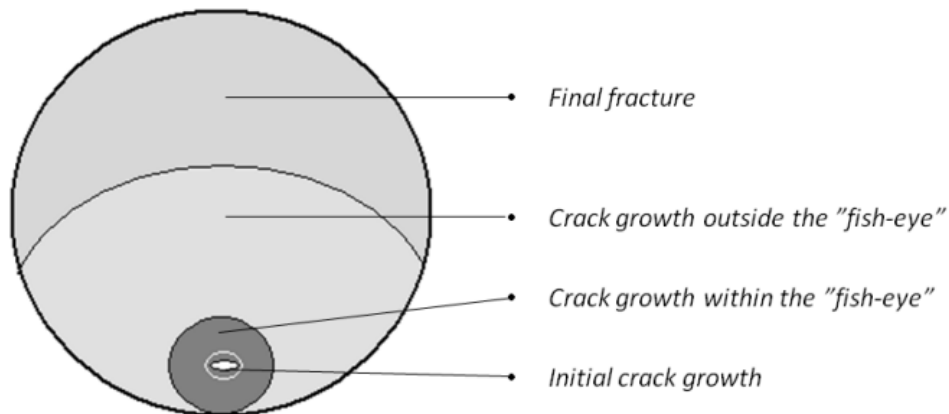


Figure 2.25: Illustration of a fracture surface showing different stages of VHCF crack development [1]

The following stage is the crack growth within the "fish-eye". As the rough area is formed, the crack is increasing and reaches the size representative of the threshold stress intensity factor range for crack propagation (ΔK_{th}). From that point a steady crack growth within the "fish-eye" begins resulting in a smooth fracture surface morphology. The crack growth rates are slowly increasing as the crack approaches the "fish-eye" border. Then, it occurs the crack growth outside the "fish-eye". The crack spreads from the "fish-eye's" border until it reaches a critical size, at which point it fractures completely [1].

As stated above in the present subsection, there are mainly two fatigue failure initiation sites. For the most cases, such as for low and medium strength steels subjected to high stresses, fatigue failure is initiated at the surface of the material. For those cases, the fatigue behaviour can be schematize by a traditional $S-N$ curve as the one demonstrated in the Figure 2.26 [30].

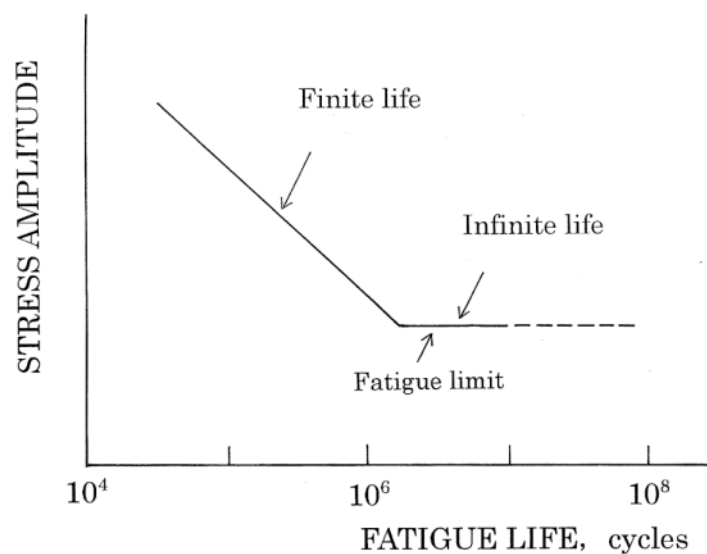


Figure 2.26: Traditional concept of $S-N$ curve (Adapted from [30])

The traditional concept of the $S-N$ curve, plots the correlation between the stress range and the number of cycles to failure of a given material [4]. This concept consists of a sloping regression which represents the finite life range of a material, which is connected, at normally around 10^6 cycles, to a leveled part that represents the infinite life range of the material. The stress at which the leveled part is established is recognized as fatigue limit. The fatigue failure in the finite life range is triggered by the progressive propagation of microcracks, which are initiated at the specimen surface. Additionally, the fatigue limit corresponds to a critical stress value in which this microcracks do not propagate [30]. However, as demonstrated earlier, the fatigue failures can be initiated from the interior of the material, as an example for cases of materials that present strengthened surfaces and are subjected to relative low stresses and a high number of loading cycles, nonetheless, these same materials could have a failure initiated at the surface if higher stresses are originated [9]. And so, two types of failure modes can occur, leading to the conclusion that the traditional $S-N$ curve does not fully express the fatigue behaviour of materials, especially in the case of surface strengthened materials. Since the present dissertation is related to the VHCF regime, in which the initiation sites are usually located in an internal zone, it becomes essential to fully understand the fatigue failure mechanisms of different materials [6].

With the development of ultrasonic fatigue testing machines, which operate at extremely high frequencies, it is now possible to test specimens to a very high number of cycles in a short amount of time, when compared with the conventional fatigue machines. And so, experimental data, like the two-fold curve presented in the Figure 2.27, can be obtained in a relative short amount of time [4].

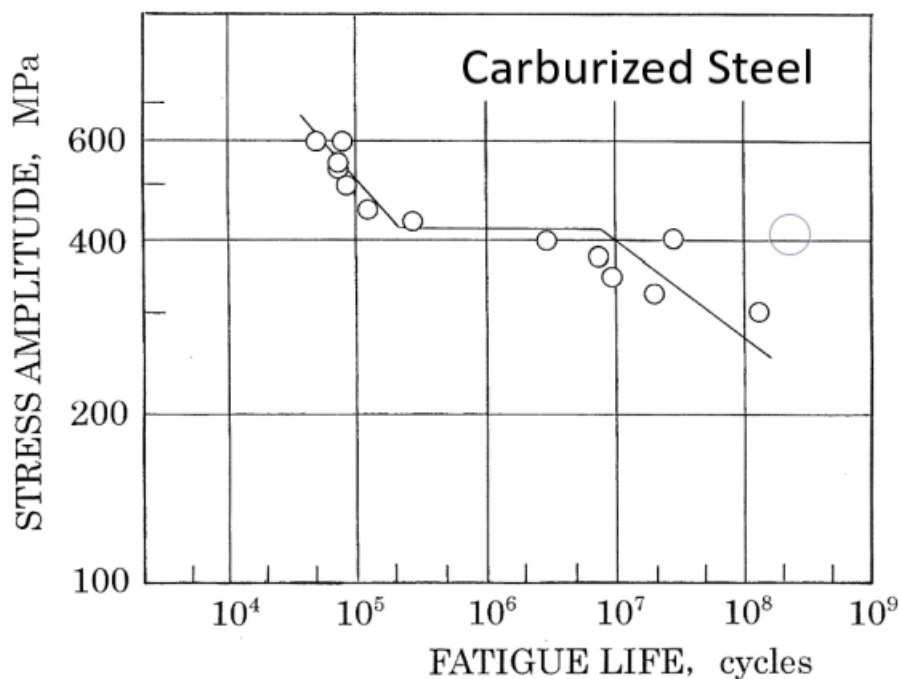


Figure 2.27: Stepwise $S-N$ curve for a carburized steel (Adapted from [30])

In the Figure 2.27, it is presented a plot of data for a carburized steel. It is notable the existence of two sloping parts, and the plot can be divided into two groups of fatigue failure, one below 10^6 cycles and the other above 10^7 cycles. The fatigue failure group below 10^6 cycles is characterized by crack initiation from the specimen's surface, therefore it is designated as the surface fatigue mode. Additionally, the second fatigue failure group, above 10^7 cycles, is characterized by internal crack initiation and usually the surface fracture presents a "fish-eye", similar to the one seen in Figure 2.24. The second fatigue failure group is also known as internal fatigue mode. The leveled part between the two slopes is the fatigue limit for the surface fatigue mode. This type of plot of data is called the stepwise $S-N$ curve [30]. The stepwise $S-N$ curve describes in a more complete manner the fatigue failure behaviour of materials since it reflects in its two-fold shape the two-fold behaviour of fatigue failure, surface and internal crack initiation. In the Figure 2.28 it is presented an expected general stepwise $S-N$ curve for a high strength steel or titanium alloy [31].

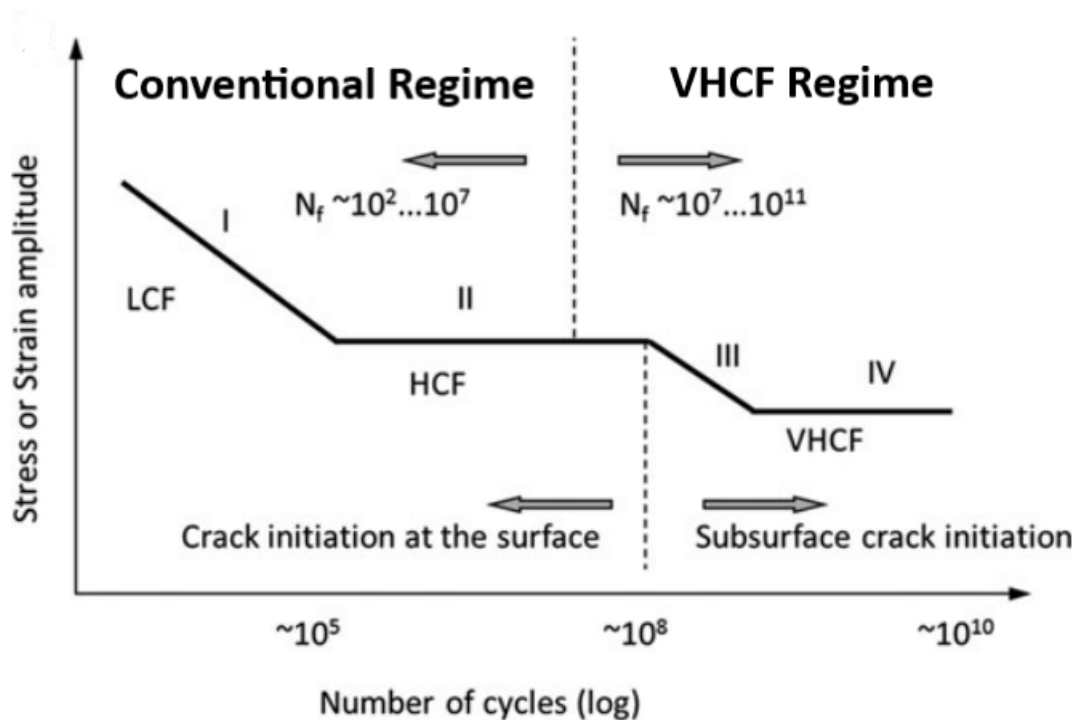


Figure 2.28: General stepwise $S-N$ curve for a high strength steel (Adapted from [31])

2.4 Fundamentals of fracture mechanics

The fracture mechanics field of study deals with the inevitability of cracks and their growth during the service life of components. Cracks can appear as a consequence of the manufacturing process, such as voids or metallurgical discontinuities like particle inclusions, or, form due to fatigue during the service life of a component [32, 33].

There are three main loading types, Mode I, Mode II and Mode III, as it is identified in the Figure 2.29. Mode I is generally called as the "opening mode" and it is the most common in fatigue. It is present during tensile loading (normal stresses). Mode II is called as "sliding mode" and occurs when in-plane shear is present. Finally, Mode III is designated as "tearing mode" and it is created by out-of-plane shear. Any other existing loading mode is a combination of the three described above [5, 32].

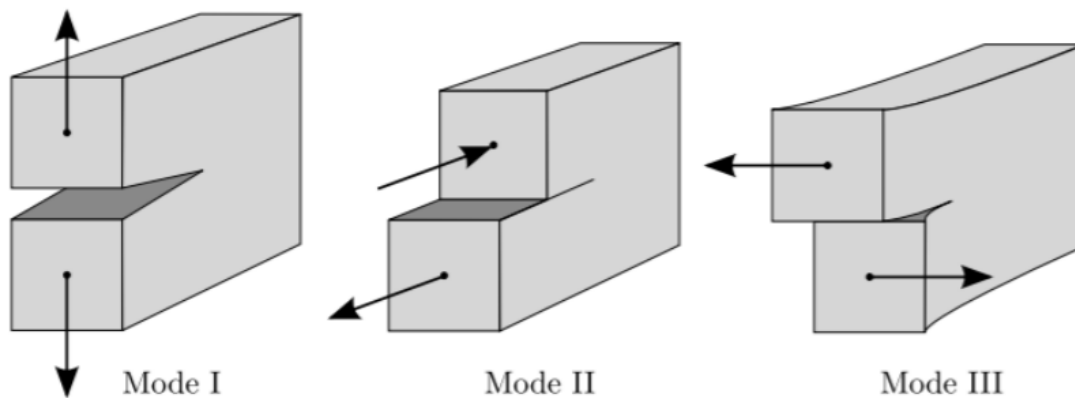


Figure 2.29: Loading modes of crack propagation [34]

Since mode I is the most common mode of failure and the predominant mode to which the dynamic system of the equipment being developed in the present document will be subjected, only this loading mode will be further discussed and using the elasticity theory it will be analyzed. Irwin, proposed the usage of the term stress intensity factor, which for the first mode is written as K_I , to characterize the stress concentration adjacent to the crack's tip. The stress intensity factor is a function of the geometry and size of the crack and loading mode [5, 35]. It is given by:

$$K_I = Y \sigma \sqrt{\pi a} \quad (2.42)$$

Where Y is the stress intensity magnification factor, σ is the applied stress which needs to be applied far enough from the crack's tip and a is the length of the crack. Clearly, the stress intensity factor increases as the crack length increases. When a certain critical value of the stress intensity factor is reached, the crack propagates in an unstable and unpredictable way. This value is called the fracture toughness of the material, K_{IC} , and it is a property of a material which depends on the

material itself, the crack, the environmental conditions and a function of the width of the specimen and the crack length. Furthermore, the fracture toughness of the material is the critical value of the stress intensity factor, for a given load, geometry and crack length necessary to cause fracture [32, 33]. It is described as:

$$K_{IC} = \sigma_c \sqrt{\pi a_c} f \left(\frac{a_c}{w} \right) \quad (2.43)$$

Where σ_c is the applied nominal stress at crack instability, a_c is the crack length at instability and w is the width of the specimen. The value of K_I below which the fatigue crack won't propagate is called the fatigue crack threshold, ΔK_{Ih} . When discussing about cyclic loads, it's more relevant to speak about the stress intensity factor range ΔK_I , and the stress range, $\Delta\sigma$, which represents $\sigma_{max} - \sigma_{min}$. Furthermore, the equation 2.42 can now be rewritten as [32, 36]:

$$\Delta K_I = Y \Delta\sigma \sqrt{\pi a} \quad (2.44)$$

In Figure 2.30, it is presented a graph with the crack length as a function of the number of stress cycles. As it can be noticed, three stress ranges are presented, $(\Delta\sigma)_3$, $(\Delta\sigma)_2$ and $(\Delta\sigma)_1$, respectively, in descending order. Since the $(\Delta\sigma)_3$ is the higher stress range, it is expected to lead to a faster crack growth rate per cycle, $\frac{da}{dN}$, than the other two stress ranges, i.e., having all the three cases the same initial crack length, the $(\Delta\sigma)_3$ case will reach a bigger crack length with lower number of stress cycles [5]. The relation between the crack growth rate per cycle and the stress intensity factor, which is dependent of the stress range, is known as the Paris law [37].

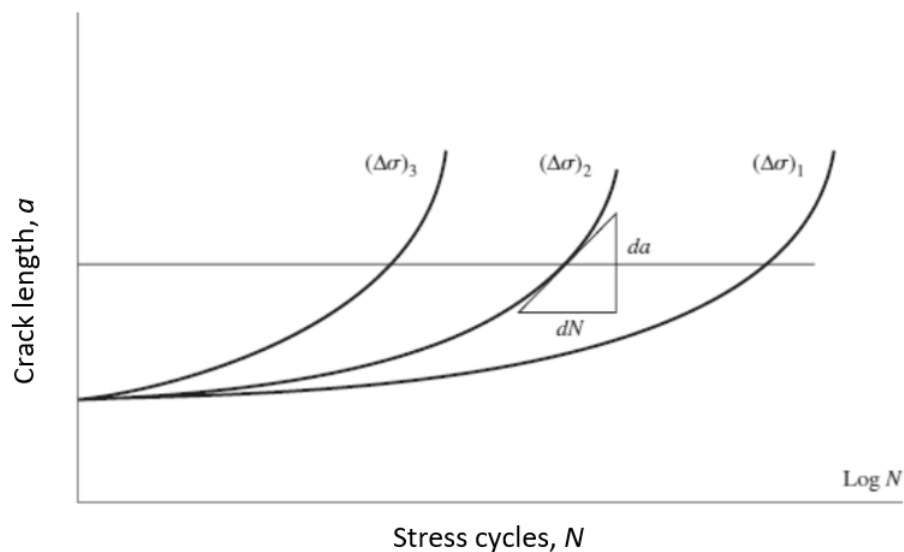


Figure 2.30: Crack length over number of cycles for different stress ranges (Adapted from [8])

The Paris law is presented in the equation 2.45 and it is only valid for the linear part of the plot presented in the Figure 2.31, Region II.

$$\frac{da}{dN} = C(\Delta K)^m \quad (2.45)$$

Where the constants C and m are empirical material constants. In the Figure 2.31, it is presented a graph in log-log coordinates with the crack growth per cycle as a function of the stress intensity range. On the leftmost portion of the graph, Region I, the crack growth per number of cycles is very small and can achieve a critical value in which there is no effective crack propagation. This critical value, as stated earlier, is defined as ΔK_{th} , fatigue crack propagation threshold. For the rightmost portion of the plot, Region III, the crack propagation becomes unstable leading to failure. This instability occurs due to the approximation of the value of the stress intensity factor to the fracture toughness of the material, K_C , as defined earlier [5].

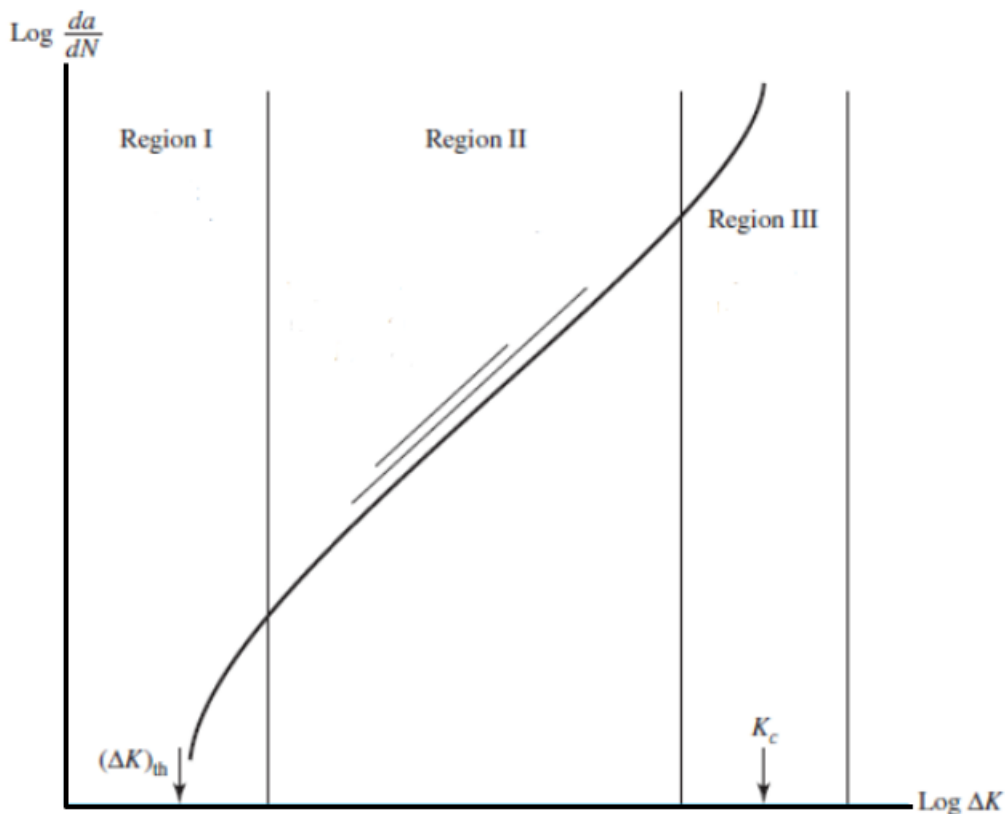


Figure 2.31: Crack growth per cycle as a function of the stress intensity range (Adapted from [8])

An essential point to highlight is that the data on the middle portion of the graph, Region II, is linear in log-log coordinates. Furthermore, the Paris law, equation 2.45, is only valid in this region and it allows the determination of the estimated number of cycles to failure after a crack is formed. The application of the Paris law on the other two regions will lead to inaccurate projections. The

number of cycles a component can withstand before failure after an initial crack is formed, N_f , can be predicted by combining the equations 2.44 and 2.45, leading to:

$$\int_0^{N_f} dN = N_f = \frac{1}{C} \int_{a_i}^{a_f} \frac{1}{(Y\Delta\sigma\sqrt{\pi a})^m} da \quad (2.46)$$

Where a_i is the initial crack length and a_f is the final crack length, which corresponds to failure [32].

Chapter 3

Structural Development of an Ultrasonic Fatigue Testing Equipment

This chapter concerns the structural development of the ultrasonic fatigue testing equipment. The pre-existing structure, requirements for the new machine, appropriate layout and all the numerical and analytical validation will be presented in the next sections within this chapter. All the decisions were made based on literature review and also according to cost, reuse of components from the original structure and ease of manufacturing.

3.1 Ultrasonic testing equipment requirements

The ultrasonic fatigue testing equipment that will be developed in this chapter must fulfill certain requirements that were imposed for this project.

The equipment must be capable of performing fully reversed ultrasonic fatigue tests, $R = -1$, it also must be able to apply a maximum 10 kN static load to the specimen in order to allow the fatigue characterization of different materials subjected to different values of R . Regarding cost containment, it is essential to reuse as many components from a given structure as possible. In addition, the simplicity of manufacturing will be a primary consideration in the design of every component. The designed dynamic system of the ultrasonic testing equipment must have a resonance frequency near the excitation frequency of the chosen piezoelectric transducer and it must be able to increase significantly the external displacement imposed by the piezoelectric transducer. Furthermore, the designed testing equipment must be capable of measuring the external applied static load to the specimen.

3.2 Pre-existing structure

In this section, the pre-existing structure will be presented. The ultrasonic fatigue testing equipment that is going to be developed as a result of this document will be planned with the reutilization of the structure that is depicted in Figure 3.1 as the basis for its design. Afterwards, in the following sections, the final layout of the developed equipment will be presented and an analysis will be made to the pre-existing structure in order to evaluate its safety when subjecting the specimens to the maximum static load (10 kN).

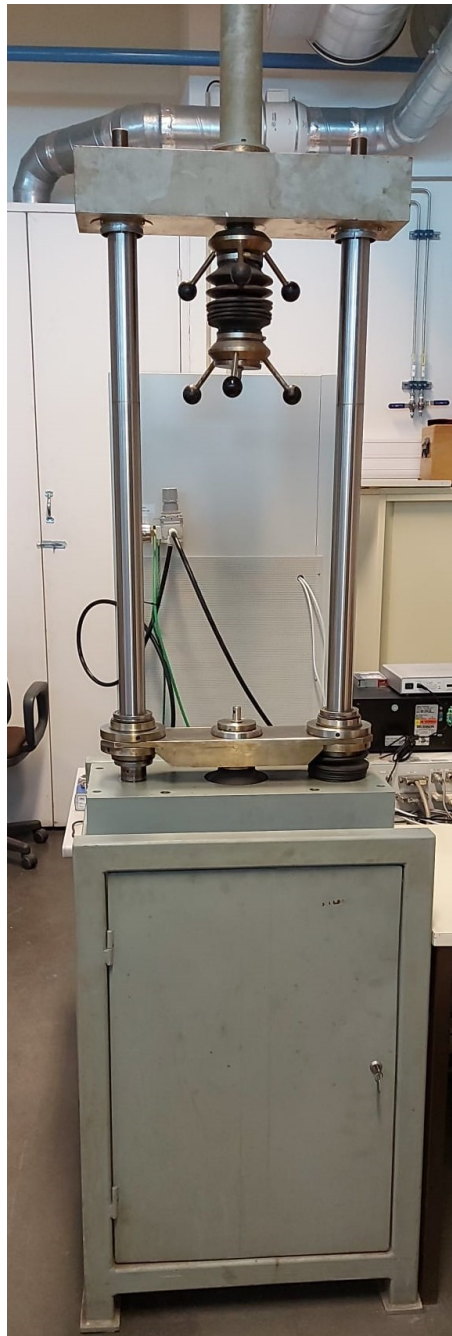


Figure 3.1: Pre-existing structure

The equipment shown in the Figure 3.1 is composed by two cast iron blocks (one at the top and the other at the bottom), a M50 X 3.0 power screw setup which is responsible for the traction, a reinforced chrome steel support which travels vertically on the two chrome steel guide shafts with the assistance of two linear ball bearings that are mounted on the support. The power screw and the linear ball bearings can be seen in more detail in the Figure 3.2. The lower block of cast iron is supported on a robust metal box that has the potential to be utilized for storing various machine components and accessories. Due to simplicity, the metallic box will be absent from the layouts presented in the subsequent section. However, it will serve as a support for one of the cast iron blocks in the final designed ultrasonic fatigue testing equipment.



Figure 3.2: Power Screw and Linear Ball Bearing existing in the original structure

Due to its robustness, compactness, and large distance between the two cast iron blocks, which is required to incorporate the ultrasonic fatigue components, the pre-existing structure shown in Figure 3.1 fits well into the project of building the ultrasonic fatigue testing equipment.

3.3 Layout of the ultrasonic machine

In this section the different iterations of the layout of the machine will be presented.

3.3.1 First iteration

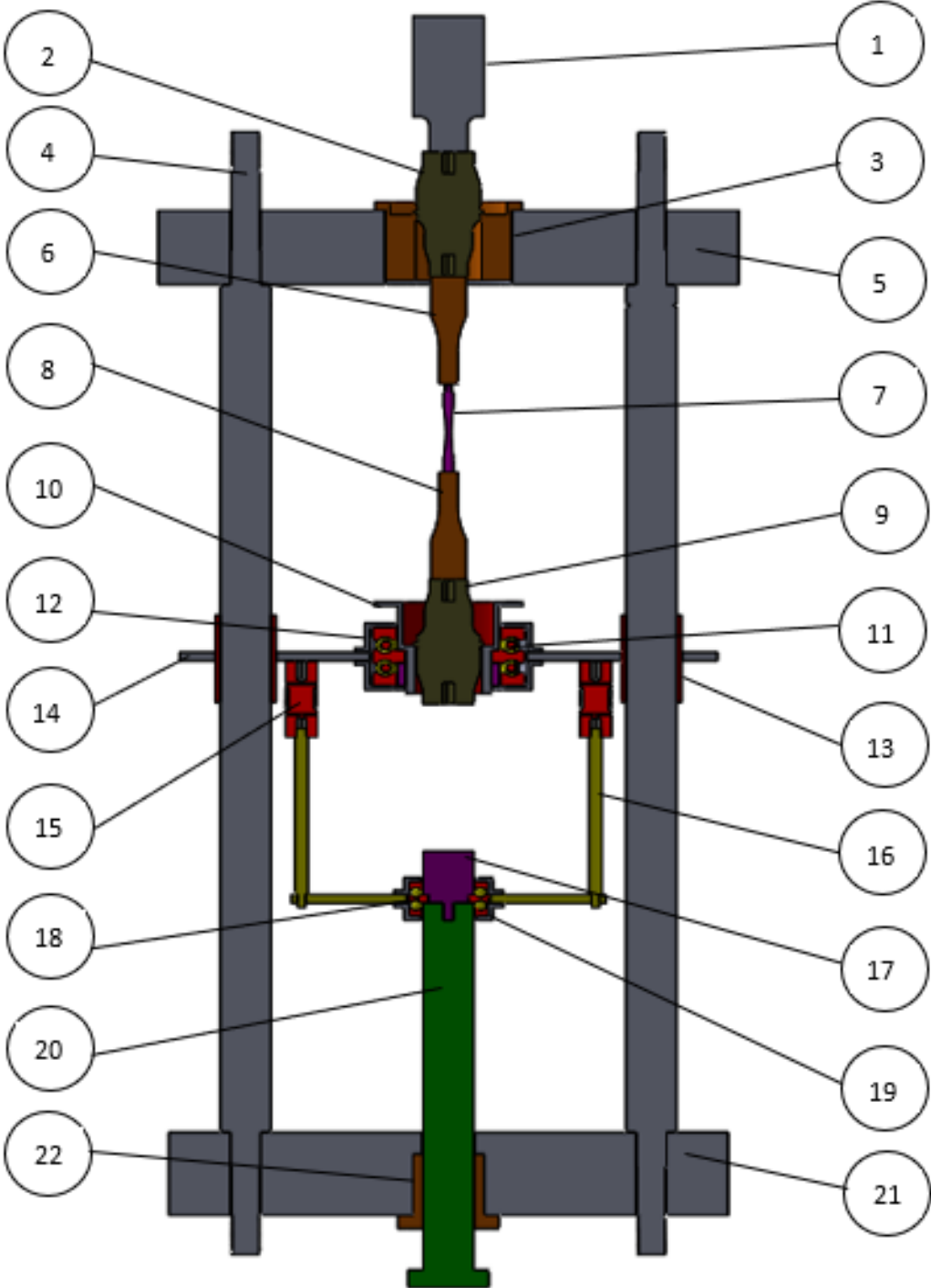


Figure 3.3: First design of the ultrasonic fatigue testing equipment

Table 3.1: Component identification of Figure 3.3

Number	Component
1	Piezoelectric Transducer
2	First Booster
3	Booster Flange
4	Chrome Steel Guide Shaft From The Original Structure
5	Original Lower Cast Iron Block
6	First Horn
7	Specimen
8	Second Horn
9	Second Booster
10	Flange Between Bearing And Booster
11	Double Direction Ball Bearing
12	Bearing Case
13	2 X Original Linear Ball Bearing
14	Support Plate
15	2 X Load Cell
16	Traction Connection Bars and Traction Support Plate
17	Accessory To Secure The Bearing (Bearing Holder)
18	Bearing Case
19	Double Direction Ball Bearing
20	Original M50 X 3.0 Power Screw
21	Original Upper Cast Iron Block
22	Original Power Screw Flange

The first preliminary sketch of the ultrasonic machine that is being developed in this document is present in the Figure 3.3 with the Figure 2.4 serving as the inspiration for its development. This first preliminary draft is shown in a sectional view in order to allow a better comprehension and to aid in the presentation of the concept.

According to the Bathias theory that is mentioned in chapter 2, ultrasonic fatigue testing equipment are able to carry out tests with a static force being applied to the specimen if the machine's configuration includes a second set of horn and booster. The second set of horn and booster are necessary to ensure the symmetry of the fatigue equipment and to enable a correct application of the static load, from the power screw to the specimen. In addition, one of the requirements for the project is that the developed machine must be able to carry out tests with a stress ratio equal to -1, which means without any applied static force, and also must be able to carry out tests with different values of R . This requirement must be met in order for the project to be considered successful.

Another objective of the project is to reuse the original structure's components as much as possible. Therefore, it was decided to utilize the pre-structure chrome steel guide shafts and cast iron blocks to create a foundation for the introduction of the new components.

As it can be seen in the Figure 3.3, it was chosen to have the first booster and horn, fed by the piezoelectric transducer, coupled through a flange to the upper cast iron block. The primary justification for this decision is the need for adequate vertical space to be able to conduct tests

without any static force applied. Thus, one of the ultrasonic machine's primary requirements is met through this design.

After a choice has been made about the first pair of booster and horn, another decision would need to be taken regarding the second pair of booster and horn, as well as the system via which they will transmit the static force.

One of the considered ideas was to attach the second booster to a support plate that would be moved vertically by ball screws driven by an electric motor, similar to the scheme shown in the Figure 3.4. And so, the static force would be originated by the displacement of the support plate after the specimen was threaded on both horns.

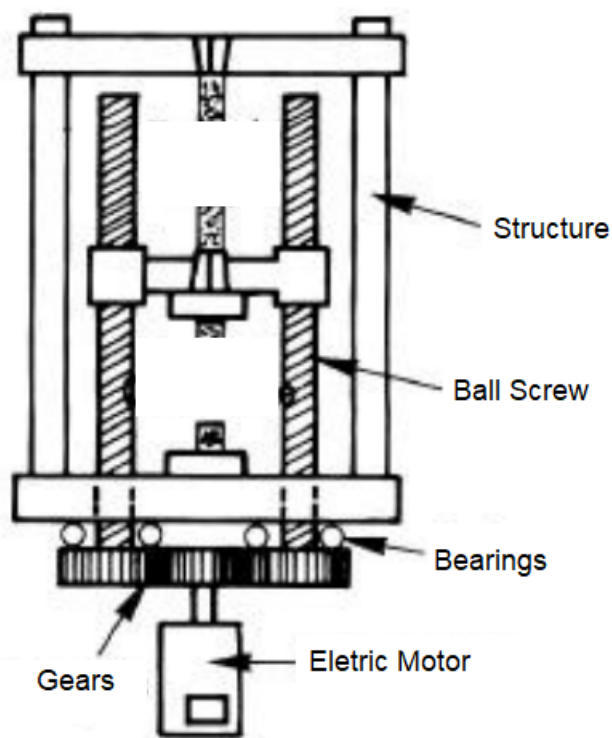


Figure 3.4: Schematic figure of an universal traction machine (Adapted from [38])

This idea, however, was discarded due to cost concerns as well as the desire to reuse the maximum number of components from the initial structure. Therefore, it was decided to utilize the original power screw and its flange to move the booster and to create the static force. The booster will be attached to a support plate, which will travel up and down on the guide shafts with the aid of the original linear ball bearings. And so, the static force will be created manually after the specimen is threaded on both horns. It can be seen in the Figure 3.1 that the power screw and its flange are connected to the upper cast iron block, however it was decided to rearrange the order of the cast iron blocks in the new ultrasonic machine so that the block that is connected with the power screw would be placed in the lower position in order to facilitate the manual rotation. Everything that has been presented up until this point may be seen in Figure 3.3.

The power screw will transmit the movement and static force to the support plate through the traction connection bars and the traction support plate. A double direction ball bearing is utilized to assure the correct connection between the power screw and the traction support plate. Two load cells are added between the support plate and the traction connection bars in order to verify and to guarantee that the correct static load is being applied. Additionally, another double direction ball bearing was added to the support plate in order to allow the rotation of the second horn that is coupled to the second booster. This rotation is required for threading the specimen into the second horn.

Unfortunately, the sketch presented in Figure 3.3 and described above presents a practical difficulty which led to the need of reevaluating the presented concept and developing a new layout for the ultrasonic fatigue testing equipment. Due to the pitch difference between the power screw and the specimen, it would be very difficult to synchronize the upward manual movement of the second booster, originated by the rotation of the power screw, with the screwing of the specimen onto one of the boosters, assuming that the specimen had already one of the ends already screw onto the other booster.

This first draft, presented in Figure 3.3, was extremely simplified. However its presentation and explanation are of greatest importance since the final layout will be presented and discussed in the following subsection, and it will be based on this initial one but with a practical solution for the problem stated above.

3.3.2 Final design of the ultrasonic fatigue testing equipment

In this subsection, the final layout of the ultrasonic fatigue testing equipment will be presented. A very detailed and complete version of the machine design will be displayed. In the next section, an analytical and numerical analysis to the original structure and to the different component sub-assemblies will be carried out in order to fully validate the concept and to ensure the machine's reliability when carrying out tests at its maximum load.

To assist the understanding and the discussion of the machine's architecture, the layout of the machine was divided into four sections, A, B, C and D. In the Figure 3.5 it is possible to see a section view of the final design of the ultrasonic machine as well as the identification of the different sections. The components that are required in order to carry out fully reversed longitudinal ultrasonic fatigue tests are included in Section A. The specimen utilized to perform fully reversed longitudinal ultrasonic fatigue tests only needs to have one threaded end, to ensure the connection with the upper horn. Section B includes the original linear ball bearings from the pre-structure, two load cells and a valid solution for the introduction of the second booster and horn. Section C will demonstrate the necessary connection to the original M50 X 3.0 power screw be able to move the second booster and horn vertically to induce a static load to the specimen. Finally, Section D will present the power screw flange connected to the original upper cast iron block. Each section will be presented and explained next in detail, as well as the bolted connections within each section. The different mechanical components chosen for this project, will be defined and justified within each respective section.

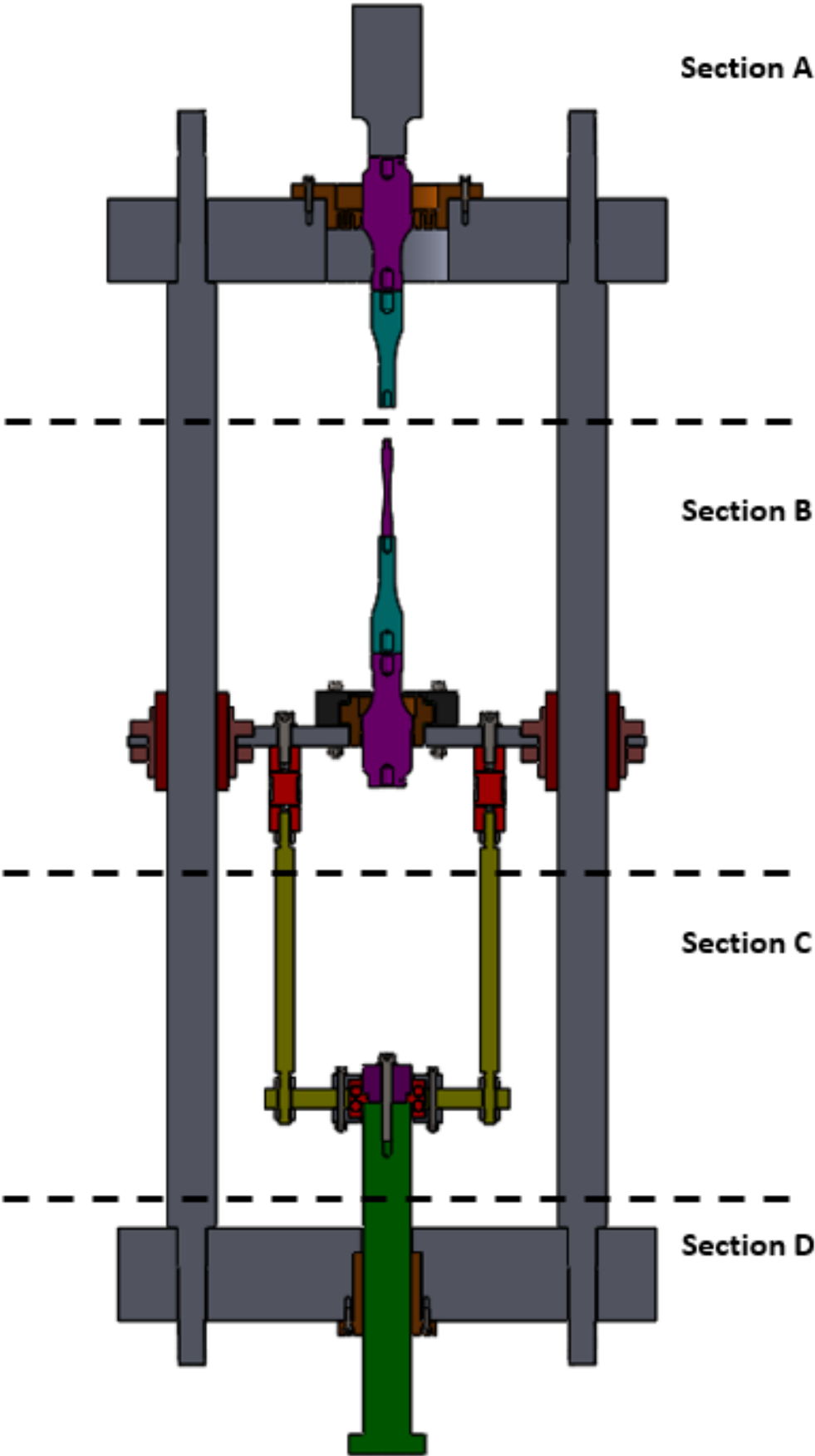


Figure 3.5: Section view of the final design of the ultrasonic machine with the identification of the corresponding sections

The base structure of the design depicted in Figure 3.5 consists of the two guide shafts and the two cast iron blocks from the original pre-structure shown in Figure 3.1, with the block that is connected to the power screw placed in the lower position, as in the layout of Figure 3.3. These four original components will not be mentioned or identified further owing to simplicity.

3.3.2.1 Section A

Section A is depicted in greater detail in Figure 3.6 and in Figure 3.7 it is presented a section view with all the components of this subassembly identified. The component identification is shown in Table 3.2.

This section contains all required components to produce an ultrasonic fatigue testing equipment capable of producing fully reversed longitudinal tests, $R = -1$. The booster and horn presented must have their first longitudinal natural frequency equal to the excitation frequency of the piezoelectric transducer, approximately 20 kHz. The first longitudinal natural frequency is dependent on the booster and horn geometry and material. Their main characteristics and manufacturing material will be presented in the next section. The piezoelectric transducer, booster and horn are linked through threaded studs, which have been omitted from the Figure 3.7 for convenience. The chosen Piezoelectric transducer for this project was bought from the online store MPInterconsulting [39], and it is shown in Figure 3.8. It works between a range of 20 ± 1.2 kHz when no other component is attached and its maximum vibration amplitude is between $17 - 20$ μm .

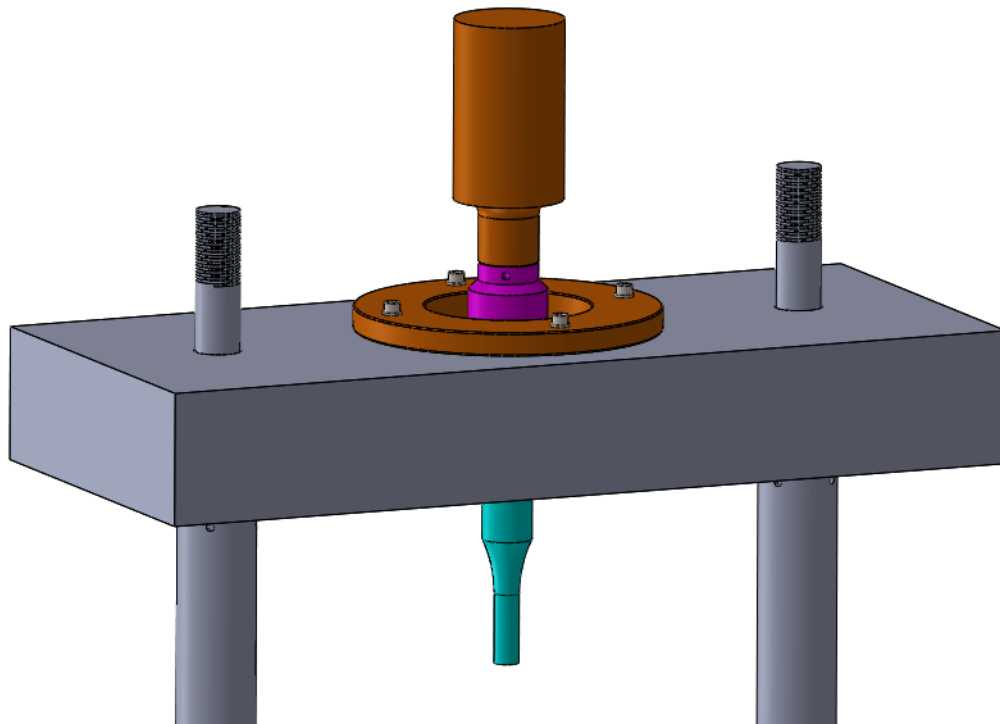


Figure 3.6: Section A shown in more detail

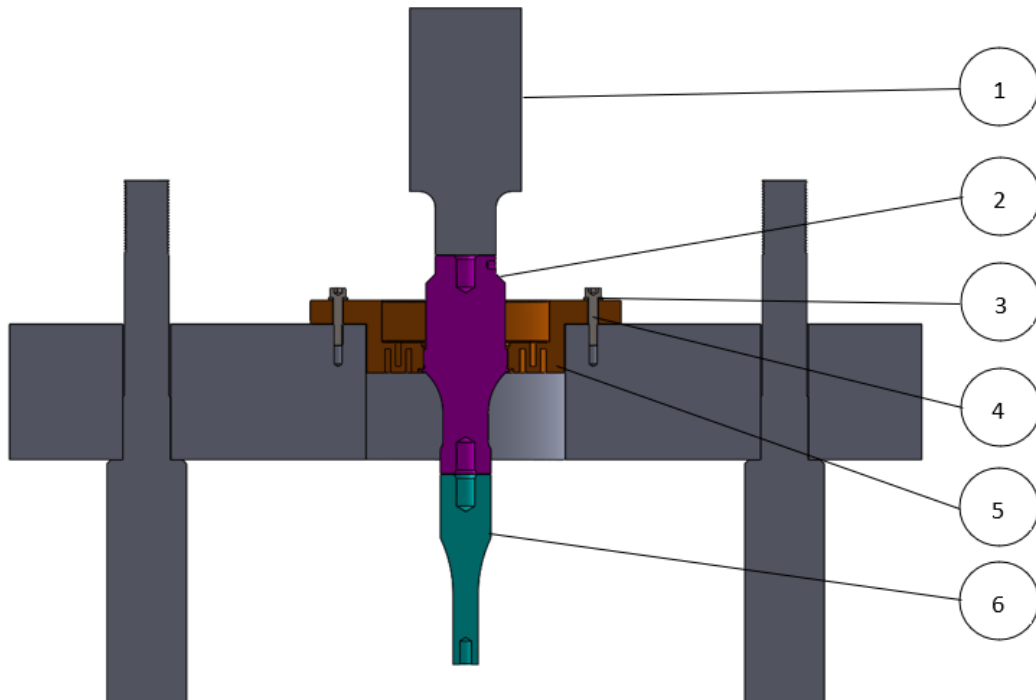


Figure 3.7: Section view of Section A with respective component identification

Table 3.2: Component identification of Figure 3.7

Number	Component
1	Piezoelectric Transducer
2	First Booster
3	4 X ISO 7089 - M6 Washers
4	4 X ISO 4762 - M6 X 30 - 12.9 Bolts
5	Vibration Absorbing Flange
6	First Horn



Figure 3.8: 20 kHz Piezoelectric Transducer MPIinterconsulting - 3KW

As it can be seen in the Figure 3.7, the booster is threaded to the vibration absorbing flange, which has an internal threaded section. The vibration absorbing flange can be seen in more detail in the figures below. The threaded part on the booster needs to be a vibration node, in order to induce the minimal vibration into the system as possible. The adoption of the use of a vibration absorbing flange is necessitated to avoid the transmission of unwanted vibrations from the dynamic system to the structure. The vibration absorbing flange has internal grooves, as it can be seen in the Figure 3.10, which minimize the transmission of unwanted vibrations. The vibration absorbing flange is fixed to the superior cast iron block through the use of four ISO 4762 - M6 X 30 - 12.9 Bolts with four ISO 7089 - M6 Washers. This component needs to be able to resist the static load of 10 kN. The flange and cast iron block connection will be numerically analysed in the next section in order to assure safety when the ultrasonic fatigue testing equipment is operating. Next, Section B from Figure 3.5 will be displayed.

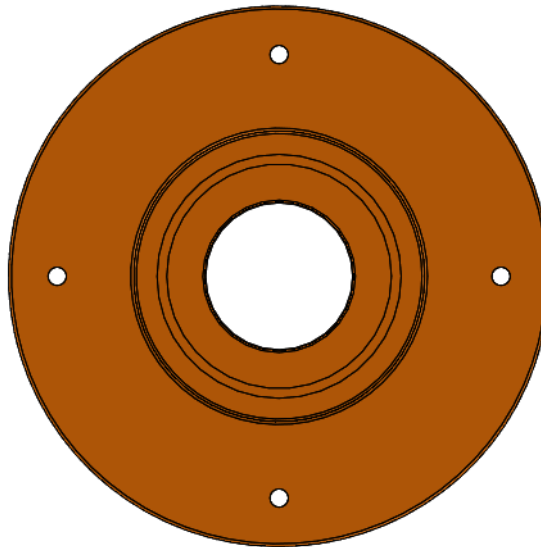


Figure 3.9: Top view of the Vibration Absorbing Flange

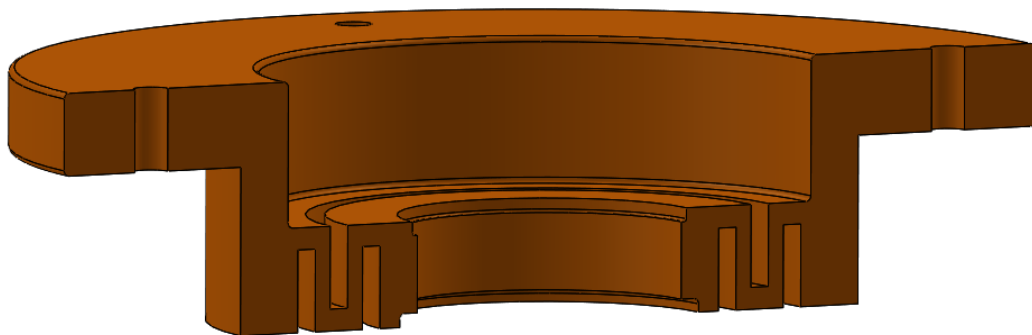


Figure 3.10: Section view of the Vibration Absorbing Flange

3.3.2.2 Section B

In the Figures 3.11 and 3.12, Section B is presented. The bolted connections are not identified in the Figure 3.12 due to enhance the image's readability, however, they will be addressed as the text progresses. The main purpose of Section B is to introduce a practical assembly capable of correctly securing the second pair of booster and horn in safety, when the specimen is under load. Furthermore, it allows the correct fixation of the specimen as well as the measurement of the applied static force.

The connection between the booster and horn is ensured throughout a threaded stud, which is not represented in the Figure 3.12. The booster is threaded to a booster support, on its vibration node in order to minimize unwanted vibrations. The concept is to first screw the specimen into the second horn, and then raise the specimen, the second horn, the second booster, and the booster support subassembly manually in order to screw it into the first horn. After the specimen is threaded into both horns, the booster support can now be placed on the support plate. The upward vertical movement of the support plate is guaranteed through the manual rotation of the power screw as it can be seen in the Figure 3.5. Once the booster support is in its correct place on the support plate, two locking supports are used to secure it via a screw and nut bolted connection, six ISO 4762 - M8 x 70 - 12.9 bolts, six ISO 4033 - M8 - 12 nuts and twelve ISO 7089 - M8 washers are used.

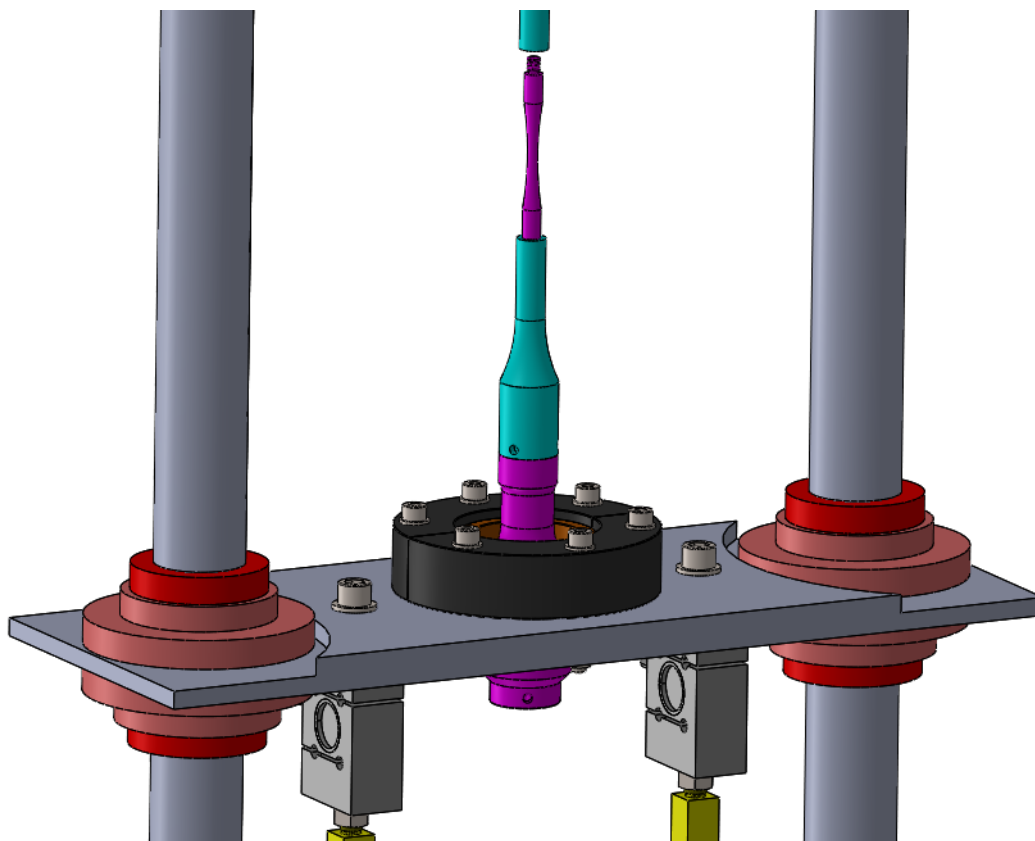


Figure 3.11: Section B shown in more detail

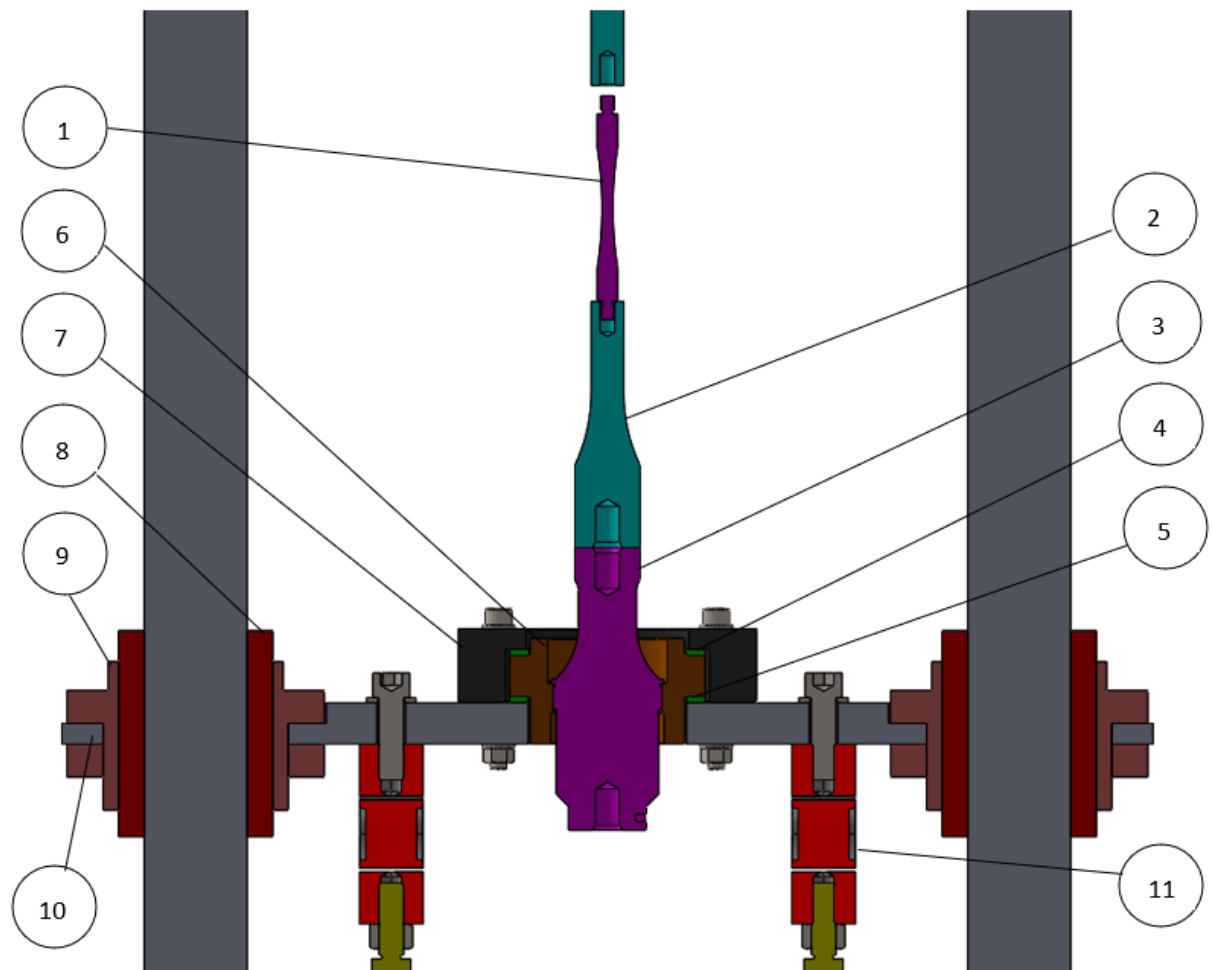


Figure 3.12: Section view of the Section B

Table 3.3: Component identification of Figure 3.12

Number	Component
1	Specimen
2	Second Horn
3	Second Booster
4	Upper rubber ring
5	Lower rubber ring
6	Booster Support
7	2 X Locking Support
8	2 X Original Linear Ball Bearing
9	2 X Original Linear Ball Bearing fixing hardware
10	Support Plate
11	2 X Load Cell

In the next section, the connection between the two locking supports and the booster support will be numerically analyzed. Between the booster support, support plate and locking support, two rubber rings, one on top of the booster support and the other at the bottom, were designed in order to reduce the metal to metal contact of the components and to minimize the transfer of unwanted vibrations to the ultrasonic machine structure.

In order to aid the upward and downward movement of the support plate, the original linear ball bearings were used. The original linear ball bearing fixing hardware from the original pre-structure, which are shown in Figure 3.13, were also integrated into the final design to decrease manufacturing expenses. To ensure compatibility, it was required to reduce the thickness of the support plate in the installation area as it can be seen in Figure 3.11, from 20 mm to 10 mm.

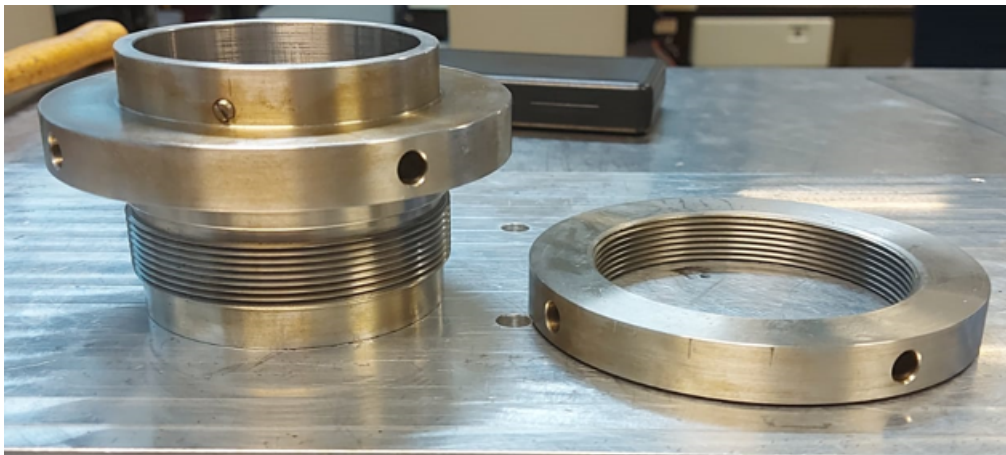


Figure 3.13: Original Linear Ball Bearing fixing hardware

As it can be seen in the Figures 3.11 and 3.12, two load cells were added to the support plate. The load cells are essential for ensuring that the static force is distributed equally through the entire support plate. In addition, it is possible to identify the magnitude of the force that is being applied through the use of them. The load cells are secured to the support plate through the use of two ISO 4762- M12 x 40 - 12.9 bolts and two ISO 7089 - M12 washers.

Two S-type tension load cells, each with a capacity of weighing up to 500 kgf, 1-RSCC3/500KG-1 sold by HBM, were selected as the load cells of choice. The maximum load applied by the ultrasonic fatigue testing equipment being developed in this document is 1000 kg and the load cells can be seen in Figure 3.14. This decision was influenced by a large number of considerations, including their compact size, affordable price and speedy delivery.



Figure 3.14: 1-RSCC3/500KG-1 Load Cell from HBM [40]

3.3.2.3 Section C

Section C is demonstrated in greater detail in the Figures 3.15 and 3.16 with all the components being identified in Table 3.4. In order to improve the clarity of Figure 3.16, the bolted connections are not labeled; nonetheless, they will be discussed as the text develops. The connection between Section B and Section C is made by two squared section bars with threaded ends; however, this connection elements will be covered in greater detail in a later section of this present text.

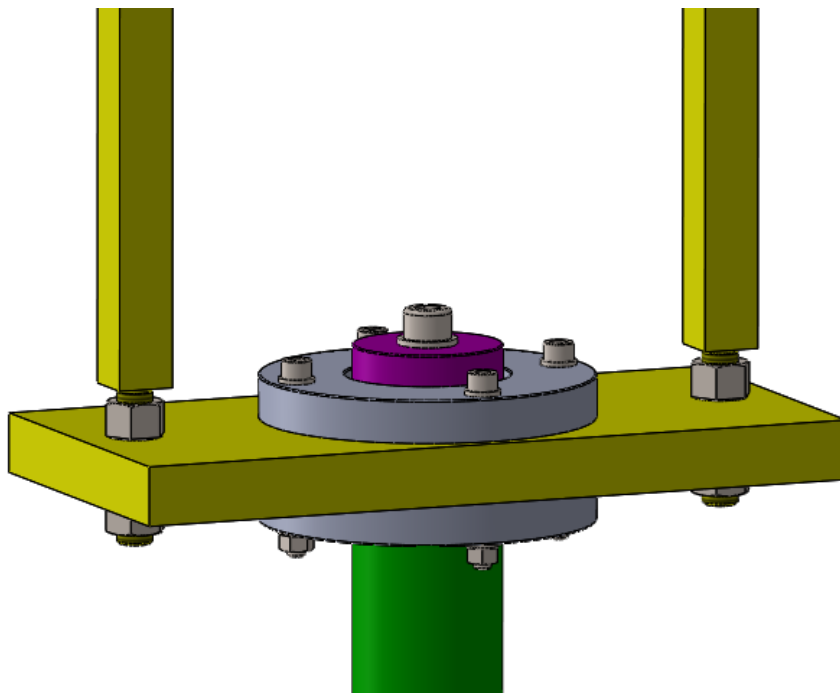


Figure 3.15: Zoomed view of section C

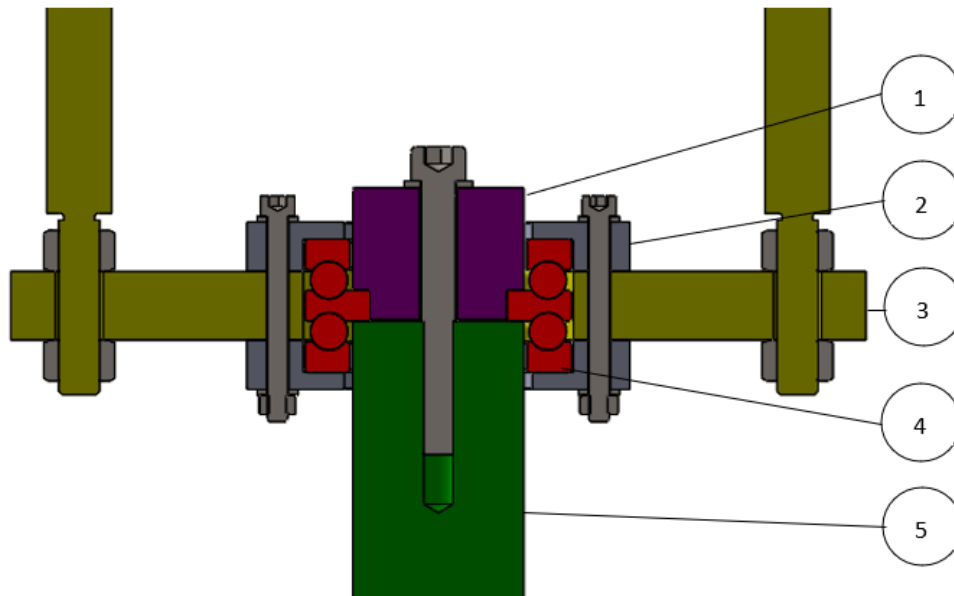


Figure 3.16: Section view of the Section C

Table 3.4: Component identification of Figure 3.16

Number	Component
1	Accessory To Secure The Bearing (Bearing holder)
2	2 X Bearing Case
3	Traction Plate
4	Double Direction Thrust Ball Bearing
5	Original M50 X 3.0 Power Screw

The bearing connection is the main aspect of Section C since it enables the correct attachment between the power screw and the traction plate. It allows for the rotation of the power screw without causing the rotation of the traction plate. The chosen bearing needs to be able to accommodate axial loads in both directions since the power screw can have an upward and downward vertical movement. The bearing will not be subjected to any radial load and in addition of that, the requirements of the project specify a maximum static load of 10 kN to be applied to the specimen. Regardless of the fact that the bearing fixes the dynamic system, it is predominantly subject to static loads, so in practise the applied dynamic load to the bearing will be very small. Additionally the bearing would have to be compatible with the diameter of the original M50 X 3.0 Power Screw. After further investigation, it was determined that the 52210- Double direction thrust ball bearing, shown in Figure 3.17, sold by SKF would be the best option since it satisfies all of the aforementioned criteria, in addition to having a low cost and a high level of reliability. However, due to the requirement of the selected bearing compatibility with the diameter of the Power Screw, the chosen bearing can withstand greater loads than required. The performance parameters of the

52210 Double direction thrust ball bearing are shown in the Table 3.5 and the abutment dimensions are demonstrated and tabled on Figure 3.18 and Table 3.6, respectively.



Figure 3.17: 52210 - SKF - Double direction thrust ball bearing (Adapted from [41])

Table 3.5: Performance parameters of the 52210 - SKF - Double direction thrust ball bearing [41]

Basic dynamic load rating, C	49.4 kN
Basic static load rating, C_0	116 kN
Reference speed	2 400 r/min
Limiting speed	3 400 r/min

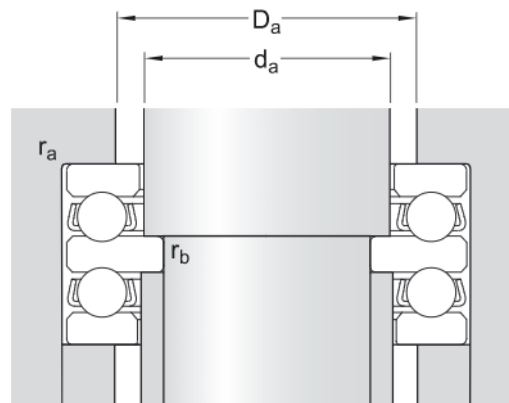


Figure 3.18: Nomenclature and identification of the different abutment dimensions of the double direction thrust ball bearing [41]

Table 3.6: Abutment dimensions [41]

Abutment diameter shaft, d_a	50 mm
Abutment diameter housing, D_a	max.61 mm
Fillet radius housing, r_a	max.1 mm
Fillet radius shaft, r_b	max.0.6 mm

As it can be seen in the Figure 3.16, the double direction thrust ball bearing is secured through the use of two bearing cases and one bearing holder. The bearing cases are fixed to each other and to the traction plate through a screw and nut bolted connection, as shown in the Figure 3.15. For this connection are used a total of four ISO 4762- M6 x 60 - 12.9 bolts, four ISO 4033 - M6 - 12 nuts and eight ISO 7089 - M6 washers. The bearing holder is connected to the original Power Screw through an ISO 4762 - M10 x 80 - 12.9 bolt and ISO 7089 - M10 washer. The connection between the two bearing cases with the traction plate and the connection between the bearing holder and the power screw will be numerically analyzed in the next section in order to evaluate its influence on the double direction thrust ball bearing.

As already mentioned above, the connection between Section B and Section C is made by two squared section bars with M12 threaded ends. It can be seen in more detail in the Figures 3.19 and 3.20. The two squared section bars are identified with the number 1 in the Figure 3.20. To prevent load unevenness and to guarantee that the static load is spread evenly throughout the sections, the threaded portion of the squared section bars are designed with extra length and nuts are utilized to regulate the connections.

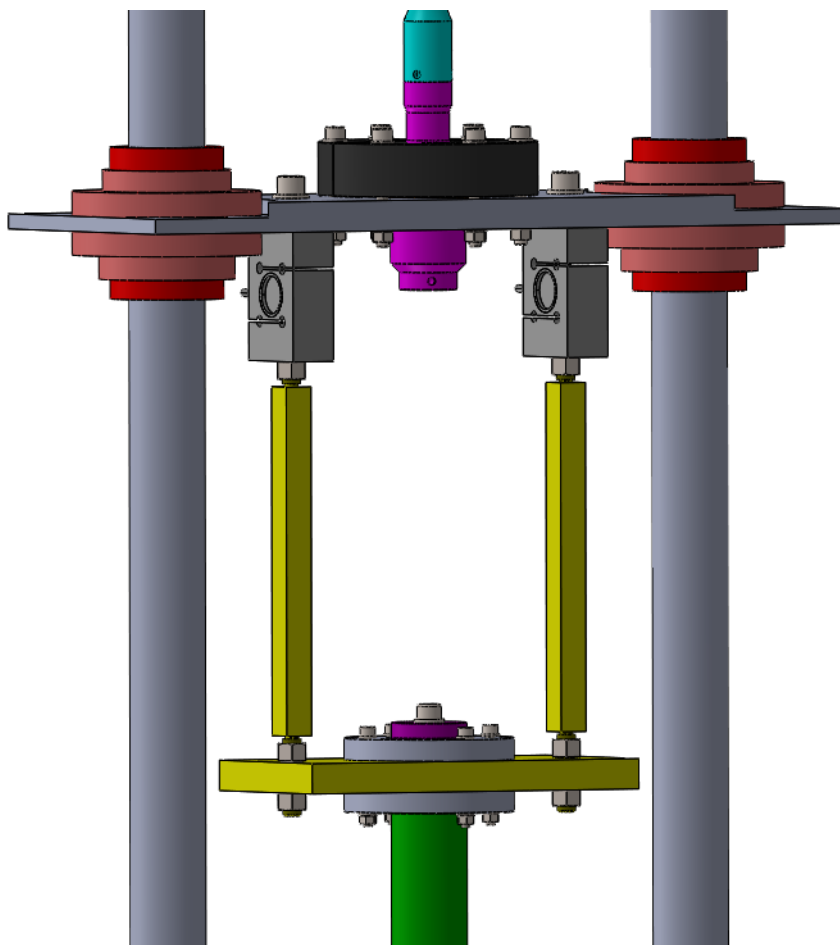


Figure 3.19: View of the connection between Section B and Section C

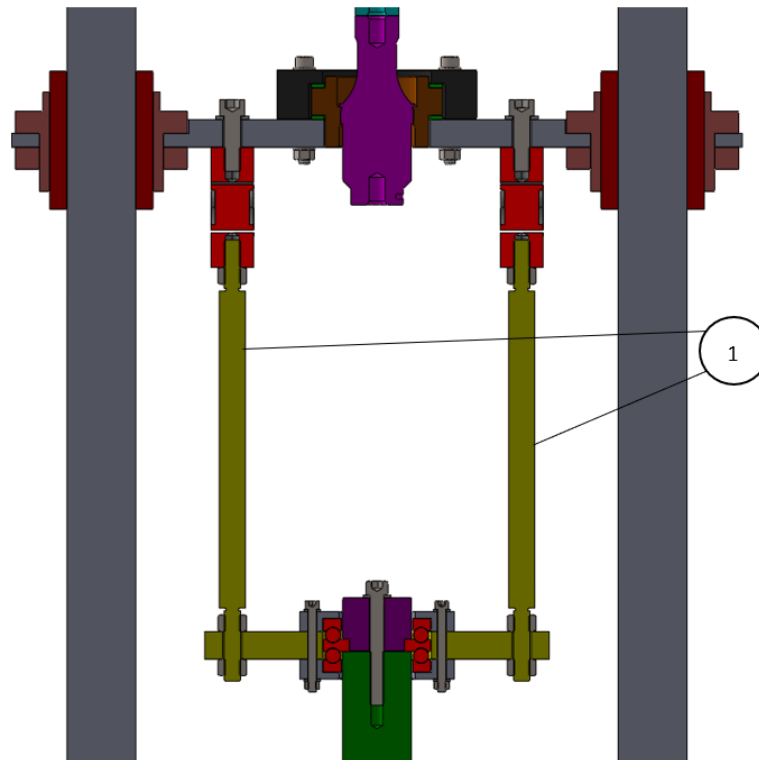


Figure 3.20: Section view of the connection between Section B and Section C

3.3.2.4 Section D

Section D is detailed in the Figures 3.21 and 3.22 with all the component identification being illustrated in Table 3.7. In an effort to reuse as many components from the original pre-structure as feasible and save the expense of machining a new bushing, it was decided to utilize the original power screw bushing and replace just the old bolts. The power screw bushing is connected to the cast iron block through four ISO 4762 - M6 x 20 - 12.9 Bolts.

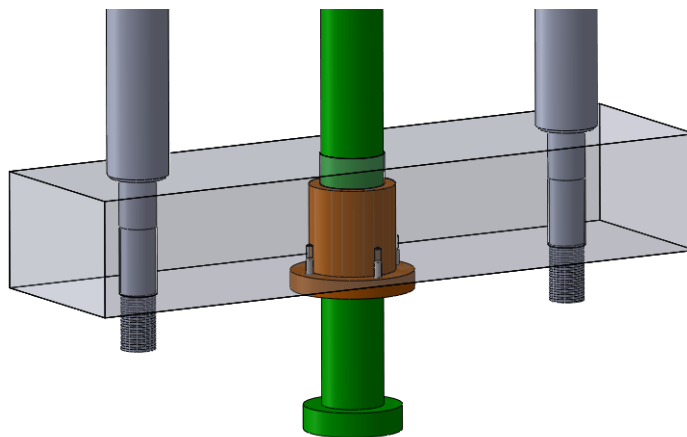


Figure 3.21: Close-up view of Section D with increased transparency in the lower cast iron block

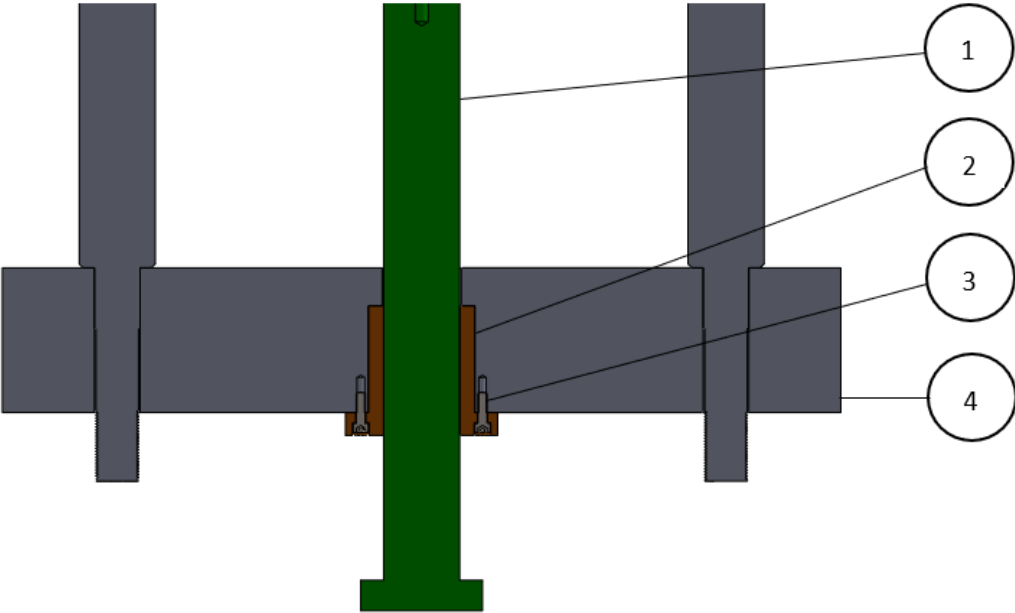


Figure 3.22: Section view of the Section D

Table 3.7: Component identification of Figure 3.22

Number	Component
1	Original M50 X 3.0 Power Screw
2	Original Power Screw Bushing
3	4 X ISO 4762 - M6 x 20 - 12.9 Bolts
4	Original Upper Cast Iron Block

An analytical and numerical stress and strain analysis will be carried out in the next section on the pre-structure, as well on various components and subassemblies of the ultrasonic fatigue testing equipment that was designed, presented, and discussed in this section.

3.4 Analytical and numerical analysis of the designed ultrasonic fatigue equipment

In this section, an analytical and numerical analysis will be presented concerning the safety of the ultrasonic fatigue testing equipment when performing tests with the maximum static load applied to the specimen (design check). All calculations and considerations will be presented and discussed, additionally the numerical analysis will be performed using the Abaqus software.

First, the original pre-structure will be analyzed to ensure that it can be utilized as a stable foundation for this project. Then, various components and subassemblies of the final design, presented and discussed in the previous section, will be examined both analytically and numerically to ensure the fatigue ultrasonic machine's proper operation. After the results of analytical and numerical analyses, the manufacturing material of the new components will be selected and presented. The definition drawing of each component is presented in Appendix C.

3.4.1 Analysis of the original pre-structure

First, a thorough examination of the original guide shafts will be conducted. As the connection between the two cast iron blocks and the mounting spots of the linear ball bearings, these guide shafts are crucial. The maximum static load to which the ultrasonic fatigue machine is capable of subjecting the specimens is 10 kN. Ignoring the weight of the other machine components, which are significantly smaller, the forces acting on the guide shafts can be simplified as seen in Figure 3.23. So, each guide shaft will be submitted to an uniaxial compression of 5 kN.



Figure 3.23: Chrome Steel Guide Shaft From The Original Structure

The radius of the vital part of the guide shaft is 25 millimeters, hence the stress can be calculated as follows:

$$\sigma = \frac{F}{A} = \frac{5000}{\pi \cdot 25^2} = 2.6 \text{ MPa} \quad (3.1)$$

Since the exact material of manufacture of the guide shafts was unknown, a yield strength of 200 MPa was assumed. This value is conservative because the guide shafts are made of stainless steel, which generally have a higher yield strength than it was considered. Furthermore, a Safety Factor, SF , could be obtained.

$$SF = \frac{200}{2.5} = 78.5 \quad (3.2)$$

The calculated Safety Factor is very high, but because it relates to an original structure component, guide shaft, it was decided to retain its use and not incur additional costs to produce or buy new components to replace it.

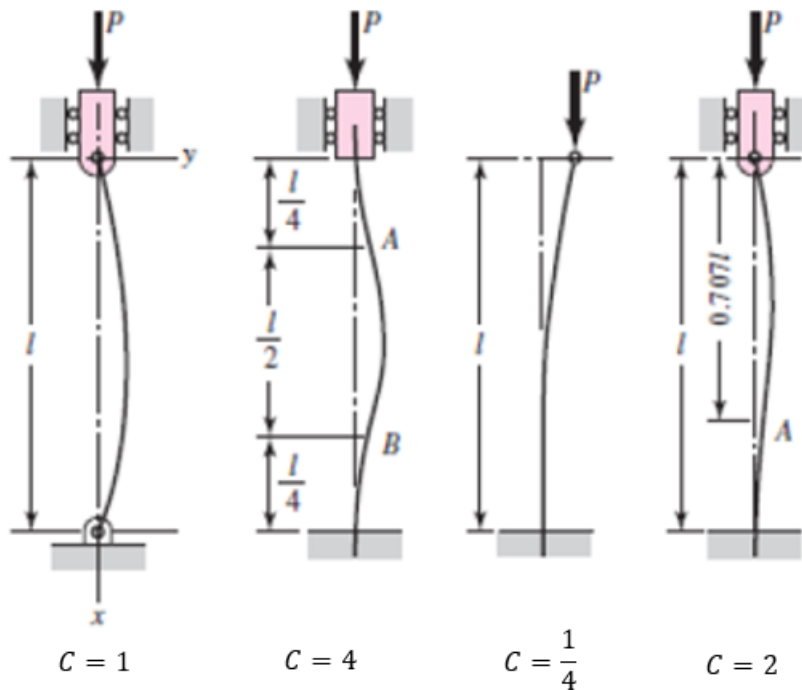


Figure 3.24: Buckling end conditions (Adapted from [8])

The buckling critical load is the load at which instability and, ultimately, the collapse of a structure can occur. The buckling critical load, P_{cr} , of the guide shafts can be determined by the following formula [42][43]:

$$\frac{P_{cr}}{A} = \frac{C\pi^2 E}{\lambda^2} \quad (3.3)$$

Where A is the transversal area, C is a coefficient given by the buckling end conditions, it can be seen in the Figure 3.24, E the Young's modulus and λ the slenderness ratio.

The slenderness ratio is determined by:

$$\lambda = \frac{l}{i} \quad (3.4)$$

Where l is the guide shaft length and i is the radius of gyration. The radius of gyration, i , can be calculated through the moment of Inertia of the guide shaft, I , and the cross-sectional area, A . The moment of inertia of the guide shaft, I , is given by the following equation.

$$I = \frac{\pi \cdot r^4}{4} = \frac{\pi \cdot 25^4}{4} = 306796.2 \text{ mm}^4 \quad (3.5)$$

And so, the radius of gyration, i , can now be determined through:

$$i = \sqrt{\frac{I}{A}} = 12.5 \text{ mm} \quad (3.6)$$

The length of the guide shaft, l , is 970 mm, and the slenderness ratio, λ , can now be calculated through the equations 3.4 and 3.6.

$$\lambda = \frac{970}{12.5} = 77.6 \quad (3.7)$$

Assuming a Young's modulus of 200 GPa for the material of the guide shafts, and determining the coefficient C by considering the worst case scenario, $C = \frac{1}{4}$, which coincides with the present case due to the upper cast iron block being free and the lower being fixed, it is possible now to calculate the buckling critical load by returning to the equation 3.3.

$$P_{cr} = 160907.5 \text{ N} \quad (3.8)$$

As it can be seen from the results that are demonstrated in the equations 3.2 and 3.8, the use of the pre-structure guide shafts offers the essential safety that is required for the proper performance of the ultrasonic fatigue testing equipment when testing specimens loaded with 10 kN statically. These conclusions, on the other hand, may only be considered an approximation due to the lack of information on the guide shafts material's properties.

Now, an analysis of the cast iron pre-structure blocks will be presented. As both blocks have similar dimensions and are made off the same material, only the upper cast iron block will be analyzed. In the Figure 3.25 it is possible to see the upper cast iron block correctly mounted on the original guide shafts.

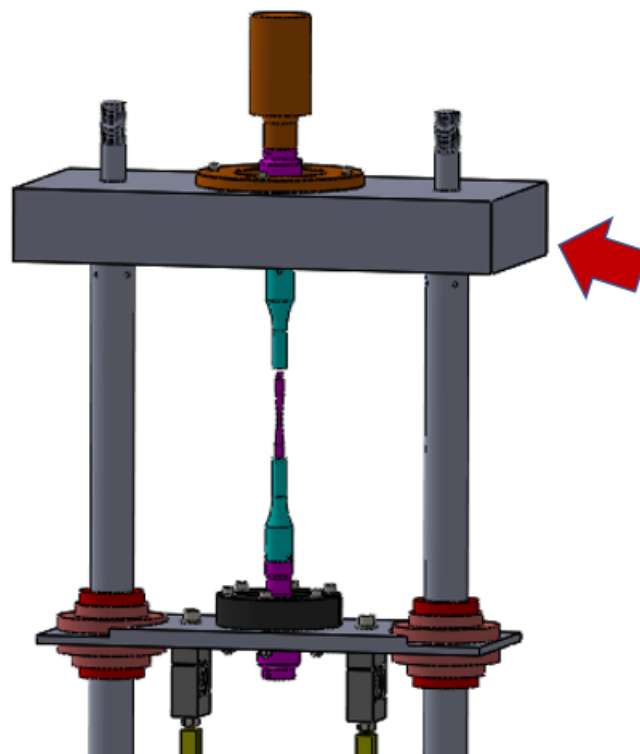


Figure 3.25: Identification of the original upper cast iron block

As the material mechanical properties of the cast iron blocks are not known, the following properties will be assumed, which represent a conservative value among different types of cast iron:

- Tensile strength, $\sigma_y = 200$ MPa
- Young's modulus, $E = 100$ GPa
- Poisson's ratio, $\nu = 0.3$

The cross sectional area of the upper cast iron block has the following dimensions:

- width, $b = 0.254$ m
- height, $h = 0.085$ m
- area = 0.023 m²

The free body diagram of the upper cast iron block is presented in the figure bellow. When the ultrasonic fatigue testing equipment performs tests subjecting the specimen to 10 kN, the top cast iron block will be subjected to a force of the same magnitude, F , which will be assumed to be concentrated for the purpose of simplicity. Another simplification was taken into account, the upper cast iron block was considered to be solid, without the central hole. Since the cast iron block is supported symmetrically by both shaft guides, two vertical reactions, each with a magnitude of $\frac{F}{2}$, will develop.

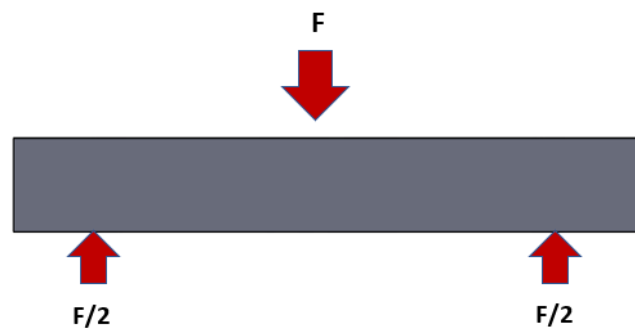


Figure 3.26: Free body diagram of the upper cast iron block

The length between the center of the two supports is $L = 0.4$ m, and so, the shear force distribution, $V(x)$, and the bending moment distribution, $M(x)$, can be obtained and are presented bellow. The coordinate x represents the distance between the two supports.

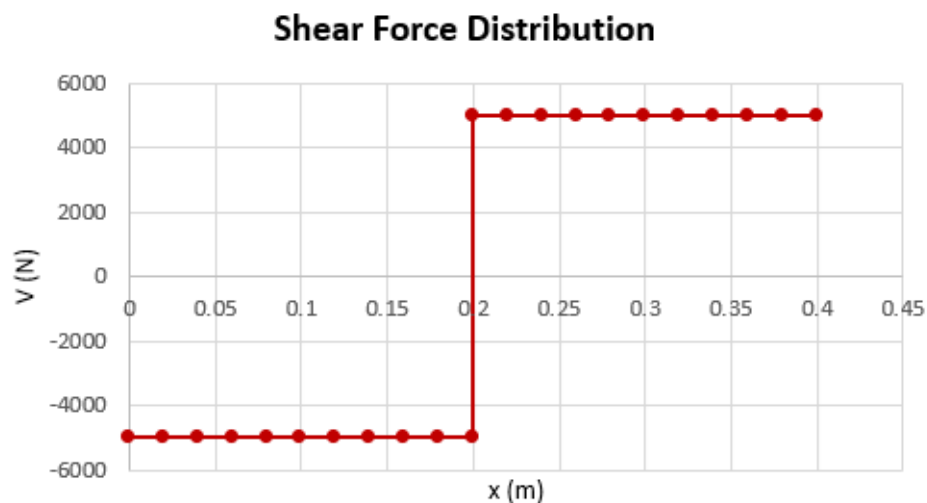


Figure 3.27: Shear force distribution of the upper cast iron block

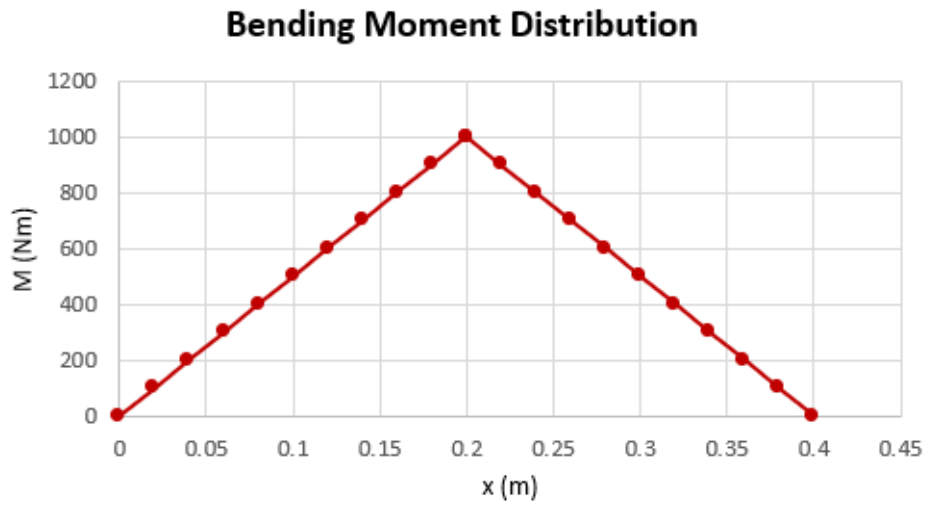


Figure 3.28: Bending moment distribution of the upper cast iron block

The Bending Moment Distribution can be divided into two sections, for $\frac{L}{2} \geq x \geq 0$:

$$M(x) = \frac{F}{2}x \quad (3.9)$$

And for $L \geq x \geq \frac{L}{2}$:

$$M(x) = \frac{F}{2}L - \frac{F}{2}x \quad (3.10)$$

The bending stress, σ_{BD} , varies linearly with the distance from the neutral axis, y , which in this case is coincident with the centroidal axis of the cross section, and is given by [8]:

$$\sigma_{BD}(x,y) = \frac{M(x)}{I}y \quad (3.11)$$

Where M is the Bending Moment presented in the Figure 3.28 and I is the the second moment of area of section of beam about its neutral axis, which can be seen in the figure bellow [8].

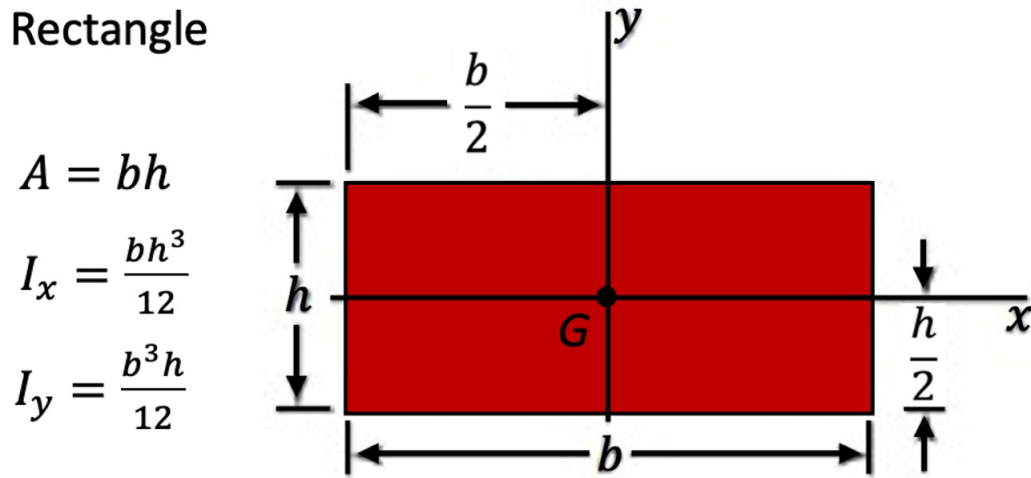


Figure 3.29: Second Moment of area of section of rectangular beam

So, for the upper cast iron block:

$$I = \frac{bh^3}{12} = 1.333 \cdot 10^{-5} \text{ m}^4 \quad (3.12)$$

And, the maximum bending moment can be seen in the Figure 3.28, $M_{max} = 1000 \text{ Nm}$, allowing for the calculation of the maximum bending stress magnitude through the equation 3.11.

$$\sigma_{BD-MAX} = \frac{1000 \cdot (\pm 0.0425)}{1.333 \cdot 10^{-5}} = \pm 3269487.508 \text{ Pa} \quad (3.13)$$

$$\sigma_{BD-MAX} = \pm 3.269 \text{ MPa} \quad (3.14)$$

Now, the Safety Factor, SF , in relation to the tensile strength, σ_y , can be determined:

$$SF = \frac{200}{3.270} = 61.172 \quad (3.15)$$

The calculated Safety Factor is extremely high, however as it is a component of the original structure that can be reused, its integration in the ultrasonic machine will be maintained. In addition, a bending stress distribution graphic in the zone of greatest bending moment, $x = \frac{L}{2}$ as can be seen in the Figure 3.11, is presented below. This plot represents the bending stress distribution along the cross-sectional area of the upper cast iron block, at $x = \frac{L}{2}$.

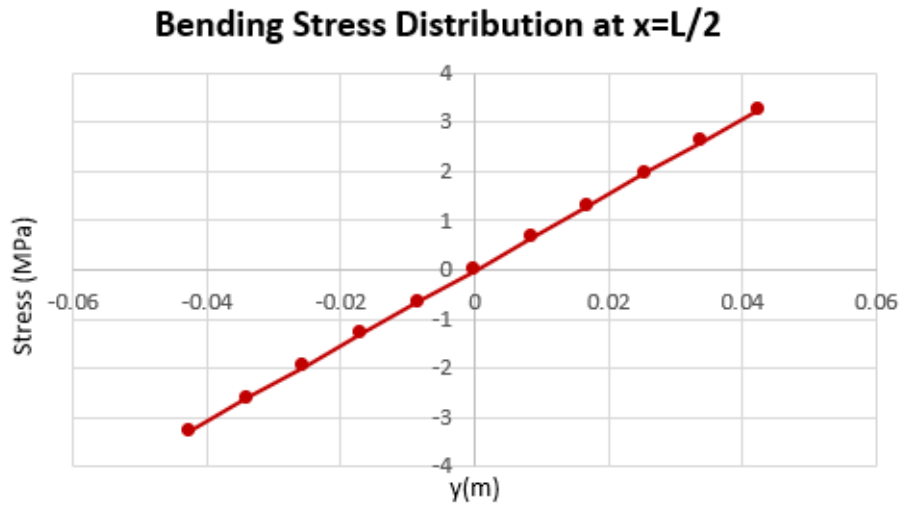


Figure 3.30: Bending stress distribution along the cross sectional area at $x = \frac{L}{2}$

Furthermore, the distribution of shear stresses, τ , in the cross section of the cast iron block will be examined. The shear stress distribution, τ , can be obtained through the following equation [44]:

$$\tau(x,y) = \frac{V(x)Q(y)}{Ib} \quad (3.16)$$

Where V is the shear force, presented in the Figure 3.27, I is the second moment of area, b is the width of the cross section and Q is the first moment of area which is given by:

$$Q(y) = \frac{b}{2} \left(\frac{h^2}{4} - y^2 \right) \quad (3.17)$$

With h being the height of the cross section and y the distance above or below the neutral axis. By combining the equations 3.16 and 3.17, and considering the highest value of shear force, $V = \pm 5000$ N, it is possible to obtain the distribution of shear stress in the cross section of the cast iron block. The obtained equation and shear stress distribution are presented below.

$$\tau(y) = \frac{V}{2I} \left(\frac{h^2}{4} - y^2 \right) \quad (3.18)$$

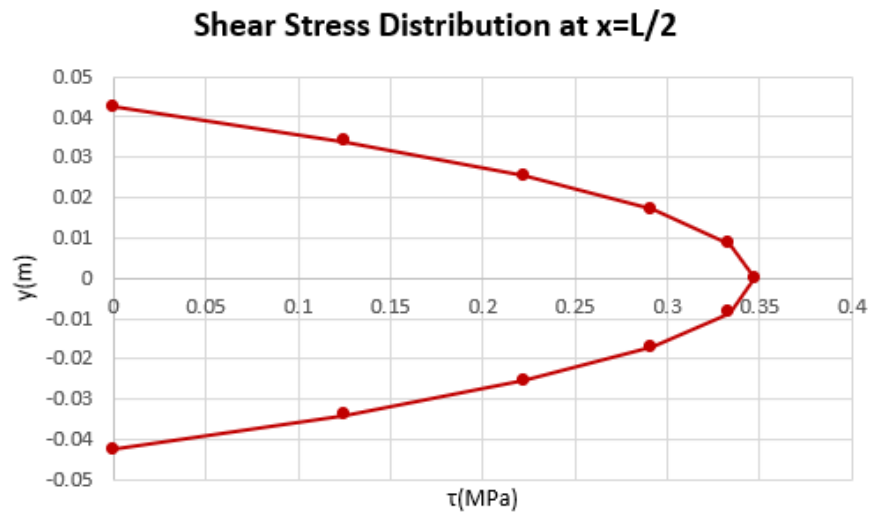


Figure 3.31: Shear stress distribution along the cross sectional area at $x = \frac{L}{2}$

As it was expected, the maximum shear stress, $\tau = 0.347$ MPa, occurs at the middle of the height of the cast iron block cross section, unlike the bending stress which is maximum at the tops of the cast iron block cross section. Now, after obtaining the distribution of both the bending stress and shear stress at $x = \frac{L}{2}$, it is possible to plot the Von Mises equivalent stress distribution, $\sigma_{VM}(y)$, through the following equation [8].

$$\sigma_{VM} = \sqrt{\frac{1}{2} [(\sigma_{11} - \sigma_{22})^2 + (\sigma_{22} - \sigma_{33})^2 + (\sigma_{33} - \sigma_{11})^2] + 3(\sigma_{12}^2 + \sigma_{23}^2 + \sigma_{31}^2)} \quad (3.19)$$

Which leads to the following stress distribution across the cross sectional area of the cast iron block:

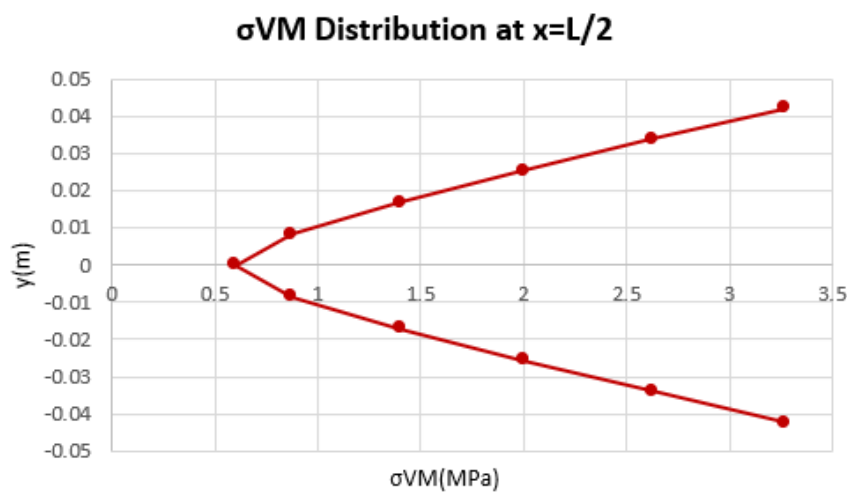


Figure 3.32: Von Mises equivalent stress distribution along the cross sectional area at $x = \frac{L}{2}$

The maximum σ_{VM} stress occurs at the tops of the cast iron block cross section, due to the high contribution of the bending stress. With its maximum being $\sigma_{VM} = 3.270$ MPa, leading to a Safety Factor of 61.172, which is high, however as the upper cast iron block is available it will be used. After the stress analysis presented above, a deflection analysis of the upper cast iron block was performed. The double integration method was utilized in order to obtain the deflection, $y(x)$. Following is the primary equation of this approach [8][45].

$$\frac{\partial^2 y}{\partial x^2} = \frac{M(x)}{EI} \quad (3.20)$$

$$\Leftrightarrow \frac{\partial y}{\partial x} = \int \frac{M(x)}{EI} \partial x \quad (3.21)$$

$$\Leftrightarrow y(x) = \int \int \frac{M(x)}{EI} \partial x \partial x \quad (3.22)$$

By applying the formula 3.22 to the equations 3.9 and 3.10, it is possible to obtain the following two expressions:

For $\frac{L}{2} \geq x \geq 0$:

$$y_1 = \frac{1}{EI} \left[\frac{Fx^3}{12} + C_1x + C_2 \right] \quad (3.23)$$

And for $L \geq x \geq \frac{L}{2}$:

$$y_2 = \frac{1}{EI} \left[-\frac{Fx^3}{12} + \frac{FL}{4}x^2 + C_3x + C_4 \right] \quad (3.24)$$

With C_1 , C_2 , C_3 and C_4 being integration constants. The analytical value of these constants will be obtained through the imposition of the following four different boundary conditions.

- $y_1(0) = 0$, no deflection on the support;
- $y_2(L) = 0$, no deflection on the support;
- $y_1(\frac{L}{2}) = y_2(\frac{L}{2})$, continuity condition;
- $\theta_1(\frac{L}{2}) = \theta_2(\frac{L}{2})$, continuity condition.

Being $\theta = \frac{dy}{dx}$, the slope. By replacing the values of the four constants into the equations 3.23 and 3.24, it is possible to generate the graphic below, which depicts the deflection distribution along the upper cast iron block.

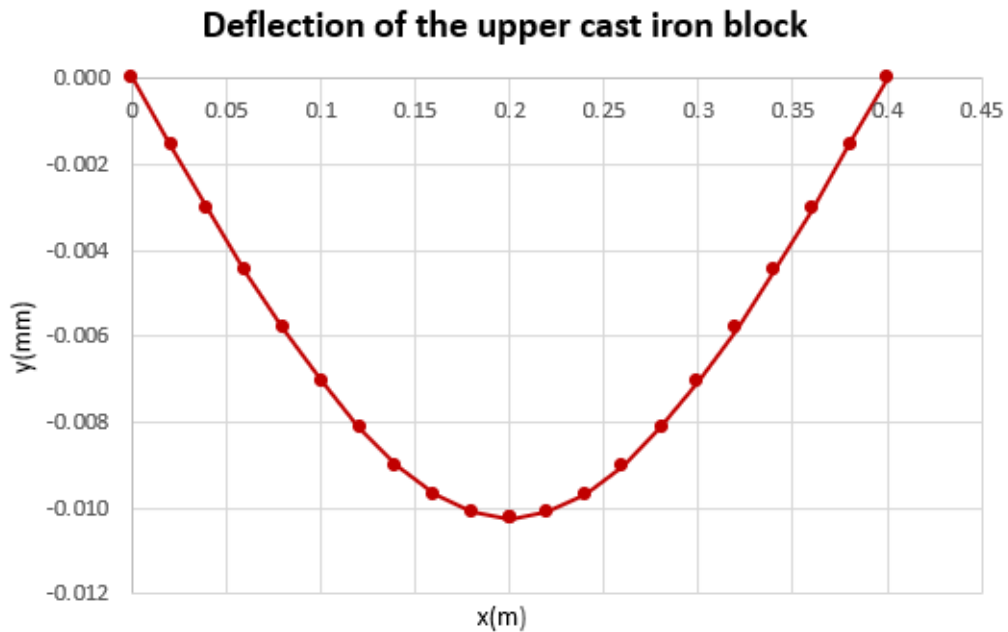


Figure 3.33: Deflection of the upper cast iron block

According to the analysis performed and detailed above, the original pre-structure's cast iron blocks are compatible with the project. The exceptional robustness of the blocks results in a very high safety factor, around 61.2, when the ultrasonic fatigue testing equipment applies a static 10 kN load to the specimen. In addition to the high safety factor, there is extremely minimal deflection, its maximum is around 0.01 mm as it can be seen in the Figure 3.33, making the use of the original blocks even more desirable. However, the mechanical properties of the cast iron blocks are not known, so the results need to be considered as an approximation.

3.4.2 Analysis of the new designed components and subassemblies

In this subsection, an analytical and numerical analysis of different new designed components and subassemblies presented in the subsection 3.3.2 will be conducted and discussed. The definition drawing of each component is presented in Appendix C. The main goals of this subsection are to specify the manufacture material and to evaluate the behaviour of different designed components and subassemblies when the ultrasonic fatigue testing equipment is performing tests with a static 10 kN load applied to the specimen. The ultrasonic booster and horn will be presented in the subsection 3.4.4.

All of the screws used in the fastened connections are ISO 4762 - 12.9, the nuts are ISO 4033 - 12 and ISO 7089 washers were also used. The bolt grade 12.9 was chosen owing to the fact

that it provided screws with the highest yield and tensile strength. In order to make the reading of this document easier to comprehend, from this point forward it will only be stated the nominal diameter of the utilized screws, nuts and washers. The different preloads and tightening torques applied to the screws are listed in the tables presented in Appendix D.

In all of the upcoming Finite Element analysis, all the adjacent pairs of surfaces were considered to have a surface to surface interaction with a penalty tangential behaviour with a friction coefficient of 0.14 and a hard contact normal behaviour. Additionally, the threaded portion of the bolts was considered to be tied to the surrounding surface.

3.4.2.1 Analysis and validation of Section A subassembly

The first subassembly to be analyzed will be the connection between the upper cast iron block and the vibration absorbing flange. This subassembly can be seen in more detail in the Figures 3.6 and 3.7. The primary purpose of this study will be to validate the design of the vibration absorbing flange and choose its material of manufacture. This subassembly will be numerically analyzed through the software Abaqus and only a static analysis will be performed due to the booster being fixed on a vibration node, i.e. no relevant dynamic forces on the subassembly.

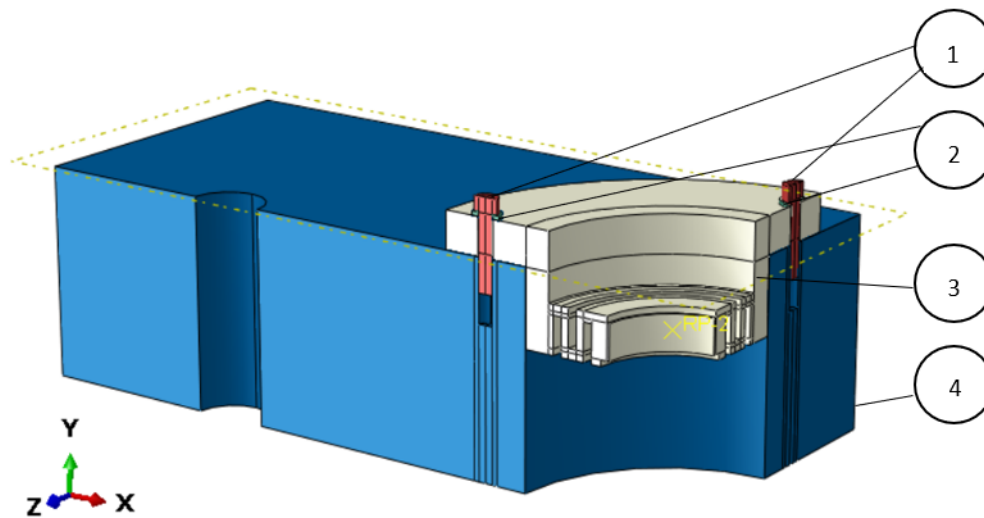


Figure 3.34: Symmetry view of the subassembly of upper cast iron block and vibration absorbing flange on Abaqus

For this analysis, it was considered two half M6 screws (1), two half M6 washers (2), the vibration absorbing flange (3) and the upper cast iron block (4) as it can be seen in the Figure 3.34. In the Figure 3.34 it is possible to see the symmetry view, with regard to the XY and YZ symmetry plane, of the Section A subassembly on Abaqus. It was taken advantage of the subassembly's symmetry in order to make the Abaqus analysis less mathematically expensive. Furthermore, it was necessary to apply different symmetry conditions on the symmetry planes of the subassembly as it can be seen in the Figure 3.35. On the XY symmetry plane, the displacement according to the Z coordinate and the rotation according to the X and Y axis was considered to be null. On the

YZ symmetry plane, the displacement according the X coordinate and the rotation according the Y and Z axis was considered to be zero.

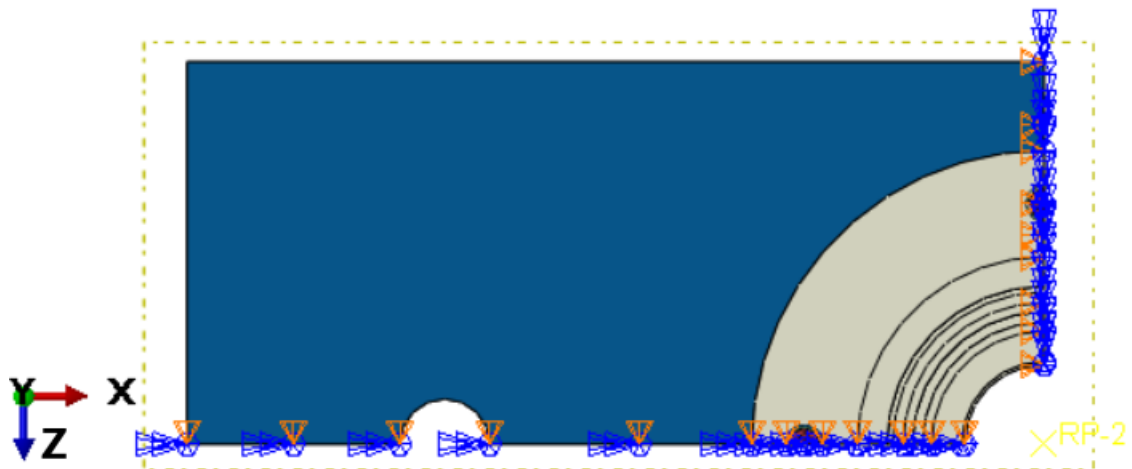


Figure 3.35: Demonstration of the application of symmetry conditions on the Section A subassembly

The mechanical properties considered for the cast iron were the same as those used in the analytical calculation in the previous subsection. The material of the vibration absorbing flange, screws and washers, steel, were considered to have a Young's modulus, E , of 200 GPa and a Poisson's ratio, ν , of 0.3. In the Figure 3.36 is presented the mesh density of this Abaqus analysis. It was utilized the hexahedron element type with reduced integration, C3D8R, to save computational time and to relax the mathematical model. The elements within each component are presented in the Table 3.8.

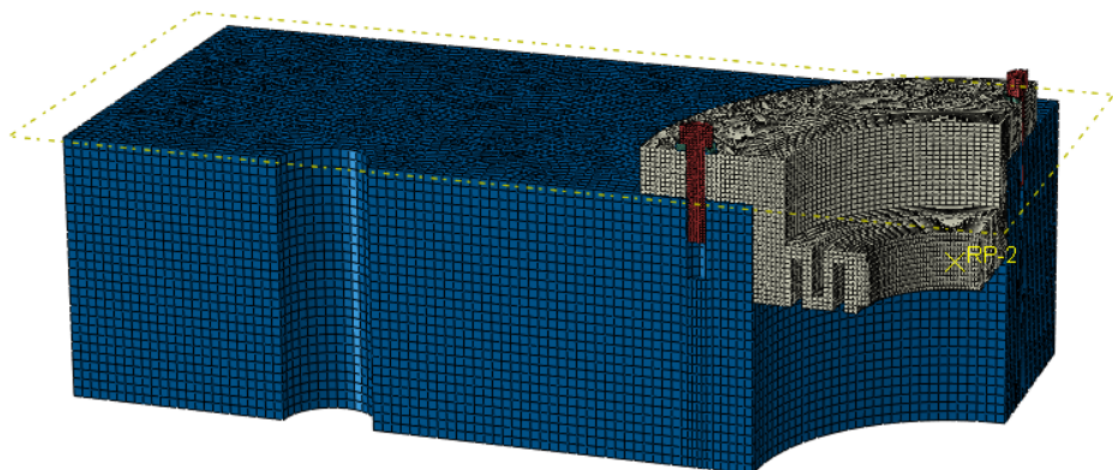


Figure 3.36: Mesh density of the Section A subassembly

Table 3.8: Number of elements of each component of the subassembly presented in the Figure 3.36

Component	Number of elements
Upper cast iron block	124280
Vibration absorbing flange	32620
Each M6 half bolt	912
Each M6 half washer	522

In the Figure 3.37 it is presented the subassembly with the bolt preloads, the static applied load and the boundary condition. However, due to simplification the symmetry conditions are not identified in the figure. This analysis represents the case where the ultrasonic fatigue testing machine exerts a static load of 10 kN on the specimen, as described previously. And so, the vibration absorbing flange will also be under a 10 kN load. In order to simulate this static load, a reference point, RP-2, was created and coupled to the the threaded part of the vibration absorbing flange, where the booster threads. Therefore, the static force is applied to the reference point, which is only -2500 N owing to symmetry. The preload of the bolts was specified according to the table in Appendix D. However, due to symmetry, only half of this load was applied to each bolt, 7592.2 N. For this analysis it were considered two consecutive steps. The first one regarding the bolts preload and the second one regarding the considered external load.

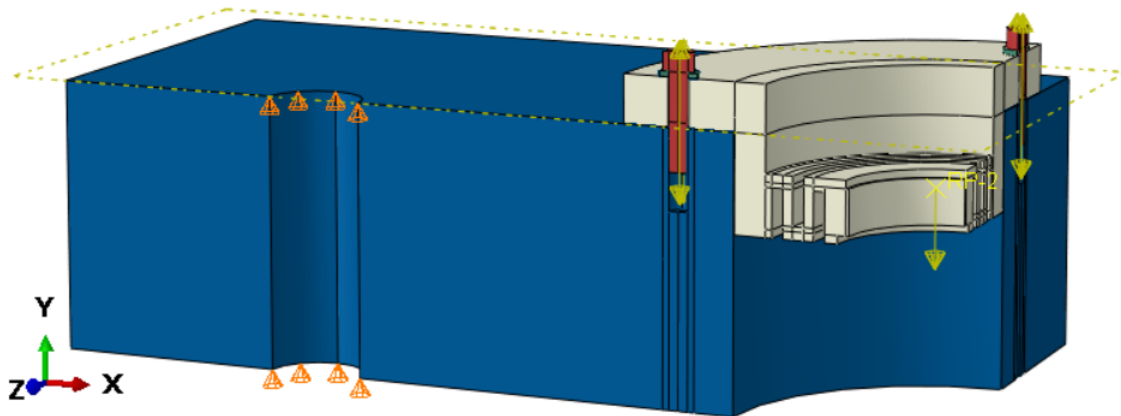


Figure 3.37: Boundary condition and loads on the Section A subassembly without the symmetry conditions

In addition to the symmetry conditions, another boundary condition was considered. As it can be seen in the Figure above, the displacement on the Y direction was considered to be null in the location where the guide shafts support the upper cast iron block. The Abaqus analysis results will be presented next.

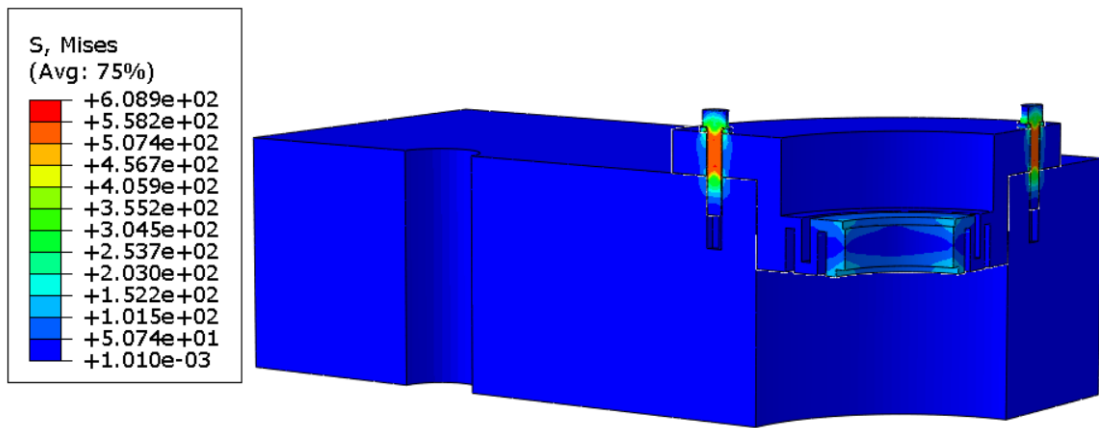


Figure 3.38: Von Mises stress on the full Section A subassembly (MPa)

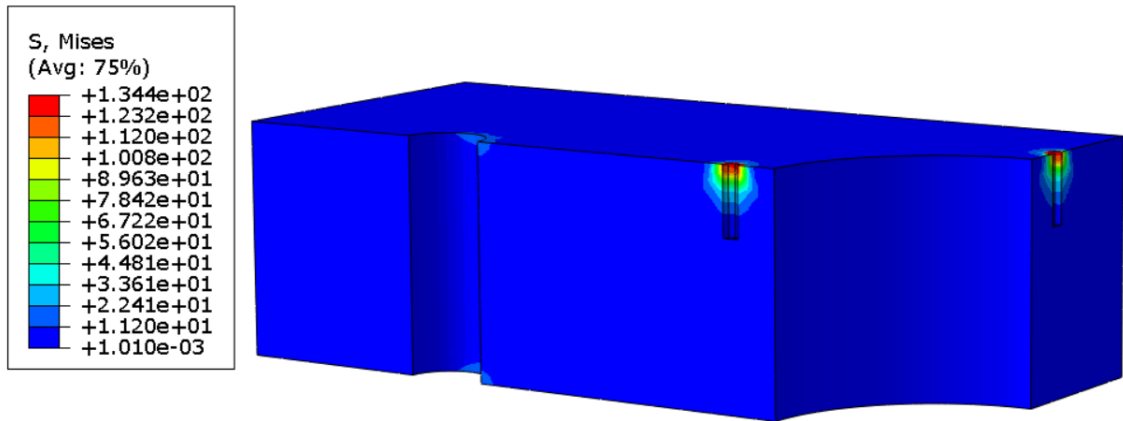


Figure 3.39: Von Mises stress on the upper cast iron block (MPa)

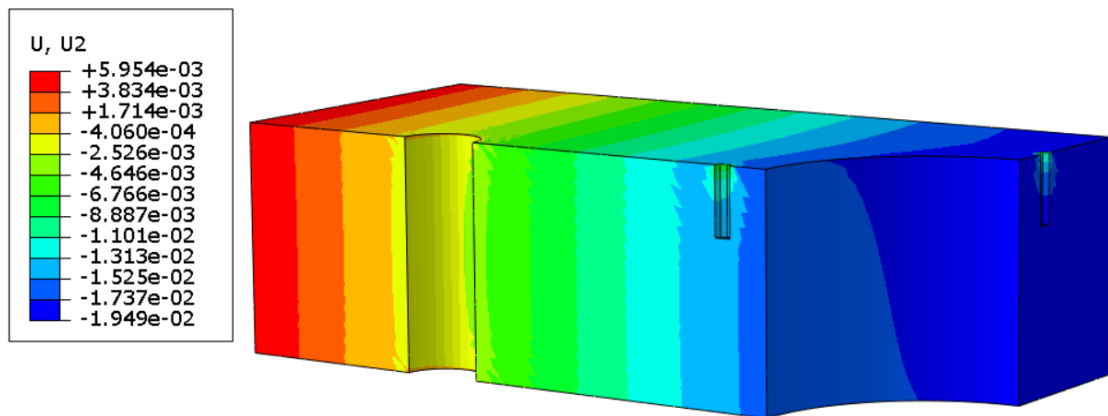


Figure 3.40: Vertical displacement on the upper cast iron block (mm)

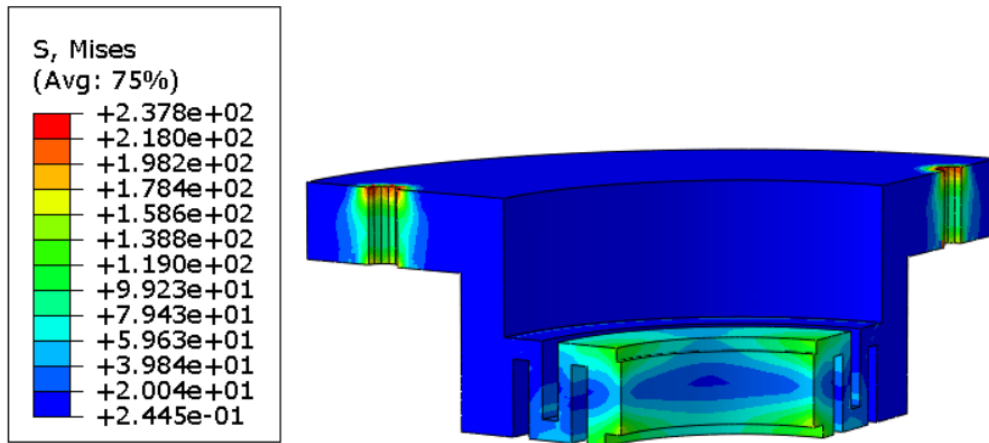


Figure 3.41: Von Mises stress on the vibration absorbing flange (MPa)

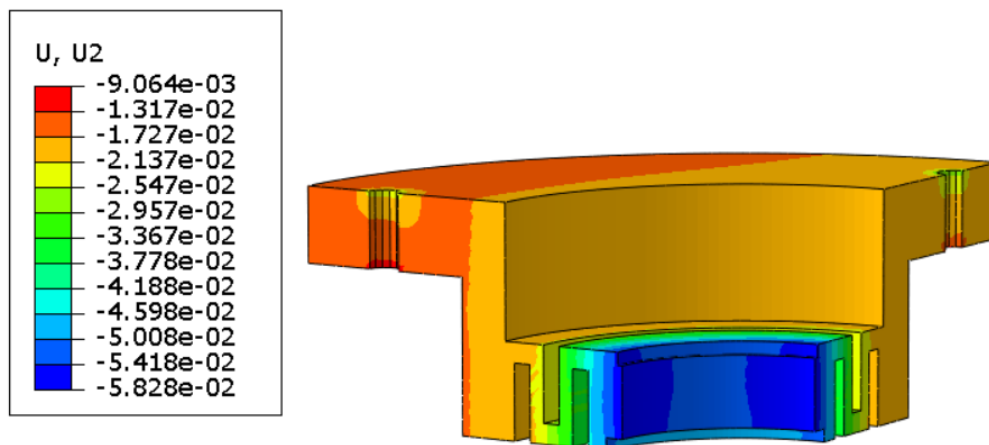


Figure 3.42: Vertical displacement on the vibration absorbing flange (mm)

The results of the Abaqus analysis presented above demonstrate that the maximum Von Mises stress occurs at the bolts, with its value being around 609 MPa. The maximum Von Mises stress on the top cast iron block is around 134 MPa, however this is owing to the theoretical high stress concentration factor in the bolt holes, in practice, this concentration factor will be reduced due to the rounded edges of the holes. The maximum vertical displacement of the upper cast iron block is very minimal, with its value being $-1.95 \cdot 10^{-2}$ mm. The differences noted on the analytical and numerical results regarding the upper cast iron block can be justified by the model used for the analytical analysis. For the analytical analysis it was considered a simplified cast iron block with no holes, i.e. with improved rigidity. Furthermore, the numerical results with regard to the upper cast iron block provide evidence that supports the claims made in the preceding subsection. It is desirable to employ the cast iron blocks in the structure of the ultrasonic fatigue testing machine due to its high robustness leading to low vertical displacement and low stresses when

the equipment is testing the specimen with a 10 kN static load applied. This Abaqus analysis also indicates that due to the bolt holes, the highest Von Mises stresses in the vibration absorbing flange also occur in the zone of high theoretical stress concentration, 238 MPa. Nonetheless, stresses of 160 MPa and vertical displacements of $-5.83 \cdot 10^{-2}$ mm are verified at the region where the booster threads into the vibration absorbing flange.

The material that will be used to manufacture the vibration absorbing flange was selected after taking a number of factors into consideration, including economics, the stresses and displacements that were verified in the present numerical analysis, and the fact that it is a material that will be used to manufacture additional components of the ultrasonic fatigue machine, which will be presented later in this subsection. The selected material was the EN 40 CrMnNiMo 8-6-4 steel, designated at Ramada Aços as PM300. This Cr-Ni-Mo-alloyed steel is supplied in the hardened and tempered condition and offers the advantages of having good machinability, a high purity, good homogeneity and an uniform hardness, which makes him suitable to be utilized as the manufacturing steel of machine components requiring improved reliability. The mechanical properties of the EN 40 CrMnNiMo 8-6-4 steel, also known as AISI P20, are presented in the Table 3.9[46]. The definition drawing of the vibration absorbing flange can be seen in the Appendix C.

Table 3.9: Mechanical Properties of the AISI P20 steel at 20°C [46]

Yield strength, σ_y	900 MPa
Ultimate tensile strength, σ_R	1020 MPa
Density, ρ	7800 kg/m ³
Modulus of elasticity, E	205 GPa
Poisson's ratio, ν	0.3

3.4.2.2 Analysis and validation of Section B subassembly

After completing the analysis of the first subassembly, an analytical and numerical analysis of the subassembly presented in the Figures 3.11 and 3.12 will be conducted and discussed. The primary goals of this analysis are to validate the design of the booster support, locking support and support plate in order to ensure the safety and proper operation of the ultrasonic fatigue testing machine when the maximum static load is applied to the specimen during testing.

To reduce the cost of the project described in this document, it was chosen to use an existing S690 steel plate at INEGI to produce the support plate. The original thickness of the plate was 20 mm, and it was decided to retain it to avoid incurring further machining expenses. However, it was required to reduce the thickness to 10 mm in the regions where the original linear ball bearing pre-structure mounting hardware, shown in Figure 3.13, would be installed. The final design of the support plate can be seen in the Figure 3.43. The mechanical properties of the S690 steel can be seen in the Table 3.10.

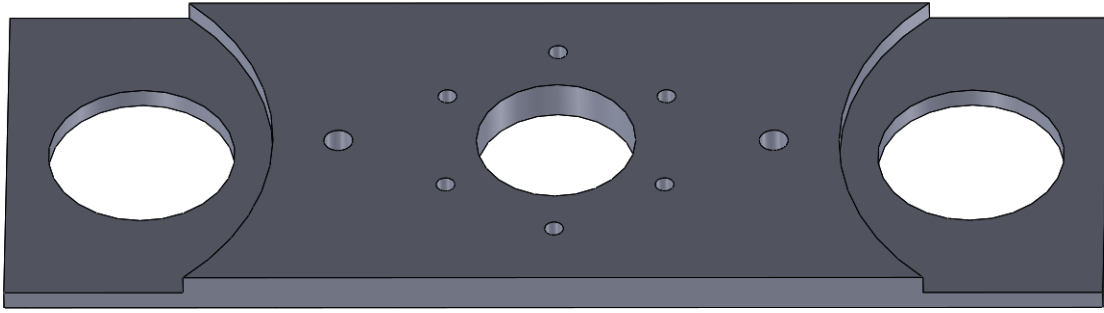


Figure 3.43: Final design of the S690 steel support plate

Table 3.10: Mechanical Properties of the S690 Structural Steel [47]

Yield strength, σ_y	781 MPa
Ultimate tensile strength, σ_R	819 MPa
Density, ρ	7815.66 kg/m ³
Modulus of elasticity, E	211593 MPa
Poisson's ratio, ν	0.3

The following analytical and numerical study will consist only in a static analysis because the booster is fixed to the structure on a vibration node, therefore, the components of this subassembly are not subjected to any considerable dynamic forces. The primary step of this analysis is going to consist of an analytical study on the S690 steel support plate presented in the Figure 3.43.

The free body diagram of the S690 structural steel support plate is presented in the figure below. When the ultrasonic fatigue testing equipment performs tests subjecting the specimen to a static load of 10 kN, F , the support plate will be subjected to two vertical forces of half the magnitude, $\frac{F}{2}$, at the connecting point with the load cells, originated due to the vertical displacement of the power screw. The load cells are tractioned due to the propagation of the vertical movement of the power screw through the traction plate and the two squared section bars, as can be better perceived through the Figures 3.19 and 3.20. Additionally, a force with the maximum magnitude, F , with the opposite direction of the forces discussed above, is developed in the support plate due to the traction applied to the specimen by the second pair of booster and horn. All the forces will be assumed to be concentrated for the purpose of simplicity and only the segment of interest of the support plate will be analyzed, the region between the two load cells connecting point, which as a length of $L = 0.21$ m. Furthermore, the support plate will be considered without any holes in order to simplify this first analytical approach.

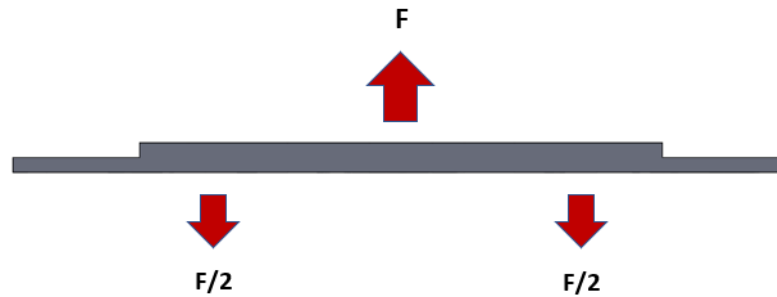


Figure 3.44: Free body diagram of the support plate

The cross sectional area of interest of the support plate has the following dimensions:

- width, $b = 0.19$ m
- height, $h = 0.02$ m
- area = $0.38 \cdot 10^{-2}$ m²

And so, the second moment of area, I , can be calculated through the Figure 3.29:

$$I = \frac{bh^3}{12} = 1.27 \cdot 10^{-7} \text{ m}^4 \quad (3.25)$$

The shear force distribution, $V(x)$, and the bending moment distribution, $M(x)$, are presented in the figures bellow. The coordinate x represents the distance between the two load cells.

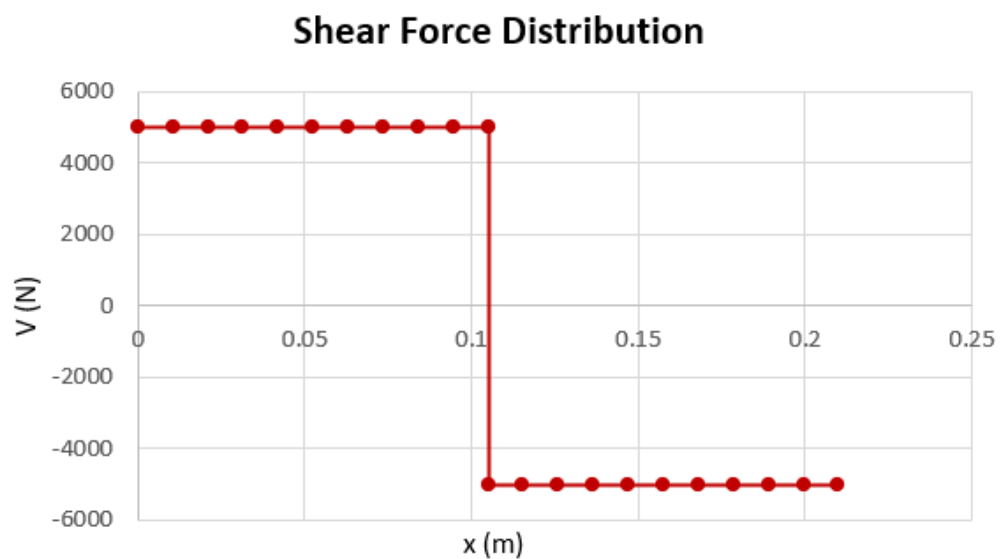


Figure 3.45: Shear force distribution of the support plate

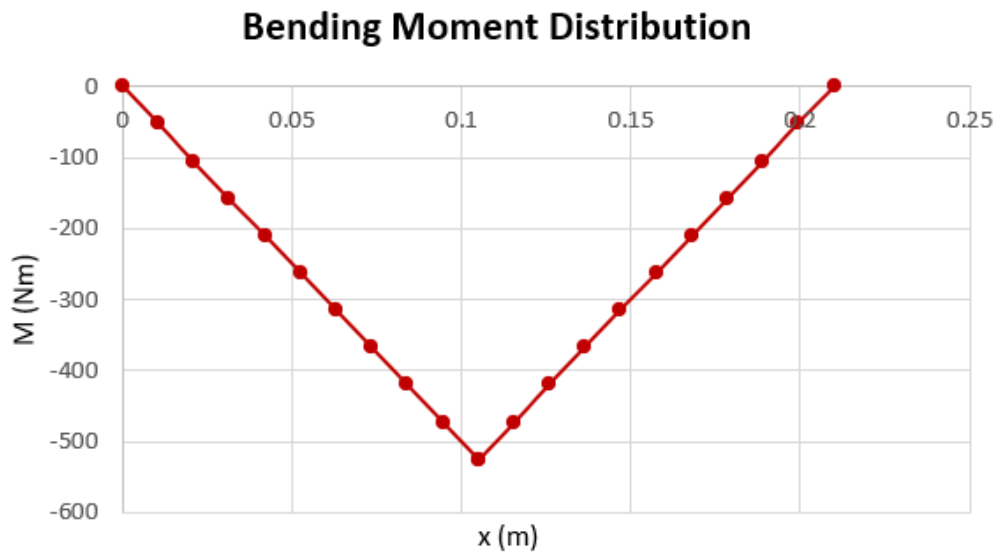


Figure 3.46: Bending moment distribution of the support plate

It is possible to divide the bending moment distribution into two sections.

For $\frac{L}{2} \geq x \geq 0$:

$$M(x) = -\frac{F}{2}x \quad (3.26)$$

And for $L \geq x \geq \frac{L}{2}$:

$$M(x) = \frac{F}{2}x - \frac{F}{2}L \quad (3.27)$$

Through the Figure 3.46, it is possible to identify the maximum bending moment, $M_{MAX} = -525$ Nm and it occurs at $x = \frac{L}{2}$. The bending stress distribution graphic in the zone of greatest bending moment, $\sigma_{BD}(y)$, can be obtained through the equation 3.11, and it is presented in the Figure 3.47. This plot represents the bending stress distribution along the cross sectional area of the support plate, at $x = \frac{L}{2}$ and y is the distance above or below the neutral axis.

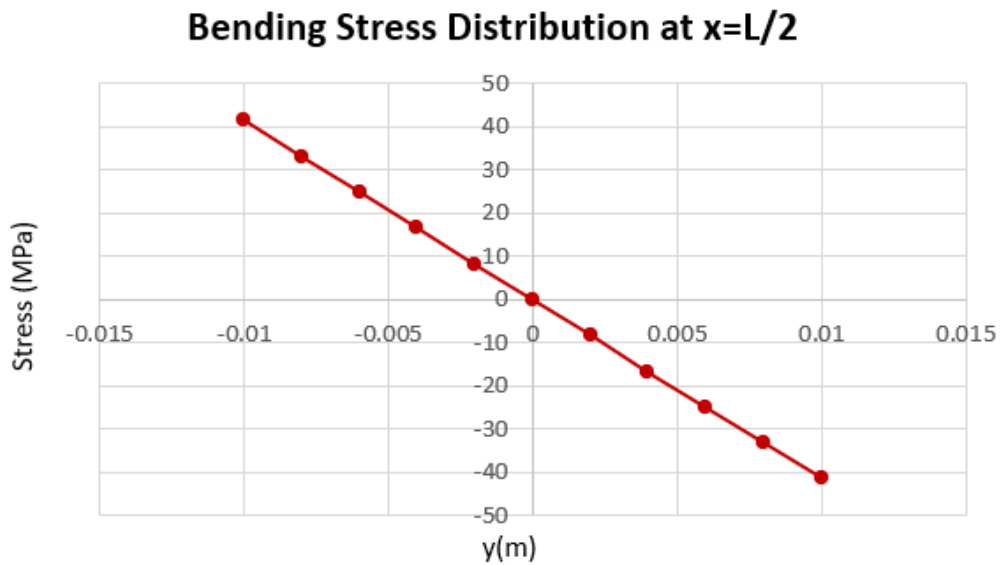


Figure 3.47: Bending stress distribution along the cross sectional area of the support plate at $x = \frac{L}{2}$

Additionally, the shear stress distribution, $\tau(y)$, along the cross section of the support plate at $x = \frac{L}{2}$ can be obtained through the equation 3.18. The highest value of shear force, $V = \pm 5000$ N, can be seen in the Figure 3.45 and the shear stress distribution is presented bellow.

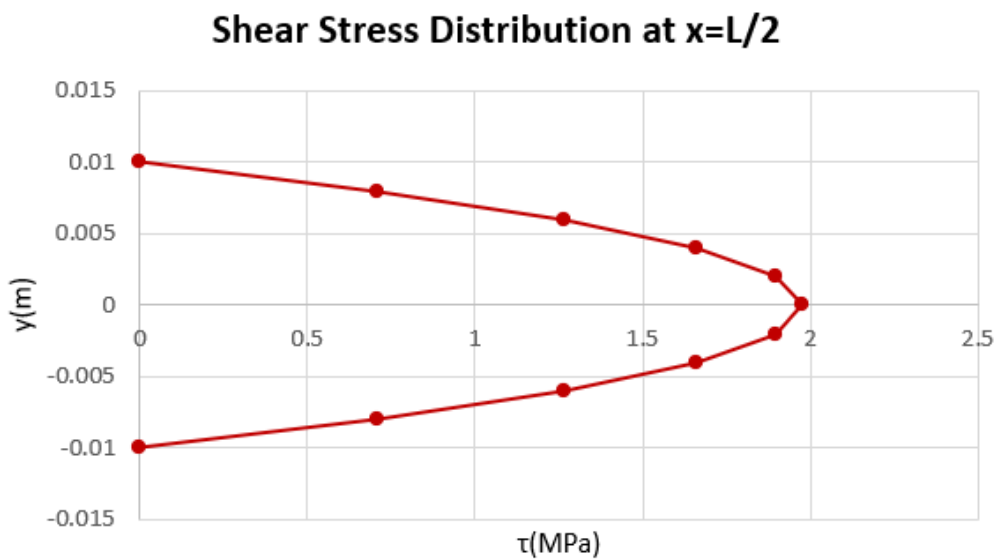


Figure 3.48: Shear stress distribution along the cross sectional area of the support plate at $x = \frac{L}{2}$

Furthermore, after getting the bending stress and shear stress distributions at $x = \frac{L}{2}$, it is feasible to plot the Von Mises equivalent stress distribution of the support plate, $\sigma_{VM}(y)$, using the equation 3.19. The Von Mises equivalent stress distribution is presented next.

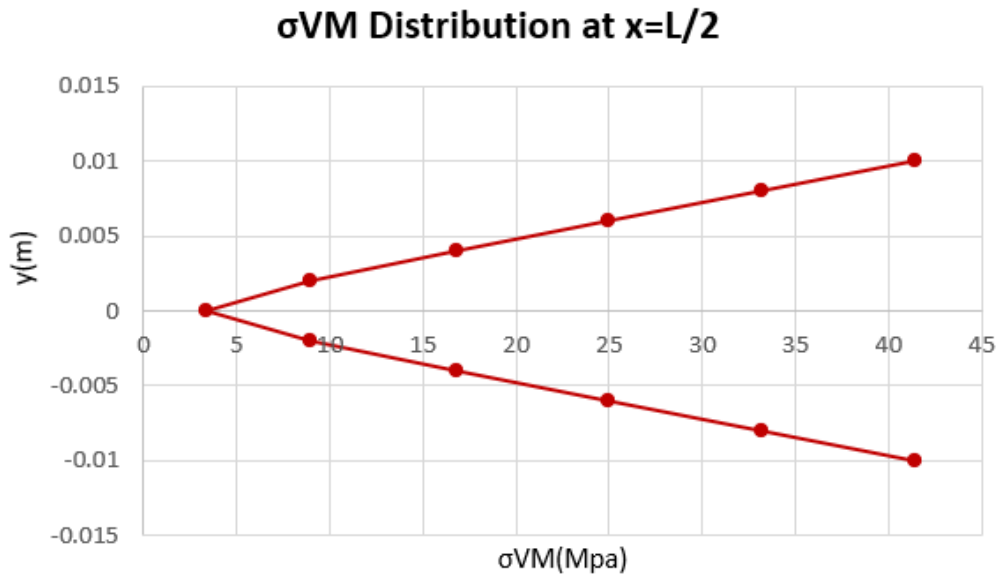


Figure 3.49: Von Mises equivalent stress distribution along the cross sectional area of the support plate at $x = \frac{L}{2}$

Due to the significant contribution of the bending stress, the highest σ_{VM} stress occurs at the tops of the support plate cross section, as it can be seen from the figure above. The maximum value of the σ_{VM} is 41.45 MPa, leading to a safety factor $SF = \frac{41.45}{779} = 18.79$.

A deflection analysis of the support plate was undertaken after it was determined that the outcomes of the stress analysis that were provided above were favorable. In order to calculate the deflection, $y(x)$, the double integration method was employed. So, the formula 3.22 was applied to the two bending moment distribution equations, 3.26 and 3.27, and the results are presented next.

For $\frac{L}{2} \geq x \geq 0$:

$$y_1(x) = \frac{1}{EI} \left[\frac{-Fx^3}{12} + C_1x + C_2 \right] \quad (3.28)$$

And for $L \geq x \geq \frac{L}{2}$:

$$y_2(x) = \frac{1}{EI} \left[\frac{Fx^3}{12} + \frac{-FLx^2}{4} + C_3x + C_4 \right] \quad (3.29)$$

Being C_1, C_2, C_3 and C_4 the integration constants. The implementation of the following distinct boundary conditions will result in the determination of the analytical value of these constants, allowing the generation of the the graphic illustrating the deflection distribution along the support plate. This graphic is presented in the Figure 3.50.

- $y_1(0) = 0$, zero deflection at the beginning of the length of interest of the support plate;
- $y_2(L) = 0$, zero deflection at the end of the length of interest of the support plate;
- $y_1(\frac{L}{2}) = y_2(\frac{L}{2})$, continuity condition on the deflection;
- $\theta_1(\frac{L}{2}) = \theta_2(\frac{L}{2})$, continuity condition on the slope;
- $\theta(\frac{L}{2}) = 0$, no slope on the middle of the length of interest of the support plate.

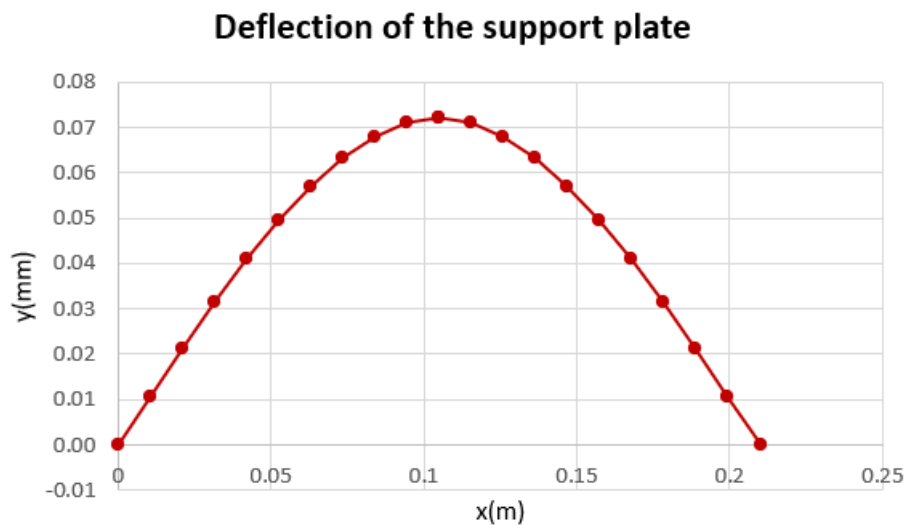


Figure 3.50: Deflection of the support plate

Through the examination of the data depicted in the Figures 3.49 and 3.50, it is possible to perceive that the support plate will offer the required level of safety to be included in the ultrasonic fatigue testing equipment. The maximum deflection of the support plate is 0.07 mm as can be seen in the figure above. This level of deflection is advantageous to the design since it provides some flexibility which facilitates the use of the power screw to generate the static load. The design of the support plate is advantageous to the project due to its high safety factor and low manufacturing cost, which result from the utilization of an existing S690 steel plate at INEGI.

After the validation of the support plate was completed through the analytical analysis provided and discussed above, a numerical analysis was conducted on the subassembly presented in the Figures 3.11 and 3.12. The primary objectives of this analysis, which will be carried out using the Abaqus software, are to validate the design of the remaining subassembly components, i.e., to ensure that they are capable of providing the necessary safety when the ultrasonic fatigue testing machine is applying the maximum static load to the specimen, and to define their manufacturing material. In the Figure 3.51 it is presented the symmetry view of the subassembly on Abaqus with regard to the XY and YZ symmetry planes. For this analysis, the locking support (1), the booster support (2), the support plate (3), two M8 bolts, two M8 nuts and four M8 washers were taken into account, the fixing hardware are not numbered in the Figure 3.51 for simplicity. As said before,

the ultrasonic booster and horn will be analyzed and discussed in the subsection 3.4.4. The locking support (1) must have no direct contact with the support plate (3) before the bolts being tightened, a gap of 0.5 mm exists before the tightening of the bolts, in order to ensure the correct clamping of the booster support (2). In order to simplify the analysis, the rubber rings presented in the Figures 3.11 and 3.12 were disregarded.

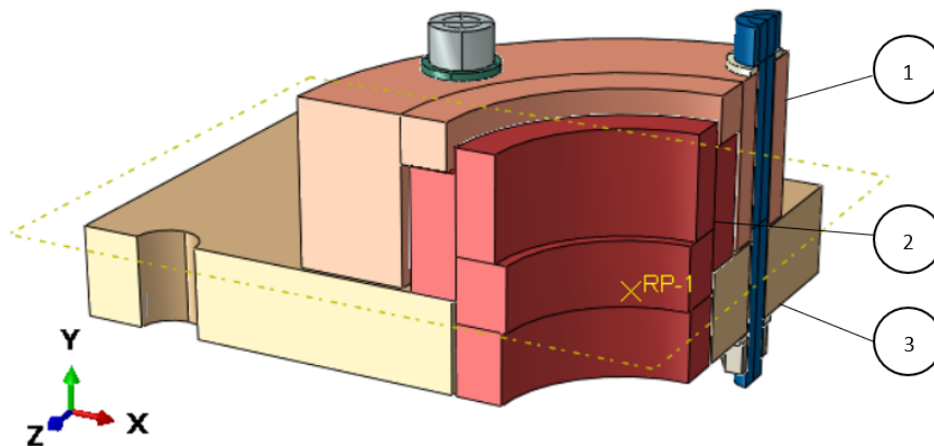


Figure 3.51: Symmetry view of the Section B subassembly presented in the Figures 3.11 and 3.12 on Abaqus

The mechanical properties of the S690 steel support plate are the same as shown in Table 3.10. The rest of the components were considered to be manufactured out of a regular steel with a Young's modulus, E , of 200 GPa and a Poisson's ratio, ν , of 0.3. For this numerical analysis only the hexahedron element type with reduced integration, C3D8R, was utilized and in the figure below the mesh density of this Abaqus analysis can be seen. The Table 3.52 provides an overview of the total number of elements that constitute each component.

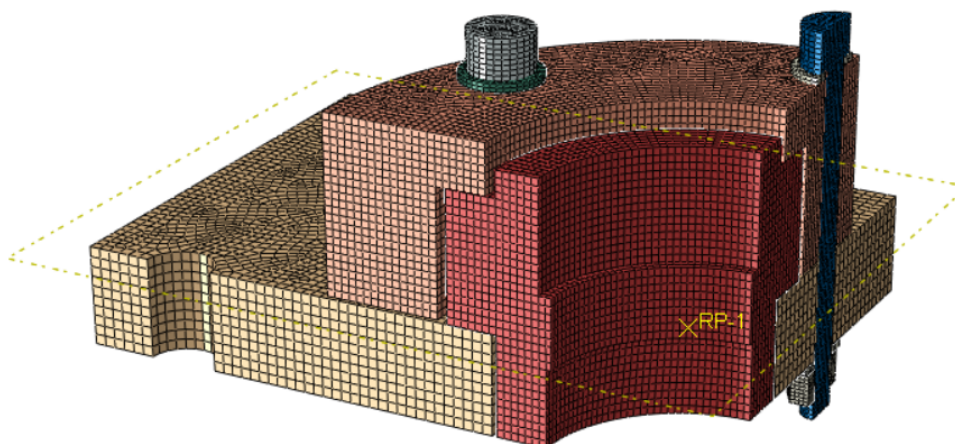


Figure 3.52: Mesh density of the Section B subassembly

Table 3.11: Number of elements of each component of the subassembly presented in the Figure 3.52

Component	Number of elements
Support plate	32110
Locking support	28176
Booster support	12285
Full M8 bolt	6376
Full M8 nut	2160
Full M8 washer	320

The M8 half bolt, M8 half nut and M8 half washers visible in the Figure 3.51 are not identified in the table above as they have half of the entire component elements. To reduce the mathematical cost and to save computational time of the Abaqus analysis, it was taken advantage of the symmetry of the subassembly; hence, it was required to impose different symmetry requirements on the subassembly's symmetry planes, as shown in the Figure 3.53. As in the Abaqus analysis of Figure 3.35, on the XY symmetry plane, the displacement according to the Z coordinate and the rotation according to the X and Y axis was considered to be null. Furthermore, the displacement according to the X coordinate and the rotation according to the Y and Z axis was considered to be zero on the YZ symmetry plane.

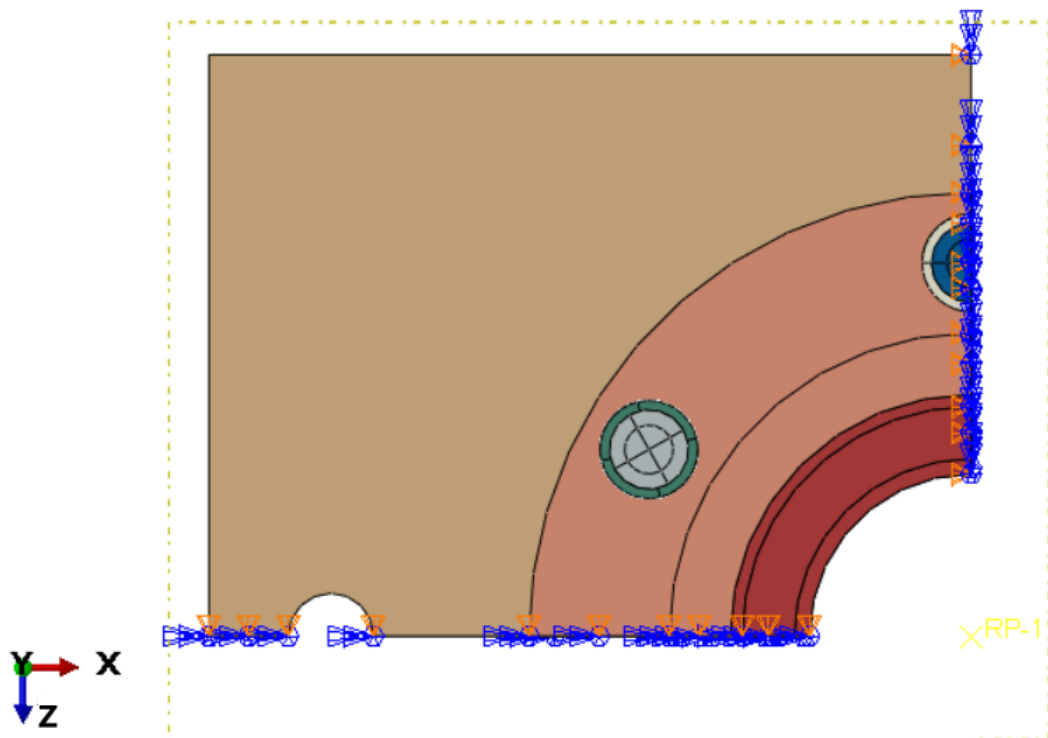


Figure 3.53: Demonstration of the application of symmetry conditions on the Section B subassembly

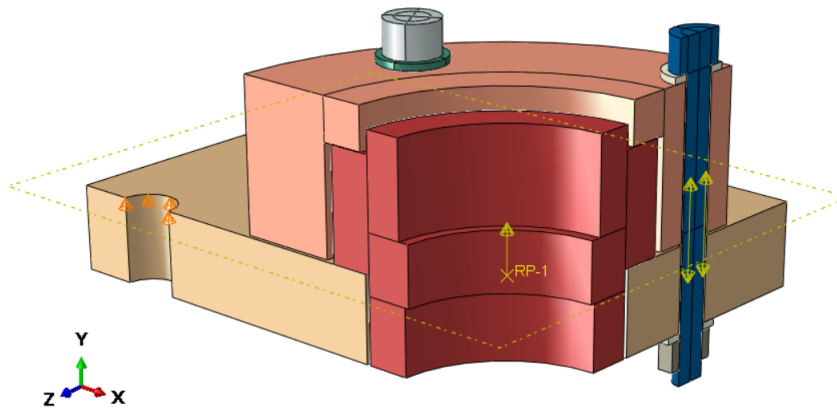


Figure 3.54: Boundary condition and loads on the Section B subassembly without the symmetry conditions

The figure above illustrates the subassembly with the bolt preloads, the applied static load and the boundary condition considered in this Abaqus analysis. The figure was simplified, so the symmetry conditions presented in the Figure 3.53 are not shown. This numerical analysis represents the situation in which the ultrasonic fatigue testing machine is performing tests with the maximum static load applied to the specimen, 10 kN. To replicate the aforementioned condition, a reference point, RP-1, was coupled to the threaded portion of the booster support, where the booster screws, and a positive static force of 2500 N, due to symmetry, was applied to the reference point. The M8 bolts preload was specified based on the data in the Appendix D, so a preload of 27896.5 N was applied to the full M8 bolt and a preload of 13948.3 N was applied to the half M8 bolt. Additionally, the vertical displacement on the upper zone of the bolt hole that connects the support plate with the load cell was considered to be null, since the load cell is fixed through a bolt. For this finite element analysis, two consecutive steps were utilized. The first one regarding the bolts preload and the second one regarding the considered external load. The results of this numerical analysis are presented next.

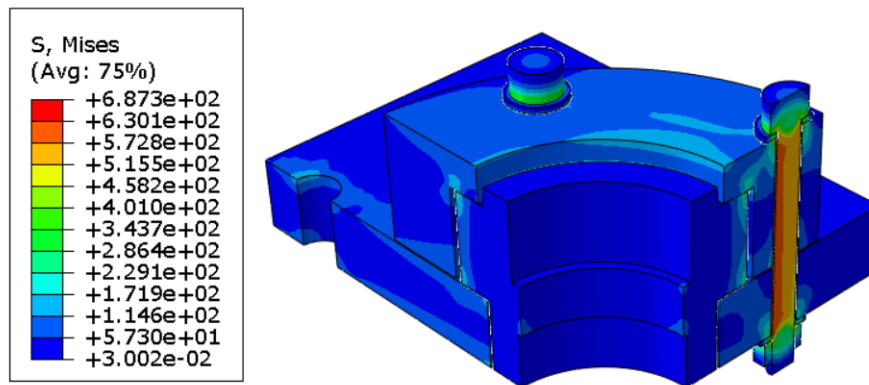


Figure 3.55: Von Mises stress on the full Section B subassembly (MPa)

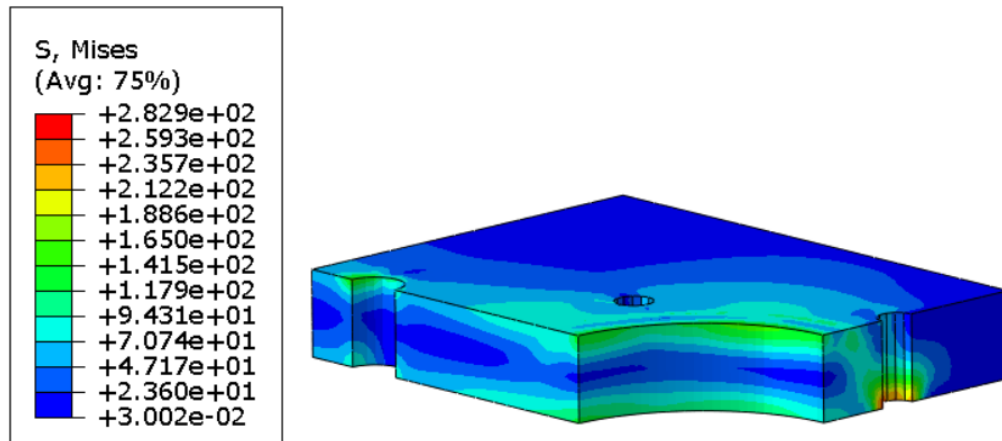


Figure 3.56: Von Mises stress on the support plate (MPa)

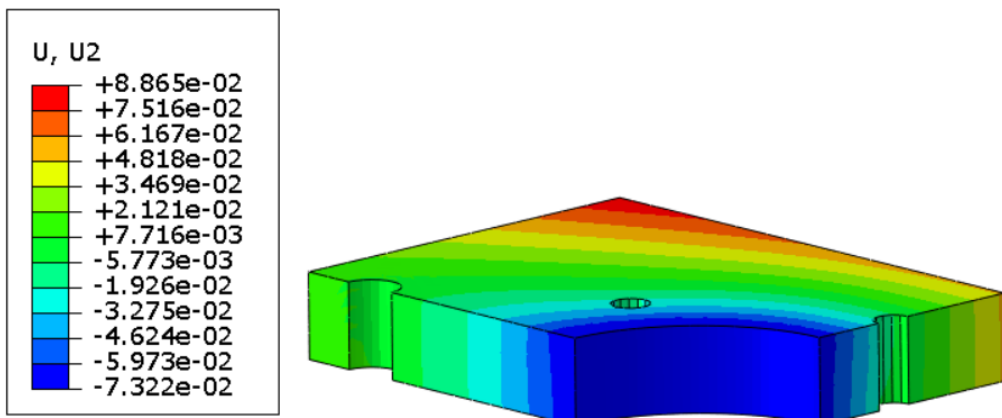


Figure 3.57: Vertical displacement on the support plate (mm)

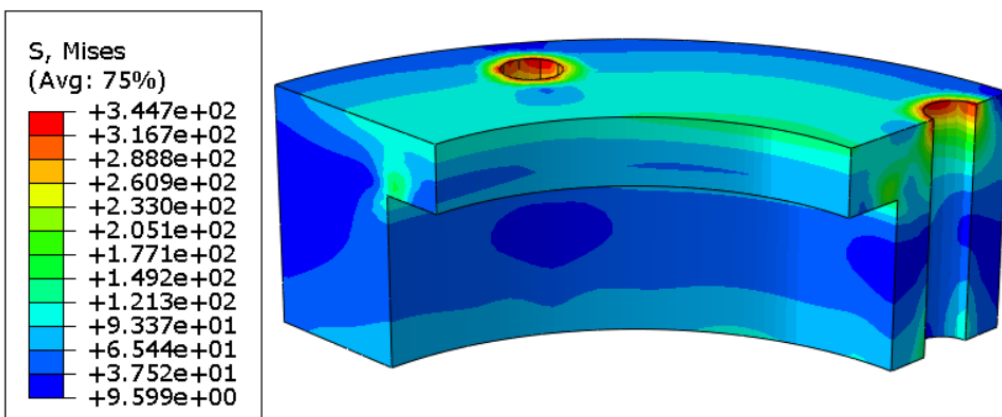


Figure 3.58: Von Mises stress on the locking support (MPa)

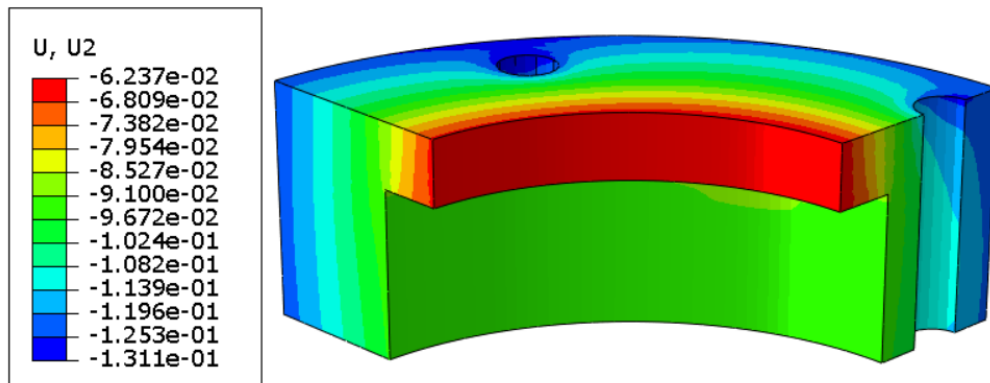


Figure 3.59: Vertical displacement on the locking support (mm)

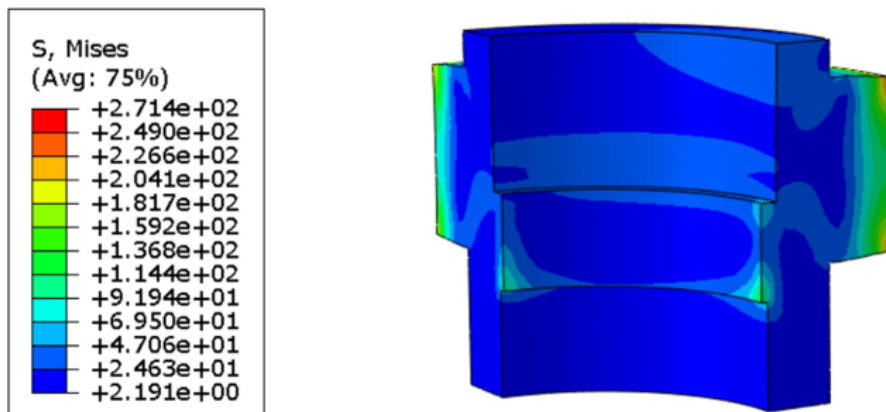


Figure 3.60: Von Mises stress on the booster support (MPa) - Front

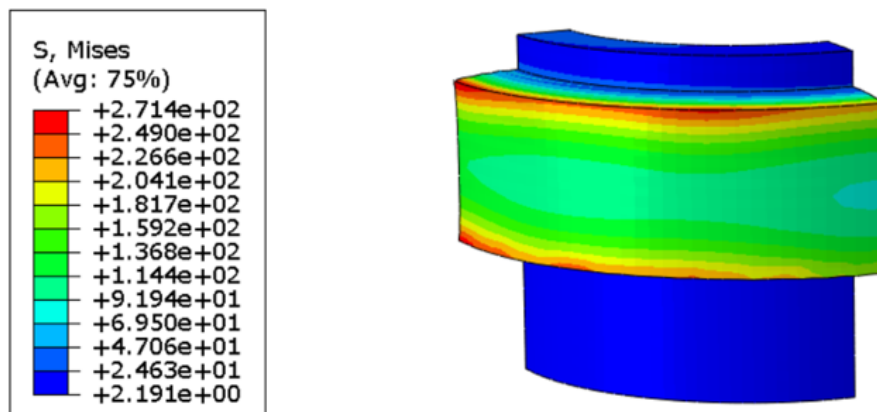


Figure 3.61: Von Mises stress on the booster support (MPa) - Back

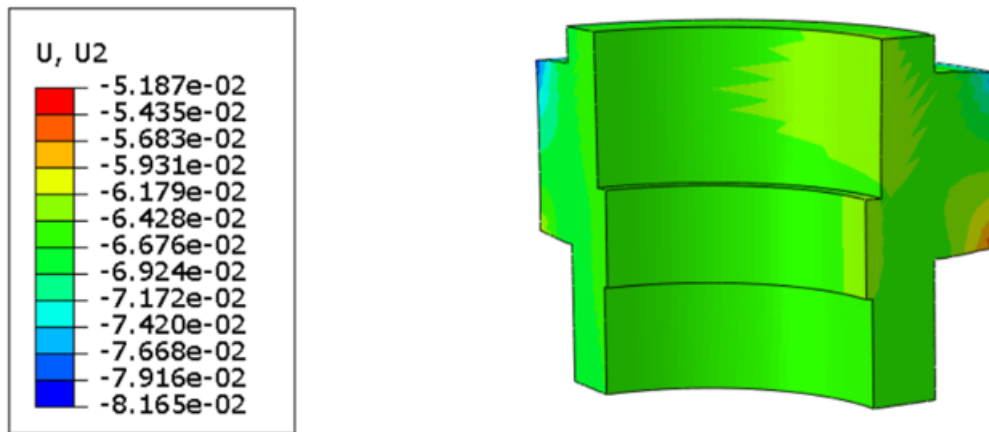


Figure 3.62: Vertical displacement on the booster support (mm) - Front

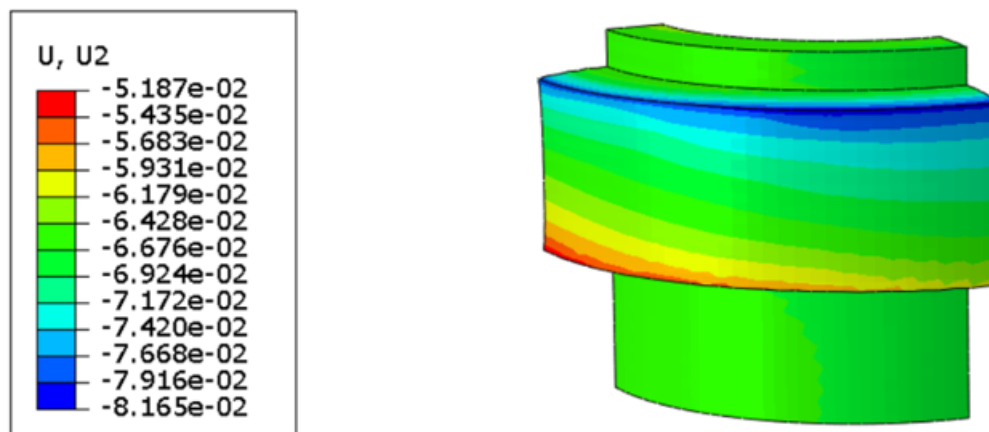


Figure 3.63: Vertical displacement on the booster support (mm) - Back

In the Figure 3.55, it is presented the Von Mises stress distribution on the full Section B sub-assembly, with its maximum stress occurring on the M8 bolts, around 687 MPa. The maximum Von Mises stress presented in the support plate is around 283 MPa, as it can be seen in the Figure 3.56, and the maximum vertical displacement is $8.87 \cdot 10^{-2}$ mm, as shown in the Figure 3.57. These results differ from the ones obtained analytically due to the simplified support plate model utilized to the analytical analysis. Despite that, the numerically obtained results still ensure the needed safety for the ultrasonic fatigue equipment proper operation. As mentioned before, the primary objectives of this analysis are the validation of the design of the booster support and locking support, and the establishment of their manufacturing material based on the results presented above. Through the Figure 3.58 it is possible to identify that the locking support presents a maximum Von Mises stress of around 345 MPa on the top of the through holes for the M8 bolts. The booster support, as it can be seen in the Figures 3.60 and 3.61, presents a maximum stress of around 271 MPa on the edges that are contacting with the locking support and the support plate. Both of the previously identified maximum stress locations are zones of high theoretical stress concentration due to being sharp edges. In practice, owing to the manufacturing processes, these edges will have

some radius of curvature, fillets, decreasing the verified stresses in the present analysis. The maximum vertical displacement for both locking support and booster support is, as it can be identified in the Figures 3.59 and 3.63, $-1.31 \cdot 10^{-1}$ mm and $-8.17 \cdot 10^{-2}$ mm, respectively. Considering the results that were mentioned previously, it was decided that the manufacturing material of both of the components, locking support and booster support, is going to be the AISI P20 steel. The mechanical properties of this steel are already listed in the Table 3.9. This selection was primarily influenced by the material's ease of machining, accessible price and high yield strength.

3.4.2.3 Analysis and validation of Section C subassembly

Following the conclusion of the analytical and numerical analysis of the Section B subassembly, an analytical and numerical analysis of the Section C subassembly, which is depicted in Figures 3.15 and 3.16, will be carried out, presented and then discussed.

In order to guarantee the safety and correct operation of the ultrasonic fatigue testing equipment, being developed in the present document, when the maximum static load is being applied to the specimen during testing, this analytical and numerical analysis seeks to validate the design and define the material of manufacture of the bearing holder, bearing cases and traction plate, presented in the Figure 3.16 and identified in the Table 3.4. First, an analytical evaluation and validation of the traction plate will be presented. Then, two numerical analyses using the Abaqus software will be performed. The primary goals of these two numerical analyses are to define the final design of the bearing holder and bearing cases and to examine how the applied tightening torque to the bolts affects the double direction thrust ball bearing.

Identically to the support plate presented in the Figure 3.43, the traction plate will similarly be fabricated using the existing S690 steel plates at INEGI. The original thickness of the plate, 20 mm, will be maintained in order to prevent any additional costs associated with machining. The mechanical properties of the S690 steel are already presented in the Table 3.10. The final design of the S690 steel traction plate is presented in the Figure 3.64 and the considered free body diagram of the S690 steel traction plate for the analytical analysis is presented in the Figure 3.65. When the ultrasonic fatigue testing equipment is subjecting the specimen to a static load of 10 kN, the traction plate will be subjected to a concentrated force, F , of the same magnitude being applied in the middle of its length. This force, F , is originated due to the downward vertical movement of the power screw. In addition, there are two vertical reactions of magnitude $\frac{F}{2}$, with the opposite direction of F , at the center of the through holes where the traction plate connects with the two squared section bars, as can be seen in the Figures 3.19 and 3.20.

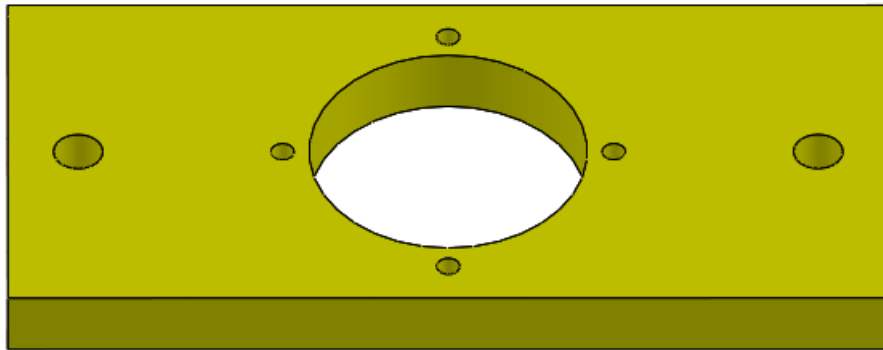


Figure 3.64: Final design of the S690 steel traction plate

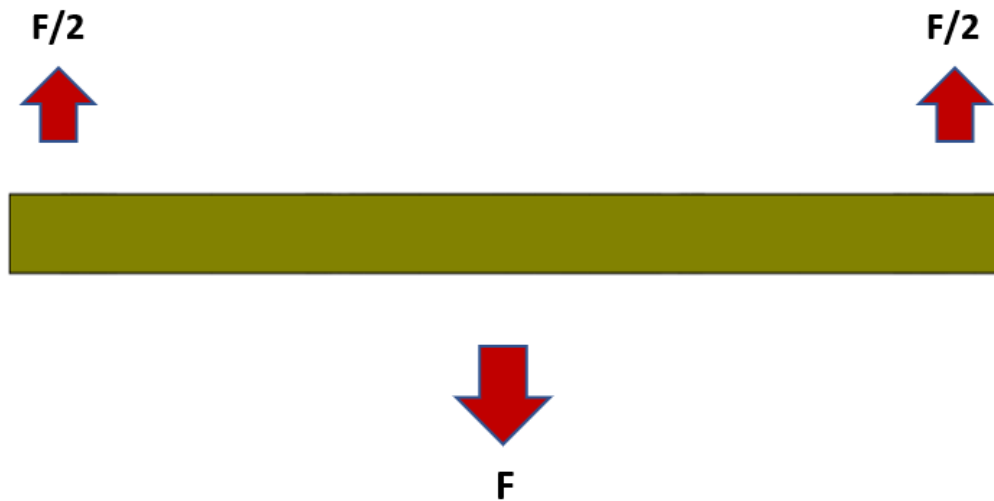


Figure 3.65: Free body diagram of the S690 steel traction plate

All the forces will be assumed to be concentrated for the purpose of simplicity and only the segment of interest of the traction plate will be analyzed, the region between the center points of the through holes, where the reactions are considered. So, the considered length of the traction plate is $L = 0.21$ m, which is the distance between the supports. Furthermore, the traction plate will be considered without holes for the analytical analysis.

The cross sectional area of the traction plate has the following dimensions:

- width, $b = 0.12$ m
- height, $h = 0.02$ m
- area = $0.24 \cdot 10^{-2}$ m²

The second moment of area, I , can be calculated through the Figure 3.29 and the dimensions presented above:

$$I = \frac{bh^3}{12} = 8 \cdot 10^{-8} \text{ m}^4 \quad (3.30)$$

The Figures below illustrate the shear force distribution, denoted by the notation $V(x)$, as well as the bending moment distribution, denoted by the notation $M(x)$. The coordinate x represents the distance between the center points of the through holes.

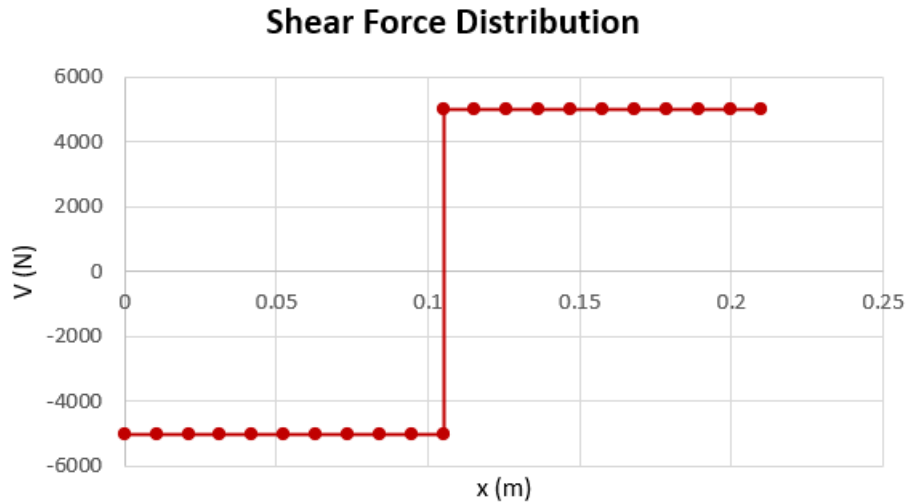


Figure 3.66: Shear force distribution of the traction plate

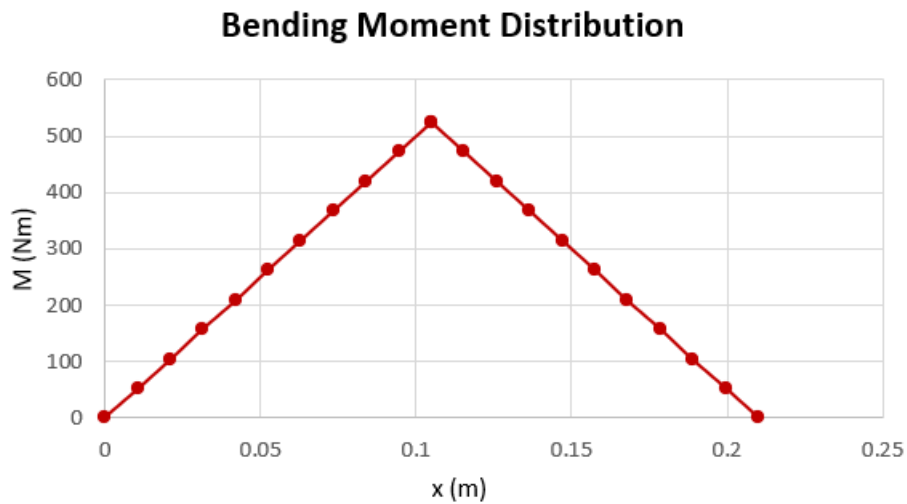


Figure 3.67: Bending moment distribution of the traction plate

The Bending moment distribution, shown in the Figure 3.67, can be partitioned into two distinct sections.

For $\frac{L}{2} \geq x \geq 0$:

$$M(x) = \frac{Fx}{2} \quad (3.31)$$

And for $L \geq x \geq \frac{L}{2}$:

$$M(x) = \frac{F}{2}L - \frac{F}{2}x \quad (3.32)$$

The maximum bending moment, $M_{MAX} = 525 \text{ N m}$, occurs at $x = \frac{L}{2}$ as it can be seen in the Figure 3.67. The graphic representation of the bending stress distribution in the zone of highest bending moment, $\sigma_{BD}(y)$, can be determined through the utilization of the equation 3.11, and it is shown below in the Figure 3.68.

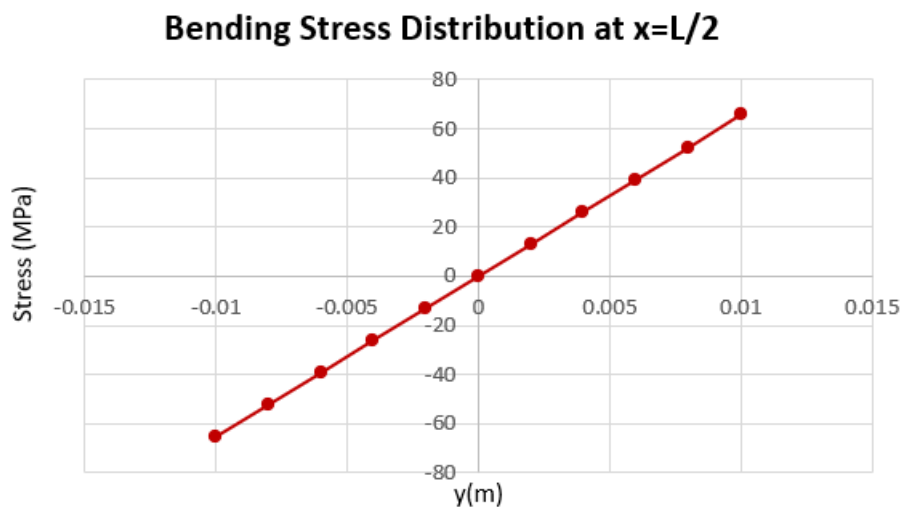


Figure 3.68: Bending stress distribution along the cross sectional area of the traction plate at $x = \frac{L}{2}$

The graphic shown above illustrates the distribution of bending stress throughout the cross sectional area of the traction plate at $x = \frac{L}{2}$ and y is the distance above or below the neutral axis of the traction plate. The maximum shear force can be identified in the Figure 3.66 as being $V = \pm 5000 \text{ N}$. And so, the shear stress distribution, $\tau(y)$, along the cross section of the traction support at $x = \frac{L}{2}$ can be obtained through the equation 3.18. The shear stress distribution is presented in the Figure 3.69.

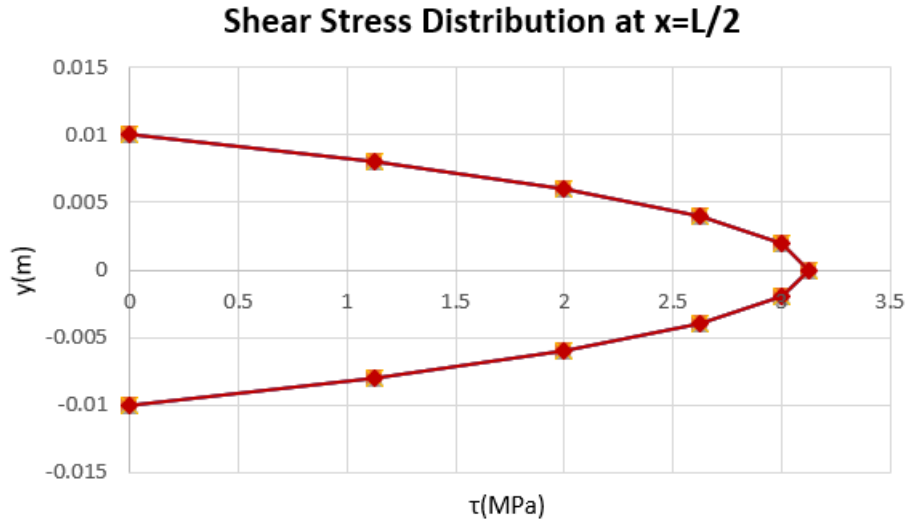


Figure 3.69: Shear stress distribution along the cross sectional area of the traction plate at $x = \frac{L}{2}$

The maximum bending stress occurs at the tops of the traction plate cross section, as it can be seen in the Figure 3.68, with its value being $\sigma_{BD} = \pm 65.63$ MPa, whereas the maximum shear stress, $\tau = 3.13$ MPa, occurs at the middle of the height of the traction plate cross section as can be verified in the figure bellow. Now that the distributions of both the bending stress and the shear stress have been determined and presented at $x = \frac{L}{2}$, it is possible to plot the Von Mises equivalent stress distribution, $\sigma_{VM}(y)$, using the equation 3.19. The Von Mises distribution at $x = \frac{L}{2}$ of the traction plate is presented bellow.

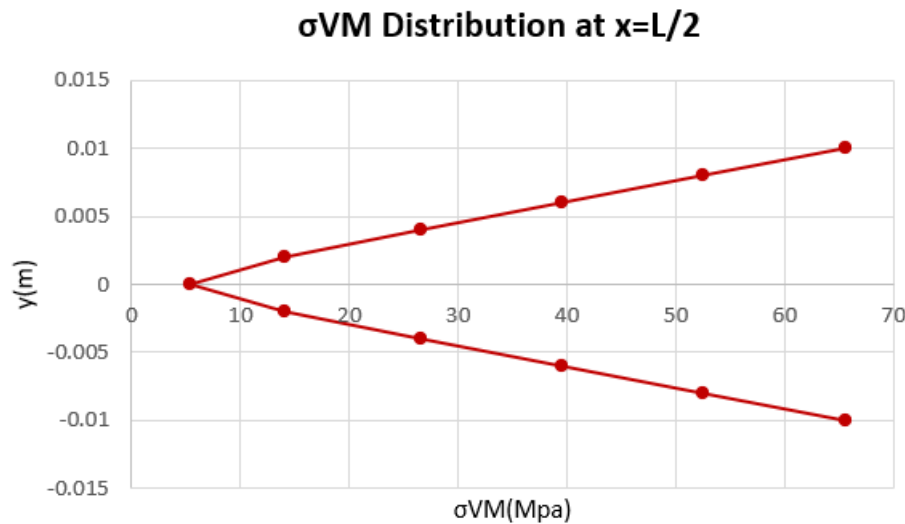


Figure 3.70: Von Mises equivalent stress distribution along the cross sectional area of the traction plate at $x = \frac{L}{2}$

Through the Figure 3.70, it is possible to perceive that the tops of the traction plate cross section experience the highest σ_{VM} stresses due to the superior contribution of the bending stress.

The maximum value of the σ_{VM} is 65.63 MPa, leading to a high safety factor of $SF = \frac{65.63}{779} = 11.87$.

Following the results of the stress analysis presented before, a deflection analysis of the traction plate was carried out. In order to calculate the deflection, $y(x)$, the double integration method was utilized, and so, the following two deflection equations were obtained through the two bending moment distribution equations, 3.31 and 3.32.

For $\frac{L}{2} \geq x \geq 0$:

$$y_1 = \frac{1}{EI} \left[\frac{Fx^3}{12} + C_1x + C_2 \right] \quad (3.33)$$

And for $L \geq x \geq \frac{L}{2}$:

$$y_2 = \frac{1}{EI} \left[-\frac{Fx^3}{12} + \frac{FL}{4}x^2 + C_3x + C_4 \right] \quad (3.34)$$

Where C_1, C_2, C_3 and C_4 are the integration constants. The application of four of the following distinct boundary conditions will result in the calculation of the analytical value of these constants, which will enable to generate a graphic that illustrates the deflection distribution along the length of the traction plate.

- $y_1(0) = 0$, no deflection at the beginning of the length of interest of the traction plate;
- $y_2(L) = 0$, no deflection at the end of the length of interest of the traction plate;
- $y_1(\frac{L}{2}) = y_2(\frac{L}{2})$, continuity condition on the deflection;
- $\theta_1(\frac{L}{2}) = \theta_2(\frac{L}{2})$, continuity condition on the slope;
- $\theta(\frac{L}{2}) = 0$, no slope on the middle of the length of interest of the traction plate.

The deflection distribution along the traction plate can be seen in the Figure 3.71.

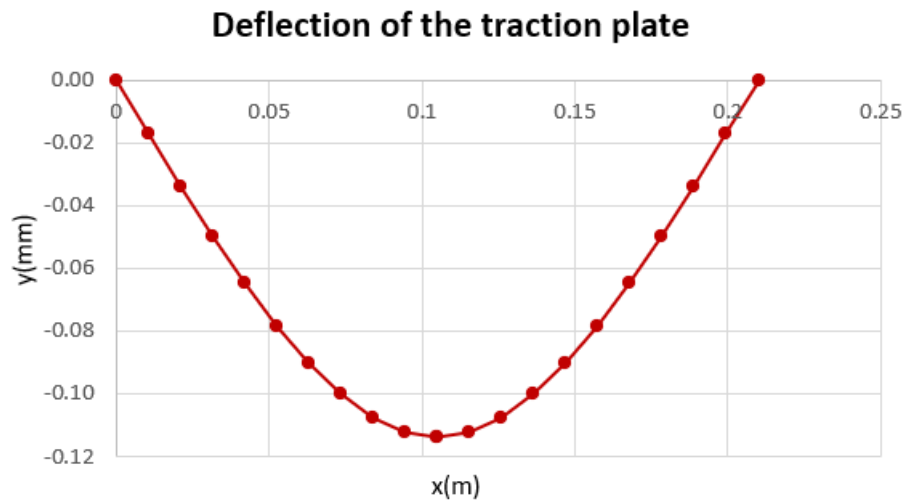


Figure 3.71: Deflection of the traction plate

The designed traction plate is compatible with the project being developed in this document, based on the analytical analysis completed and described above. The maximum deflection of the traction plate is 0.11 mm as can be seen in the Figure 3.71. The high safety factor, $SF = 11.87$, and flexibility of the traction plate benefits the project. In addition of that, there is no need to purchase S690 steel since it already exists at INEGI.

Following the discussion of the traction plate design and the subsequent validation of the design through the analysis presented previously, two distinct numerical analyses, using the Abaqus software, regarding the subassembly presented in the Figures 3.15 and 3.16 are going to be presented and the results will be discussed. The key goals of these two analyses are to establish the final design of the remaining subassembly components, define the manufacturing material for those components and evaluate the effect that the applied tightening torque on the bolts has on the bearing.

In the Figure 3.72, the first finite element analysis on Abaqus is displayed. This analysis considered an M10 bolt (1), an M10 washer (2), the bearing holder (3), a solid ring representing a section of the bearing (4) and a portion of the original power screw (5). The bearing holder (3) was designed in order to left a 0.5 mm gap between it and the power screw (5) before the tightening of the M10 bolt (1), in order to ensure the correct clamping of the bearing. All of the components of this analysis were considered to be manufactured out of a regular steel with a Young's modulus, E , of 200 GPa and a Poisson's ratio, ν , of 0.3. The mesh density of this analysis is presented in the Figure 3.73 and the total number of elements within each component is displayed in the Table 3.12. For this numerical analysis only the hexahedron element type with reduced integration, C3D8R, was utilized. It is possible to visualize in the Figure 3.72 the boundary conditions and loads considered in this analysis. The bottom of the power screw was considered to be fixed and since this analysis considers that the ultrasonic fatigue testing equipment is performing tests with the maximum static load applied to the specimen, a 10 kN distributed force was considered to

be applied on the upper surface of the bearing solid ring to replicate the aforementioned situation, which is the most critical case. For this analysis, two different and consecutive steps were assumed. The first one regarded the bolt load and the second one the external force.

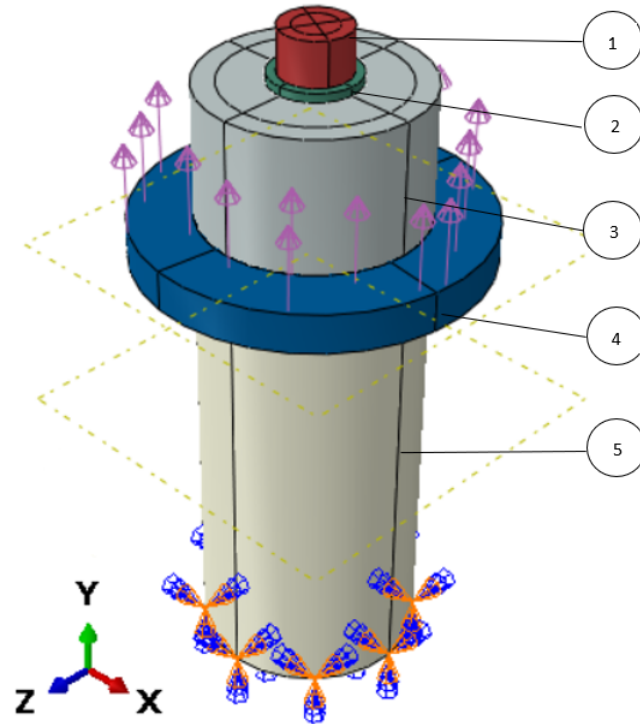


Figure 3.72: Bolt tightening torque influence analysis assembly on Abaqus

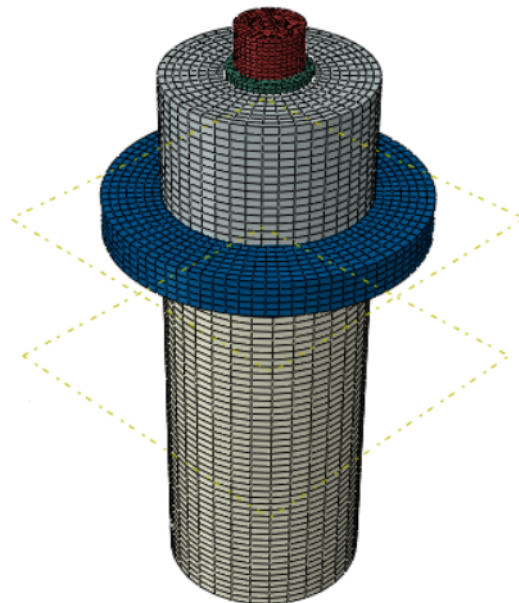


Figure 3.73: Mesh density of the bolt tightening torque influence analysis

Table 3.12: Number of elements of each component of the subassembly presented in the Figure 3.73

Component	Number of elements
Portion of the power screw	19806
Full M10 bolt	11520
Bearing holder	8010
Bearing solid ring	4100
Full M10 washer	480

Additionally, the M10 bolt preload was specified based on the data displayed in the Appendix D, so a preload of 44440 N was considered. The results of this finite element analysis are going to be presented next.

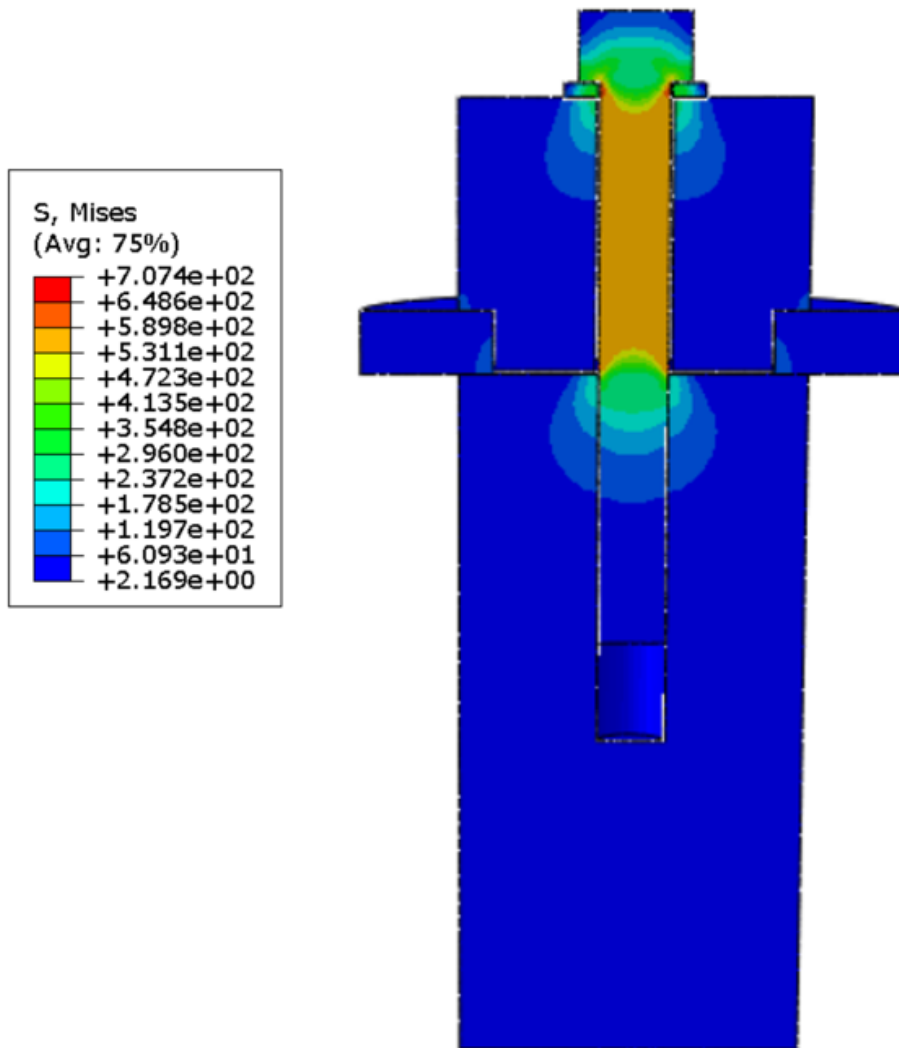


Figure 3.74: Von Mises stress on the section view of the assembly of the bolt tightening torque influence analysis (MPa)

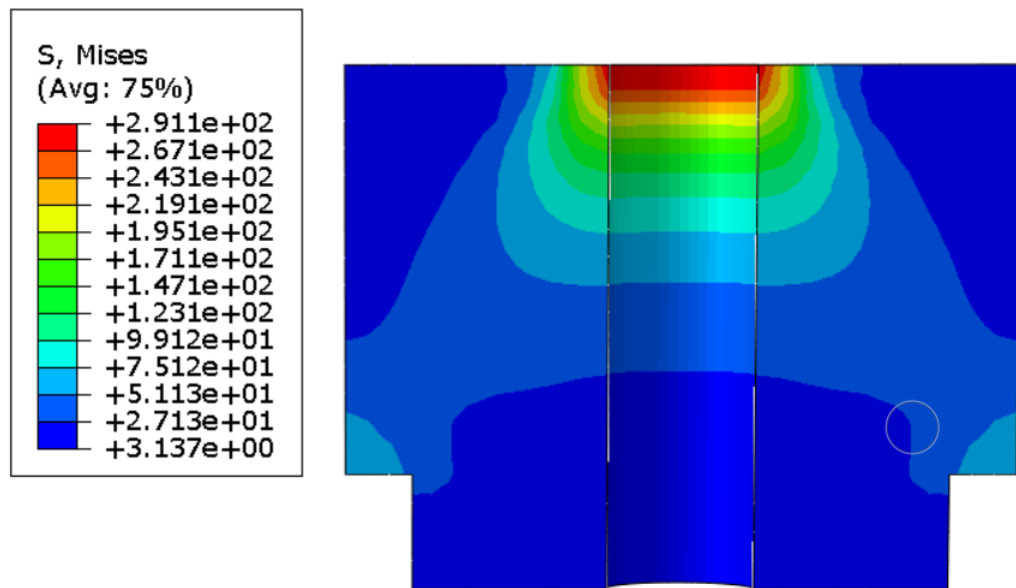


Figure 3.75: Von Mises stress on the section view of the bearing holder (MPa)

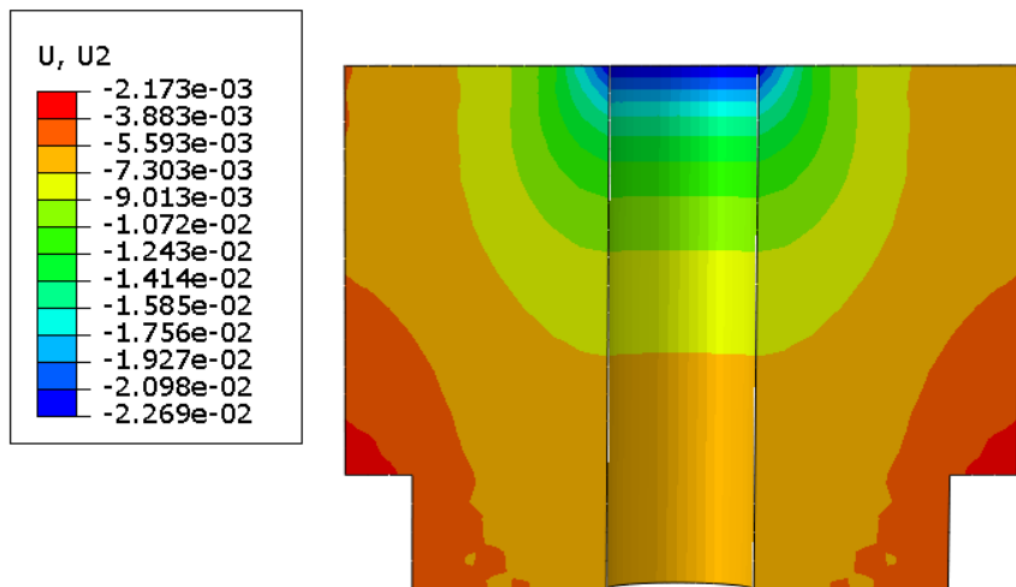


Figure 3.76: Vertical displacement on the section view of the bearing holder (mm)

As it is possible to identify in the Figure 3.74, the maximum Von Misses stress occurring in the present finite element analysis is located in the M10 bolt, on the sharp edge where it is connected with the washer, being its value around 707 MPa. Through the Figures 3.75 and 3.76 it is possible to point out that the bearing holder presents a maximum Von Mises stress of around 291 MPa and a maximum vertical displacement of $-2.27 \cdot 10^{-2}$ mm which both occur on the top of the through hole for the M10 bolt. Due to the top of the through hole being a sharp edge, it is a high stress concentration zone which in practice will have a radius of curvature due to the

manufacturing process, decreasing the stresses. One of the objectives of the present analysis is to define the manufacturing material of the bearing holder, and so, through the consideration of the present results and the ease of machining it was decided to manufacture the bearing holder in AISI P20 steel, whose mechanical properties are listed in the Table 3.9. Furthermore, in the Figure 3.77 it is presented the Von Mises stress distribution on the bearing solid ring. It can be noticed that the maximum Von Mises stress is 91 MPa allowing to conclude that the applied M10 bolt tightening torque will not lead to an incorrect bearing behavior when in operation, i.e. the bolt tightening torque will not cause the plastic deformation of the bearing.

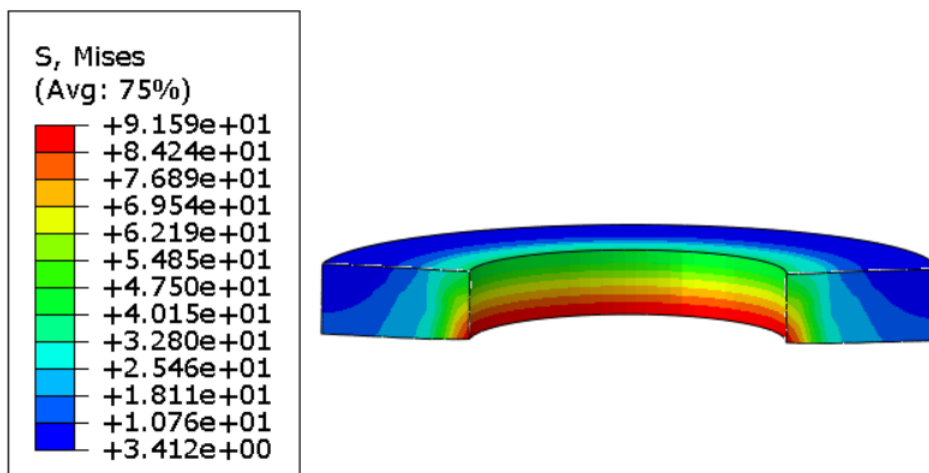


Figure 3.77: Von Mises stress on the section view of the bearing solid ring (MPa)

Following the conclusion of the preceding numerical analysis, the second and last finite element analysis on Abaqus of the Section C subassembly, which can be seen in the Figures 3.15 and 3.16, is going to be presented next. In order to decrease the computational time of this Abaqus analysis, as it is more mathematically expensive than the previous finite element analysis, the symmetry of the Section C subassembly was considered with regard to the XY and YZ symmetry planes, and the symmetry view of the subassembly on Abaqus is displayed in the Figure 3.78. For this analysis, the traction plate (1), the two bearing cases (2) & (3), a simplified solid bearing (4), two M6 bolts, two M6 nuts and four M6 washers visible in the Figures 3.15 and 3.16 were taken into account. The fixing hardware is not numbered in the Figure 3.78 for simplicity. In order to ensure the correct installation of the bearing, before the tightening of the bolts there's a 0.04 mm gap between both of the bearing cases (2) & (3) and the traction plate (1), which will guarantee the correct bearing clamping and functioning after the tightening of the bolts. The primary goals of this analysis are identical to those of the preceding one. In the Figure 3.79, it is presented the mesh density of this finite element analysis and in the Table 3.13 it is listed the number of finite elements that constitute each component. This numerical analysis was carried out by only using hexahedron elements with reduced integration, C3D8R elements. As it was stated before, it was taken advantage of the symmetry of the subassembly and in the Figure 3.80 it is presented the different symmetry conditions that were considered.

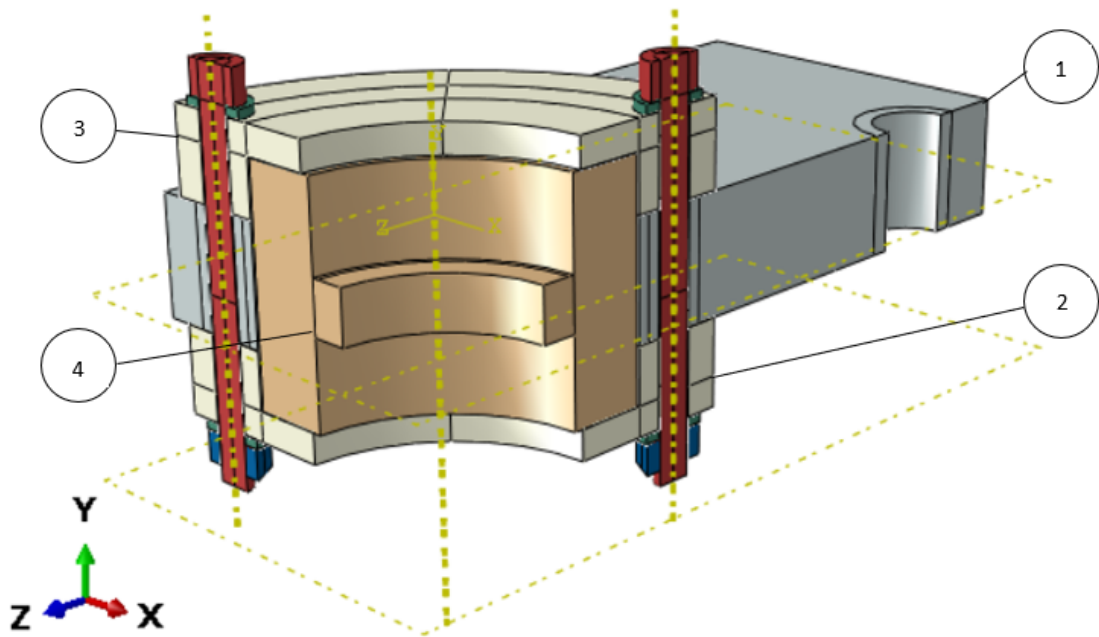


Figure 3.78: Symmetry view of the Section C subassembly presented in the Figures 3.15 and 3.16 on Abaqus

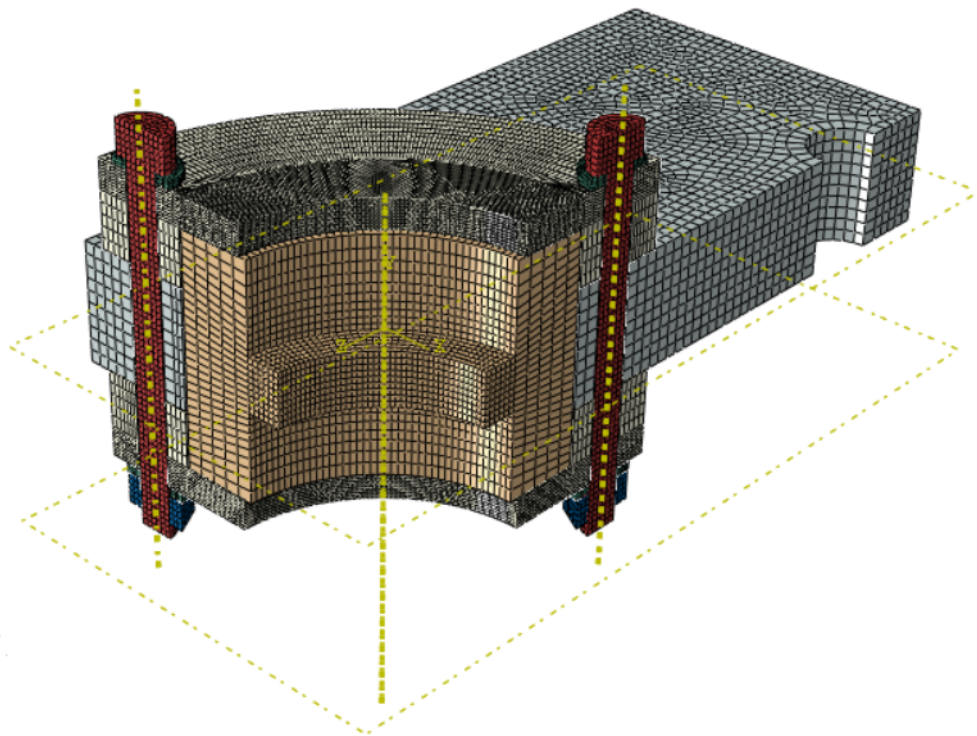


Figure 3.79: Mesh density of the Section C subassembly on Abaqus

Table 3.13: Number of elements of each component of the subassembly presented in the Figure 3.79

Component	Number of elements
Each bearing case	47160
Traction plate	17660
Simplified solid bearing	8159
Each M6 half bolt	1572
Each M6 half washer	684
Each M6 half nut	210

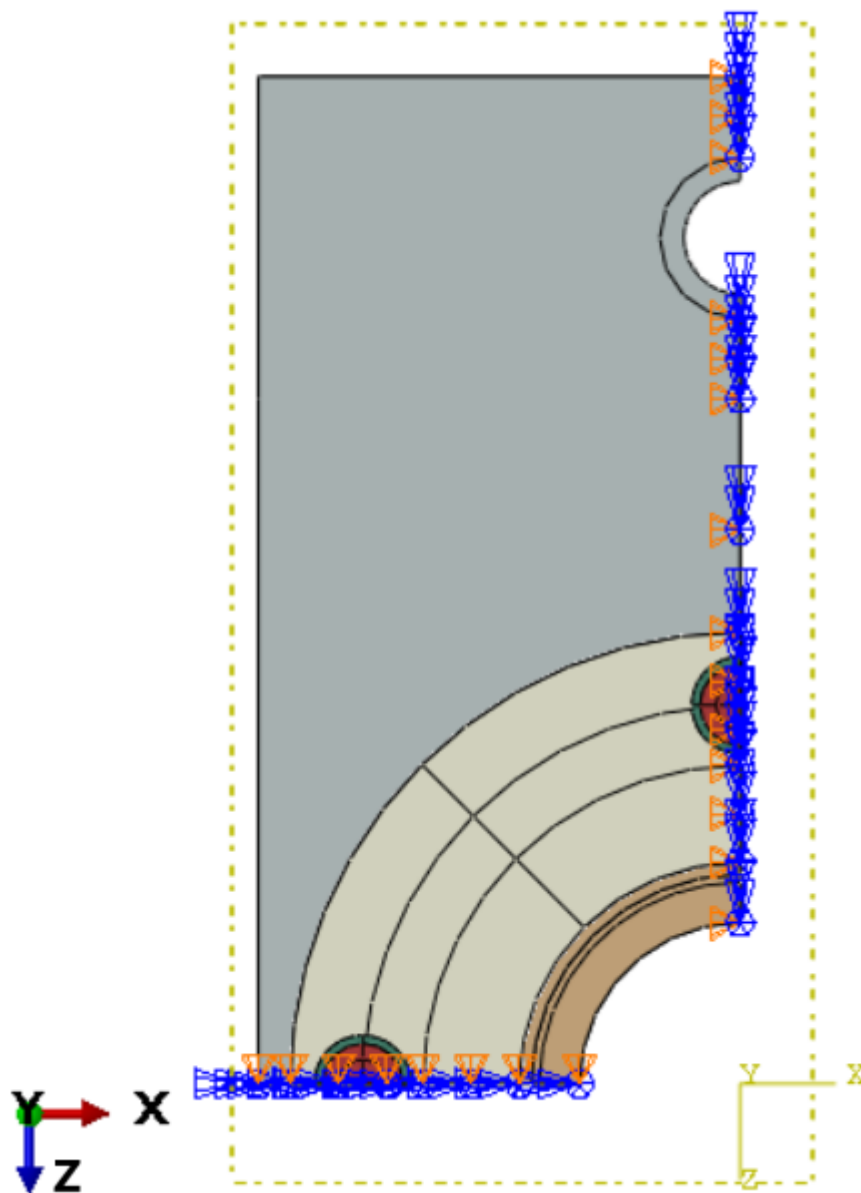


Figure 3.80: Demonstration of the application of symmetry conditions on the Section C subassembly

As in the previous Abaqus analysis of the present document, where different symmetry conditions were employed, on the XY symmetry plane, the displacement according to the Z coordinate and the rotation according the X and Y axis was considered to be null. In addition, on the YZ symmetry plane, the displacement according to the X coordinate and the rotation according to the Y and Z axis were considered to be zero.

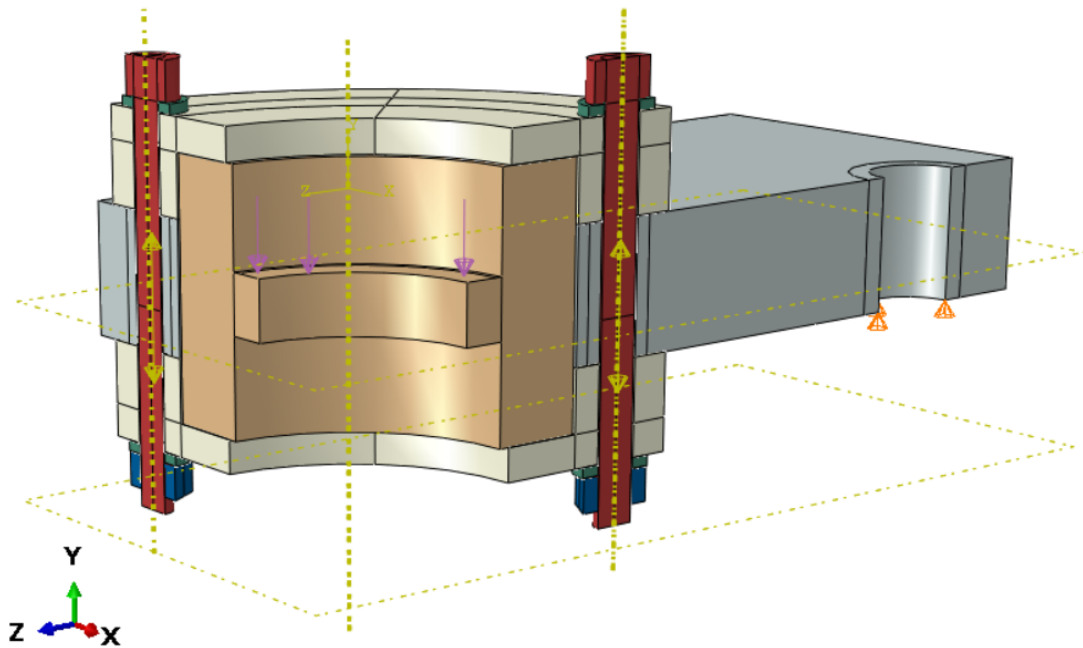


Figure 3.81: Boundary condition and loads on the Section C subassembly without the symmetry conditions

The S690 steel traction plate was considered to have the mechanical properties displayed in the Table 3.10 and all the other components of the present analysis were considered to be manufactured out of steel, Young's modulus, E , of 200 GPa and a Poisson's ratio, ν , of 0.3. In the Figure 3.81 it is presented the section C subassembly without the symmetry conditions presented in the Figure 3.80 and discussed earlier, due to simplification. However, the half bolt preloads, considered static load and boundary condition taken into account in this Abaqus analysis are illustrated. For this finite element analysis, two consecutive steps were utilized. The first one regarding the bolts preload and the second one regarding the considered external load. The M6 half bolts preload were specified based on the data displayed in the Appendix D, so both of the M6 half bolts were subjected to a preload of 7592.2 N. The vertical displacement on the lower zone of the through hole in the traction plate, where it connects with the squared section bar as it is possible to identify in the Figures 3.19 and 3.20, is defined to be zero. A distributed static load of 2500 N was applied to the simplified solid bearing in order to simulate the most extreme scenario in which the ultrasonic fatigue testing equipment is conducting tests with the specimen subjected to the maximum static load, 10 kN. The results of this finite element analysis are going to be presented next.

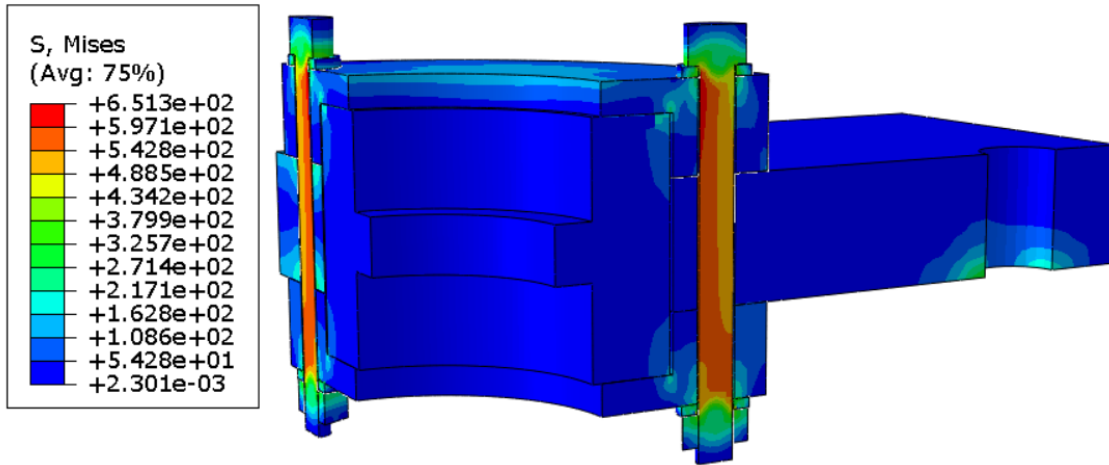


Figure 3.82: Von Mises stress on the full Section C subassembly (MPa)

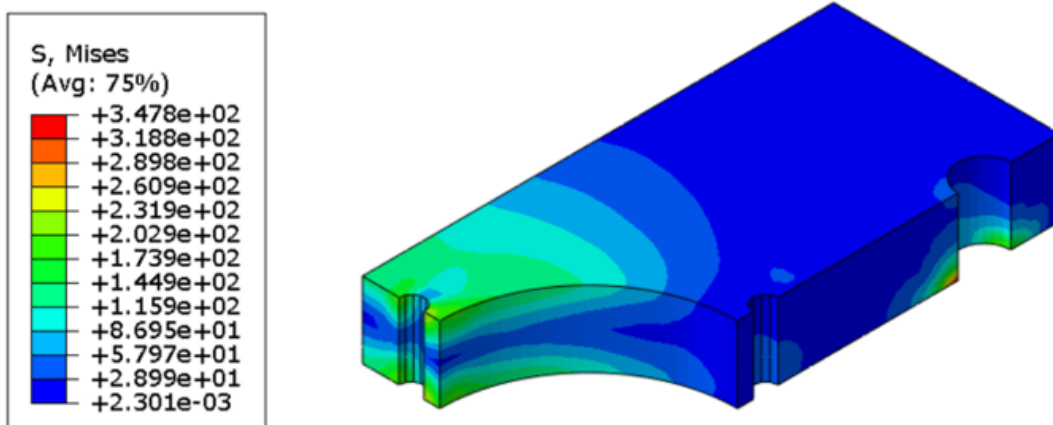


Figure 3.83: Von Mises stress on the traction plate (MPa)

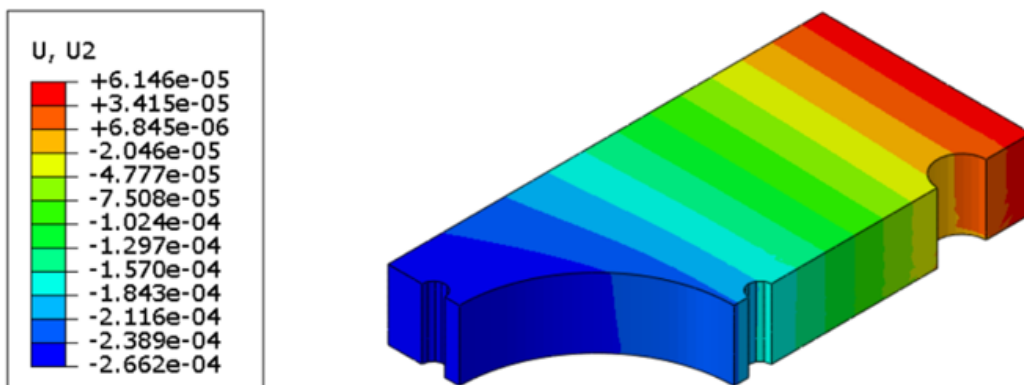


Figure 3.84: Vertical displacement on the traction plate (mm)

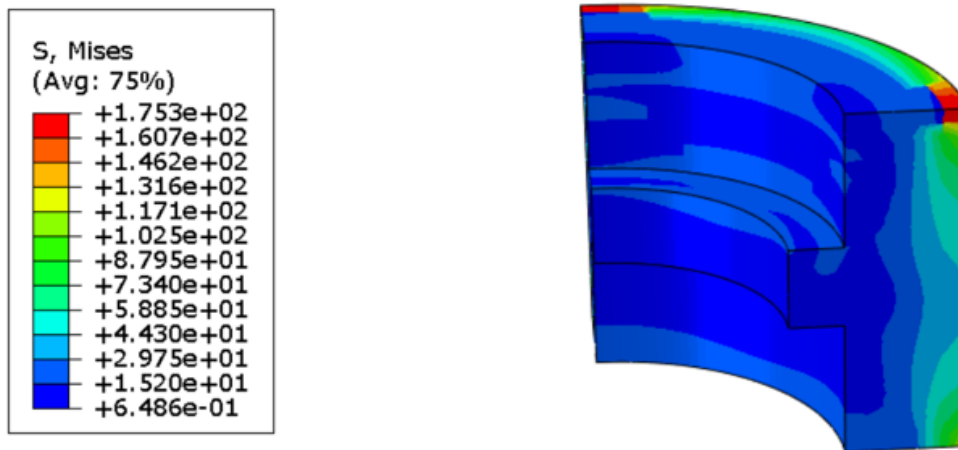


Figure 3.85: Von Mises stress on the simplified solid bearing (MPa)

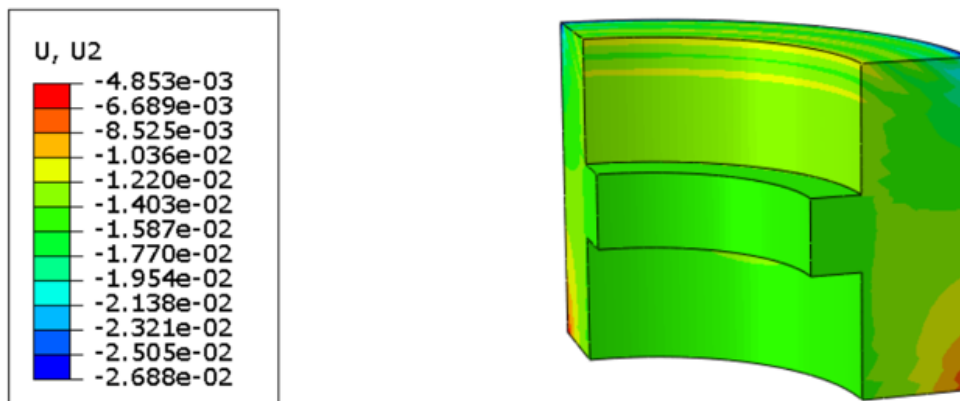


Figure 3.86: Vertical displacement on the simplified solid bearing (mm)

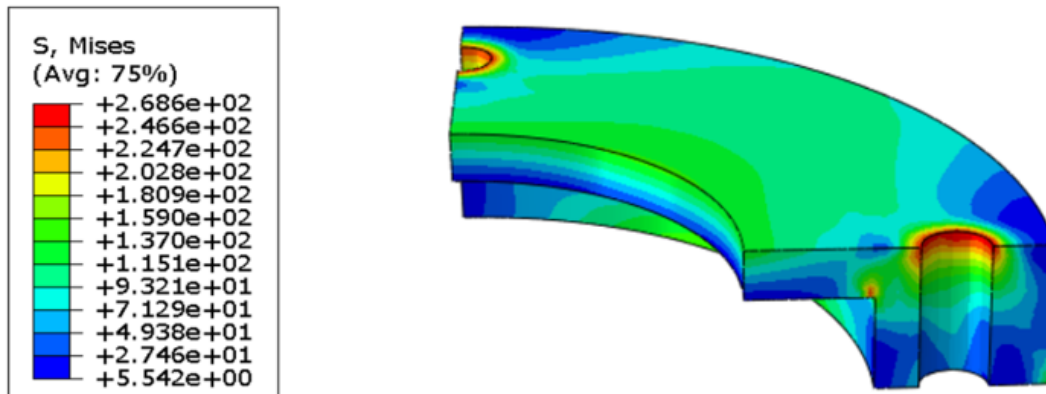


Figure 3.87: Von Mises stress on the upper bearing case (MPa)

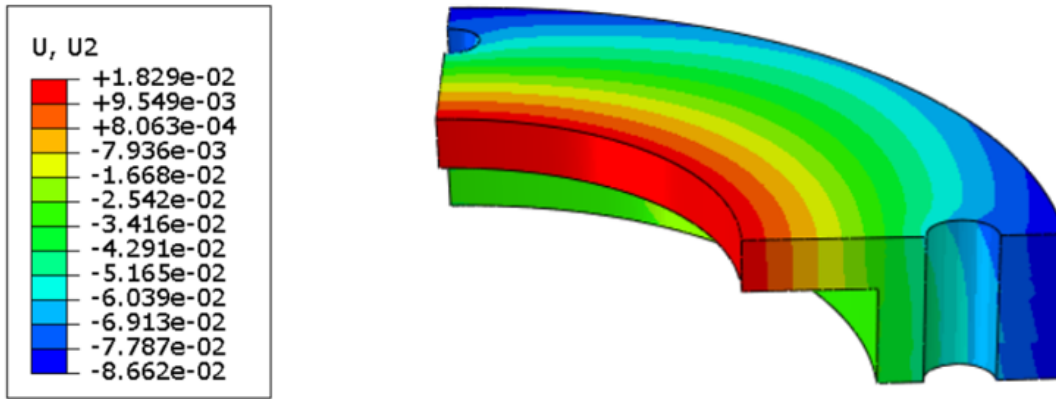


Figure 3.88: Vertical displacement on the upper bearing case (mm)

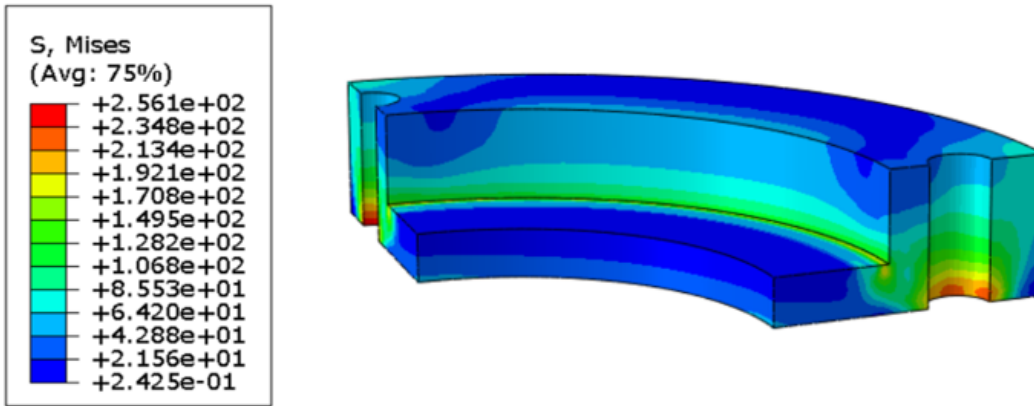


Figure 3.89: Von Mises stress on the lower bearing case (MPa)

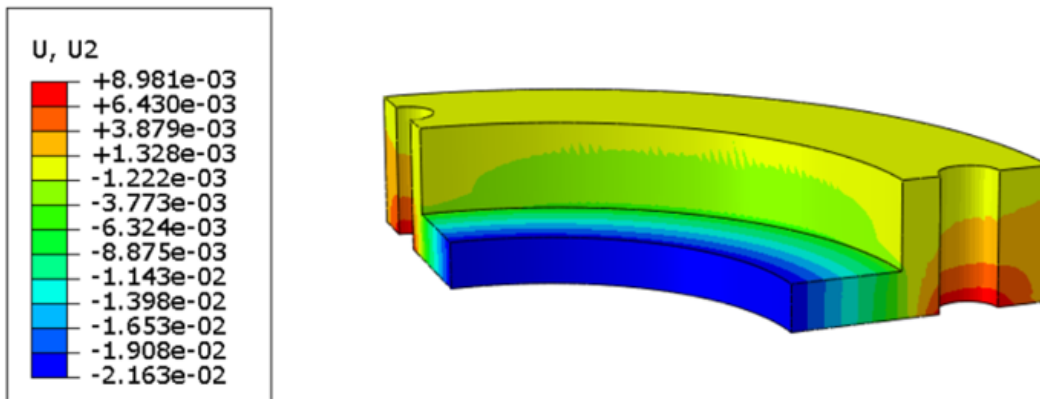


Figure 3.90: Vertical displacement on the lower bearing case (mm)

The maximum Von Mises stress occurring in the present Abaqus analysis of the section C subassembly was verified in the M6 half bolts, as it can be noted through the Figure 3.82, being its value around 651 MPa. The maximum Von Mises stress verified on the traction plate was around 348 MPa, as it can be seen in the Figure 3.83, and the maximum vertical displacement

can be noted on the Figure 3.84 as being $-2.66 \cdot 10^{-4}$ mm. These results differ from the ones obtained analytically due to the high stress concentration factor zones considered on the numerical analysis and due to the simplifications made on the analytical model. Furthermore, the traction plate offers and ensures the necessary safety for the correct operation of the ultrasonic fatigue equipment. As stated previously, one of the key purposes of this analysis was to guarantee the bearing's proper performance in the most extreme operating condition of the fatigue equipment being developed in the present document, i.e. the bearing's proper functioning in the most extreme scenario without suffer plastic deformation. Through the Figure 3.85, it is possible to verify that the higher Von Mises stress occurring in the simplified solid bearing was around 175 MPa. The maximum stress verified on the bearing is confined to relatively localized areas and will not interfere with the bearing's proper operation. Furthermore, through the results presented in the Figures 3.87, 3.88, 3.89 and 3.90 it is possible to validate the design of the bearing cases and define their manufacturing material. Both of the bearing cases present the maximum Von Mises stress around the edge of the through hole for the M6 bolts, with the upper bearing case presenting a stress of around 269 MPa and the lower bearing case presenting a stress of around 256 MPa, as it can be seen in the Figures 3.87 and 3.89. The maximum vertical displacement of the upper and lower bearing case is minimal. The maximum vertical displacement occurring in the upper bearing case is $-8.62 \cdot 10^{-2}$ mm, as it can be denoted in the Figure 3.88, and for the lower bearing case, a maximum vertical displacement of $-2.16 \cdot 10^{-2}$ mm can be verified in the Figure 3.90. In light of the results that were presented earlier, it was determined that the AISI P20 steel, whose mechanical properties are already listed in the Table 3.9, would be the material of choice for the manufacture of the bearing cases. This option was principally driven by the material's high yield strength, low cost and ease of machining. The final definition drawings of the traction plate, bearing holder and bearing cases are presented in the Appendix C.

3.4.3 Thread stresses

In the present subsection, the thread stresses on the most critical points of the threaded portion of the vibration absorbing flange and booster support will be analytically analyzed. This analysis's primary purpose is to supplement the finite element analyses whose results are presented in the Figures 3.41, for the vibration absorbing flange, and 3.60, for the booster support. These two components are manufactured from the the same material, AISI P20 steel, have the same thread dimensions and have the same effective number of threads in the engagement zone, hence, the following analysis will be valid for both the vibration absorbing flange and booster support.

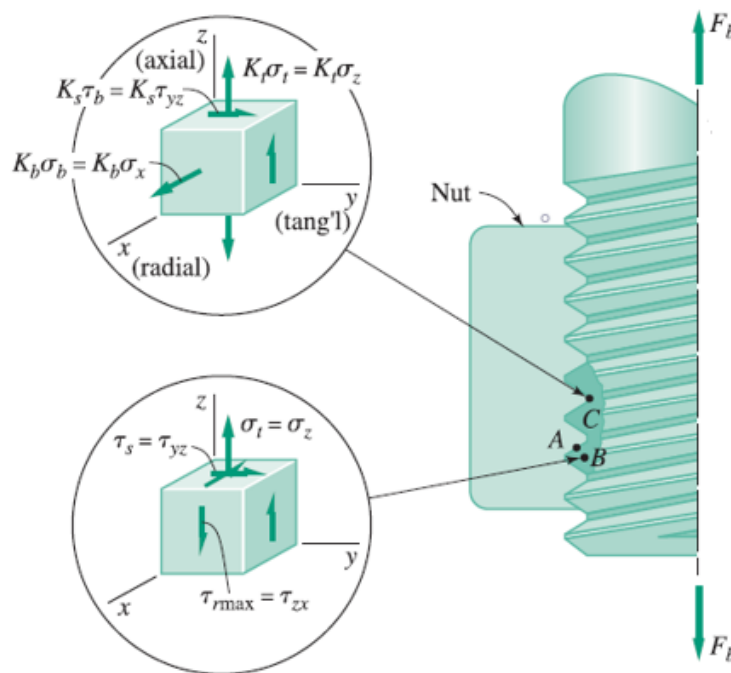


Figure 3.91: Critical points and stress components (Adapted from [48])

In the figure above, it is presented the most critical points in a threaded connection. The point A is only considered for power screw threads, so, this analysis will only be focused on the points B and C. At critical point B, the most likely to occur failure modes are stripping and fatigue. As it can be seen in the Figure 3.91, the stress components acting on the critical point B are the direct tensile stress, σ_t , due to the tensile force acting on the threads, the torsional shear, τ_s , due to the tightening and the transverse shearing stress, τ_{tr-max} , due to the thread bending [48].

The direct tensile stress, σ_t , can be calculated through the following equation:

$$\sigma_t = \frac{4F_b}{\pi d_r^2} \text{ (MPa)} \quad (3.35)$$

Where F_b is the tensile force, which includes the preload, and d_r the root diameter of the thread. Furthermore, the torsional shear, τ_s , is given by the following equation:

$$\tau_s = \frac{16(T_t - T_{nf})}{\pi d_r^3} \text{ (MPa)} \quad (3.36)$$

With T_{nf} being the torque to overcome friction at the contact face of the considered nut and T_t the tightening torque to produce the desired preload, which can be calculated through:

$$T_t = K_T F_b d_b \text{ (Nmm)} \quad (3.37)$$

Where K_T is the torque coefficient and d_b the nominal diameter of the thread. Finally, the transverse shearing stress, τ_{tr-max} , is given by the equation 3.38.

$$\tau_{tr-max} = \frac{3F_b}{\pi d_r p n_e} \text{ (MPa)} \quad (3.38)$$

Where p is the thread pitch and n_e the effective number of threads in the engagement zone. At critical point C, the most critical failure modes are yielding and fatigue, with the stress components being the direct tensile stress, σ_t , presented in the equation 3.35, the torsional shear, τ_s , given by the equation 3.36 and the thread bending stress, σ_b , presented in the following equation, with d_p being the pitch diameter of the thread [48].

$$\sigma_b = \frac{12F_b (d_p - d_r)}{\pi d_r n_e p^2} \text{ (MPa)} \quad (3.39)$$

The thread dimensions, regarding the threaded portion of the vibration absorbing flange and booster support, are going to be presented next [49].

- Nominal diameter (d_b) = 53 mm;
- Pitch diameter (d_p) = 52.4 mm;
- Root diameter (d_r) = 51.9 mm;
- Pitch (p) = 1 mm;

The effective number of threads, n_e , will be calculated through the following equation:

$$n_e = \frac{\text{Smaller length of the threaded connection}}{\text{Pitch}} = 9.5 \quad (3.40)$$

The result presented above, took into account the smaller threaded length of the components of the two connections, vibration absorbing flange & booster and booster support & booster. The threaded lengths can be seen in more detail in the technical drawings presented in the Appendix C. Nonetheless, a value of n_e equal to 8 will be considered due to being more conservative. Furthermore, the present analysis will consider a null value for the T_{nf} in order to simulate the most extreme scenario, F_b will be considered as 15 kN, a value of 0.2 will be considered to the torque coefficient due to being a common and conservative value for this types of connections [48]. In light of the preceding information and according to the equations 3.35, 3.36, 3.37, 3.38 and 3.39 it is possible to reach the following results:

$$\sigma_t = 7.1 \text{ MPa} \quad (3.41)$$

$$\sigma_b = 59.7 \text{ MPa} \quad (3.42)$$

$$\tau_s = 5.8 \text{ MPa} \quad (3.43)$$

$$\tau_{tr-max} = 34.5 \text{ MPa} \quad (3.44)$$

Additionally, through the results presented above and through the use of the equation 3.19, it is possible to calculate the equivalent Von Mises stress on the critical points B and C. The verified Von Mises equivalent stress on point B was 61.0 MPa and the verified Von Mises equivalent stress on point C was 57.4 MPa, so, the point B is the most critical in the present analysis. Finally, a safety factor can be calculated on point B with the use of the mechanical properties presented in the Table 3.9. The safety factor presents a value of 14.8, which ensures the necessary safety for the correct operation of the ultrasonic fatigue testing equipment.

3.4.4 Ultrasonic booster and horn

In this subsection, the ultrasonic booster and horn selected to be utilized in the project being developed in this document will be presented and discussed. Ti-6Al-4V was chosen as the manufacturing material for both the booster and the horn. One of the primary reasons that led for this decision were the titanium's low loss coefficient, η , as can be seen highlighted in green in the Figure 3.92. The loss coefficient, η , of a material is directly related with the material's damping [50]. As a result, the higher the loss coefficient, the higher the mechanical energy dissipation.

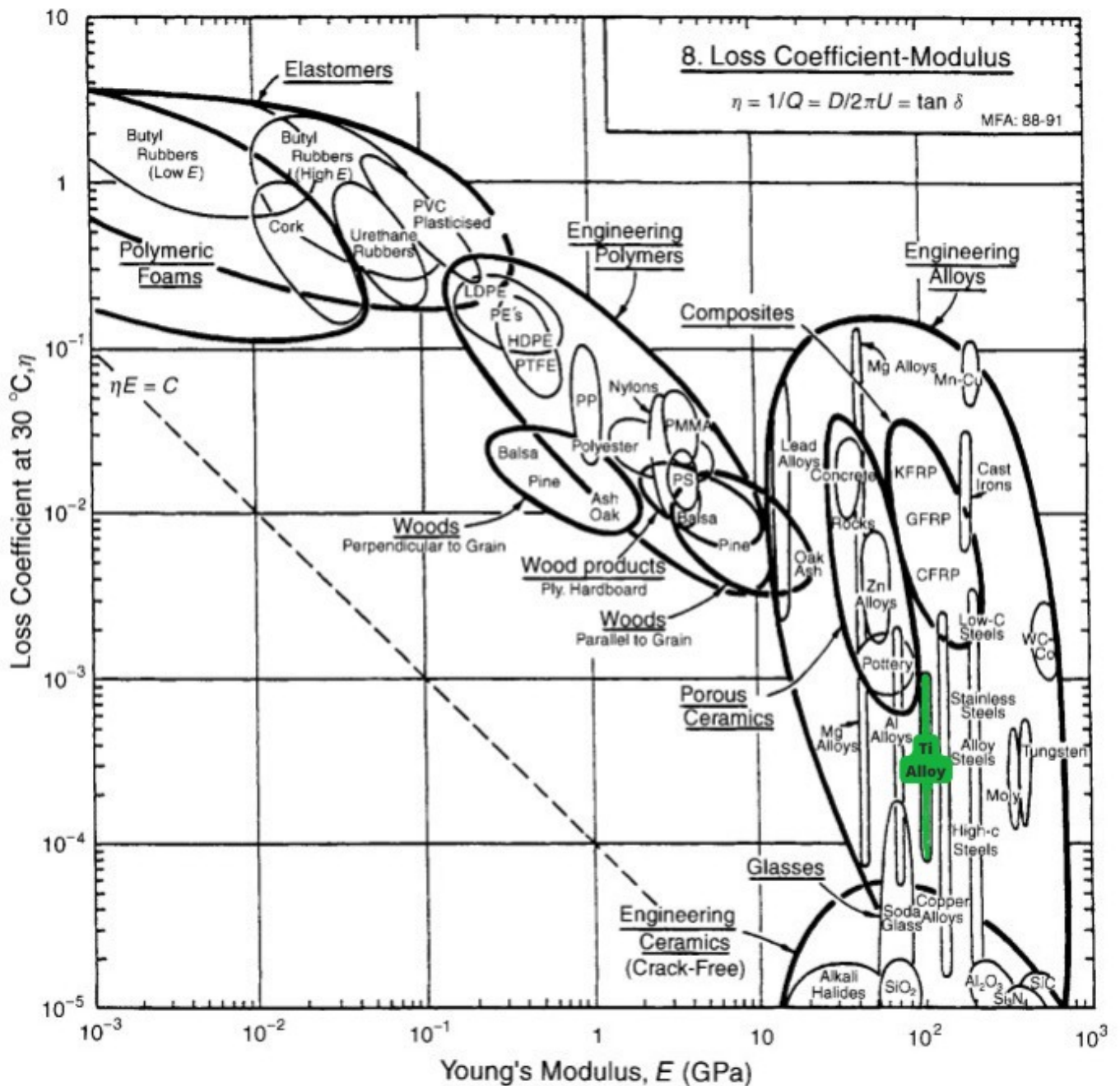


Figure 3.92: Loss coefficient, η , against Young's Modulus, E , chart (Adapted from [51])

In steady state, the ultrasonic fatigue machine must provide the same quantity of mechanical energy that was lost. Using a material with a higher damping, implies a higher loss coefficient, which would result in a greater quantity of mechanical energy being dissipated, which would be largely dissipated as heat, affecting the ultrasonic system and the expected results, leading to an increase in the ultrasonic fatigue machine's energy consumption. The following equation, correlates the average specimen power density dissipated, \dot{q} , with the loss coefficient, η [52]:

$$\dot{q} = \eta E \pi f_0 \varepsilon^2 \quad (3.45)$$

Where E is the Young's modulus, f_0 is the resonance frequency of the specimen and ε is the strain amplitude. As it can be noted, the dissipated power is proportional to the loss coefficient, so, it is desirable to have a low loss coefficient. Another of the primary factors that contributed to the titanium's selection as the manufacturing material for the booster and horn, was its relatively constant Elastic Modulus, E , when compared with the materials that present a lower loss coefficient. Additionally, the Ti-6Al-4V is the most standard solution for the choice of the manufacturing materials of the ultrasonic boosters and horns. Furthermore, the low variation of the modulus of elasticity, E , presented by the Ti-6Al-4V increases the reliability of the design/project. Two Ti-6Al-4V cylinders were purchased from JACQUET Portugal for the production of the two boosters and the two horns. Both cylinders have a length of 300 mm, however, one has a diameter of 60 mm, to manufacture the boosters, and the other a diameter of 40 mm, to manufacture the horns, in order to reduce material loss during machining operation. The mechanical properties of the bought titanium, Ti-6Al-4V, are demonstrated in the Appendix B. A table summarizing the mechanical properties of the Ti-6Al-4V will be presented below.

Table 3.14: Minimum Values of the Mechanical Properties of the Ti-6Al-4V at room temperature [53]

Yield strength, σ_y	825 MPa
Ultimate tensile strength, σ_R	895 MPa
Density, ρ	4430 kg/m ³
Modulus of elasticity, E	114 GPa
Poisson's ratio, ν	0.3

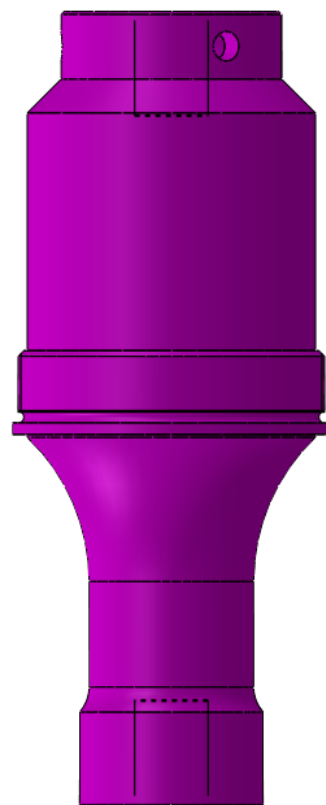
The connection between the piezoelectric transducer, presented in the Figure 3.8, and the booster is ensured through a $\frac{1}{2}$ - 20 stud. Therefore, it was decided that a $\frac{1}{2}$ - 20 stud would also be used to secure the connection between the booster and the horn. Additionally, the $\frac{1}{2}$ - 20 studs will be made from titanium. An existing Ti-6Al-4V plate at INEGI will be used to manufacture them.

In Chapter 2, it was stated that the ultrasonic booster and horn needed to be designed so that their first natural longitudinal frequency corresponds with the excitation frequency of the piezoelectric transducer, 20 kHz in the present project. The chosen booster design can be seen in

the Figure 3.93 (a), and it was provided by MPIInterconsulting [39]. The booster definition drawing is presented in Appendix C. This booster's first longitudinal frequency is set to be near to 20 kHz. In order to confirm what had been stated, an Abaqus modal analysis of the titanium booster with two titanium half studs was conducted, as can be seen in the Figure 3.93 (b). The contact between the booster and the studs was assumed to be a tie constraint and the modal simulation was performed on a free body condition, so, the first vibration modes of the present modal analysis will present rigid body motion and so will be discarded. The utilized titanium mechanical properties are listed in the Table 3.14. For this finite element analysis, it was utilized the tetrahedron element type with quadratic geometric order, C3D10, and the considered mesh density is presented in the following table.

Table 3.15: Number of elements of each component of the Booster Modal Analysis

Component	Number of elements
Booster	68414
Each Stud	10561



(a) Booster 3D design [39]



(b) Section View of the Abaqus Modal Analysis assembly on the Booster

Figure 3.93: 3D Booster design and Abaqus Modal Analysis assembly

The results of the Abaqus modal analysis are presented in the figures bellow. As it can be noticed, the corresponding first natural longitudinal frequency is 19770 Hz, very close to the 20 kHz, as expected. One of the main features of this booster is the existence of a threaded part, which can be seen in more detail in the definition drawing presented in the Appendix C, where it will thread on a flange, vibration absorbing flange and booster support in the present project.

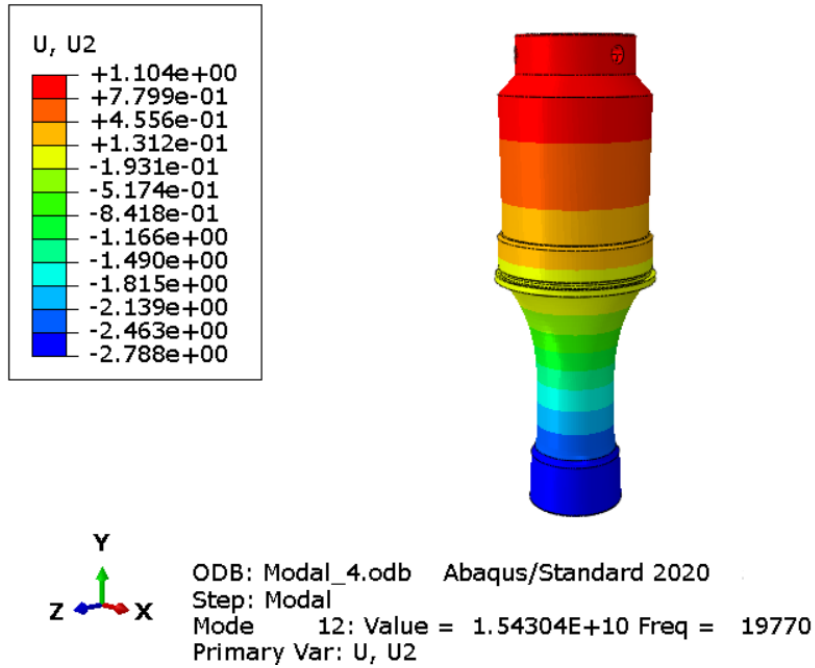


Figure 3.94: Abaqus Modal Analysis on the chosen Booster (m)

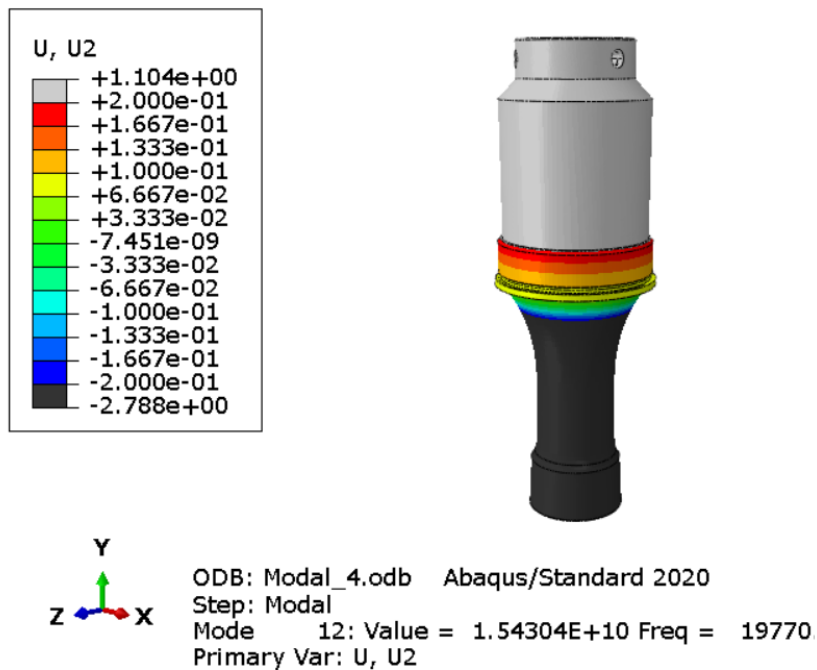


Figure 3.95: Abaqus Modal Analysis on the chosen Booster - Vibration Node (m)

Through the Figure 3.95, it is possible to notice a vertical displacement node on the threaded part of the booster, very important to reduce the transmission of unwanted vibrations to the other components. This booster also has 3 X $\phi 5.1$ blind holes, on the top portion of the booster, that enable a torque application in order to ensure a properly connection between the booster and horn. Additionally, this booster features a vibration amplification equal to $\frac{\text{top diameter}}{\text{bottom diameter}} = \frac{38.1}{31.7} = 1.2$. In order to match the total vibration amplification of the Shimadzu USF-2000 longitudinal ultrasonic testing machine existing at INEGI, 2.46, which results from the multiplication of the booster amplification with the horn amplification, the designed ultrasonic horn must have a vibration amplification of 2.04, it will be considered 2.0. The ultrasonic horn was developed using an iterative method. It is known that the first longitudinal natural frequency of the horn must be equal to the piezoelectric transducer's excitation frequency, 20 kHz. In addition, it must have a vibration factor of amplification of 2.0. In light of what was stated previously and using the Figure 3.96 (a) as a reference, the ϕ_{Top} diameter of the horn was considered to be equal to the bottom diameter of the booster, $\phi_{\text{Top}} = 31.7$ mm, leading to a ϕ_{Bottom} of the horn of 15.85 mm and ensuring the correct factor of amplification. The total length of the horn was split into three sections, L1, L2 and L3, as shown in Figure 3.96 (a). Where L1 is the length of the horn constant section with the higher diameter, L2 is the length of the portion of the horn with variable section and L3 is the length of the horn constant section with the lower diameter. Parameterizing these values simplifies the project/design and may result in fewer iterations.

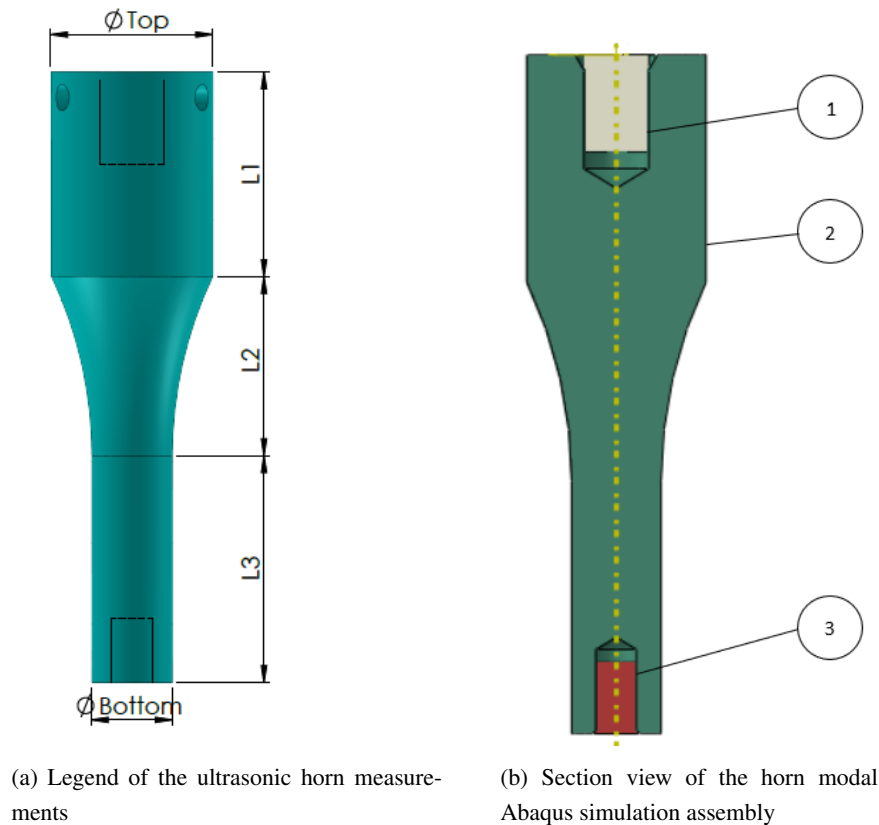


Figure 3.96: Horn measurements and modal analysis

The length L1 was considered to be equal to 40 mm, the length L2 was defined has 35 mm and the length L3 was determined through diverse modal Abaqus simulations in order to achieve the intended first longitudinal natural frequency of the horn. An initial value of L3 was arbitrated and the generated horn was numerically simulated. A section view of the modal Abaqus simulation assembly can be seen in the Figure 3.96 (b). In this simulation, a whole horn (2) with an arbitrated value for L3 was considered, together with a half titanium stud (1), and a steel stud (3), simulating the titanium stud that connects the booster to the horn, and the threaded portion of a steel specimen. The utilized mechanical properties of the titanium for the horn and stud are listed in the Table 3.14, and for the steel it was considered a Density, ρ , of 7800 kg/m³, a Modulus of elasticity, E of 200 GPa and a Poisson's ratio, ν , of 0.3. The contact between the horn and the studs was assumed to be a tie constraint. Furthermore, this finite element simulation was carried out with the utilization of tetrahedron elements with quadratic geometric order, C3D10 elements, and the mesh density is presented in the Table 3.16.

Table 3.16: Number of elements of each component of the Horn Modal Analysis

Component	Number of elements
Titanium Horn	43967
Titanium Stud	10725
Steel Stud	3576

It is know that the stiffness of a bar, k , is given by $\frac{EA}{L}$ and that the frequency is proportional to $\sqrt{\frac{k}{m}}$, so, if the numerically obtained frequency is bellow 20 kHz, that implies that the numerical system is excessively flexible. Thereby, it is necessary to reduce the L3 length in order to improve the stiffness of the horn. Thus, another L3 value, smaller than the previous one, needs to be chosen and another numerical simulation, similar to the one described above in the Figure 3.96 (b), on the new generated horn needs to be computed. Furthermore, after diverse simulations with different L3 length values, the obtained results can be approximated to a linear regression which is capable of estimating the final value of the L3 length, which will lead to the expected frequency.

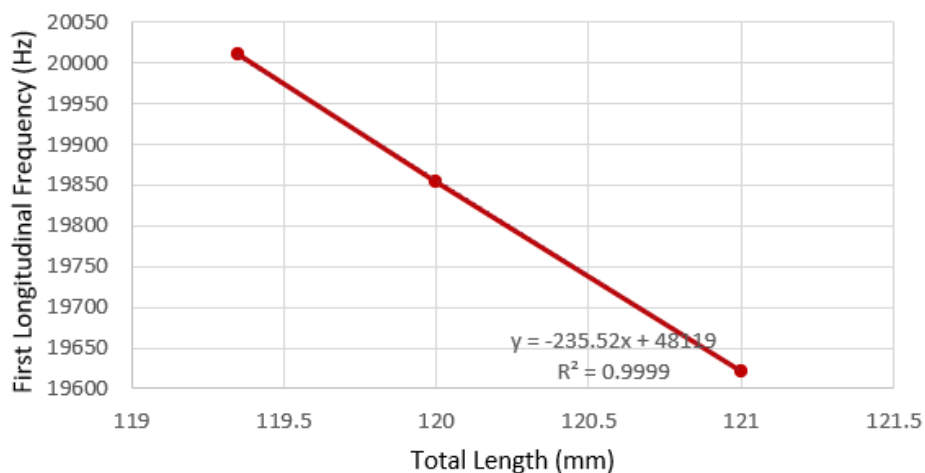


Figure 3.97: Results of the different Abaqus modal simulations regarding the Horn

The results of the various simulations, linear regression, are depicted in the Figure 3.97, which compares the total length of the horn to its first longitudinal natural frequency. Furthermore, a frequency of 20010 Hz was considered, the additional 10 Hz were included to allow for post-manufacturing adjustments, and a L3 length of 44.35 mm was obtained. Subsequently, the simulation of Figure 3.96 (b) was repeated, with the previously defined L3 length.

The results of the final modal analysis are presented in the Figure 3.98 and it can be verified that the first longitudinal natural frequency of the horn is 20010 Hz, as intended. Next, a stress analysis of the horn will be performed and presented. In this analysis, the situation were the ultrasonic fatigue testing equipment is performing tests with the maximum static load applied to the specimen will be simulated, and so, the horn will be under a dynamic load and additionally under a static load of 10 kN.

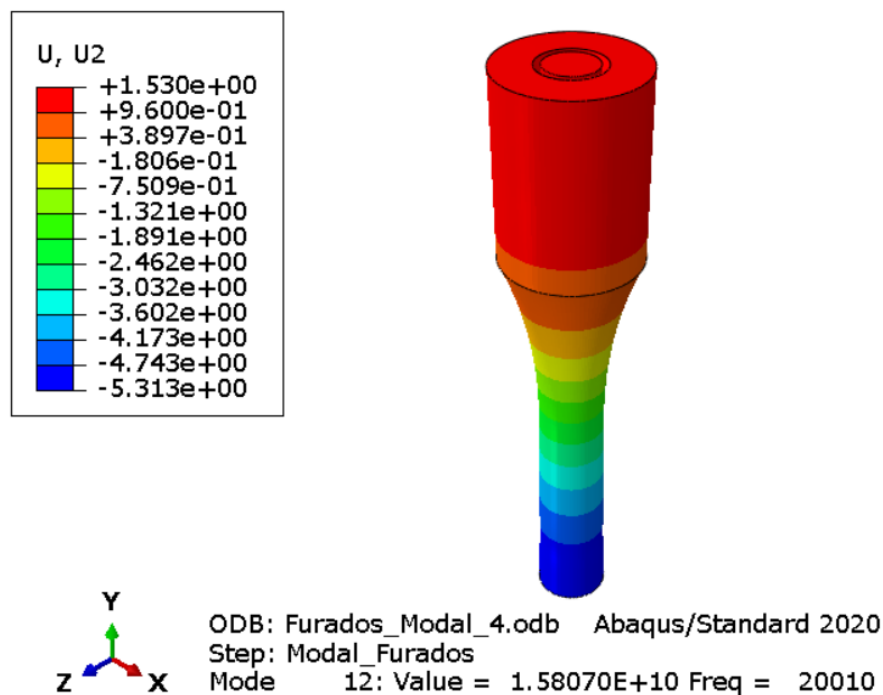


Figure 3.98: Results of the final Abaqus modal simulation regarding the Horn

First, a static simulation on Abaqus was carried out. For this static simulation, only the titanium horn was considered and only tetrahedron elements with quadratic geometric order, C3D10 elements, were utilized. In total, it was generated 50181 finite elements. The considered titanium for the simulation has the mechanical properties listed in the Table 3.14. The horn was considered to be fixed on the top end and subjected to a static 10 kN load on the other end, as can be seen in the Figure 3.99. The results of this static analysis are presented in the Figure 3.100. The maximum Von Mises stress, σ_{static} , can be identified has being 51.99 MPa. Following the completion of the static analysis, a dynamic analysis was carried out and it is going to be presented next.

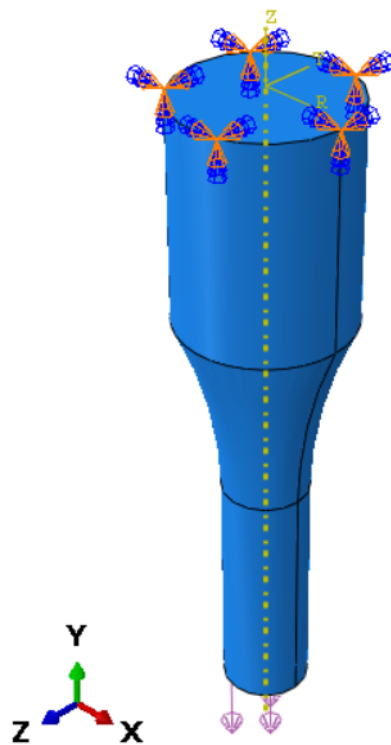


Figure 3.99: Load and boundary condition of the static Abaqus simulation regarding the Horn

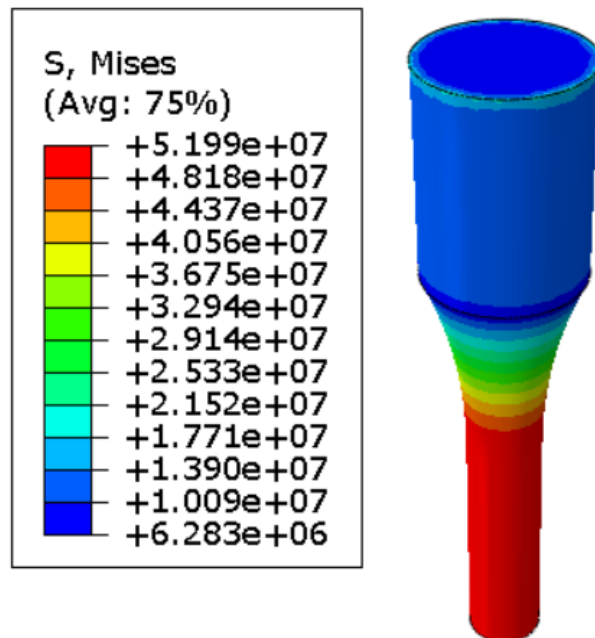


Figure 3.100: Results of the static Abaqus simulation regarding the Horn (Pa)

A modal analysis in Abaqus was used to accomplish the dynamic analysis. Only the titanium ultrasonic horn was taken into account, with no applied loads or boundary conditions. The primary purpose of this analysis is to determine the stress distribution in the ultrasonic horn when it is merely subject to its own inertia, on its first natural longitudinal mode. The horn model taken into account was the same as the one used to perform the static analysis presented before, Figures 3.99 and 3.100, thus, the number of finite elements and the mechanical properties of the titanium are the same as previously. In the Figures 3.101 and 3.102 are presented the results of the modal analysis described above.

It is possible to conclude from the Figure 3.101, that the maximum dynamic stress amplitude, $\sigma_{dynamic}$, occurring in the ultrasonic horn is $14.45 \cdot 10^{12}$ Pa. This maximum stress value amplitude, on the other hand, has to have a correction made to it due to the maximum vertical displacement that can be identified in the Figure 3.102, $|5.334|$ m. The maximum vertical displacement, most extreme scenario in which the higher dynamic stresses are originated, for the new designed ultrasonic horn is set to be $60 \mu\text{m}$, as it was the value measured in the Shimadzu longitudinal ultrasonic testing machine existing at INEGI, Shimadzu USF-2000. So, the following proportional factor is going to be applied to the $\sigma_{dynamic}$:

$$\text{Proportional Factor} = \frac{\text{FEM Vertical Displacement}}{\text{Desired Vertical Displacement}} = \frac{5.334}{6 \cdot 10^{-5}} = 88900 \quad (3.46)$$

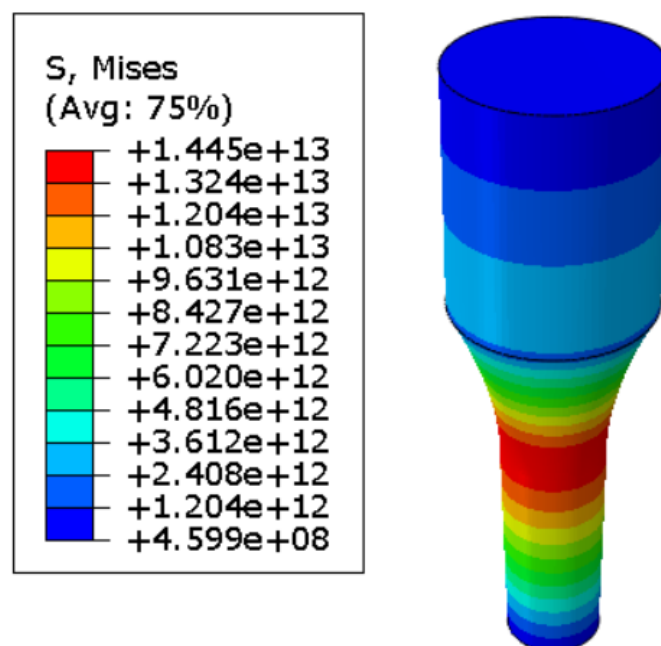


Figure 3.101: Results of the dynamic Abaqus simulation regarding the Horn (Pa)

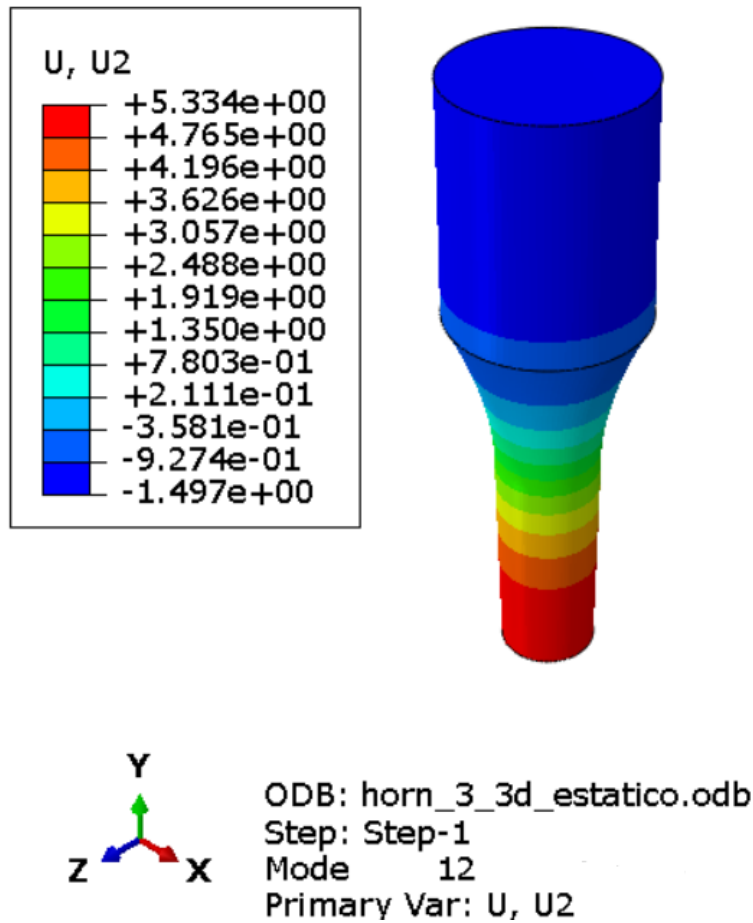


Figure 3.102: Results of the dynamic Abaqus simulation regarding the Horn (m)

Through the application of the *Proportional Factor* on the $\sigma_{dynamic}$ it is possible to obtain the corrected dynamic stress amplitude, $\sigma_{dynamicc}$:

$$\sigma_{dynamicc} = \frac{\sigma_{dynamic}}{Proportional\ Factor} = 162542182.2\ Pa \quad (3.47)$$

$$\Leftrightarrow \sigma_{dynamicc} = 162.54\ MPa \quad (3.48)$$

Finally, it is feasible to calculate the maximum and minimum stresses estimated in the ultrasonic horn by taking into account the static and dynamic stresses previously determined. Since the entire system is linear elastic, the loads can be added or subtracted using the principle of superposition. In the most extreme case, the component is subjected to both a dynamic load and a static load.

$$\sigma_{MAX} = \sigma_{static} + \sigma_{dynamicc} = 214.53\ MPa \quad (3.49)$$

$$\sigma_{MIN} = \sigma_{static} - \sigma_{dynamic_c} = -110.55 \text{ MPa} \quad (3.50)$$

Following the determination of the σ_{MAX} and σ_{MIN} , the Soderberg criteria will be utilized in order to obtain a safety factor and to complete the ultrasonic horn analysis. The main equation of the Soderberg criteria that will lead to the definition of a safety factor is presented next [54].

$$\frac{K_f \cdot \sigma_a}{\sigma_{f0}^c} + \frac{\sigma_m}{\sigma_y} = \frac{1}{SF} \quad (3.51)$$

Where K_f is the practical stress concentration factor, σ_{f0}^c is the practical endurance limit, σ_m is the average stress, σ_a is the stress amplitude, σ_y is the yield strength and SF is the safety factor. Starting by defining the σ_{f0}^c [8]:

$$\sigma_{f0}^c = C_1 \cdot C_2 \cdot C_3 \cdot C_4 \cdot \sigma_{f0} \quad (3.52)$$

The endurance limit, σ_{f0} , stress to cause failure of a material at a fully reversed stress solicitation in 10^7 cycles, takes the value of 430 MPa as it can be seen in the Appendix B. The constants C_1 , C_2 , C_3 and C_4 are the Marin factors and their value will be defined next. Starting by the load modification factor, C_1 , it will take the value of 0.85 due to the horn being only subject to axial loading. The various possible values for the load modification factor, C_1 , are depicted in the scheme below [8].

$$C_1 = \begin{cases} \text{Bending} - 1 \\ \text{Axial} - 0.85 \\ \text{Torsion} - 0.59 \end{cases}$$

The Marin factor C_2 is the size modification factor and for axial loading there is no size effect, so $C_2 = 1$. The surface condition modification factor is represented by C_3 and its value is defined by the following equation [8].

$$C_3 = a \cdot \sigma_R^b \quad (3.53)$$

Where the factor a and exponent b depend on the surface finish of the horn and take the values presented in the Table 3.17.

Table 3.17: Surface Condition Modification Factor [8]

Surface Finish	Factor a	Exponent b
Ground	1.58	-0.085
Machined	4.51	-0.265
Hot-rolled	57.7	-0.718
As-forged	272	-0.995

Assuming a machined surface finish and utilizing the titanium mechanical properties presented in the Table 3.14, it is possible to obtain the following surface condition modification factor, C_3 , analytical value.

$$C_3 = 4.51 \cdot 895^{-0.265} = 0.744 \quad (3.54)$$

The C_4 Marin factor is related to other factors such like reliability factor and miscellaneous-effects modification factor. Nonetheless, it will be considered $C_4 = 1$ because there isn't any factor that needs to be considered for the present project. Finally, it is possible to obtain [54]:

$$\sigma_{f0}^c = 0.85 \cdot 1 \cdot 0.744 \cdot 1 \cdot 430 = 272.164 \text{ MPa} \quad (3.55)$$

Now, the practical stress concentration factor, K_f , is going to be calculated through the following equation [8].

$$K_f = 1 + q \cdot (K_t - 1) \quad (3.56)$$

Where q is the notch sensitivity factor and K_t the stress concentration factor. In order to get more conservative estimates, the notch sensitivity factor, q , will be considered to be equal to 1. The stress concentration factor, K_t , is going to be determined through the following equations [55].

$$K_t = B_1 + B_2 \left(\frac{2t}{D} \right) + B_3 \left(\frac{2t}{D} \right)^2 + B_4 \left(\frac{2t}{D} \right)^3 \quad (3.57)$$

$$B_1 = 0.926 + 1.157\sqrt{\frac{t}{r}} - 0.099\frac{t}{r} \quad (3.58)$$

$$B_2 = 0.012 - 3.036\sqrt{\frac{t}{r}} + 0.961\frac{t}{r} \quad (3.59)$$

$$B_3 = -0.302 + 3.977\sqrt{\frac{t}{r}} - 1.744\frac{t}{r} \quad (3.60)$$

$$B_4 = 0.365 - 2.098\sqrt{\frac{t}{r}} + 0.878\frac{t}{r} \quad (3.61)$$

The necessary dimensions of the ultrasonic horn, D , r and t , are identified in the figure bellow and presented in the Table 3.18.

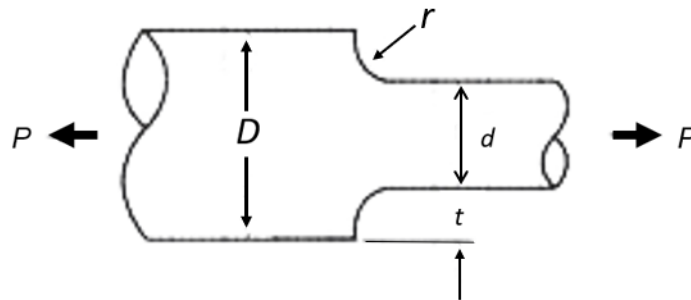


Figure 3.103: Identification of the dimensions for the K_t calculation (Adapted from [55])

Table 3.18: Ultrasonic Horn Dimensions

Identification	Dimension
D	31.7 mm
r	81.25 mm
t	7.925 mm

Through the substitution of the values presented in the Table above in the Equations 3.57, 3.58, 3.59, 3.60 and 3.61 the following K_t value is obtained.

$$K_t = 1.025 \quad (3.62)$$

Finally, returning to the equation 3.56 and considering all the information presented above, it is possible to obtain:

$$K_f = 1.025 \quad (3.63)$$

Now, the average stress, σ_m , and the stress amplitude, σ_a , will be calculated based on the results given in the equations 3.49 and 3.50.

$$\sigma_m = \frac{\sigma_{MAX} + \sigma_{MIN}}{2} = 51.99 \text{ MPa} \quad (3.64)$$

And

$$\sigma_a = \frac{\sigma_{MAX} - \sigma_{MIN}}{2} = 162.54 \text{ MPa} \quad (3.65)$$

Finally, by returning to the equation 3.51 and taking the outcomes of equations 3.55, 3.63, 3.64 and 3.65 into consideration, it is possible to acquire a safety factor, SF , of 1.48, which ensures the necessary safety for its efficient performance. In practice, the calculated safety factor is lower than the one presented because the σ_{f0} was calculated for 10^7 cycles and the horn will be subjected to a much higher number of cycles. Nonetheless, in a normal testing scenario, static loads greater than 3 or 4 kN will hardly be applied. It was chosen to connect the specimens to the horn via a M8X0.75 threaded connection. Assuming an analogy with a bolt and by knowing the utilized titanium properties, presented in the Table 3.14, it is possible to acquire through the tables presented in the Appendix D that an M8X1.0 bolt with an 8.8 grade, the most similar to the titanium, presents a maximum permissible preload of 19.6 kN, which is higher than the maximum static load considered for the developed testing equipment. A M8X0.75 thread presents a higher resistant section than an M8X1.0, so, the considered threaded connection is conservative. And so, the horn design is validated. The final definition drawing of the ultrasonic horn can be seen in the Appendix C.

3.5 Stiffness evaluation of the fatigue equipment

The main objective of the present section is the calculation of the ratio between the angle of rotation of the power screw and the force generated. To that end, a stiffness evaluation of the ultrasonic fatigue testing equipment will be presented and discussed. First, the vertical displacements of the different components and subassemblies that constitute the fatigue equipment are going to be calculated and listed. Furthermore, the stiffness of the equipment is going to be calculated through a parallel/series spring analogy and later on the present section, the ratio between the angle of rotation of the power screw and the force generated will be discussed.

The rotation of the power screw that subjects the ultrasonic fatigue testing equipment to the total vertical displacement that occurs when the ultrasonic equipment is performing tests with the maximum static load applied to the specimen can be calculated by the following equation.

$$\text{Rotation } (^{\circ}) = \frac{\text{Total Displacement} \cdot 360}{\text{Power Screw Pitch}} \quad (3.66)$$

The *Total Displacement* regards the total vertical displacements of the different ultrasonic machine components through the assumption of an equivalent system of springs of the different components that constitute the ultrasonic fatigue testing equipment. The generated force by 1° of rotation of the power screw can be calculated through the following formula:

$$\text{Generated Force (N)} = \frac{1^{\circ} \cdot \text{Maximum Load}}{\text{Rotation for the Maximum Displacement}} \quad (3.67)$$

So, it is essential to calculate the vertical displacement of the different components and subassemblies that constitute the fatigue equipment in the most extreme scenario, when the equipment is testing specimens with a 10 kN static load applied. In order that, the equivalent spring system presented in the Figure 3.104 was considered. Section 1 regards the vibration absorbing flange and the upper cast iron block, whose numerical analysis is presented in the Figure 3.37. Furthermore, Section 2 is related to the support plate, to the booster support, to the locking supports and rubber rings, which were numerically analyzed in the Figure 3.51. Additionally, Section 3 is related with the bearing, bearing cases, bearing holder and the traction plate, whose numerical analysis is presented in the Figure 3.78. The resonant system regards the the two ultrasonic boosters, the two horns and the specimen and will be numerically analyzed within the present section, Figure 3.107.

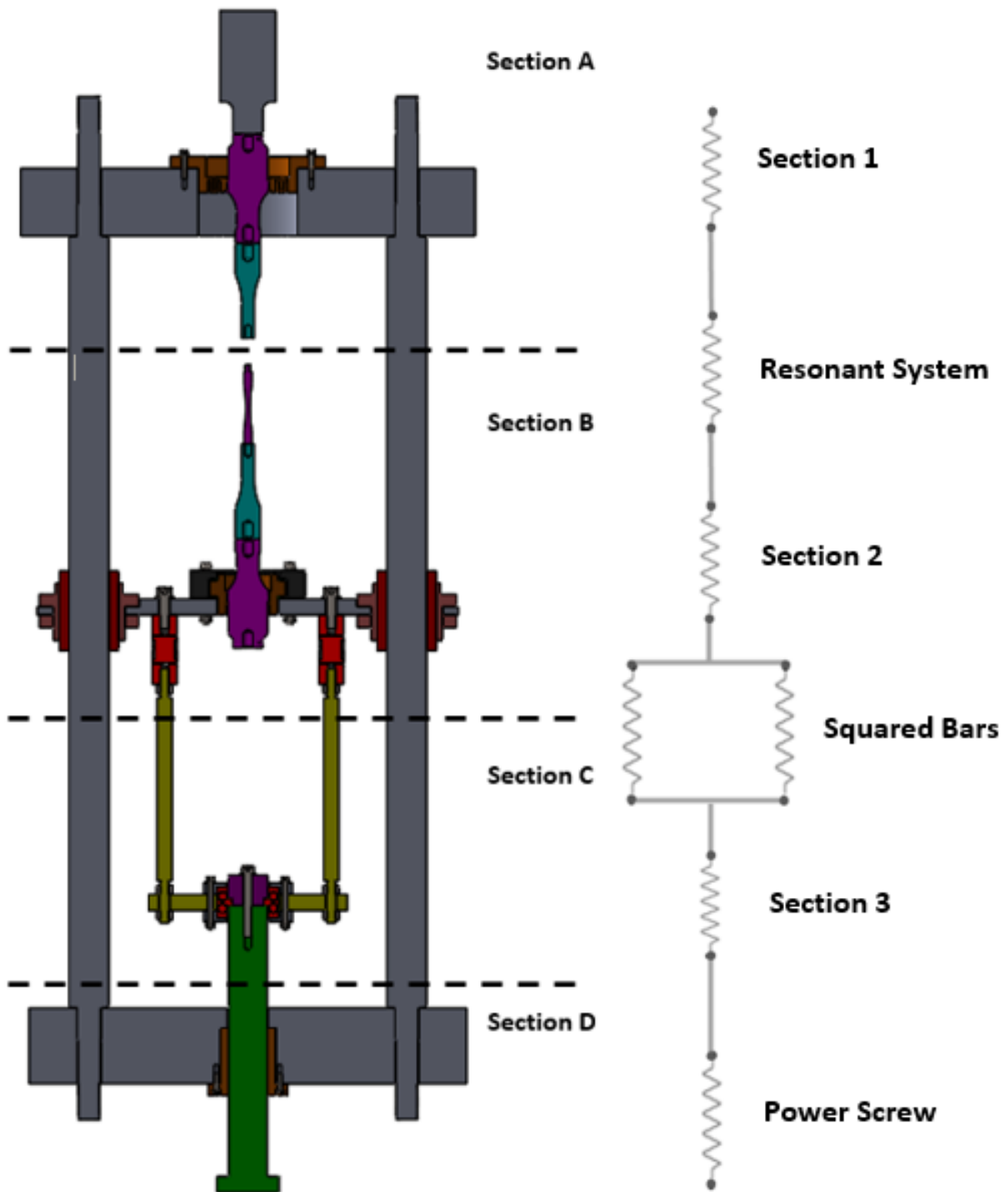


Figure 3.104: Equivalent spring system of the ultrasonic fatigue equipment

First, the vertical displacement of the original power screw, when its originating a static load of 10 kN, is going to be calculated and presented. The power screw will be only analyzed analytically hence it is already a physical component which came from the original structure. The following equations allows for the calculation of the vertical displacement of the power screw.

$$\Delta L = L \cdot \varepsilon \quad (3.68)$$

Where ΔL is the vertical displacement, L the considered length of the power screw and ε the strain. Additionally:

$$\sigma = \frac{F}{A} = E \cdot \varepsilon \quad (3.69)$$

$$\Leftrightarrow \varepsilon = \frac{F}{A \cdot E} \quad (3.70)$$

With F being the 10 kN, A the cross sectional area of the power screw and E the Young's modulus of the power screw. Through the combination of the Equations 3.68 and 3.70, it is possible to achieve:

$$\Delta L = L \cdot \frac{F}{A \cdot E} \quad (3.71)$$

Thus, by assuming that the length of interest of the power screw is 210 mm, a diameter of 50 mm and a Young's modulus of 200 GPa it is possible to obtain that :

$$\Delta L = 0.0054 \text{ mm} \quad (3.72)$$

Now, the vertical displacement of the squared section bars, that connect the Section B with Section C of the fatigue equipment as it can be seen in the Figures 3.19 and 3.20, are going to be computed through a finite element analysis on the Abaqus software. As this is a newly designed CAD component, a numerical analysis will be performed. In this analysis, only the squared section part of the bar was considered and 2772 hexahedral elements with reduced integration were generated. As it can be seen in the Figure 3.105 (a), the top of the squared section bar was considered to be fixed and the bottom was subjected to a distributed load of 5000 N. When the ultrasonic fatigue testing equipment is performing tests with the maximum static load applied to the specimen, each of the squared section bars is submitted to a traction of 5000 N, due to being in parallel.

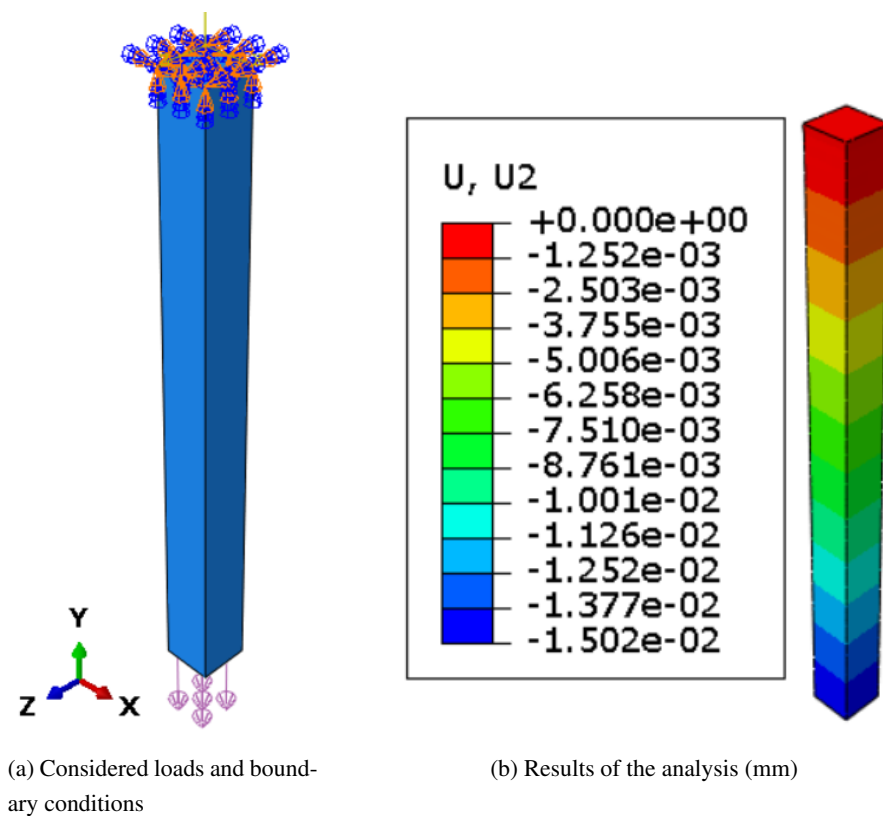


Figure 3.105: Finite element analysis on the Squared Section Bar

The maximum vertical displacement of the squared section bar can be seen in the Figure 3.105 (b), and, it is going to be considered as 0.015 mm for the calculation of the fatigue equipment stiffness. Next, the vertical displacement regarding the resonant system of the equipment is going to be calculated through the Abaqus software. The resonant system of the fatigue equipment being developed in the present document compiles the two ultrasonic boosters, the two horns and the specimen, for this analysis a regular steel specimen was considered. It was chosen a specimen with a large test section, i.e. a specimen with a high stiffness. The utilized ultrasonic booster and horn are illustrated in the previous subsection, 3.4.4. And the considered specimen is presented in the Figure 3.106. In order to simplify the finite element analysis, the symmetry of the resonant system will be taken advantage off and only a quarter of the complete resonant system will be analyzed. So, different symmetry conditions were employed to the mathematical model and for the interest of straightforwardness, they will not be demonstrated.

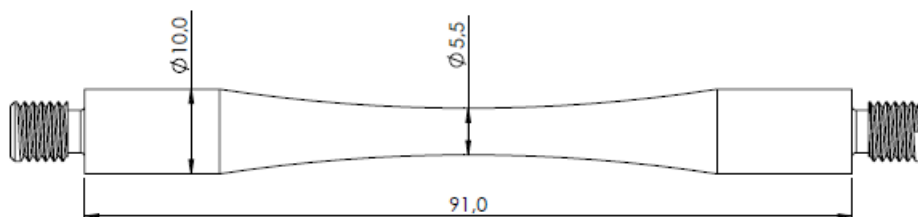


Figure 3.106: Specimen drawing

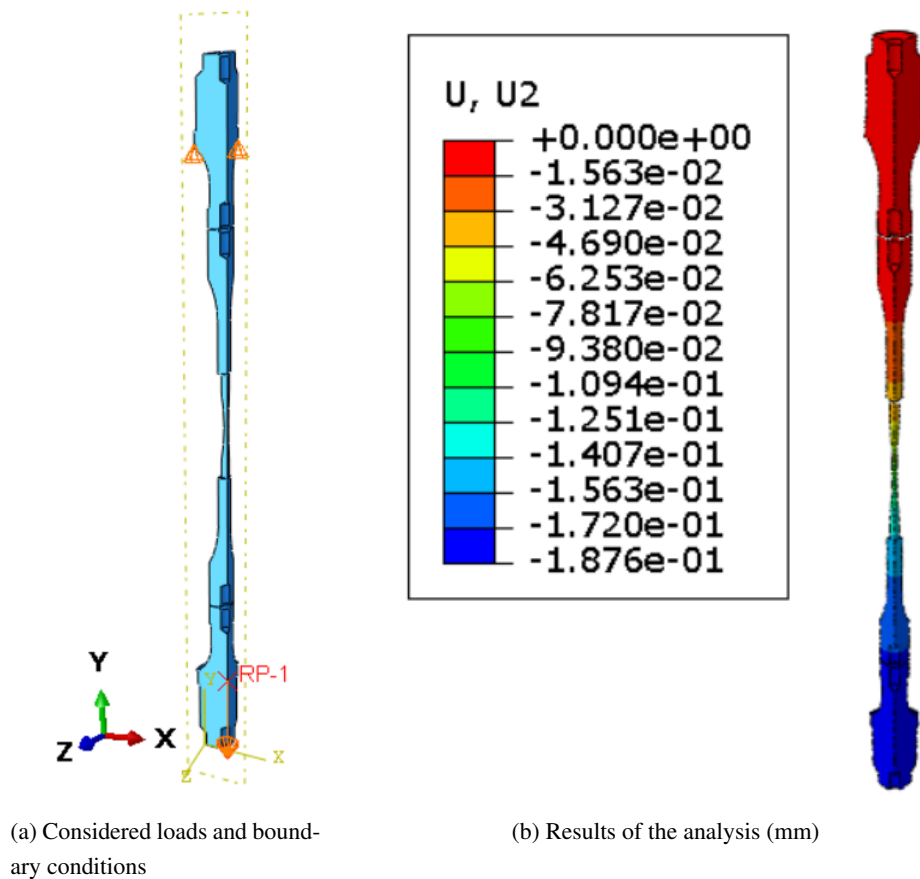


Figure 3.107: Finite element analysis on the Resonant System

In the Figure 3.107 (a), it is presented the loads and boundary conditions considered for this Abaqus analysis. The vertical displacement on the threaded portion of the upper booster was considered to be null and a force of -2500 N was coupled to the reference point, RP-1. This reference point is attached to the middle of the lower booster. The force of -2500 N represents the situation in which the ultrasonic fatigue testing equipment is performing tests at its maximum static load. Furthermore, in this analyses where utilized two different types of finite elements. The tetrahedron element type with quadratic geometric order was utilized to mesh the boosters and horns. The hexahedron element type with reduced integration was utilized in the specimen. The mesh density is displayed in the following table.

Table 3.19: Number of elements of each component of the Resonant Static Analysis

Component	Number of elements
Each Booster	47417
Each Horn	13416
Specimen	2116

The results of the finite element analysis described above, are presented in the Figure 3.107 (b), with the maximum vertical displacement of the resonant system being 0.188 mm. Finally, it is possible to calculate the total vertical displacement of the ultrasonic fatigue equipment by considering the equivalent system of springs, presented in the Figure 3.104. It will be taken into account the vertical displacement of the middle portion of each of the different sections of the fatigue testing equipment, that were considered for the equivalent spring system, in order to achieve the same relative position in the different subassemblies. For the Section 1, it will be considered the vertical displacement on the middle part of the vibration absorbing flange, 0.053 mm as it can be noted in the Figure 3.42, for the Section 2, the considered displacement will be that off the central section of the booster support, 0.066 mm as can be noted in the Figure 3.62, and for the Section 3, it will be considered the vertical displacement occurring in the middle portion of the simplified solid bearing, noted in the Figure 3.86 as 0.015 mm. The table below lists the different vertical displacements of the various parts of the ultrasonic fatigue testing equipment.

Table 3.20: Vertical displacement of the different parts of the fatigue equipment

Part	Vertical displacement (mm)
Section 1	0.053
Section 2	0.066
Section 3	0.015
Power Screw	0.005
Squared Section Bar	0.015
Resonant System	0.188
Total	0.342 mm

As it can be noticed from the Table 3.20, the total vertical displacement of the ultrasonic fatigue testing equipment is 0.342 mm. The most flexible section is the resonant system with a vertical displacement of 0.188 mm. A further analysis on the finite element analysis presented in the Figure 3.107 (a) and (b), indicates that the maximum vertical displacement of the specimen was 0.108 mm. This result signifies that the specimen, presented in the Figure 3.106, is the most flexible component of the ultrasonic fatigue testing equipment. Furthermore, this flexibility can be rearranged by changing the material and geometry of the specimen. Next, the stiffness of the fatigue equipment will be calculated through the following equation:

$$F = k \cdot d \quad (3.73)$$

Where F is the applied load, k is the stiffness and d the vertical displacement. By assuming an applied load of 10 kN and the total vertical displacement depicted in the Table 3.20, it is possible to obtain the stiffness of the equipment:

$$k = \frac{F}{d} = \frac{10000}{0.342} = 29205608 \text{ N m}^{-1} \quad (3.74)$$

$$\Leftrightarrow k = 29205.608 \text{ N mm}^{-1} \quad (3.75)$$

The result reported above indicates the predicted stiffness of the ultrasonic fatigue testing equipment. This result is highly influenced by the vertical displacement of the resonant system, as it can be noted from the Table 3.20, being the specimen the component that has the most influence on the stiffness of the ultrasonic fatigue testing equipment. Now, the ratio between the angle of rotation of the power screw and the generated force can be calculated. The utilized power screw, identified in the Figure 3.2 (a), has a pitch of 3 mm. And so, for a full 360° rotation it is assumed to originate a vertical displacement of 3 mm. Additionally, the necessary rotation of the power screw that originates the total vertical displacement depicted in the Table 3.20 can be calculated through the equation 3.66, which leads to the following result:

$$\textit{Rotation} (^{\circ}) = 41.088^{\circ} \quad (3.76)$$

Finally, the generated force by 1° of rotation of the power screw is going to be calculated through equation 3.67:

$$\textit{Generated Force} = \frac{1 \cdot 10000}{41.088} = 243.380 \text{ N} \quad (3.77)$$

The result presented in the equation 3.77 implies that for each degree of rotation of the original power screw, an additional force of 243.380 N is originated. This outcome is positive and it means that the "operator" will have good control and will be able to apply the desired force accurately. Finally, it is possible to conclude that the use of the original power screw will be advantageous.

3.6 Assembly procedure to execute a VHCF test in the developed equipment

In the present section, the required assembly steps necessary for testing specimens on the developed fatigue testing equipment will be detailed. In the subsection 3.6.1, it will be explained the mounting procedure of the specimen in order to carry out fully reversed longitudinal ultrasonic fatigue tests. Furthermore, in the subsection 3.6.2 it will be presented the steps regarding the realization of ultrasonic fatigue tests with a static load applied to the specimen. All the considered tightenings are according to the recommended torques.

3.6.1 Testing specimens at a $R=-1$ constant stress ratio

In order to realize fully reversed ultrasonic fatigue tests, $R=-1$, in the fatigue equipment developed in the present document, it is only necessary to use the Section A components, Figures 3.6 and 3.7, hence the specimen should be threaded to the upper horn with the appropriate torque through the use of the INEGI's pre-existing tightening tool, which consists of a torque wrench with an adaptor which enables the specimen's tightening. The specimens utilized to realize fully reversed ultrasonic fatigue tests only present one threaded end, and so, the final assembly should be similar to the one presented in the figure bellow.

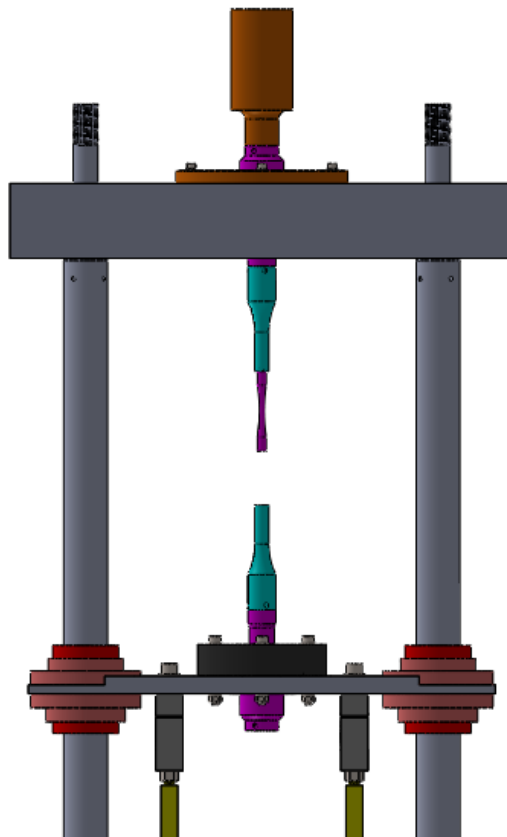


Figure 3.108: Assembly to realize fully reversed ultrasonic fatigue tests

3.6.2 Testing specimens at a $R > -1$ stress ratio

In order to conduct ultrasonic fatigue tests at a stress ratio $R > -1$ in the developed equipment, it is necessary to apply an external static load to the specimen. This static load will be applied through the use of the power screw and the second pair of booster and horn will be utilized. So, a different assembly procedure, than the one explained for the fully reversed ultrasonic fatigue tests, will be detailed. The pre-existing tightening tool used for the $R = -1$ case can't be used in this assembly procedure, because it requires that the specimen has one free end, which will not be verified further in the steps of the Figure 3.110 (a) and (b). Hence, a new adaptor needs to be designed.

The initial step is preliminary, because it only needs to be performed once. It consists to attach together the second pair of ultrasonic booster and horn, with the use of a $\frac{1}{2}$ -20 stud. Afterwards, the second booster needs to be threaded to the booster support, which can be identified in the Figures 3.11 and 3.12, creating the subassembly depicted in the Figure 3.109 (a). There's no need to disassemble this subassembly after the specimen is tested. The next step is to thread the specimen to the subassembly, shown in Figure 3.109 (a), with the use of a new tightening tool to apply the specified torque. The specimen utilized for the fatigue tests at a stress ratio $R > -1$ have two threaded ends, as it can be seen in the Figure 3.106. The result is depicted in the Figure 3.109 (b)

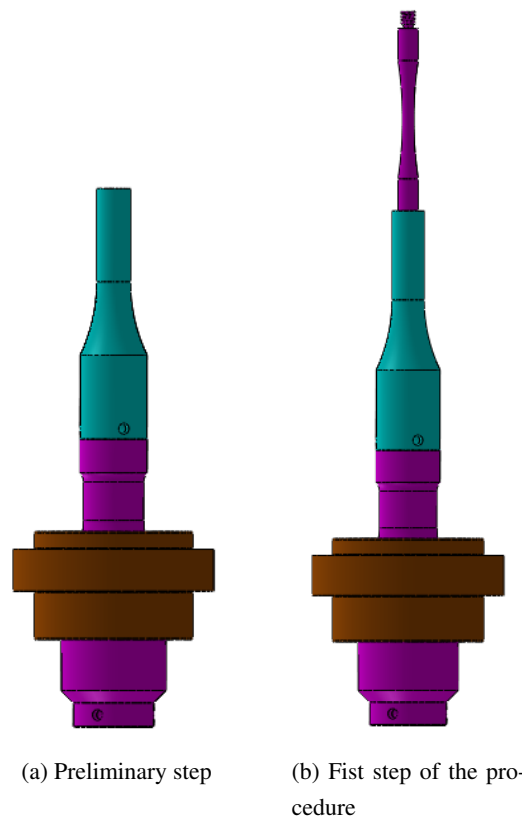


Figure 3.109: First part of the assembly procedure to conduct ultrasonic fatigue tests at a stress ratio $R > -1$

Now, it is convenient to place both of the rubber rings on its correct installation sites. As it can be seen in the Figure 3.12, the upper rubber ring is installed on the second level of the booster support and the lower rubber ring is installed around the central hole of the support plate. The next step is to thread all of the subassembly depicted in the Figure 3.109 (b), with the rubber ring installed, to the upper horn, as can be seen in the Figure 3.110 (a). For this step, it is convenient to have the support plate lowered in order to have more free vertical space. The new tightening tool needs to be used for the correct application of the defined torque. Furthermore, the utilization of the power screw is required to move vertically the support plate in order for the booster support to sit on top of the lower rubber ring, as illustrated in the Figure 3.110 (b).

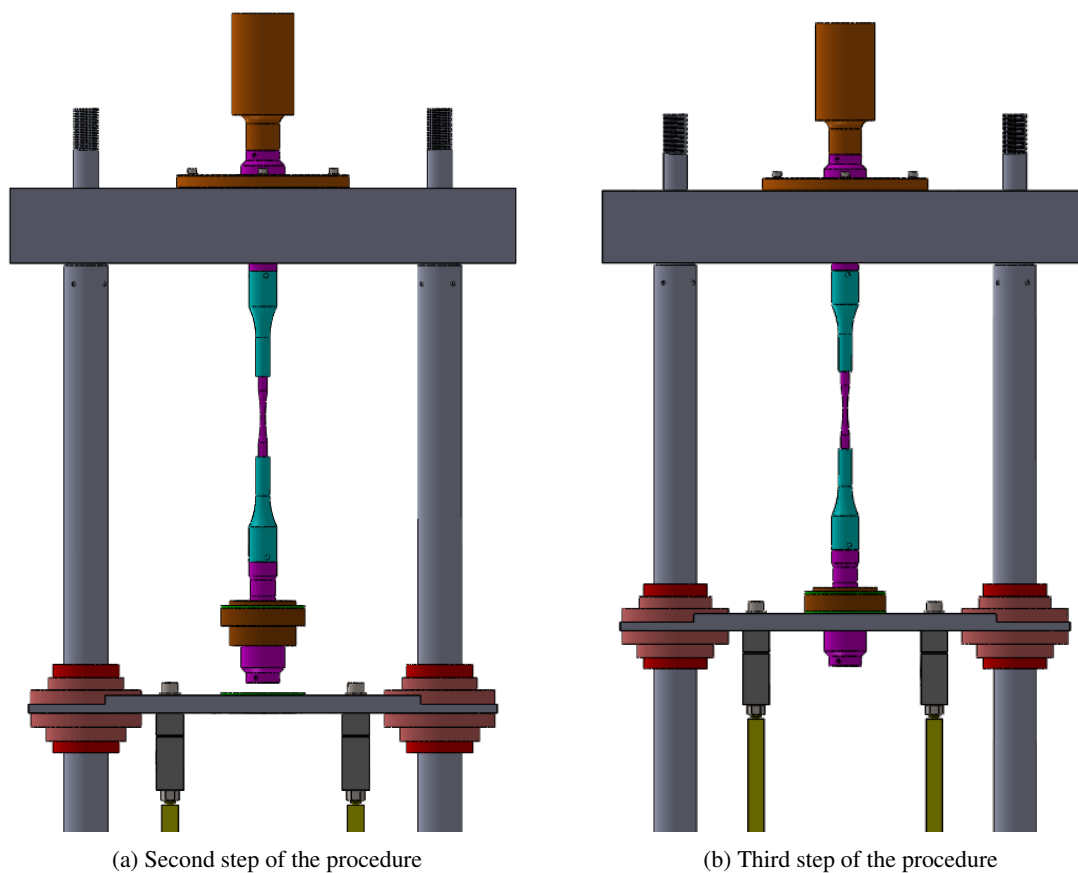


Figure 3.110: Second part of the assembly procedure to conduct ultrasonic fatigue tests at a stress ratio $R > -1$

Now, the two locking supports, identified in the Figure 3.12, can be installed around the booster support. Finally, all the fixing hardware, bolts, nuts and washers, selected for this connection can be installed properly. The bolts tightening torque is defined in the Appendix D and there is a tightening sequence for the six screws. In the Figure 3.111 it is presented the complete dynamic assembly of the ultrasonic fatigue testing equipment which conducts ultrasonic fatigue tests at a stress ratio $R > -1$. The defined external static load is applied through the rotation of the power screw and the incorporation of the load cells allows to ensure that the applied load is symmetric

and the defined one. The original power screw has a mechanism that allows it to lock in position after applying the desired load.

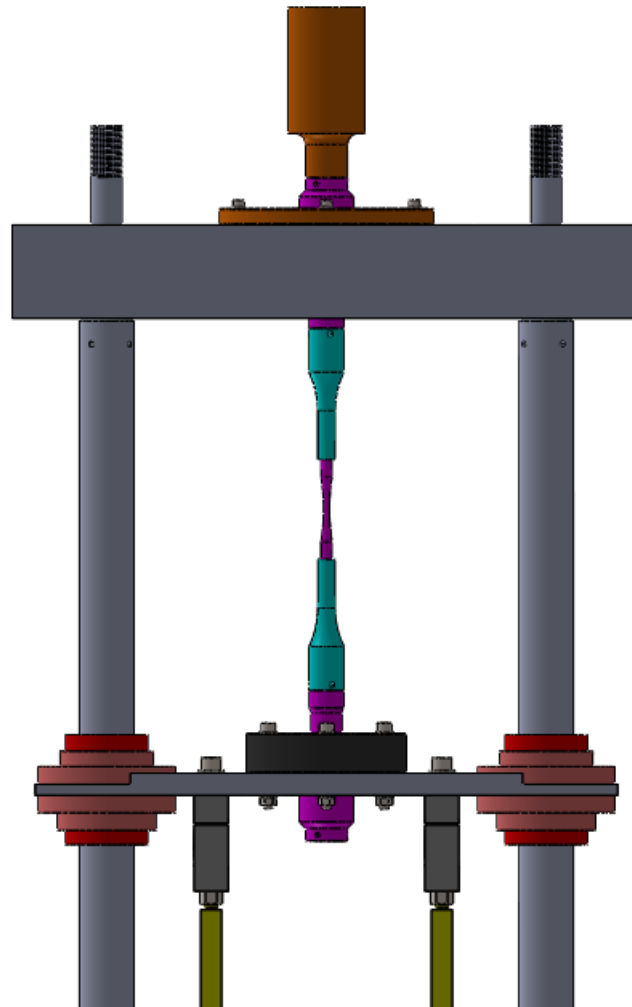


Figure 3.111: Last part of the assembly procedure to conduct ultrasonic fatigue tests at a stress ratio $R > -1$

3.7 Bill of Materials

In this section, three different tables regarding a complete bill of materials regarding the mechanical components of the project developed in this document are going to be presented. In the Table 3.21 is presented a list with the components that were utilized from the original structure, additionally, in the Table 3.22 it is exposed the designed components and their manufacturing material, finally, in the Table 3.23 it is presented the different fixing hardware necessary for the different fastened connections of the present project. In addition to all the mechanical components listed below, there's also the electrical components of the ultrasonic fatigue testing equipment, which includes the piezoelectric transducer, data acquisition system, strain gauges, sensors to measure displacement (or velocities) during tests, pyrometers, wave generator and computer.

Table 3.21: Utilized Components from the Original Structure

Component	Quantity
Chrome Steel Guide Shaft	2
Linear Ball Bearing	2
Linear Ball Bearing Fixing Hardware	2
Lower Cast Iron Block	1
M50 X 3.0 Power Screw	1
Power Screw Flange	1
Upper Cast Iron Block	1

Table 3.22: Designed and Chosen Components

Component	Material	Quantity
Bearing Case	AISI P20 Steel	2
Bearing Holder	AISI P20 Steel	1
Booster Support	AISI P20 Steel	1
Locking Support	AISI P20 Steel	1
Lower Rubber Ring	Rubber	1
Squared Section Bars	S690 Steel	2
Support Plate	S690 Steel	1
Traction Plate	S690 Steel	1
Ultrasonic Booster	Ti-6Al-4V	2
Ultrasonic Horn	Ti-6Al-4V	2
Upper Rubber Ring	Rubber	1
Vibration Absorbing Flange	AISI P20 Steel	1
$\frac{1}{2}$ - 20 Studs	Ti-6Al-4V	4
1-RSCC3/500KG-1 Load Cell	Stainless Steel	2
52210 - SKF - Double Direction Thrust Ball Bearing	Steel	1

Table 3.23: Fixing Hardware

Component	Part	Quantity
ISO 4762 - M12 x 40 - 12.9	Bolt	2
ISO 4762 - M10 x 80 - 12.9	Bolt	1
ISO 4762 - M8 x 70 - 12.9	Bolt	6
ISO 4762 - M6 x 60 - 12.9	Bolt	4
ISO 4762 - M6 x 30 - 12.9	Bolt	4
ISO 4762 - M6 x 20 - 12.9	Bolt	4
ISO 4033 - M12 - 12	Nut	6
ISO 4033 - M8 - 12	Nut	6
ISO 4033 - M6 - 12	Nut	4
ISO 7089 - M12	Washer	2
ISO 7089 - M10	Washer	1
ISO 7089 - M8	Washer	12
ISO 7089 - M6	Washer	12

3.8 Estimated cost of the ultrasonic fatigue equipment

In this section, the estimated cost of the designed ultrasonic fatigue testing equipment is going to be listed, the presented prices don't include VAT. In the Table 3.24, the manufacturing plus material prices of the designed components are going to be presented. Additionally, in the Table 3.25 the prices of the chosen components are listed.

Table 3.24: Estimated Price for Manufacturing the Designed Components

Component	Quantity	Price per unit (€)	Total (€)
Bearing Case	2	35.0	70.0
Bearing Holder	1	30.0	30.0
Booster Support	1	100.0	100.0
Locking Support	2	75.0	150.0
Lower Rubber Ring	1	32.9	32.9
Squared Section Bars	2	40.0	80.0
Support Plate	1	180.0	180.0
Traction Plate	1	80.0	80.0
Ultrasonic Booster	2	352.5	705.0
Ultrasonic Horn	2	261.9	523.8
Upper Rubber Ring	1	32.9	32.9
Vibration Absorbing Flange	1	245.0	245.0
$\frac{1}{2}$ - 20 Studs	4	15.0	60.0
Total Price (€)			2289.6 €

Table 3.25: Price of the Chosen Components

Component	Quantity	Price per unit (€)	Total (€)
Generator MPI - 2KW	1	4800.0	4800.0
1-RSCC3/500KG-1 Load Cell	2	484.0	968.0
20 kHz Transducer MPI	1	4650.0	4650.0
52210 - SKF - Double Direction Thrust Ball Bearing	1	70.7	70.7
Total Price (€)			10488.7 €

The total price of the ultrasonic fatigue testing equipment if only fully reversed ultrasonic fatigue tests were going to be conducted, $R=-1$, is 10339.4 € and the total price for the full equipment, capable of applying a 10 kN static load to the specimen, is 12778.3 €.

Chapter 4

Conclusions and Future Work

The main purpose of this dissertation was to design an ultrasonic fatigue testing equipment, which complied with the present project's specifications. All the conclusions that were reached along the realization of this work are described in Section 4.1. Additionally, Section 4.2 of this chapter provides suggestions for future work.

4.1 Conclusions

The primary objective of the present work was to design and develop structurally an ultrasonic fatigue testing equipment, capable of performing fully reversed ultrasonic fatigue tests and additionally capable of applying a maximum 10 kN static load to the specimen, in order to realize tests at different values of R . This objective was successfully accomplished. Through the incorporation of load cells into the layout of the machine it will be possible to measure the load applied to the specimen, which was another of the ultrasonic fatigue machine's primary objectives. Furthermore, the development of a dynamic system with a resonance frequency near 20 kHz, as well as the ability to considerably amplify the external displacement imposed by the piezoelectric transducer was another of the primary goals that were fulfilled. The subsequent phase, the manufacture of the new designed components for the ultrasonic fatigue equipment, was carried out with the knowledge that all the primary objectives had been achieved.

Currently, the designed components required to conduct fully reversed ultrasonic fatigue tests are being manufactured, however, they will not be finished in time to be included in the present document. Following the manufacturing of the first ultrasonic booster and horn, a phase of testing will be conducted to determine whether they exhibit the first longitudinal natural frequency approximately equal to the excitation frequency of the piezoelectric transducer, 20 kHz, and if their vibration amplification matches the one for which they were designed. If the tested frequency doesn't match the piezoelectric transducer excitation frequency range or if the vibration amplification of the ultrasonic components doesn't match the desired one, due to material properties variations or fabrication tolerances, these components will have to be rectified or adjusted in order to ensure the correct operation of the ultrasonic fatigue equipment.

Regarding the utilized pre-existing structure and original components, the precise values of the mechanical properties of the different utilized components were unknown, hence conservative values for these mechanical properties were assumed. Nevertheless, for the most extreme scenario of the ultrasonic equipment operation, where the specimens are subjected to an additional static load of 10 kN, high safety factors were obtained, guaranteeing the usability of the original pre-existing components and the ultrasonic equipment safety when testing specimens.

Furthermore, the enhancement of the newly designed components for the ultrasonic fatigue testing equipment is an iterative process, that takes time and study. The different FEA, using the Abaqus software, on the different subassemblies and components of the ultrasonic equipment developed in the present document, presented many stress concentrations and some singularities which influenced the verified stresses. Nevertheless, the manufacturing material of the different designed components was chosen taken into account the higher stresses for a more conservative approach. Regarding the manufacturing material of the ultrasonic booster and horn, the Ti-6Al-4V was chosen due to being the most standard material for the manufacturing of these type of ultrasonic components and due to its low variation of the modulus of elasticity, E , which decreases the chance of these components needing to be adjusted after their manufacture due to having their first longitudinal natural frequency fundamentally different of the excitation frequency range of the piezoelectric transducer. The ultrasonic horn is the most critical component of the ultrasonic fatigue equipment developed in this work, presenting a safety factor of 1.48, although ensuring the necessary safety for its correct operation.

4.2 Future work

In order to continue developing the work presented in this thesis, the following suggestions are provided:

- Full manufacture of the remaining ultrasonic equipment's components. The second pair of ultrasonic booster and horn needs to be tested regarding their first longitudinal natural frequency and vibration amplification. Despite the fact that the theoretical geometry is the same as the first pair, there are always imperfections in the manufacturing process, geometric variations, and minor variations in the manufacturing material properties. If the ultrasonic components are within the expected specs, the total ultrasonic testing equipment can be assembled;
- This dissertation's development was largely theoretical and numerical; the resulting ultrasonic testing equipment requires experimental validation. Therefore, it would be beneficial to perform ultrasonic fatigue tests and then compare the results with the ones available in the academy, or, compare with the results obtained through the use of the Shimadzu USF-2000 longitudinal ultrasonic testing machine existing at INEGI;
- Continuation of the development of the ultrasonic machine, so that it may be capable of conducting ultrasonic fatigue testing at unconventional conditions, such as under extreme

pressures and temperatures. Implementation of a gripping system that enables the developed ultrasonic testing equipment to perform fatigue tests on unconventional specimens;

- In order to dissipate undesirable vibrations in the areas where the booster is threaded onto the ultrasonic fatigue machine, if necessary, vibration dissipating grooves may be produced on the Section B structural components of the ultrasonic equipment;
- With the current configuration of the ultrasonic fatigue testing equipment, if someone applied an extremely high static load that would cause damage to the machine, the first part of the fatigue equipment to fail would be one of the ultrasonic horns, which would be catastrophic and extremely expensive. It would be interesting to convert on purpose another component of the ultrasonic testing equipment into "the weakest link", while yet maintaining the safety required to conduct testing with the maximum static load applied to the specimen, such as the bolts that connect the squared section bars with the other components. Therefore, if an individual "incorrectly" applied an extreme load to the machine, while testing specimens, the bolts would fail instead of the ultrasonic horns, decreasing the possible financial damage.

Bibliography

- [1] Vitaliy Kazymyrovych. *Very high cycle fatigue of tool steels*. PhD thesis, Karlstad University, 2010.
- [2] B Pyttel, D Schwerdt, and C Berger. Very high cycle fatigue—is there a fatigue limit? *International Journal of fatigue*, 33(1):49–58, 2011.
- [3] Paul Ilie, Xavier Lesperance, and Ayhan Ince. Development of an ultrasonic fatigue testing system for gigacycle fatigue. *Material Design & Processing Communications*, 2(6):e120, 2020.
- [4] Claude Bathias and Paul C Paris. *Gigacycle fatigue in mechanical practice*. CRC Press, 2004.
- [5] Felipe Klein Fiorentin. *A Numerical and Experimental Study on Residual Stresses, Distortion and Fatigue Behaviour of Additive Manufactured Components*. PhD thesis, Inegi, 2020.
- [6] Claude Bathias. There is no infinite fatigue life in metallic materials. *Fatigue & fracture of engineering materials & structures (Print)*, 22(7):559–565, 1999.
- [7] Marcos Fernando Pacheco. Projeto de máquina ultrassônica para testes em aços submetidos à fadiga giga-ciclo. Master’s thesis, PUC-Rio, Rio de Janeiro, Brasil, 2016.
- [8] Richard Gordon Budynas, J Keith Nisbett, et al. *Shigley’s mechanical engineering design*, volume 9. McGraw-hill New York, 2011.
- [9] Qingyuan Wang, Muhammad Kashif Khan, and Claude Bathias. Current understanding of ultra-high cycle fatigue. *Theoretical and Applied Mechanics Letters*, 2(3):031002, 2012.
- [10] Pedro Costa, Richard Nwawe, Henrique Soares, Luís Reis, Manuel Freitas, Yong Chen, and Diogo Montalvão. Review of multiaxial testing for very high cycle fatigue: From ‘conventional’ to ultrasonic machines. *Machines*, 8(2):25, 2020.
- [11] X Kong. Theoretical and numerical study on vibratory fatigue. *These de doctorat, University of technology of Compiègne*, 1987.
- [12] Pedro Ferreira Rodrigues da Costa. Estudo e desenvolvimento de novos componentes de uma máquina de vhcfc em regime multiaxial. Master’s thesis, IST, Lisbon, 2017.
- [13] Claude Bathias. Piezoelectric fatigue testing machines and devices. *International Journal of Fatigue*, 28(11):1438–1445, 2006.
- [14] Tieying Wu, Jingang Ni, and Claude Bathias. An automatic ultrasonic fatigue testing system for studying low crack growth at room and high temperatures. In *Automation in fatigue and fracture: testing and analysis*. ASTM International, 1994.

- [15] Alexander Nikitin, Claude Bathias, and Thierry Palin-Luc. A new piezoelectric fatigue testing machine in pure torsion for ultrasonic gigacycle fatigue tests: application to forged and extruded titanium alloys. *Fatigue & Fracture of Engineering Materials & Structures*, 38(11):1294–1304, 2015.
- [16] Israel Marines-Garcia, Jean-Pierre Doucet, and Claude Bathias. Development of a new device to perform torsional ultrasonic fatigue testing. *International journal of fatigue*, 29(9-11):2094–2101, 2007.
- [17] M Vieira, M De Freitas, L Reis, and AMR Ribeiro. Development of a very high cycle fatigue (vhcf) multiaxial testing device. *Frattura ed Integrita Strutturale*, 10(37):131–137, 2016.
- [18] M Vieira, L Reis, M Freitas, and A Ribeiro. Strain measurements on specimens subjected to biaxial ultrasonic fatigue testing. *Theoretical and Applied Fracture Mechanics*, 85:2–8, 2016.
- [19] Pedro Costa, Mário Vieira, Luis Reis, António Ribeiro, and Manuel de Freitas. New specimen and horn design for combined tension and torsion ultrasonic fatigue testing in the very high cycle fatigue regime. *International Journal of Fatigue*, 103:248–257, 2017.
- [20] HQ Xue, Hong Tao, F Montembault, QY Wang, and C Bathias. Development of a three-point bending fatigue testing methodology at 20 khz frequency. *International Journal of Fatigue*, 29(9-11):2085–2093, 2007.
- [21] ZD Sun, C Bathias, and G Baudry. Fretting fatigue of 42crmo4 steel at ultrasonic frequency. *International Journal of Fatigue*, 23(5):449–453, 2001.
- [22] Y Furuya, S Matsuoka, and T Abe. Gigacycle fatigue in high-strength steels. *Denki Seiko(Electric Furnace Steel)*, 75(1):55–60, 2004.
- [23] 3R labo. Fully reversed fatigue tests – meg20. <https://3r-labo.com/en/produit/fully-reversed-fatigue-tests/>. Accessed June, 2022.
- [24] SHIMADZU. Ultrasonic fatigue testing system. <https://www.shimadzu.eu/usf-2000>. Accessed June, 2022.
- [25] Sonic Power. Ultrasonic transducer 3300 watt – 20 khz – ip 72. <https://sonic-power.com/Product/ultrasonic-transducer-3300-watt-20-khz/>. Accessed June, 2022.
- [26] Emerson. Ultrasonic horn catalog. <https://www.emerson.com/documents/automation/catalog-ultrasonic-horn-branson-en-us-160126.pdf>. Accessed June, 2022.
- [27] Sonitek. 20 khz catenoidal tapped horn. <https://www.sonitek.com/20-khz-catenoidal-tapped-horn-ti/>. Accessed June, 2022.
- [28] Perez Mora Ruben. *Study of the fatigue strength in the gigacycle regime of metallic alloys used in aeronautics and off-shore industries*. PhD thesis, Arts et Métiers ParisTech, 2010.
- [29] QY Wang, C Bathias, N Kawagoishi, and Q Chen. Effect of inclusion on subsurface crack initiation and gigacycle fatigue strength. *International Journal of Fatigue*, 24(12):1269–1274, 2002.

- [30] S Nishijima and K Kanazawa. Stepwise sn curve and fish-eye failure in gigacycle fatigue. *Fatigue & fracture of engineering materials & structures (Print)*, 22(7):601–607, 1999.
- [31] M Zimmermann. Very high cycle fatigue. *Handbook of Mechanics of Materials*, pages 1–38, 2018.
- [32] Duarte de Araújo Maciel. Fatigue behaviour of inconel 625 produced by directed energy deposition. Master’s thesis, FEUP, Porto, 2021.
- [33] Ralph I Stephens, Ali Fatemi, Robert R Stephens, and Henry O Fuchs. *Metal fatigue in engineering*. John Wiley & Sons, 2000.
- [34] D Kammer. Slip fronts at frictional interfaces: A numerical and theoretical study. *EPFL Thesis*, 12, 2014.
- [35] David Broek. *Elementary engineering fracture mechanics*. Springer Science & Business Media, 1982.
- [36] Subra Suresh. *Fatigue of materials*. Cambridge university press, 1998.
- [37] Paul Paris and Fazil Erdogan. A critical analysis of crack propagation laws. *Journal of Basic Engineering*, 85, 1963.
- [38] Willy Ank de Moraes. Elasticidade e plasticidade avaliada através do ensaio de tração. *Conformação Plástica dos Metais - UNISANTA*, 2009.
- [39] MPIinterconsulting PowerUltrasonics. Mpinterconsulting powerultrasonics - switzerland. <https://www.mpi-ultrasonics.com/>. Accessed June, 2022.
- [40] HBM. Rsccl tension load cell. https://www.hbm.com/en/2708/rsccl-stainless-steel-s-type-tension-load-cell/?product_type_no=RSCC%20S-Type%20Tension%20Load%20Cell. Accessed April, 2022.
- [41] Skf. Double direction thrust ball bearing. <https://www.skf.com/group/products/rolling-bearings/ball-bearings/thrust-ball-bearings/productid-52210>. Accessed April, 2022.
- [42] Hugo Monteiro Freire. Desenvolvimento de um dispositivo experimental para medir a resistência à fluência de ligações adesivas. Master’s thesis, FEUP, Porto, 2015.
- [43] Luis Pedro Laja Pina. Development of a multi-station creep testing machine for adhesive joints. Master’s thesis, FEUP, Porto, 2016.
- [44] The efficient Engineer. Understanding stresses in beams. <https://www.youtube.com/watch?v=f08Y39UiC-o&t=534s>. Accessed June, 2022.
- [45] The efficient Engineer. Understanding the deflection of beams. <https://www.youtube.com/watch?v=MvBqCeZ1lpQ&t=487s>. Accessed June, 2022.
- [46] UDDEHOLM. Uddeholm impax® supreme. *UDDEHOLM Catalogue*, 2014.
- [47] Michael Ascensão Gouveia. Giga-cycle fatigue behaviour of the structural steel s690. document under review. Master’s thesis, FEUP, Porto, 2022.

- [48] Jack A Collins, Henry R Busby, and George H Staab. *Mechanical design of machine elements and machines: a failure prevention perspective*. John Wiley & Sons, 2009.
- [49] ENGINEERS EDGE. Iso 68-1 metric thread profile specifications and equations. https://www.engineersedge.com/hardware/iso_681_metric_thread_14599.htm. Accessed April, 2022.
- [50] COMSOL Blog. Damping in structural dynamics : Theory and sources. <https://www.comsol.com/blogs/damping-in-structural-dynamics-theory-and-sources/>. Accessed June, 2022.
- [51] Michael F.Ashby. *Materials Selection in Mechanical Design*, volume 1. Butterworth-Heinemann, 2000.
- [52] A Tridello, DS Paolino, G Chiandussi, and M Rossetto. Gaussian specimens for gigacycle fatigue tests: Damping effects. *Procedia Engineering*, 74:113–118, 2014.
- [53] JACQUET PORTUGAL. Titanium grade 5. <https://portugal.myjacquet.com/>. Accessed June, 2022.
- [54] Carlos Fernades. *Dimensionamento à Fadiga - Apontamentos teóricos OMI*. FEUP, 2021.
- [55] Walter D Pilkey, Deborah F Pilkey, and Zhuming Bi. *Peterson's stress concentration factors*. John Wiley & Sons, 2020.
- [56] Impacto Ferramentas. Tabelas de conversão e forças de aperto. <https://www.impacto-ferramentas.pt/noticias/tabelas-de-conversao-e-forcas-de-aperto/>. Accessed April, 2022.

Appendix A

Derivation of Equations Presented in Chapter 2

This appendix provides the derivation of several final equations stated in Chapter 2.

A.1 Dynamic Equilibrium Equation

In this section, the equation 2.27 from Chapter 2 will be obtained. The complete procedure is presented below [7].

First, let's assume an element of length dx from a variable cross section bar, the forces acting on that same element can be represented as shown in the figure below:

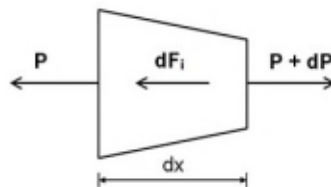


Figure A.1: Balance of forces on an element of length dx [7]

Through the figure A.1 it is possible to perceive that:

$$dP = \frac{\partial P}{\partial x} dx \quad (\text{A.1})$$

The elementary inertial force, dF_i is given by:

$$dF_i = dm \frac{\partial^2 u}{\partial t^2} \quad (\text{A.2})$$

Which can be decomposed into:

$$dF_i = \rho S(x) \frac{\partial^2 u}{\partial t^2} dx \quad (\text{A.3})$$

Then, by assuming that:

$$dP = dF_i \quad (\text{A.4})$$

It is possible to obtain the following equation:

$$\frac{\partial P}{\partial x} = \rho S(x) \frac{\partial^2 u}{\partial t^2} \quad (\text{A.5})$$

The internal force P , is given by the product of stress and cross sectional area. By applying the Hooke's law, it is possible to perceive that:

$$P = E \varepsilon S(x) = ES(x) \frac{\partial u}{\partial x} \quad (\text{A.6})$$

By introducing the equation A.6 into the equation A.5, we obtain:

$$\frac{\partial}{\partial x} \left(ES(x) \frac{\partial u}{\partial x} \right) = \rho S(x) \frac{\partial^2 u}{\partial t^2} \quad (\text{A.7})$$

Developing the above equation will lead to the following form:

$$\frac{E}{\rho} \left(\frac{\partial^2 u}{\partial t^2} + \frac{S'(x)}{S(x)} \frac{\partial u}{\partial x} \right) = \frac{\partial^2 u}{\partial t^2} \quad (\text{A.8})$$

As was shown in chapter 2, the longitudinal wave velocity, c , is given by:

$$c = \sqrt{\frac{E}{\rho}} \quad (\text{A.9})$$

And, by substituting the equation A.9 into the equation A.8 it is possible to obtain the following equation:

$$c^2 \left(\frac{\partial^2 u}{\partial t^2} + \frac{S'(x)}{S(x)} \frac{\partial u}{\partial x} \right) = \frac{\partial^2 u}{\partial t^2} \quad (\text{A.10})$$

The solution to the preceding equation is:

$$u(x, t) = U(x) \sin(\omega t) \quad (\text{A.11})$$

Substituting the equation A.11 into the equation A.10, we obtain:

$$c^2 \left(U''(x) \sin(\omega t) + \frac{S'(x)}{S(x)} U'(x) \sin(\omega t) \right) = -\omega^2 U(x) \sin(\omega t) \quad (\text{A.12})$$

Finally, assuming that $k = \frac{\omega}{c}$, $p(x) = \frac{S'(x)}{S(x)}$ and dividing the equation A.12 by $\sin(\omega t)$ we obtain the equation 2.27.

$$U''(x) + p(x)U'(x) + k^2U(x) = 0 \quad (\text{A.13})$$

A.2 Resonance Length and Amplitude of Vibration

In this section, the complete procedure to formulate the equations of the resonance length, equation 2.33, and the amplitude of vibration, equations 2.35 and 2.36, presented in Chapter 2, is going to be fully presented [4].

Firstly, it is going to be defined the cross sectional area, $S(x)$, for both the cylindrical and the reduced section part of the specimen shown in figure 2.7.

$$S(x) = \pi R_2^2, \quad L_2 < |x| \leq L \quad (\text{A.14})$$

$$S(x) = \pi R_1^2 \cosh^2(x), \quad |x| \leq L_2 \quad (\text{A.15})$$

For the cylindrical part, the cross sectional area keeps constant, so:

$$p(x) = \frac{S'(x)}{S(x)} = 0 \quad (\text{A.16})$$

Consequently the equation 2.27 simplifies to:

$$U''(x) + k^2U(x) = 0 \quad (\text{A.17})$$

The equation show above is an ordinary differential equation of second order, and its general solution is given by:

$$U(x) = C_1 \cos(kx) + C_2 \sin(kx) \quad (\text{A.18})$$

For the reduced section part, it is possible to perceive that:

$$p(x) = \frac{S'(x)}{S(x)} = 2\alpha \tanh(\alpha x) \quad (\text{A.19})$$

The outcome of combining the equations 2.27 and A.19 can be seen bellow:

$$U''(x) + 2\alpha \tanh(\alpha x)U'(x) + k^2U(x) = 0 \quad (\text{A.20})$$

In order to obtain the general solution of the equation above, the following function will be introduced:

$$w(x) = \cosh(\alpha x)U(x) \quad (\text{A.21})$$

The first two derivatives of the equation A.21 are shown below:

$$w'(x) = U'(x) \cosh(\alpha x) + \alpha \sinh(\alpha x)U(x) \quad (\text{A.22})$$

$$w''(x) = [U''(x) + 2\alpha \tanh(\alpha x)U'(x) + \alpha^2U(x)] \cosh(\alpha x) \quad (\text{A.23})$$

By comparing the equations A.20 and A.23 it is possible to establish the following equation:

$$w''(x) = (\alpha^2 - k^2) \cosh(\alpha x)U(x) \quad (\text{A.24})$$

And, consequently:

$$w''(x) - (\alpha^2 - k^2)w(x) = 0 \quad (\text{A.25})$$

Whose general solution is presented bellow:

$$w(x) = C_3 e^{\beta x} + C_4 e^{-\beta x} \quad (\text{A.26})$$

Now, by substituting the equation A.26 into the equation A.21, the general solution of the equation A.20 can be obtained and it is presented bellow:

$$U(x) = \frac{C_3 e^{\beta x} + C_4 e^{-\beta x}}{\cosh(\alpha x)} \quad (\text{A.27})$$

The solutions for the cylindrical and reduced section part of the specimen have now been presented, A.18 and A.27 respectively. The four constants, C_1 , C_2 , C_3 and C_4 , will be determined through boundary and continuity conditions.

It was stated in Chapter 2, equation 2.21 that at both ends of the specimen, we have the nodes of stress and strain, which is where the maximum displacement occurs. So, by applying these boundary conditions to the equation A.18 it is possible to obtain:

$$C_1 \cos(kL) + C_2 \sin(kL) = A_0 \quad (\text{A.28})$$

$$C_2 = C_1 \tan(kL) \quad (\text{A.29})$$

Through the combination of the two equations shown above, the following relation can be obtained:

$$C_1 [\cos(kL) + \sin(kL) \tan(kL)] = A_0 \quad (\text{A.30})$$

That leads to :

$$C_1 = A_0 \cos(kL) \quad (\text{A.31})$$

$$C_2 = A_0 \sin(kL) \quad (\text{A.32})$$

By substituting the values of the constants given above into the equation A.18, the displacement amplitude in the cylindrical portion of the specimen may be calculated. So:

$$U(x) = A_0 \cos[k(L-x)] \quad (\text{A.33})$$

Which is the equation 2.36.

In order to calculate the constants C_3 and C_4 , the continuity condition at $x = L_2$ and the boundary condition $U(0) = 0$ will be used. Therefore, the result of applying $U(0) = 0$ to the equation A.27 is present below:

$$C_3 + C_4 = 0 \quad (\text{A.34})$$

So, the equation A.27 can be now rewritten as:

$$U(x) = \frac{2C_3 \sinh(\beta x)}{\cosh(\alpha x)} \quad (\text{A.35})$$

The continuity condition at $x = L_2$, requires that the displacement amplitude and the strain amplitude calculated through the equations A.33 and A.35 must be equal. So, the following relations can be obtained:

$$A_0 \cos[k(L - L_2)] = \frac{2C_3 \sinh(\beta L_2)}{\cosh(\alpha L_2)} \quad (\text{A.36})$$

$$kA_0 \sin[k(L - L_2)] = \frac{2C_3 [\beta \cosh(\beta L_2) \cosh(\alpha L_2) - \alpha \sinh(\beta L_2) \sinh(\alpha L_2)]}{\cosh^2(\alpha L_2)} \quad (\text{A.37})$$

Finally, the constants C_3 and C_4 can be obtained through the equations A.34 and A.36:

$$C_3 = -C_4 = \frac{A_0 \cos(kL_1) \cosh(\alpha L_2)}{2 \sinh(\beta L_2)} \quad (\text{A.38})$$

Consequently, the equation 2.35 can be now obtained by substituting the constants C_3 and C_4 into the equation A.27.

Through the comparison of the equations A.36 and A.37, and considering that $L = L_1 + L_2$ the following expression can be achieved:

$$k \tan(kL_1) = \beta \coth(\beta L_2) - \alpha \tanh(\alpha L_2) \quad (\text{A.39})$$

The equation above can be rearranged, through mathematical manipulation, into the equation of the resonance length, equation 2.33 :

$$L_1 = \frac{1}{k} \arctan \left\{ \frac{1}{k} [\beta \coth(\beta L_2) - \alpha \tanh(\alpha L_2)] \right\} \quad (\text{A.40})$$

Appendix B

Titanium Ti-6Al-4V Properties

The information presented in this Appendix was provided by JACQUET Portugal [53].

TITANIUM Grade 5

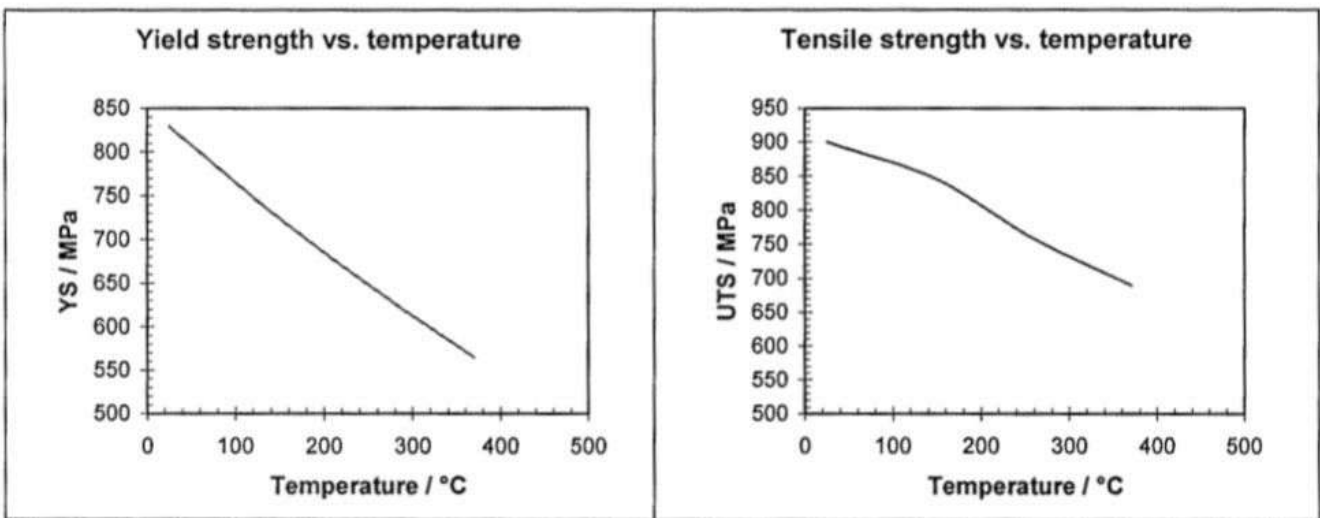
Ti - 6Al - 4V Alpha-beta alloy

The data given is for information not for design

Chemical composition (weight %) (Maximum values unless range is shown)										
O	N	C	H	Fe	Al	V	Ni	Mo	Others	Residuals
0.20	0.05	0.08	0.015	0.40	5.5-6.75	3.5-4.5				0.4

This is the most widely used titanium alloy. It has very high strength but relatively low ductility. The main application of this alloy is in aircraft and spacecraft. Offshore use is growing. The alloy is weldable and can be precipitation hardened.

Mechanical properties at room temperature		
	Minimum values	Typical values
Yield Strength	825 MPa	910 MPa
Ultimate Strength	895 MPa	1000 MPa
Elongation in 50 mm, A5	10 %	18 %
Reduction in Area	20 %	%
Hardness		330-390 HV
Modulus of elasticity		114 GPa
Charpy V-Notch Impact		20-27 J



Fatigue properties at room temperature (Stress to cause failure in 10 ⁷ Cycles)				
Rotating bend			Direct stress limit	
Smooth	K _t =1	430-520 MPa	Smooth	K _t =1 376 MPa
Notch	K _t =3	MPa	Notch	K _t =3 270 MPa

Physical properties	
Melting point, ± 15 °C	1650 °C
Density	4.43 g/cm ³
Beta transus, ± 15 °C	995 °C
Thermal expansion, 20 - 100 °C	9.0 *10 ⁻⁶ K ⁻¹
Thermal expansion, 0 - 300 °C	9.5 *10 ⁻⁶ K ⁻¹
Thermal conductivity, room temperature	6.6 W/mK
Thermal conductivity, 400 °C	13 W/mK
Specific heat, room temperature	0.57 J/gK
Specific heat, 400 °C	0.65 J/gK
Electrical resistivity, room temperature	171 μW*cm
Poisson's ratio	0.30-0.33

Heat treating		
	Temperature	Time
Solution treating temperature	950-970°C	1 hour
Ageing temperature	480-595°C	4-8hours
Annealing	710-790°C	1-4hours
Stress relieving	480-650°C	1-4hours

Weldability – good

Since the two-phase microstructure of alpha-beta titanium alloys responds to thermal treatment, the temperatures encountered during the welding cycle can affect the material being welded.

Available mill products

Bar, billet, extrusions, plate, sheet, strip, wire

Typical Applications

Compressor blades, discs and rings for jet engines, aircraft components, pressure vessels, rocket engine cases, offshore pressure vessels.

Industry specifications

ASTM Grade5, ST-AI40, AMS4911D, MIL-T-9047G

Sheet and plate

ASTM B265 Gr5, AMS 4911

Bars and billets

ASTM B348 Gr5

Bars, billets and forging (+circular forging)

AMS 4928, AMS 4965, AMS 4967

Extruded products

AMS 4935

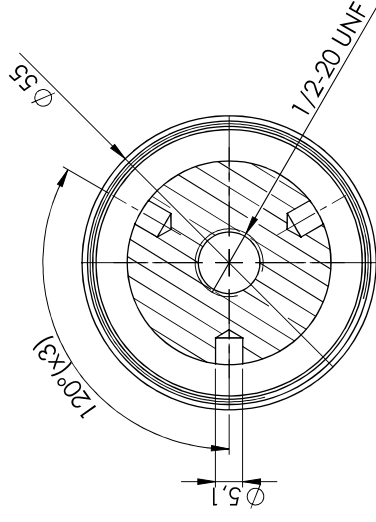
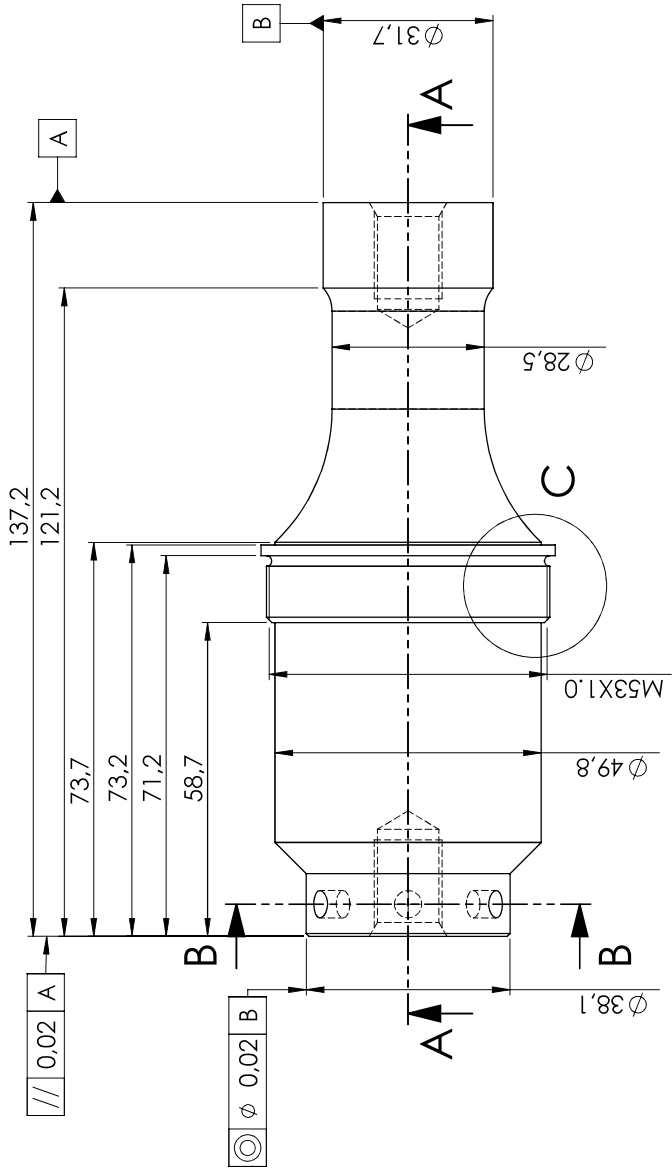
Castings

ASTM B367 Gr5

Appendix C

Definition Drawings of Components

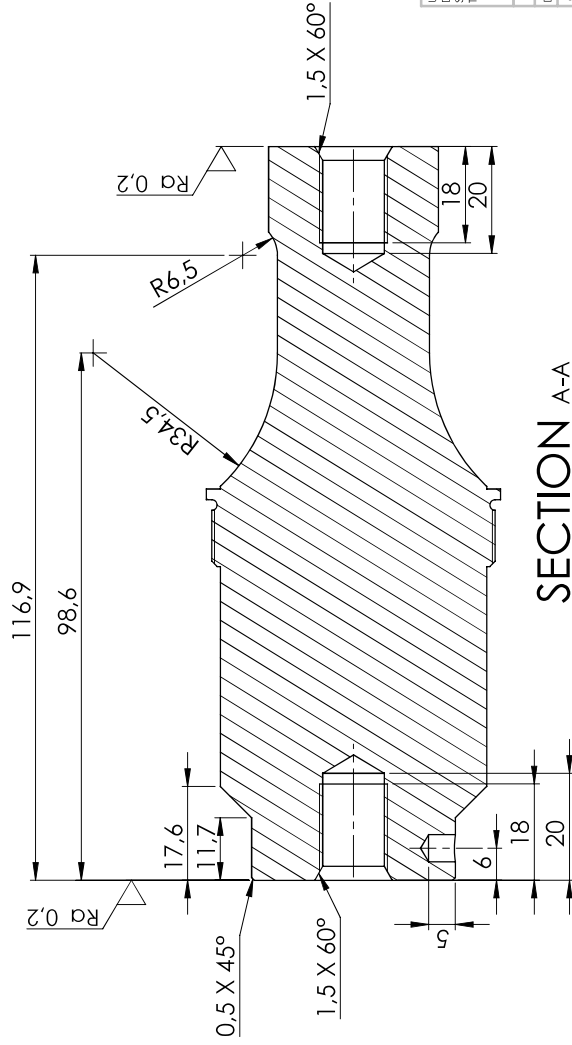
This Appendix presents the definition drawings made for the different components designed for the ultrasonic fatigue testing equipment developed in the present document.



SECTION B-B

DETAIL C

SCALE 3:1



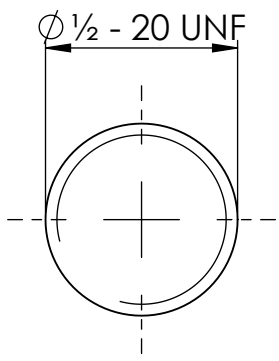
SECTION A-A

UNLESS OTHERWISE SPECIFIED: DIMENSIONS ARE IN MILLIMETERS		FINISH:		DO NOT SCALE DRAWING		REVISION	
SURFACE FINISH:		TOLERANCES ISO 2768 - FH		Tolerâncias Gerais : ISO 2768 - f H			
LINEAR:		ANGULAR:					
NAME	SIGNATURE	DATE		TITLE:			
RICARDO LOBO		04/06/22		Não quebrar arestas vivas			
CHECKED							
APPROVED							
MFG							
G.A.							
MATERIAL:		DWG NO.		SCALE: 1:1		SHEET 1 OF 1	
T16A14V		1		Booster 1:2.5		A3	
A ser fornecido pelo INEGI							
WEIGHT:		3		2		1	

4 3 2 1

F

F

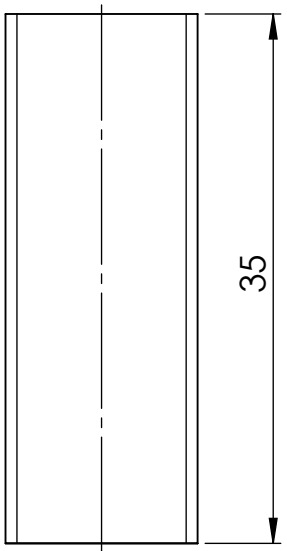


E

E

D

D



C

C

B

B

Tolerâncias gerais : ISO 2768 - m K

UNLESS OTHERWISE SPECIFIED:
 DIMENSIONS ARE IN MILLIMETERS
 SURFACE FINISH:
 TOLERANCES: ISO 2768 - m K
 LINEAR:
 ANGULAR:

FINISH:

DO NOT SCALE DRAWING

REVISION

Quantidade : 2

	NAME	SIGNATURE	DATE
DRAWN	Ricardo Lobo		04/06/2022
CHK'D			
APPV'D			
MFG			
Q.A			

TITLE:

Perno

MATERIAL:
 Ti6Al4V
 A ser fornecido pelo INEGI

DWG NO.

2

A4

SCALE:1:1

SHEET 1 OF 1

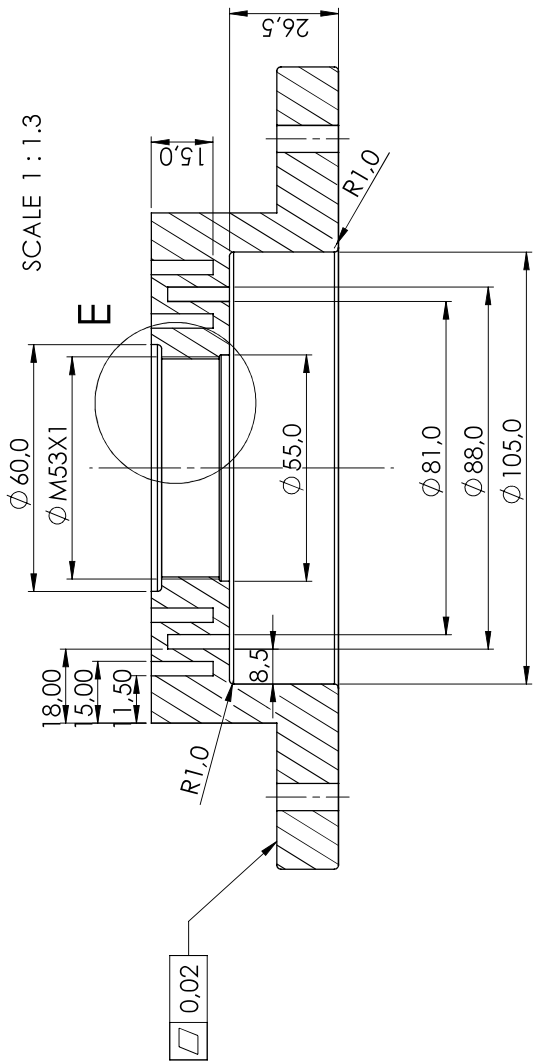
A

A

4 3 2 1

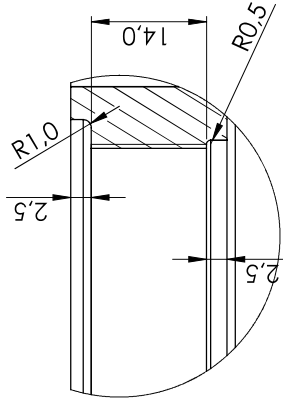
SECTION A-A

SCALE 1 : 1,3



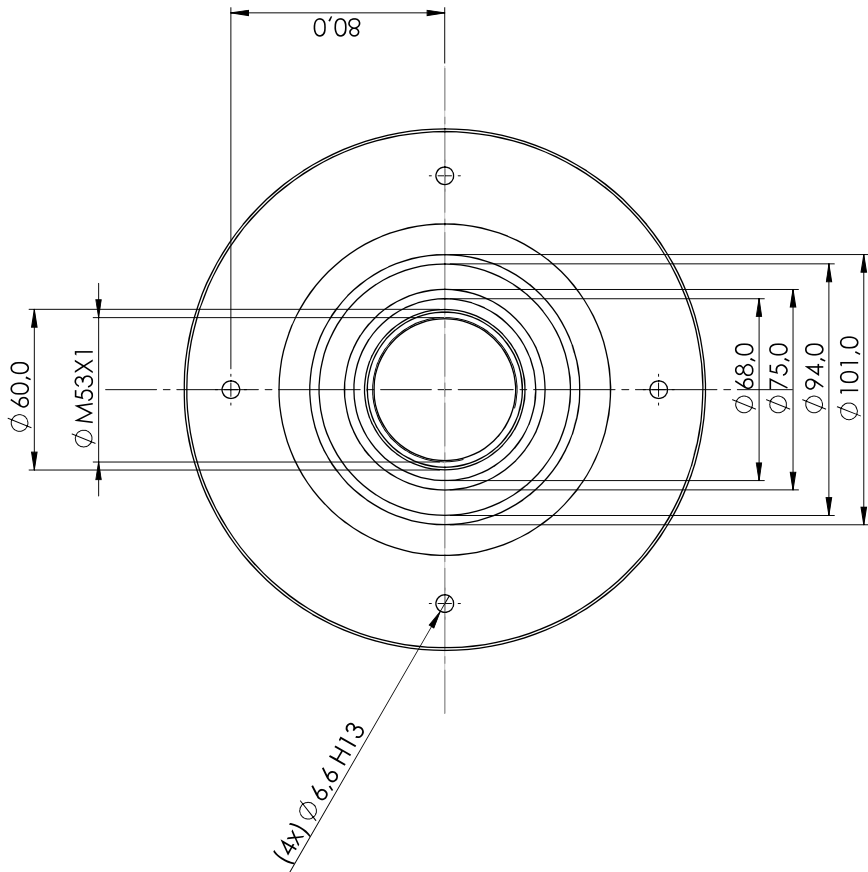
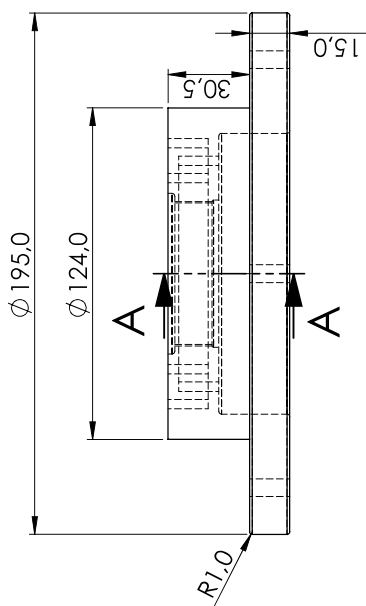
DETAIL E

SCALE 2 : 1,3



Ra 0,8

Tolerâncias Gerais : ISO 2768 - m K



UNLESS OTHERWISE SPECIFIED:
DIMENSIONS ARE IN MILLIMETERS
SURFACE FINISH:
TOLERANCES: ISO 2768 - m K
LINEAR:
ANGULAR:

FINISH:

DO NOT SCALE DRAWING

REVISION

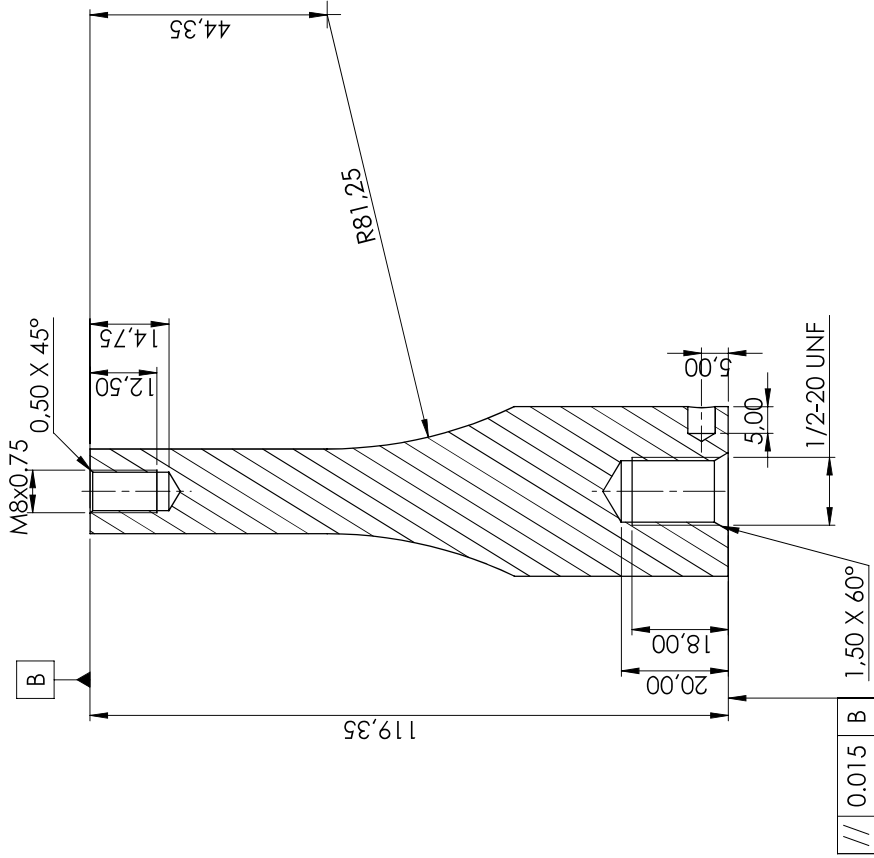
NAME	SIGNATURE	DATE
DRW/N Ricardo Lobo		04/06/22
CHK/D		
APP/V		
MFG		
Q.A.		

TITLE:	DWG NO.	SCALE: 1:2	SHEET 1 OF 1
Flange Absorsor	3	2	1

MATERIAL:
Aço P20 (PM300 F. Ramada)
A ser fornecido pela empresa de maquinaçom

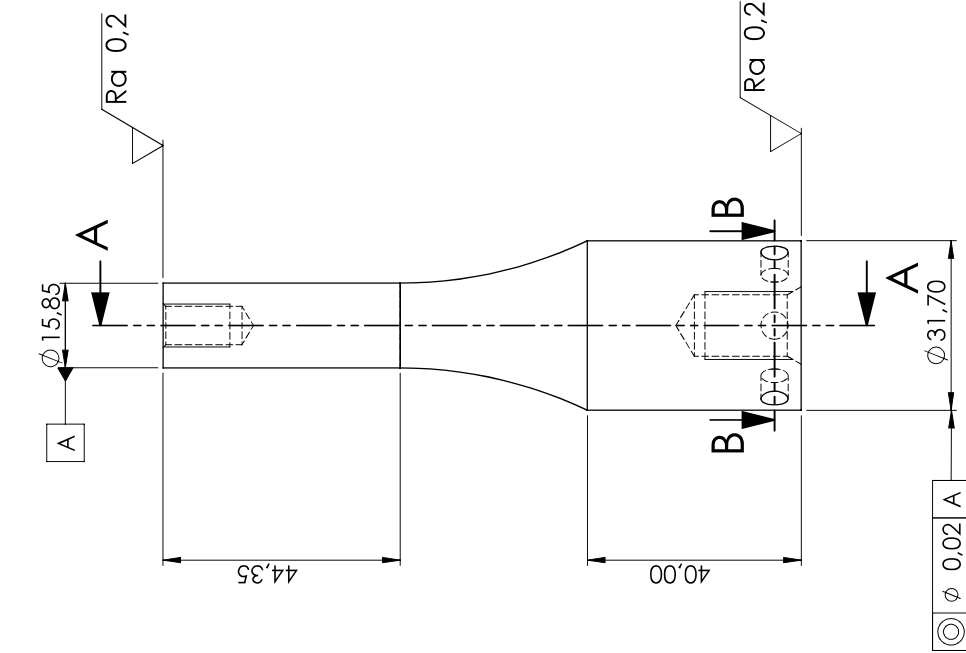
A3

SECTION A-A



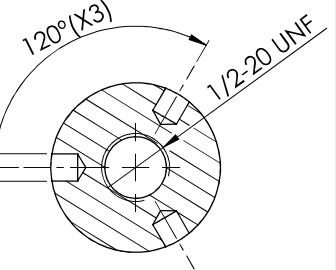
Ra 0,8

Tolerâncias Gerais : ISO 2768 - f H



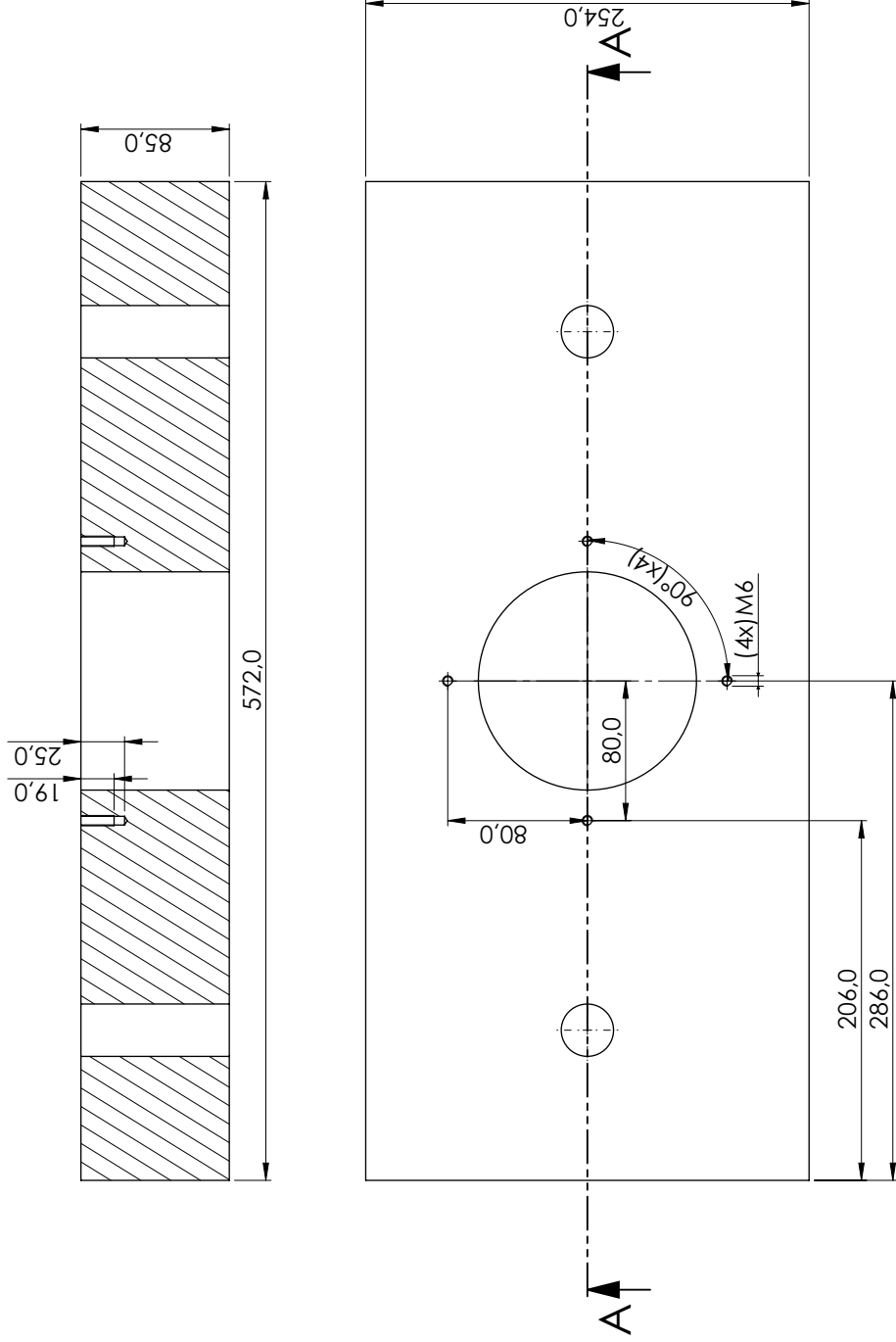
SECTION B-B

ϕ 5,10



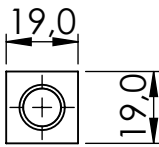
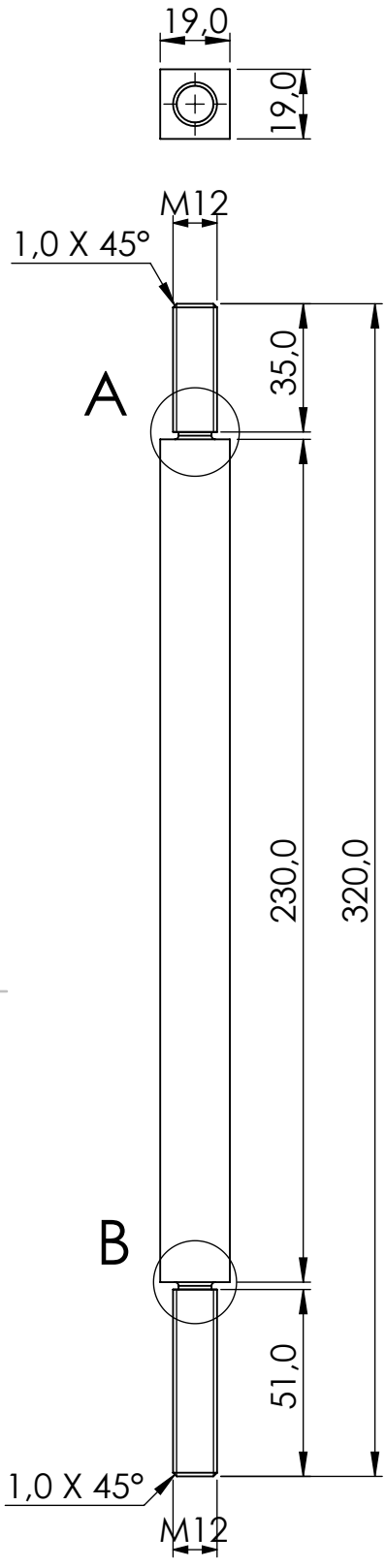
UNLESS OTHERWISE SPECIFIED: DIMENSIONS ARE IN MILLIMETERS SURFACE FINISH: TOLERANCES: ISO 2768 - f H LINEAR: ANGULAR:		FINISH: DO NOT SCALE DRAWING		REVISION
DRAWN: Ricardo Lobo		SIGNATURE		TITLE: Horn DWG NO.: 4 MATERIAL: Ti6Al4V A ser fornecido pelo INEGI
CHK'D:		DATE: 04/06/22		
APP'D:				
MFG:				
Q.A:				
SCALE: 1:1		WEIGHT: 3		SHEET 1 OF 1

SECTION A-A



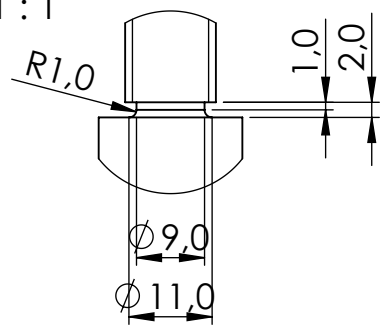
Tolerâncias gerais : ISO 2768 - m k

UNLESS OTHERWISE SPECIFIED: DIMENSIONS ARE IN MILLIMETERS		FINISH:		DO NOT SCALE DRAWING		REVISION	
SURFACE FINISH:							
TOLERANCES:							
LINEAR:							
ANGULAR:							
DRAWN	NAME	SIGNATURE	DATE	TITLE:		A3	
CHK'D	Ricardo Lobo		14/06/22	Bloco Superior		5	
APP'D				DWG NO.		SCALE: 1:3	
MFG				MATERIAL:		WEIGHT: 3	
Q.A.						SHEET 1 OF 1	



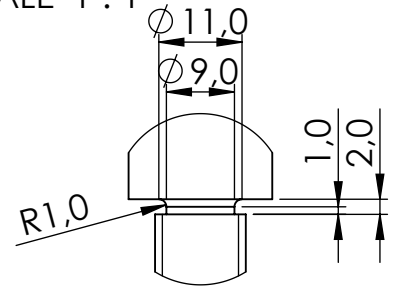
DETAIL A

SCALE 1 : 1



DETAIL B

SCALE 1 : 1



Ra 0,8

Tolerâncias Gerais: ISO 2768 - m k

UNLESS OTHERWISE SPECIFIED:
DIMENSIONS ARE IN MILLIMETERS
SURFACE FINISH:
TOLERANCES: ISO 2768 - m k
LINEAR:
ANGULAR:

FINISH:

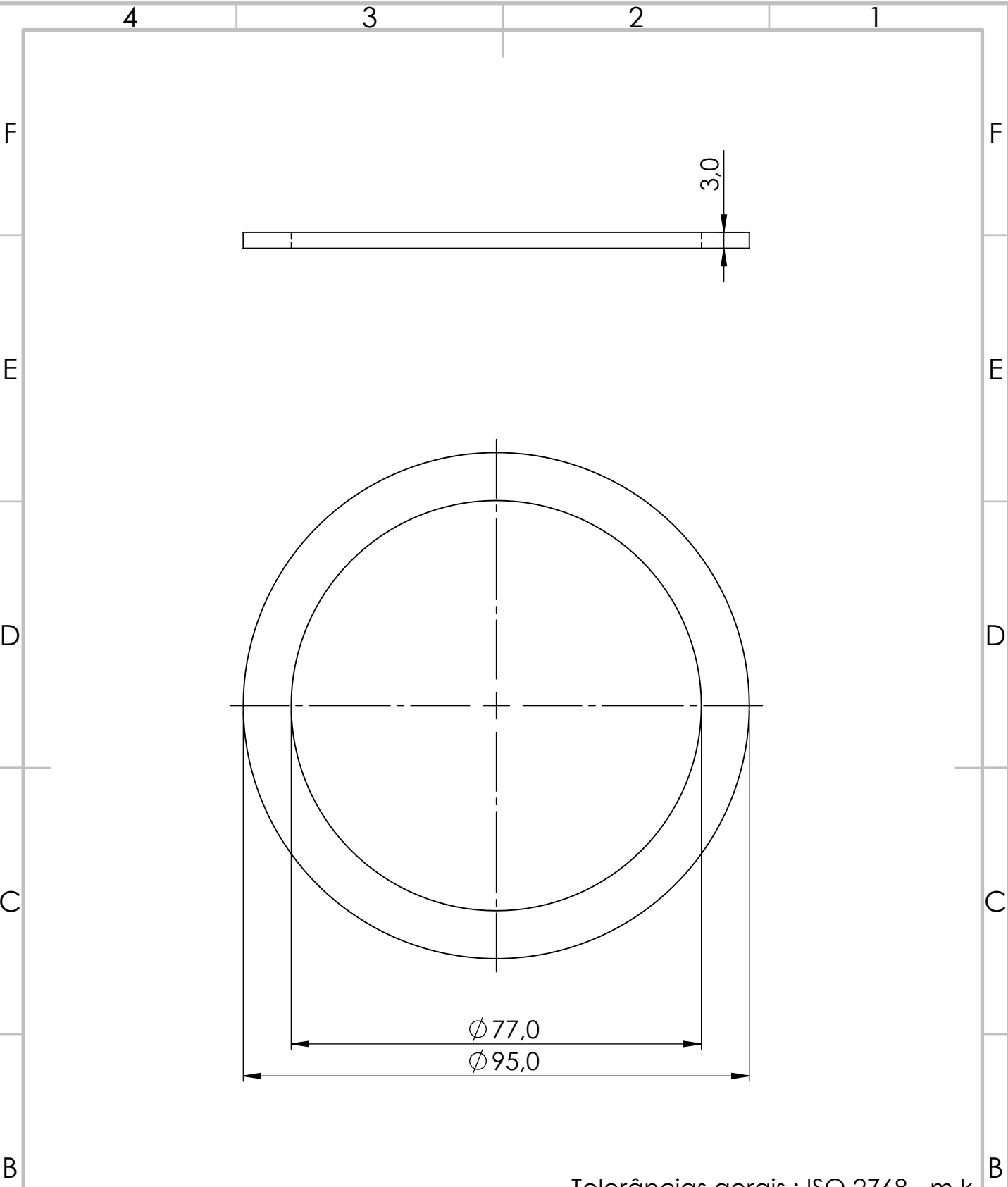
DO NOT SCALE DRAWING

REVISION

Quantidade : 2

NAME	SIGNATURE	DATE
DRAWN Ricardo Lobo		07/06/22
CHK'D		
APPV'D		
MFG		
Q.A		

TITLE:	Squared Section Bar	
MATERIAL:	Aço S690	
DWG NO.	6	A4
SCALE:1:2	SHEET 1 OF 1	



Tolerâncias gerais : ISO 2768 - m k

UNLESS OTHERWISE SPECIFIED:
 DIMENSIONS ARE IN MILLIMETERS
 SURFACE FINISH:
 TOLERANCES:
 LINEAR:
 ANGULAR:

FINISH:

DO NOT SCALE DRAWING REVISION

	NAME	SIGNATURE	DATE
DRAWN	Ricardo Lobo		07/06/22
CHK'D			
APPV'D			
MFG			
Q.A			

TITLE:
Lower Rubber Ring

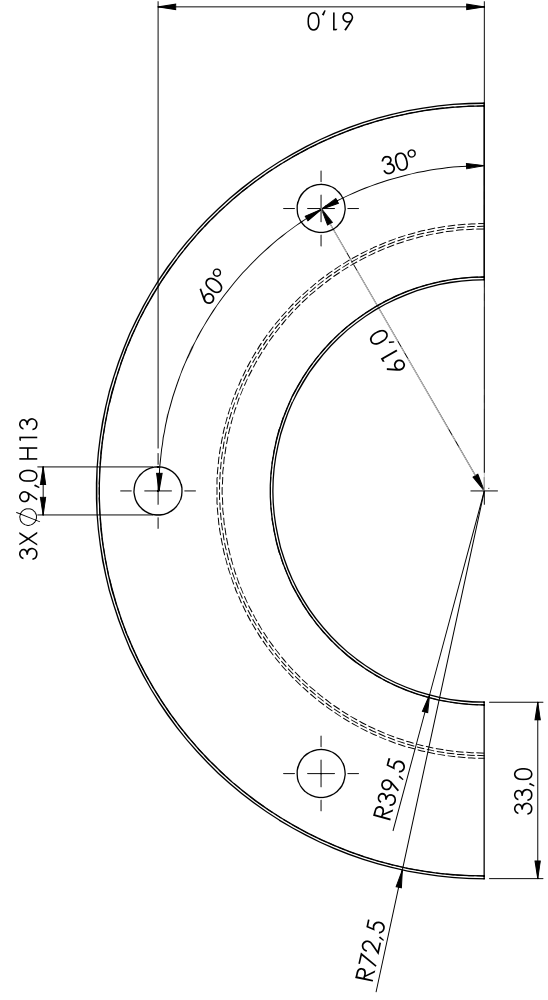
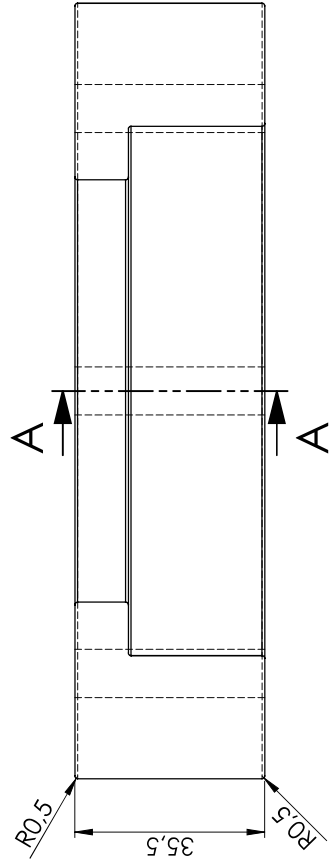
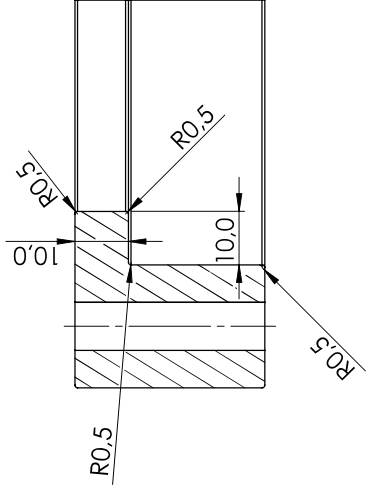
MATERIAL:
 Borracha

DWG NO.
8

SCALE:1:1 SHEET 1 OF 1

A4

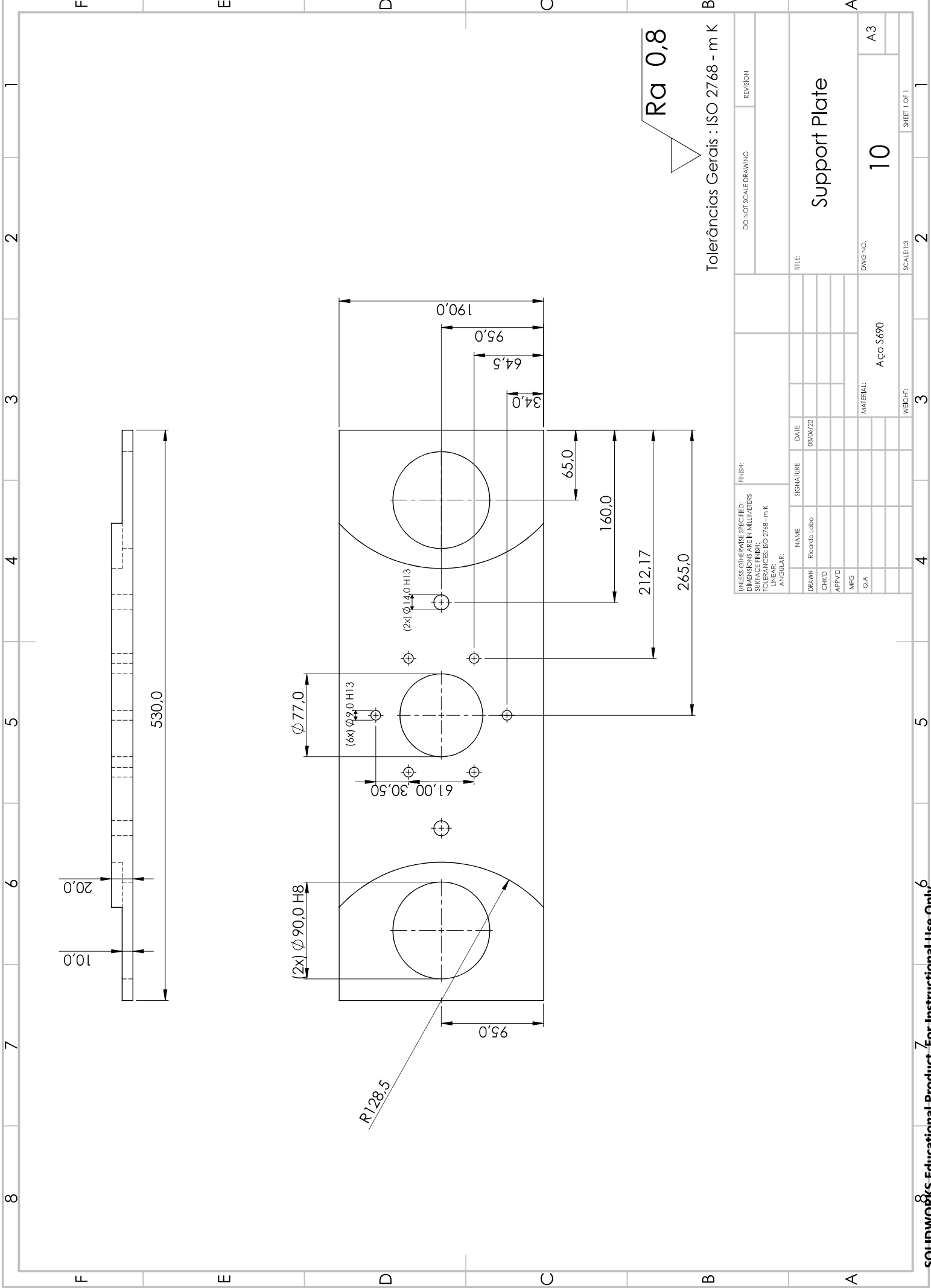
SECTION A-A



Ra 0,8

Tolerâncias Gerais : ISO 2768 - m K

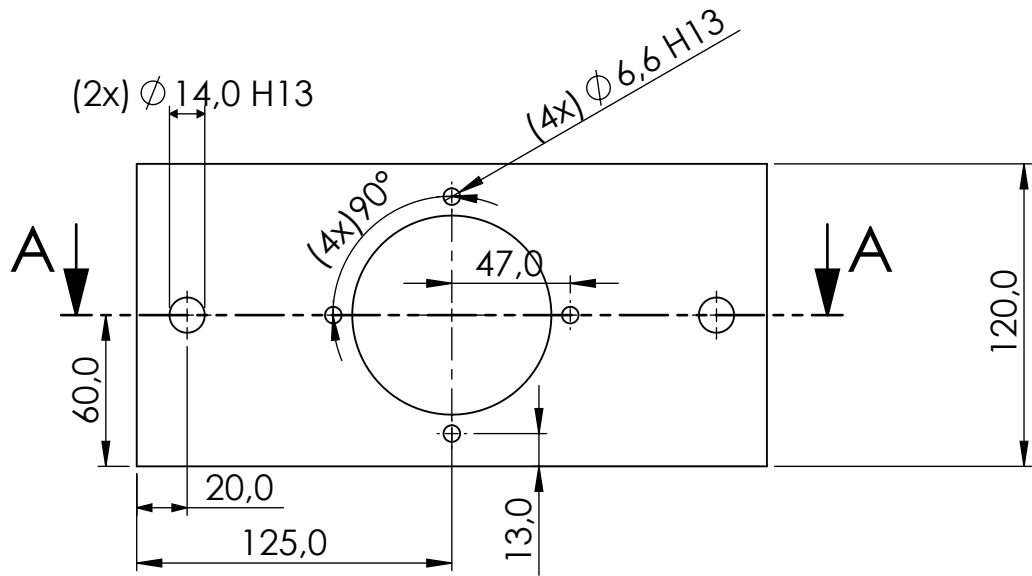
UNLESS OTHERWISE SPECIFIED: DIMENSIONS ARE IN MILLIMETERS SURFACE FINISH: TOLERANCES: ISO 2768 - m K		FINISH: BREAK SHARP EDGES		DO NOT SCALE DRAWING		REVISION		
NAME	SIGNATURE	DATE	TITLE:		DWG NO.		SHEET 1 OF 1	
DRAWN	Ricardo Lobo	08/06/22	Locking Support		9		A3	
CHECKED								
APPROVED								
MFG								
Q.A.								
MATERIAL:			P20 (PM300 F.Ramada)		SCALE: 1:1		WEIGHT:	
ANGULAR:					3		2	



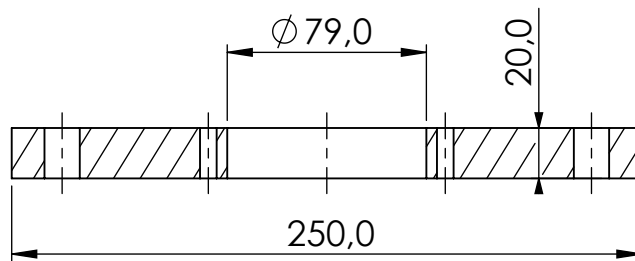
Tolerâncias Gerais : ISO 2768 - m K

Ra 0,8

DO NOT SCALE DRAWING		REVISION	
UNLESS OTHERWISE SPECIFIED: DIMENSIONS ARE IN MILLIMETERS SURFACE FINISH: TOLERANCES: ISO 2768 - m K			
LINEAR: ANGULAR:			
FINISH:	SIGNATURE	DATE	
DRAWN: Ricardo Lobo		08/06/22	
CHECKED:			
APPROVED:			
MFG:			
Q.A.			
TITLE: Support Plate		DWG NO. 10	
MATERIAL: Aço S690		SCALE: 1:3	
WEIGHT: 3		SHEET 1 OF 1	



SECTION A-A



$Ra\ 0,8$

Tolerâncias Gerais : ISO 2768 - m K

UNLESS OTHERWISE SPECIFIED:
DIMENSIONS ARE IN MILLIMETERS
SURFACE FINISH:
TOLERANCES: ISO 2768 - m K
LINEAR:
ANGULAR:

FINISH:

DO NOT SCALE DRAWING

REVISION

	NAME	SIGNATURE	DATE
DRAWN	Ricardo Lobo		14/06/22
CHK'D			
APPV'D			
MFG			
Q.A			

TITLE:

Traction Plate

MATERIAL:

Aço S690

DWG NO.

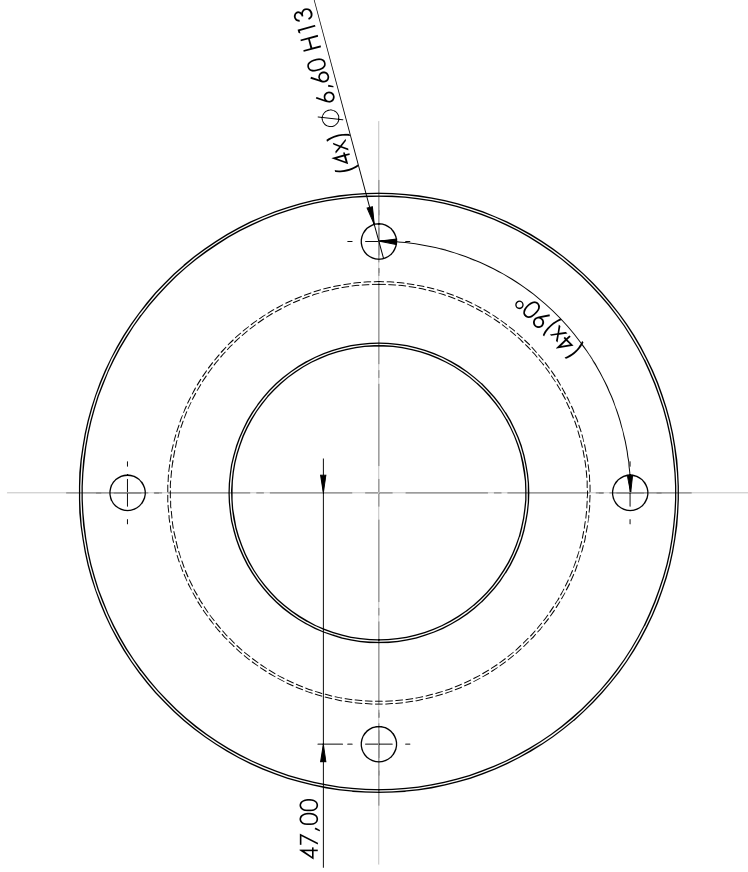
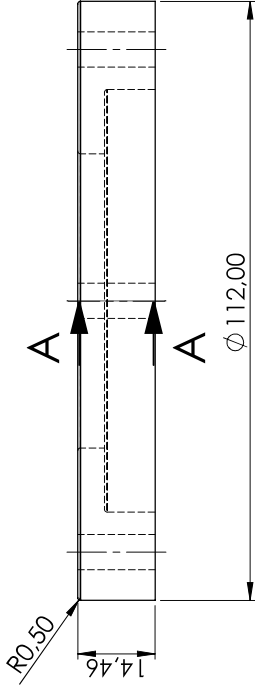
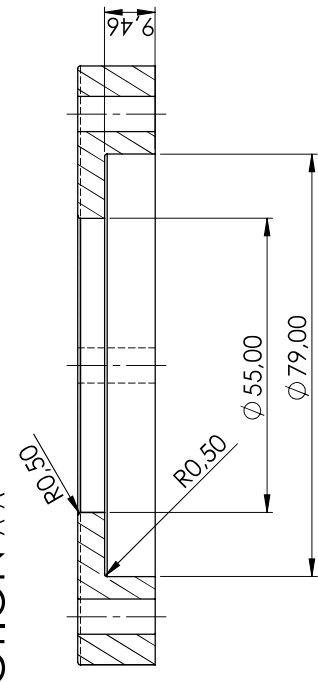
12

A4

SCALE:1:3

SHEET 1 OF 1

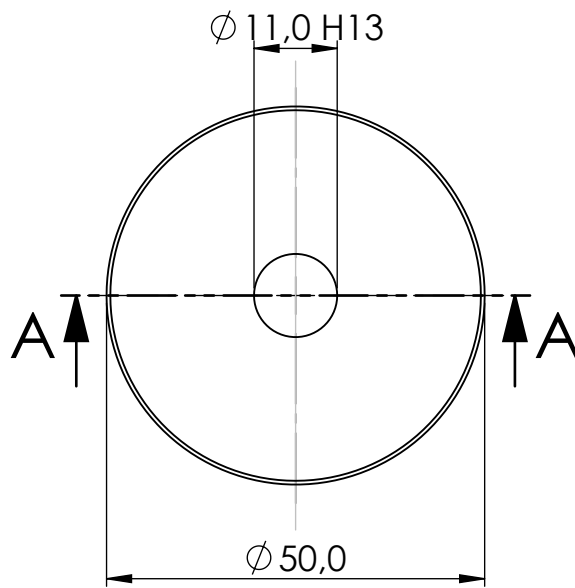
SECTION A-A



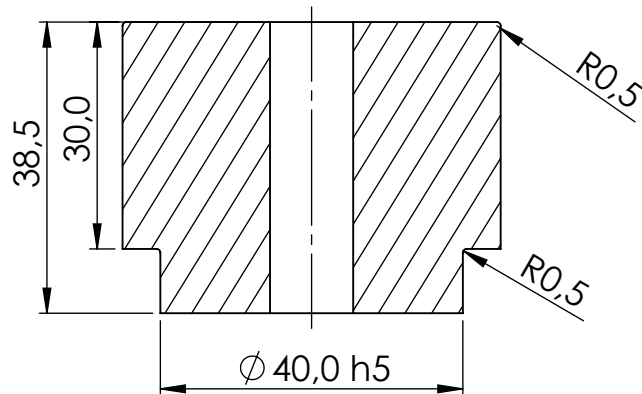
$Ra\ 0,8$

Tolerâncias Gerais : ISO 2768 - m K

UNLESS OTHERWISE SPECIFIED: DIMENSIONS ARE IN MILLIMETERS SURFACE FINISH: TOLERANCES: ISO 2768 - m K LINEAR: ANGULAR:		FINISH:		DO NOT SCALE DRAWING		REVISION	
DRAWN Ricardo Lobo		SIGNATURE		Quantidade : 2		TITLE: Bearing Case	
CHK'D		DATE 14/06/22		DWG NO. 13		A3	
APP'VD		MATERIAL: AÇO P20 (PM300 F. Ramada)		SCALE: 1:1		SHEET 1 OF 1	
MFG		G.A.		2		1	



SECTION A-A



$Ra\ 0,8$

Tolerâncias Gerais : ISO 2768 - m K

UNLESS OTHERWISE SPECIFIED:
DIMENSIONS ARE IN MILLIMETERS
SURFACE FINISH:
TOLERANCES: ISO2768 - m K
LINEAR:
ANGULAR:

FINISH:

DO NOT SCALE DRAWING

REVISION

	NAME	SIGNATURE	DATE
DRAWN	Ricardo Lobo		14/06/22
CHK'D			
APPV'D			
MFG			
Q.A			

TITLE:

Bearing Holder

MATERIAL:

Aço P20 (PM300 F.Ramada)

DWG NO.

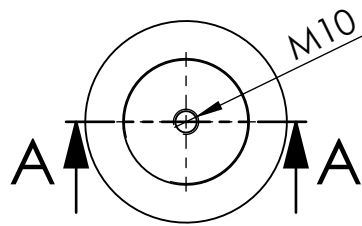
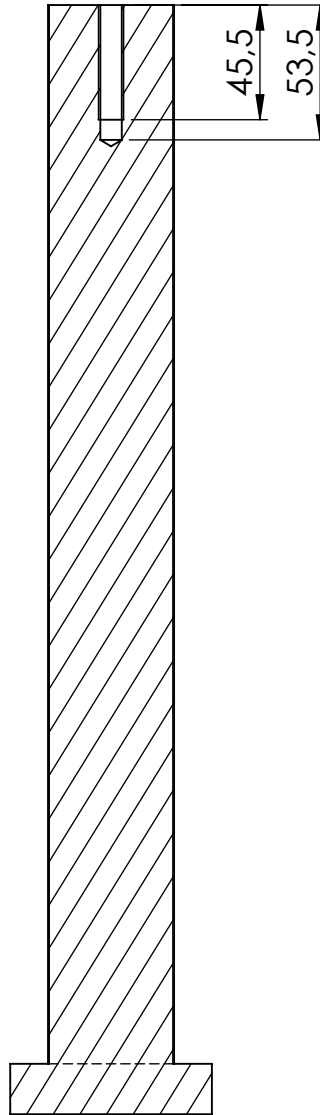
14

A4

SCALE:1:1

SHEET 1 OF 1

SECTION A-A



Tolerâncias gerais : ISO 2768 - m k

UNLESS OTHERWISE SPECIFIED:
DIMENSIONS ARE IN MILLIMETERS
SURFACE FINISH:
TOLERANCES:
LINEAR:
ANGULAR:

FINISH:

DO NOT SCALE DRAWING

REVISION

	NAME	SIGNATURE	DATE
DRAWN	Ricardo Lobo		14/06/22
CHK'D			
APPV'D			
MFG			
Q.A			

TITLE:

Power Screw

MATERIAL:

DWG NO.

15

A4

SCALE:1:3

SHEET 1 OF 1

Appendix D







Bolts Tightening Torque

The tables presented in this Appendix are exposed in [56], however, a correction was made to the subtitles.

FORÇA DE TRACÇÃO E BINÁRIO DE APERTO

			Passe largo mm	Secção resistente mm ²	Coeficiente de atrito	Classe de parafusos - Passe largo											
						4.8		5.8		6.8		8.8		10.9		12.9	
						força de tração N	binário de aperto Nm	força de tração N	binário de aperto Nm	força de tração N	binário de aperto Nm	força de tração N	binário de aperto Nm	força de tração N	binário de aperto Nm	força de tração N	binário de aperto Nm
M2	1,5	4	0,40	2,07	0,10 0,14	488,0 449,5	0,15 0,19	610,6 561,9	0,19 0,23	732,7 674,3	0,23 0,28	976,9 899,0	0,31 0,37	1373,8 1264,3	0,43 0,52	1648,6 1517,1	0,52 0,63
M2,5	2	5	0,45	3,39	0,10 0,14	813,5 749,9	0,31 0,38	1016,9 937,4	0,39 0,48	1220,2 1124,9	0,47 0,58	1627,0 1499,8	0,63 0,77	2288,0 2109,1	0,88 1,08	2745,6 2531,0	1,06 1,30
M3	2,5	5,5	0,50	5,03	0,10 0,14	1219,9 1125,9	0,54 0,60	1524,9 1407,4	0,68 0,83	1829,9 1688,9	0,82 1,00	2439,9 2251,9	1,09 1,34	3431,0 3166,7	1,53 1,88	4117,2 3800,0	1,84 2,26
M3,5	-	6	0,60	6,78	0,10 0,14	1638,2 1511,3	0,84 1,03	2047,8 1889,2	1,05 1,28	2457,3 2267,0	1,26 1,54	3276,4 3022,6	1,68 2,05	4607,5 4250,6	2,36 2,89	5528,9 5100,7	2,84 3,47
M4	3	7	0,70	8,78	0,10 0,14	2115,4 1950,9	1,25 1,53	2644,3 2438,7	1,56 1,91	3173,1 2926,4	1,88 2,29	4230,8 3901,9	2,50 3,06	5949,6 5487,0	3,52 4,30	7139,5 6584,4	4,22 5,16
M5	4	8	0,80	14,2	0,10 0,14	3461,6 3196,8	2,46 3,02	4327,0 3996,0	3,08 3,78	5192,3 4795,2	3,70 4,53	6923,1 6393,7	4,93 6,04	9735,7 8991,1	6,93 8,50	11682,8 10789,3	8,32 10,20
M6	5	10	1	20,1	0,10 0,14	4874,7 4499,1	4,24 5,19	6093,4 5623,9	5,30 6,48	7312,1 6748,6	6,35 7,78	9749,4 8998,2	8,47 10,37	13710,1 12653,7	11,92 14,59	16452,2 15184,4	14,30 17,51
M7	-	11	1	28,9	0,10 0,14	7134,5 6599,6	6,97 8,60	8918,2 8249,5	8,71 10,76	10701,8 9899,4	10,45 12,90	14269,1 13199,2	13,94 17,21	20065,9 18561,4	19,60 24,20	24079,1 22273,6	23,52 29,04
M8	6	13	1,25	36,6	0,10 0,14	8947,1 8265,6	10,20 12,54	11183,9 10332,0	12,75 15,67	13420,7 12398,4	15,30 18,80	17894,2 16531,2	20,41 25,07	25163,7 23247,0	28,70 35,26	30196,5 27896,5	34,44 42,31
M10	8	16	1,50	58	0,10 0,14	14244,5 13167,4	20,11 24,76	17805,6 16459,2	25,14 30,95	21366,8 19751,1	30,16 37,14	28489,0 26334,8	40,22 49,52	40062,7 37033,3	56,56 69,64	48075,3 44439,9	67,87 83,56
M12	10	18	1,75	84,3	0,10 0,14	20766,6 19204,0	34,43 42,42	25958,3 24005,0	43,03 53,03	31149,9 28806,0	51,64 63,63	41533,2 38408,0	68,86 84,84	58406,1 54011,2	96,83 119,31	70087,3 64813,5	116,20 143,17
M14	12	21	2	115	0,10 0,14	28389,9 26261,2	54,77 67,56	35487,4 32826,5	68,46 84,45	42584,9 39391,8	82,15 101,34	56779,8 52522,4	109,53 135,13	79846,6 73859,6	154,03 190,02	95816,0 88631,5	184,84 228,03
M16	14	24	2	157	0,10 0,14	39242,1 36364,2	85,14 105,80	49052,7 45455,3	106,43 132,26	58863,2 54546,3	127,72 158,71	78484,3 72728,5	170,29 211,61	110368,5 102274,4	239,47 297,58	132442,2 122729,3	287,36 357,09
M18	14	27	2,50	192	0,10 0,14	47533,0 43986,1	117,48 145,16	59416,3 54982,7	146,85 181,45	71299,6 65979,2	176,22 217,74	95066,1 87972,3	234,96 290,32	133686,7 123711,0	330,41 402,26	160424,1 148453,2	396,49 489,92
M20	17	30	2,50	245	0,10 0,14	61238,0 56747,1	166,08 206,39	76547,5 70933,9	207,61 257,98	91857,0 85120,6	249,13 309,58	122476,0 113494,2	332,17 412,78	172231,9 156601,2	467,11 580,47	206678,2 191521,5	560,54 696,56
M22	17	34	2,50	303	0,10 0,14	76305,2 70791,9	227,22 283,79	95381,5 88489,8	284,02 354,74	114457,8 106187,8	340,82 425,69	152610,4 141583,7	454,43 567,58	214608,3 199102,1	639,05 798,16	257530,0 238922,5	766,85 957,80
M24	19	36	3	353	0,10 0,14	88232,4 81761,8	287,16 358,84	110290,5 102202,2	358,94 446,05	132348,6 122642,7	430,73 535,26	176464,9 16,523,6	574,31 713,68	248153,7 229955,1	807,63 1003,61	297784,4 275946,1	969,15 1204,33
M27	19	41	3	459	0,10 0,14	115778,8 107441,5	420,04 525,08	144723,5 134301,9	525,05 656,35	173668,2 161162,2	630,06 787,62	231557,6 214883,0	840,08 1050,16	325627,9 302179,2	1181,36 1476,79	390753,4 362615,0	1417,63 1772,15
M30	22	46	3,50	561	0,10 0,14	140999,5 130770,6	572,83 714,49	176249,4 163463,3	716,03 893,11	211499,3 196155,9	859,24 1071,73	281999,0 261541,2	1145,65 1428,97	396561,1 367792,3	1611,08 2009,49	475873,4 441350,8	1933,29 2411,39
M33	24	50	3,50	694	0,10 0,14	175618,1 163058,0	774,65 970,43	219522,6 203822,5	968,32 1213,03	263427,1 244587,0	1161,98 1455,64	351236,2 326115,9	1549,31 1940,86	493925,8 458600,5	2178,72 2729,33	592711,0 550320,6	2614,46 3275,19
M36	27	55	4	817	0,10 0,14	206081,7 191241,8	998,60 1248,41	257602,2 239052,3	1248,25 1560,51	309122,6 286862,7	1497,89 1872,61	412163,5 382483,6	1997,19 2496,81	579604,8 537867,6	2808,55 3511,14	695525,8 645441,1	3370,26 4213,37
M39	-	60	4	976	0,10 0,14	247520,0 229902,6	1291,81 1620,96	309400,0 287378,3	1614,77 2026,20	371279,9 344853,9	1937,72 2431,44	495039,9 459805,2	2583,63 3241,92	696149,8 646601,0	3633,23 4558,96	835379,8 775921,3	4359,88 5470,75
M42	32	65	4,50	1120	0,10 0,14	283225,0 262939,0	1601,25 2005,46	354031,2 328673,8	2001,57 2506,83	424837,4 394408,5	2401,88 3008,20	566449,9 525878,0	3202,51 4010,93	796570,1 739516,0	4503,53 5640,37	955884,2 887419,2	5404,23 6768,44
M45	-	70	4,50	1310	0,10 0,14	332751,5 309151,8	2005,51 2519,55	415939,4 386439,7	2506,89 3149,43	499127,3 463727,7	3008,26 3779,32	665503,0 618303,6	4011,02 5039,09	935863,6 869489,3	5640,50 7086,23	1123036,0 1043387,0	6768,60 8503,47
M48	36	75	5	1470	0,10 0,14	372429,3 345862,9	2406,51 3018,11	465536,6 432328,7	3008,14 3772,64	558644,0 518794,4	3609,77 4527,17	744858,6 691725,8	4813,03 6036,23	1047457,0 972739,4	6768,32 8488,45	1256949,0 1167287,0	8121,98 10186,14
M52	-	80	5	1760	0,10 0,14	448108,9 416499,0	3099,96 3900,52	560136,1 520623,8	3874,95 4875,65	672163,4 624748,5	4649,93 5850,78	896217,8 832998,0	6199,91 7801,04	1260306,0 1171404,0	8718,63 10970,21	1512368,0 1405684,0	10462,36 13164,25
M56	41	85	5,50	2030	0,10 0,14	516202,9 479683,4	3838,14 4824,40	645253,6 599604,2	4797,68 6030,50	774304,4 719525,1	5757,21 7236,60	1032406,0 959366,8	7676,29 9648,80	1451821,0 1349110,0	10794,78 13568,63	1742185,0 1618931,0	12953,73 16282,36
M60	-	90	5,50	2360	0,10 0,14	602498,5 560267,5	4754,64 5992,71	753123,1 700334,4	5943,30 7490,88	903747,8 840401,2	7131,96 8989,06	1204997,0 1120535,0	9509,28 11985,42	1694527,0 1575752,0	13372,43 16854,49	2033432,0 1890903,0	16046,91 16282,36
M64	46	95	6	2680	0,10 0,14	683339,5 635299,9	5746,71 7235,13	854174,4 794124,9	7182,71 9043,92	1025009,0 952949,8	8619,25 10852,70	1366679,0 1270600,0	11492,34 14470,27	1921892,0 1786781,0	16161,10 20348,82	2306271,0 2144137,0	19393,32 24418,58
M68	-	100	6	3060	0,10 0,14	782799,9 728201,8	6939,64 8758,24	978499,8 910252,2	8674,55 10947,80	1174200,0 1092303,0	10409,46 13137,36	1565600,0 1456404,0	13879,28 17516,48	2201625,0 2048068,0	19517,74 24632,55	2641950,0 2457681,0	23421,29 29559,06

Classe de parafusos - Passe fino

  	 mm	 mm	 Passe fino mm	Secção resistente mm ²	Coeficiente de atrito	4.8		5.8		6.8		8.8		10.9		12.9	
						Força de tracção	Binário de aperto	Força de tracção	Binário de aperto	Força de tracção	Binário de aperto	Força de tracção	Binário de aperto	Força de tracção	Binário de aperto	Força de tracção	Binário de aperto
						N	Nm	N	Nm	N	Nm	N	Nm	N	Nm	N	Nm
M8	6	13	1	39,2	0,10 0,14	9798,1	10,87	12247,6	13,59	14697,1	16,31	19596,1	21,75	27557,1	30,58	33068,5	36,70
						9079,5	13,53	11349,4	16,91	13619,3	20,29	18159,1	27,05	25536,2	38,04	30643,4	45,65
M10	8	16	1,25	61,2	0,10 0,14	15296,9	21,13	19121,1	26,41	22945,3	31,69	30593,8	42,25	43022,5	59,42	51627,0	71,30
						14175,0	26,27	17718,8	32,84	21262,6	39,41	28350,1	52,55	39867,3	73,89	47840,8	88,67
M10	8	16	1	64,5	0,10 0,14	16383,6	22,12	20479,5	27,66	24575,4	33,19	32767,2	44,25	46078,8	62,23	55294,6	74,67
						15221,6	27,80	19027,0	34,75	22832,5	41,70	30443,3	55,61	42810,8	78,20	51373,0	93,84
M12	10	18	1,50	88,1	0,10 0,14	22020,7	35,83	27525,9	44,79	33031,0	53,75	44041,4	71,67	61933,2	100,78	74319,8	120,94
						20405,8	44,53	25507,2	55,66	30608,7	66,79	40811,6	89,06	57391,3	125,24	68869,5	150,29
M12	10	18	1,25	92,1	0,10 0,14	23333,7	37,26	29167,1	46,57	35000,6	55,88	46667,4	74,51	65626,1	104,78	78751,3	125,74
						21669,2	46,70	27086,5	58,38	32503,8	70,06	43338,4	93,41	60944,6	131,36	73133,5	157,63
M14	12	21	1,50	125	0,10 0,14	31610,0	59,04	39512,5	73,80	47415,0	88,57	63220,0	118,09	88903,1	166,06	106683,7	199,27
						29345,9	73,92	36682,4	92,40	44018,9	110,89	58691,9	147,85	82535,4	207,91	99042,5	1249,49
M16	14	24	1,50	167	0,10 0,14	42581,3	89,78	53226,6	112,33	63871,9	134,67	85162,5	179,56	119759,8	252,51	143711,8	303,02
						39587,8	113,06	49484,7	141,32	59381,6	169,59	79175,5	226,12	111340,6	317,98	133608,7	381,57
M18	14	27	2	204	0,10 0,14	51457,2	124,03	64321,5	155,03	77185,8	186,04	102914,4	248,06	144723,3	348,83	173668,0	418,59
						47751,7	155,02	59689,6	193,78	71627,5	232,53	95503,3	310,05	134301,6	436,00	161161,9	523,20
M18	14	27	1,50	216	0,10 0,14	55415,1	130,17	69268,9	162,72	83122,7	195,26	110830,3	260,35	155855,1	366,12	187026,1	439,34
						51577,6	164,67	64472,0	205,84	77366,4	247,01	103155,2	329,35	145062,1	463,15	174074,5	555,77
M20	17	30	2	258	0,10 0,14	65534,1	173,72	81917,7	217,16	98301,2	260,59	131068,3	347,45	184314,8	488,60	221177,8	586,32
						60886,2	218,17	76107,8	272,71	91329,3	327,26	121772,4	436,34	171242,5	613,61	205491,0	736,33
M20	17	30	1,50	272	0,10 0,14	70114,7	181,58	87643,3	226,97	105172,0	272,36	140229,3	363,15	197197,5	510,68	236637,0	612,82
						65319,1	230,55	81648,4	288,19	97978,6	345,82	130638,1	461,10	183709,9	648,42	220451,9	778,10
M22	17	34	2	318	0,10 0,14	81220,8	236,88	101526,0	296,10	121831,2	355,32	162441,5	473,76	228433,4	666,23	274120,1	799,48
						75533,9	298,75	94417,4	373,43	113300,9	448,12	151067,8	597,49	212439,1	840,22	254927,0	1008,27
M22	17	34	1,50	333	0,10 0,14	86164,2	246,02	107705,3	307,53	129246,4	369,04	172328,5	492,05	242337,0	691,94	290804,3	830,33
						80331,8	313,41	100414,7	391,76	120497,7	470,11	160663,6	626,82	225933,2	881,46	271119,8	1057,75
M24	19	36	2	384	0,10 0,14	98515,6	308,56	123144,5	385,70	147773,4	462,84	197031,1	617,12	277075,0	867,83	332490,0	1041,40
						91693,3	390,33	114616,6	487,92	137539,9	585,50	183386,5	780,67	257887,3	1097,82	309464,8	1371,38
M24	-	36	1,50	401	0,10 0,14	104079,4	319,62	130099,2	399,52	156119,0	479,43	208158,7	639,23	292723,2	898,92	351267,9	1078,71
						97096,0	408,12	121370,1	510,15	145644,1	612,18	194192,1	816,24	273082,6	1147,84	327699,1	1377,41
M27	19	41	2	496	0,10 0,14	127922,3	448,43	159902,9	560,54	191883,5	672,65	255844,7	896,87	359781,6	1261,22	431737,9	1513,46
						119185,0	569,67	148981,3	712,09	178777,5	854,51	238370,1	1139,34	335207,9	1602,20	402249,5	1922,64
M30	22	46	2	621	0,10 0,14	160817,5	623,80	201021,8	779,75	241226,2	935,70	321635,0	1247,60	452299,2	1754,43	542759,0	2105,32
						149957,0	795,14	187446,3	993,93	224935,5	1192,72	299914,0	1590,29	421754,2	2236,34	506105,0	2683,61
M33	24	50	2	761	0,10 0,14	197716,9	835,81	247146,1	1044,76	296575,4	1253,72	395433,8	1671,62	556078,8	2350,72	667294,5	2820,87
						184490,1	1068,24	230612,6	1335,30	276735,1	1602,36	368980,2	2136,49	518878,4	3004,43	622654,0	3605,32
M36	27	55	3	865	0,10 0,14	221916,8	1048,15	277396,0	1310,18	332875,1	1572,22	443833,5	2096,29	624140,9	2947,91	748969,0	3537,49
						206548,9	1326,13	258186,2	1657,66	309823,4	1989,19	413097,9	2652,26	580918,9	3729,74	697102,7	4475,68
M39	-	60	3	1030	0,10 0,14	265219,6	1351,70	331524,5	1689,63	397829,5	2027,56	530439,3	2703,41	745930,2	3801,67	895116,2	4562,00
						247027,0	1715,15	308783,8	2143,94	370540,5	2572,72	494054,1	3430,30	694763,5	4823,86	833716,1	5788,63
M42	32	65	3	1210	0,10 0,14	312529,3	1709,52	390661,6	2136,90	468793,9	2564,28	625058,5	3419,04	878988,6	4808,02	1054786,0	5769,62
						291268,7	2174,59	364085,9	2718,24	436903,1	3261,89	582537,4	4349,18	819193,3	6116,04	983031,9	7339,24
M45	-	70	3	1400	0,10 0,14	362551,7	2118,52	453189,7	2648,14	543827,6	3177,77	725103,5	4237,03	1019677,0	5958,33	1223612,0	7149,99
						338067,8	2700,72	422584,7	3375,90	507101,7	4051,08	676135,5	5401,43	950815,6	7595,77	1140979,0	9114,92
M48	36	75	3	1600	0,10 0,14	415279,0	2581,68	519098,7	3227,11	622918,5	3872,53	830558,0	5163,37	1167972,0	7260,99	1401567,0	8713,18
						387415,3	3297,46	484269,2	4121,83	581123,0	4946,20	774830,6	6594,93	1089606,0	9274,12	1307527,0	11128,94
M52	-	80	3	1900	0,10 0,14	494405,2	3299,14	618006,5	4123,92	741607,8	4948,71	988810,4	6598,28	1390515,5	9278,83	1668618,0	11134,60
						461482,7	4222,62	576853,3	5278,28	692224,0	6333,94	922965,3	8445,25	1297920,0	11876,13	1557504,0	14251,36
M56	41	85	4	2140	0,10 0,14	552738,4	4008,26	690923,0	5010,32	829107,5	6012,39	1105477,0	8016,51	1554577,0	11273,22	1865492,0	13527,87
						515137,2	5097,95	643921,5	6372,43	772705,8	7646,92	1030274,0	10195,89	1448823,0	14337,98	1738588,0	17205,57
M60	-	90	4	2480	0,10 0,14	642235,1	4950,24	802793,9	6187,80	963352,7	7425,36	1284470,0	9900,49	1806286,0	13922,56	2167544,0	16707,07
						598863,8	6309,01	748579,8	7886,27	898295,7	9463,52	1197728,0	12618,02	1684304,0	17744,10	2021165,0	21292,92
M64	46	95	4	2850	0,10 0,14	739716,3	6039,07	924645,4	7548,84	1109574,0	9058,60	1479433,0	12078,14	2080452,0	16984,88	2496543,0	20381,86
						690084,3	7710,76	862605,3	9638,45	1035126,0	11566,14	1380169,0	15421,52	1940862,0	21686,51	2329034,0	26023,81
M68	-	100	4	3240	0,10 0,14	842588,5	7263,31	1053236,0	9079,14	1263883,0	10894,97	1685177,0	14526,62	2369780,0	20428,06	2843736,0	24513,68
						786380,1	9288,98	982975,1	11611,23	1179570,0	13933,47	1572760,0	18577,96	2211694,0	26125,26	2654033,0	31350,31